

1

2

3

4

5

# Simultaneous Measurement of Oscillation Parameters in Beam and Atmospheric Neutrino Data from Tokai-to-Kamioka and Super-Kamiokande Experiments

6

Daniel Robert Clement Barrow

7

8

Magdalen College,  
Oxford University

9

Version 1.2

10

A Dissertation Submitted to Oxford University  
11 for the Degree of Doctor of Philosophy

13                   **Simultaneous Measurement of**

14                   **Oscillation Parameters in Beam and**

15                   **Atmospheric Neutrino Data from**

16                   **Tokai-to-Kamioka and**

17                   **Super-Kamiokande Experiments**

18                   *Abstract*

19                   Lorem ipsum dolor sit amet, consectetur adipiscing elit, sed do eiusmod tempor incididunt ut labore et dolore magna aliqua. Nulla aliquet porttitor lacus luctus accumsan tortor posuere. Pulvinar neque laoreet suspendisse interdum. Sem viverra aliquet eget sit. Nunc sed velit dignissim sodales ut eu sem integer vitae. At erat pellentesque adipiscing commodo elit at imperdiet dui accumsan. Fames ac turpis egestas integer eget aliquet nibh. Scelerisque eu ultrices vitae auctor eu augue. Purus non enim praesent elementum facilisis leo vel. Sollicitudin nibh sit amet commodo. Vitae auctor eu augue ut. Vel quam elementum pulvinar etiam. A condimentum vitae sapien pellentesque habitant morbi tristique senectus. Viverra accumsan in nisl nisi scelerisque eu ultrices. Sed viverra ipsum nunc aliquet bibendum enim.

## 32 Declaration

33 This dissertation is the result of my own work, except where ex-  
34 plicit reference is made to the work of others, and has not been sub-  
35 mitted for another qualification to this or any other university. This  
36 dissertation does not exceed the word limit for the respective Degree  
37 Committee.

38 Daniel Robert Clement Barrow

39 ©The copyright of this thesis rests with the author and is made available under a Creative  
40 Commons Attribution Non-Commercial No Derivatives licence. Researchers are free to copy,  
41 distribute or transmit the thesis on the condition that they attribute it, that they do not use  
42 it for commercial purposes and that they do not alter, transform or build upon it. For any  
43 reuse or redistribution, researchers must make clear to others the licence terms of this work.

44

## Acknowledgements

45 at pretium nibh ipsum. Eget nunc scelerisque viverra mauris in aliquam. Arcu vitae  
46 elementum curabitur vitae nunc sed velit dignissim. Sed arcu non odio euismod lacinia  
47 at quis risus sed. Vitae tempus quam pellentesque nec nam aliquam sem et tortor.  
48 Viverra aliquet eget sit amet tellus cras adipiscing. Purus sit amet luctus venenatis  
49 lectus magna. In aliquam sem fringilla ut morbi tincidunt augue. Fermentum dui  
50 faucibus in ornare. Aliquam malesuada bibendum arcu vitae elementum curabitur  
51 vitae nunc sed.

52 Ultricies leo integer malesuada nunc vel risus commodo. Tellus cras adipiscing  
53 enim eu turpis egestas pretium. Dictumst quisque sagittis purus sit amet volutpat  
54 consequat mauris nunc. Vitae congue mauris rhoncus aenean vel elit scelerisque  
55 mauris pellentesque. Vel facilisis volutpat est velit egestas dui id ornare. Suscipit  
56 adipiscing bibendum est ultricies. At in tellus integer feugiat scelerisque varius  
57 morbi enim. Cras semper auctor neque vitae tempus. Commodo sed egestas egestas  
58 fringilla phasellus faucibus. Cras pulvinar mattis nunc sed blandit. Pretium viverra  
59 suspendisse potenti nullam ac tortor vitae. Purus sit amet volutpat consequat. Orci  
60 sagittis eu volutpat odio facilisis mauris. Sit amet massa vitae tortor condimentum  
61 lacinia quis. Commodo sed egestas egestas fringilla phasellus. Sed libero enim sed  
62 faucibus turpis. Vitae tempus quam pellentesque nec.

63 Blandit massa enim nec dui. Viverra tellus in hac habitasse platea dictumst vestibulu-  
64 lum. Bibendum enim facilisis gravida neque convallis. Sagittis nisl rhoncus mattis  
65 rhoncus urna neque. Nisl rhoncus mattis rhoncus urna neque. Ac tortor vitae purus  
66 faucibus ornare. Aenean sed adipiscing diam donec adipiscing tristique risus. Sapien  
67 nec sagittis aliquam malesuada bibendum. Et leo duis ut diam quam nulla. Tellus  
68 rutrum tellus pellentesque eu tincidunt tortor aliquam nulla facilisi.

# **Contents**

<b>1</b>	<b>Introduction</b>	<b>1</b>
<b>2</b>	<b>Neutrino Oscillation Physics</b>	<b>2</b>
2.1	Discovery of Neutrinos . . . . .	2
2.2	Theory of Neutrino Oscillation . . . . .	4
2.2.1	Three Flavour Oscillations . . . . .	4
2.2.2	The MSW Effect . . . . .	8
2.3	Neutrino Oscillation Measurements . . . . .	9
2.3.1	Solar Neutrinos . . . . .	11
2.3.2	Atmospheric Neutrinos . . . . .	13
2.3.3	Accelerator Neutrinos . . . . .	16
2.3.4	Reactor Neutrinos . . . . .	18
2.4	Summary . . . . .	20
<b>3</b>	<b>T2K and SK Experiment Overview</b>	<b>23</b>
3.1	The Super-Kamiokande Experiment . . . . .	23
3.1.1	The SK Detector . . . . .	24
3.1.2	Calibration . . . . .	28
3.1.3	Data Acquisition and Triggering . . . . .	31
3.1.4	Cherenkov Radiation . . . . .	33
3.2	The Tokai to Kamioka Experiment . . . . .	35
3.2.1	The Neutrino Beam . . . . .	37
3.2.2	The Near Detector at 280m . . . . .	40
3.2.2.1	Fine Grained Detectors . . . . .	43
3.2.2.2	Time Projection Chambers . . . . .	44

93	3.2.2.3	$\pi^0$ Detector . . . . .	46
94	3.2.2.4	Electromagnetic Calorimeter . . . . .	46
95	3.2.2.5	Side Muon Range Detector . . . . .	48
96	3.2.3	The Interactive Neutrino GRID . . . . .	48
97	<b>4</b>	<b>Bayesian Statistics and Markov Chain Monte Carlo Techniques</b>	50
98	4.1	Bayesian Statistics . . . . .	51
99	4.2	Monte Carlo Simulation . . . . .	52
100	4.2.1	Markov Chain Monte Carlo . . . . .	53
101	4.2.2	Metropolis-Hastings Algorithm . . . . .	56
102	4.2.3	MCMC Optimisation . . . . .	58
103	4.3	Understanding the MCMC Results . . . . .	61
104	4.3.1	Marginalisation . . . . .	62
105	4.3.2	Parameter Estimation and Credible Intervals . . . . .	63
106	4.3.3	Bayesian Model Comparisons . . . . .	65
107	4.3.4	Comparison of MCMC Output to Expectation . . . . .	66
108	<b>5</b>	<b>Simulation, Reconstruction, and Event Reduction</b>	68
109	5.1	Simulation . . . . .	68
110	5.2	Event Reconstruction at SK . . . . .	73
111	5.2.1	Validation of Reconstruction in SK-V . . . . .	82
112	5.3	Event Reduction at SK . . . . .	86
113	<b>6</b>	<b>Sample Selections and Systematics</b>	92
114	6.1	Atmospheric Samples . . . . .	94
115	6.2	Near Detector Beam Samples . . . . .	101
116	6.3	Far Detector Beam Samples . . . . .	104
117	6.4	Systematic Uncertainties . . . . .	109
118	6.4.1	Beam Flux . . . . .	109

119	6.4.2 Atmospheric Flux . . . . .	111
120	6.4.3 Neutrino Interaction . . . . .	112
121	6.4.4 Near Detector . . . . .	118
122	6.4.5 Far Detector . . . . .	120
123	6.4.5.1 Beam Samples . . . . .	120
124	6.4.5.2 Atmospheric Samples . . . . .	123
125	6.4.5.3 Correlated Detector Model . . . . .	124
126	<b>7 Oscillation Probability Calculation</b>	<b>132</b>
127	7.1 Overview . . . . .	133
128	7.2 Treatment of Fast Oscillations . . . . .	141
129	7.3 Calculation Engine . . . . .	147
130	7.4 Matter Density Profile . . . . .	150
131	7.5 Production Height Averaging . . . . .	156
132	<b>8 Oscillation Analysis</b>	<b>160</b>
133	8.1 Likelihood Calculation . . . . .	160
134	<b>Bibliography</b>	<b>163</b>
135	<b>List of Figures</b>	<b>176</b>
136	<b>List of Tables</b>	<b>187</b>



<sup>138</sup> Chapter 1

<sup>139</sup> Introduction

<sup>140</sup> **Chapter 2**

<sup>141</sup> **Neutrino Oscillation Physics**

<sup>142</sup> When first proposed, neutrinos were expected to be massless fermions that only in-  
<sup>143</sup> teract through weak and gravitational forces. This meant they were very difficult to  
<sup>144</sup> detect as they can pass through significant amounts of matter without interacting. De-  
<sup>145</sup> spite this, experimental neutrino physics has developed with many different detection  
<sup>146</sup> techniques and neutrino sources being used today. In direct tension with standard  
<sup>147</sup> model physics, neutrinos have been determined to oscillate between different lepton  
<sup>148</sup> flavours, requiring them to have mass.

<sup>149</sup> The observation techniques which lead to the discovery of the neutrino are doc-  
<sup>150</sup> umented in section 2.1. The theory underpinning neutrino oscillation is described  
<sup>151</sup> in section 2.2 and includes the approximations which can be made to simplify the  
<sup>152</sup> understanding of neutrino oscillation in the two-flavour approximation. Past, current,  
<sup>153</sup> and future neutrino experiments are detailed in section 2.3, including the reactor,  
<sup>154</sup> atmospheric, and long-baseline accelerator neutrino sources that have been used to  
<sup>155</sup> successfully constrain oscillation parameters. Finally, the current state of oscillation  
<sup>156</sup> parameter measurements are summarised in section 2.4.

<sup>157</sup> **2.1 Discovery of Neutrinos**

<sup>158</sup> At the start of the 20<sup>th</sup> century, the electrons emitted from the  $\beta$ -decay of the nucleus  
<sup>159</sup> were found to have a continuous energy spectrum [1,2]. This observation seemingly  
<sup>160</sup> broke the energy conservation invoked within that period's nuclear models. Postulated

<sup>161</sup> in 1930 by Pauli as the solution to this problem, the neutrino (originally termed  
<sup>162</sup> “neutron”) was theorized to be an electrically neutral spin-1/2 fermion with a mass of  
<sup>163</sup> the same order of magnitude as the electron [3]. This neutrino was to be emitted with  
<sup>164</sup> the electron in  $\beta$ -decay to alleviate the apparent breaking of energy conservation. As a  
<sup>165</sup> predecessor of today’s weak interaction model, Fermi’s theory of  $\beta$ -decay developed  
<sup>166</sup> the understanding by coupling the four constituent particles; electron, proton, neutron,  
<sup>167</sup> and neutrino, into a consistent model [4].

<sup>168</sup> Whilst Pauli was not convinced of the ability to detect neutrinos, the first observa-  
<sup>169</sup> tions of the particle were made in the mid-1950s when neutrinos from a reactor were  
<sup>170</sup> observed via the inverse  $\beta$ -decay (IBD) process,  $\bar{\nu}_e + p \rightarrow n + e^+$  [5, 6]. The detector  
<sup>171</sup> consisted of two parts: a neutrino interaction medium and a liquid scintillator. The  
<sup>172</sup> interaction medium was built from two water tanks. These were loaded with cadmium  
<sup>173</sup> chloride to allow increased efficiency of neutron capture. The positron emitted from  
<sup>174</sup> IBD annihilates,  $e^+ + e^- \rightarrow 2\gamma$ , generating a prompt signal and the neutron is captured  
<sup>175</sup> on the cadmium via  $n + {}^{108}Cd \rightarrow {}^{109*}Cd \rightarrow {}^{109}Cd + \gamma$ , producing a delayed signal. An  
<sup>176</sup> increase in the coincidence rate was observed when the reactor was operating which  
<sup>177</sup> was interpreted as interactions from neutrinos generated in the reactor.

<sup>178</sup> After the discovery of the  $\nu_e$ , the natural question of how many flavours of neutrino  
<sup>179</sup> exist was asked. In 1962, a measurement of the  $\nu_\mu$  was conducted at the Brookhaven  
<sup>180</sup> National Laboratory [7]. A proton beam was directed at a beryllium target, generating  
<sup>181</sup> a  $\pi$ -dominated beam which then decayed via  $\pi^\pm \rightarrow \mu^\pm + (\nu_\mu, \bar{\nu}_\mu)$ , and the subsequent  
<sup>182</sup> interactions of the  $\nu_\mu$  were observed. As the subsequent interaction of the neutrino  
<sup>183</sup> generates muons rather than electrons, it was determined the  $\nu_\mu$  was fundamentally  
<sup>184</sup> different from  $\nu_e$ . The final observation to be made was that of the  $\nu_\tau$  from the DONUT  
<sup>185</sup> experiment [8]. Three neutrinos seem the obvious solution as it mirrors the known  
<sup>186</sup> number of charged lepton (as they form weak isospin doublets) but there could be

187 evidence of more. Several neutrino experiments have found anomalous results [9, 10]  
188 which could be attributed to sterile neutrinos. However, cosmological observations  
189 indicate the number of neutrino species  $N_{eff} = 2.99 \pm 0.17$  [11], as measured from  
190 the cosmic microwave background power spectrum, and LEP measured the number  
191 of active neutrino flavours to be  $N_\nu 2.9840 \pm 0.0082$  [12] from measurements of the  
192  $Z$ -decay width.

## 193 2.2 Theory of Neutrino Oscillation

194 As direct evidence of beyond Standard Model physics, a neutrino generated with  
195 lepton flavour  $\alpha$  can change into a different lepton flavour  $\beta$  after propagating some  
196 distance. This phenomenon is called neutrino oscillation and requires that neutrinos  
197 must have a non-zero mass (as seen in subsection 2.2.1). This observation is direct  
198 evidence of beyond standard model physics. This behaviour has been characterised  
199 by the Pontecorvo-Maki-Nakagawa-Sakata (PMNS) [13–15] mixing matrix which  
200 describes how the flavour and mass of neutrinos are associated. This is analogous to  
201 the Cabibbo-Kobayashi-Maskawa (CKM) [16] matrix measured in quark physics.

### 202 2.2.1 Three Flavour Oscillations

203 The PMNS parameterisation defines three flavour eigenstates,  $\nu_e$ ,  $\nu_\mu$  and  $\nu_\tau$  (indexed  
204  $\nu_\alpha$ ), which are eigenstates of the weak interaction and three mass eigenstates,  $\nu_1$ ,  $\nu_2$  and  
205  $\nu_3$  (indexed  $\nu_i$ ). Each mass eigenstate is the superposition of all three flavour states,

$$|\nu_i\rangle = \sum_\alpha U_{\alpha i} |\nu_\alpha\rangle. \quad (2.1)$$

206 Where  $U$  is the PMNS matrix which is unitary and connects the mass and flavour

207 eigenstates.

208 The weak interaction couples to flavour eigenstates so neutrinos interact with

209 leptons of the same flavour. The propagation of a neutrino flavour eigenstate, in a

210 vacuum, can be re-written as a plane-wave solution to the time-dependent Schrödinger

211 equation,

$$|\nu_\alpha(t)\rangle = \sum_i U_{\alpha i}^* |\nu_i\rangle e^{-i\phi_i}. \quad (2.2)$$

212 The probability of observing a neutrino of flavour eigenstate  $\beta$  from one which

213 originated as flavour  $\alpha$  can be calculated as,

$$P(\nu_\alpha \rightarrow \nu_\beta) = |\langle \nu_\beta | \nu_\alpha(t) \rangle|^2 = \sum_{i,j} U_{\alpha i}^* U_{\beta i} U_{\alpha j} U_{\beta j}^* e^{-i(\phi_j - \phi_i)} \quad (2.3)$$

214 The  $\phi_i$  term can be expressed in terms of the energy,  $E_i$ , and magnitude of the

215 three momenta,  $p_i$ , of the neutrino,  $\phi_i = E_i t - p_i x$  ( $t$  and  $x$  being time and position

216 coordinates). Therefore,

$$\phi_j - \phi_i = E_j t - E_i t - p_j x + p_i x. \quad (2.4)$$

217 For a relativistic particle,  $E_i \gg m_i$ ,

$$p_i = \sqrt{E_i^2 - m_i^2} \approx E_i - \frac{m_i^2}{2E_i}. \quad (2.5)$$

218 Making the approximations that neutrinos are relativistic, the mass eigenstates  
219 were created with the same energy and that  $x = L$ , where  $L$  is the distance traveled by  
220 the neutrino, Equation 2.4 then becomes

$$\phi_j - \phi_i = \frac{\Delta m_{ij}^2 L}{2E}, \quad (2.6)$$

221 where  $\Delta m_{ij}^2 = m_j^2 - m_i^2$ . This, combined with further use of unitarity relations  
222 results in Equation 2.3 becoming

$$P(\nu_\alpha \rightarrow \nu_\beta) = \delta_{\alpha\beta} - 4 \sum_{i>j} \Re \left( U_{\alpha i}^* U_{\beta i} U_{\alpha j} U_{\beta j}^* \right) \sin^2 \left( \frac{\Delta m_{ij}^2 L}{4E} \right) + (-) 2 \sum_{i>j} \Im \left( U_{\alpha i}^* U_{\beta i} U_{\alpha j} U_{\beta j}^* \right) \sin \left( \frac{\Delta m_{ij}^2 L}{2E} \right). \quad (2.7)$$

223 Where  $\delta_{\alpha\beta}$  is the Kronecker delta function and the negative sign on the last term is  
224 included for the oscillation probability of antineutrinos.

225 Typically, the PMNS matrix is parameterised into three mixing angles, a charge  
226 parity (CP) violating phase  $\delta_{CP}$ , and two Majorana phases  $\alpha_{1,2}$ ,

$$U = \underbrace{\begin{pmatrix} 1 & 0 & 0 \\ 0 & c_{23} & s_{23} \\ 0 & -s_{23} & c_{23} \end{pmatrix}}_{\text{Atmospheric, Accelerator}} \underbrace{\begin{pmatrix} c_{13} & 0 & s_{13}e^{-i\delta_{CP}} \\ 0 & 1 & 0 \\ -s_{13}e^{-i\delta_{CP}} & 0 & c_{13} \end{pmatrix}}_{\text{Reactor, Accelerator}} \underbrace{\begin{pmatrix} c_{12} & s_{12} & 0 \\ -s_{12} & c_{12} & 0 \\ 0 & 0 & 1 \end{pmatrix}}_{\text{Reactor, Solar}} \underbrace{\begin{pmatrix} e^{i\alpha_1/2} & 0 & 0 \\ 0 & e^{i\alpha_2/2} & 0 \\ 0 & 0 & 1 \end{pmatrix}}_{\text{Majorana}}. \quad (2.8)$$

<sup>227</sup> Where  $s_{ij} = \sin(\theta_{ij})$  and  $c_{ij} = \cos(\theta_{ij})$ . The oscillation parameters are often  
<sup>228</sup> grouped; (1,2) as “solar”, (2,3) as “atmospheric” and (1,3) as “reactor”. Many  
<sup>229</sup> neutrino experiments aim to measure the PMNS parameters from a wide array of  
<sup>230</sup> origins, as is the purpose of this thesis.

<sup>231</sup> The Majorana phase,  $\alpha_{1,2}$ , included within the fourth matrix in Equation 2.8 is only  
<sup>232</sup> included for completeness. For an oscillation analysis experiment, any terms contain-  
<sup>233</sup> ing this phase disappear due to taking the expectation value of the PMNS matrix.  
<sup>234</sup> Measurements of these phases are typically performed by experiments searching for  
<sup>235</sup> neutrino-less double  $\beta$ -decay [17].

<sup>236</sup> A two flavour approximation can be obtained when one assumes the third mass  
<sup>237</sup> eigenstate is degenerate with another. As discussed in section 2.3, it is found that  
<sup>238</sup>  $\Delta m_{21}^2 \ll |\Delta m_{31}^2|$ . This results in the two flavour approximation being reasonable for  
<sup>239</sup> understanding the features of the oscillation. In this two flavour case, the mixing  
<sup>240</sup> matrix becomes,

$$U_{2 \text{ Flav.}} = \begin{pmatrix} \cos(\theta) & \sin(\theta) \\ -\sin(\theta) & \cos(\theta) \end{pmatrix}. \quad (2.9)$$

<sup>241</sup> This culminates in the oscillation probability,

$$\begin{aligned} P(\nu_\alpha \rightarrow \nu_\alpha) &= 1 - \sin^2(2\theta) \sin^2\left(\frac{\Delta m^2 L}{4E}\right), \\ P(\nu_\alpha \rightarrow \nu_\beta) &= \sin^2(2\theta) \sin^2\left(\frac{\Delta m^2 L}{4E}\right). \end{aligned} \tag{2.10}$$

<sup>242</sup> Where  $\alpha \neq \beta$ . For a fixed neutrino energy, the oscillation probability is a sinusoidal  
<sup>243</sup> function depending upon the distance over which the neutrino propagates. The  
<sup>244</sup> frequency and amplitude of oscillation are dependent upon  $\Delta m^2/4E$  and  $\sin^2 2\theta$ ,  
<sup>245</sup> respectively. The oscillation probabilities presented thus far assume  $c = 1$ , where  
<sup>246</sup>  $c$  is the speed of light in vacuum. In more familiar units, the maximum oscillation  
<sup>247</sup> probability for a fixed value of  $\theta$  is given at  $L[km]/E[GeV] \sim 1.27/\Delta m^2$ . It is this  
<sup>248</sup> calculation that determines the best  $L/E$  value for a given experiment to be designed  
<sup>249</sup> around for measurements of a specific value of  $\Delta m^2$ .

## <sup>250</sup> 2.2.2 The MSW Effect

<sup>251</sup> The theory of neutrino oscillation in a vacuum has been described in subsection 2.2.1.  
<sup>252</sup> However, the beam neutrinos and atmospheric neutrinos originating from below the  
<sup>253</sup> horizon propagate through matter in the Earth. The coherent scattering of neutrinos  
<sup>254</sup> from a material target modifies the Hamiltonian of the system. This results in a change  
<sup>255</sup> in the oscillation probability. Notably, charged current scattering ( $\nu_e + e^- \rightarrow \nu_e + e^-$ ,  
<sup>256</sup> propagated by a  $W$  boson) only affects electron neutrinos whereas the neutral current  
<sup>257</sup> scattering ( $\nu_l + l^- \rightarrow \nu_l + l^-$ , propagated by a  $Z^0$  boson) interacts through all neutrino  
<sup>258</sup> flavours equally. In the two-flavour approximation, the effective mixing parameter  
<sup>259</sup> becomes

$$\sin^2(2\theta) \rightarrow \sin^2(2\theta_m) = \frac{\sin^2(2\theta)}{(A/\Delta m^2 - \cos(2\theta))^2 + \sin^2(2\theta)}, \quad (2.11)$$

where  $A = 2\sqrt{2}G_F N_e E$ ,  $N_e$  is the electron density of the medium and  $G_F$  is Fermi's constant. It is clear to see that there exists a value of  $A = \Delta m^2 \cos(2\theta)$  for  $\Delta m^2 > 0$  which results in a divergent mixing parameter. This resonance is termed the Mikheyev-Smirnov-Wolfenstein (MSW) effect (or more colloquially, the matter resonance) which regenerates the electron neutrino component of the neutrino flux [18–20]. The density at which the resonance occurs is given by

$$N_e = \frac{\Delta m^2 \cos(2\theta)}{2\sqrt{2}G_F E}. \quad (2.12)$$

At densities lower than this critical value, the oscillation probability will be much closer to that of vacuum oscillation. For antineutrinos,  $N_e \rightarrow -N_e$  [21]. The resonance occurring from the MSW effect depends on the sign of  $\Delta m^2$ . Therefore, any neutrino oscillation experiment which observes neutrinos and antineutrinos which have propagated through matter can have some sensitivity to the ordering of the neutrino mass eigenstates.

## 2.3 Neutrino Oscillation Measurements

As evidence of beyond standard model physics, the 2015 Nobel Prize in Physics was awarded to the Super-Kamiokande (SK) [22] and Sudbury Neutrino Observatory (SNO) [23] collaborations for the first definitive observation of solar and atmospheric

<sup>276</sup> neutrino oscillation [24]. Since then, the field has seen a wide array of oscillation  
<sup>277</sup> measurements from a variety of neutrino sources. As seen in subsection 2.2.1, the  
<sup>278</sup> neutrino oscillation probability is dependent on the ratio of the propagation baseline,  $L$ ,  
<sup>279</sup> to the neutrino energy,  $E$ . It is this ratio that determines the type of neutrino oscillation  
<sup>280</sup> a particular experiment is sensitive to.

<sup>281</sup> As illustrated in Figure 2.1, there are many neutrino sources that span a wide  
<sup>282</sup> range of energies. The least energetic neutrinos are from diffuse supernovae and  
<sup>283</sup> terrestrial neutrinos at  $O(1)$  MeV whereas the most energetic neutrinos originate from  
<sup>284</sup> atmospheric and galactic neutrinos of  $> O(1)$  TeV.

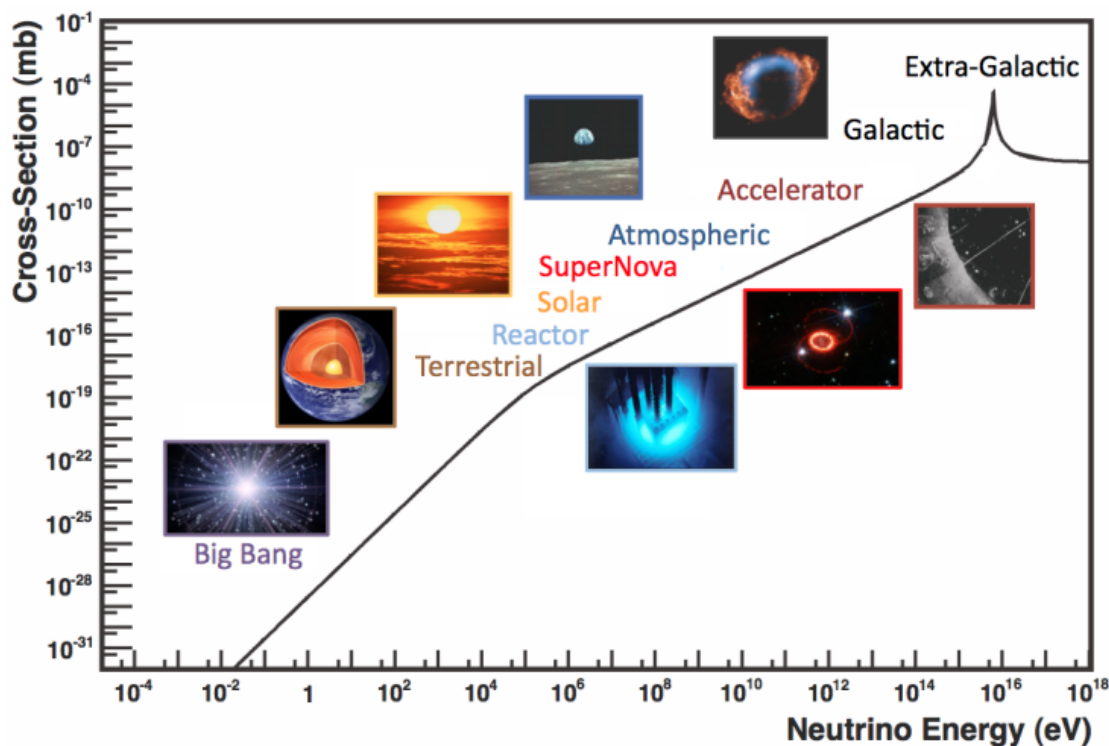


**Figure 2.1:** The cross-section of neutrinos from various natural and man-made sources as a function of neutrino energy. Taken from [25]

### <sup>285</sup> 2.3.1 Solar Neutrinos

<sup>286</sup> Solar neutrinos are emitted from fusion reaction chains at the center of the Sun. The  
<sup>287</sup> solar neutrino flux, given as a function of neutrino energy for different fusion and  
<sup>288</sup> decay chains, is illustrated in Figure 2.2. Whilst proton-proton fusion generates the  
<sup>289</sup> largest flux of neutrinos, the neutrinos are of low energy and are difficult to reconstruct  
<sup>290</sup> due to the IBD interaction threshold of 1.8MeV. Consequently, most experiments focus  
<sup>291</sup> on the neutrinos from the decay of  $^8B$  (via  $^8B \rightarrow ^8Be^* + e^+ + \nu_e$ ), which are higher  
<sup>292</sup> energy.

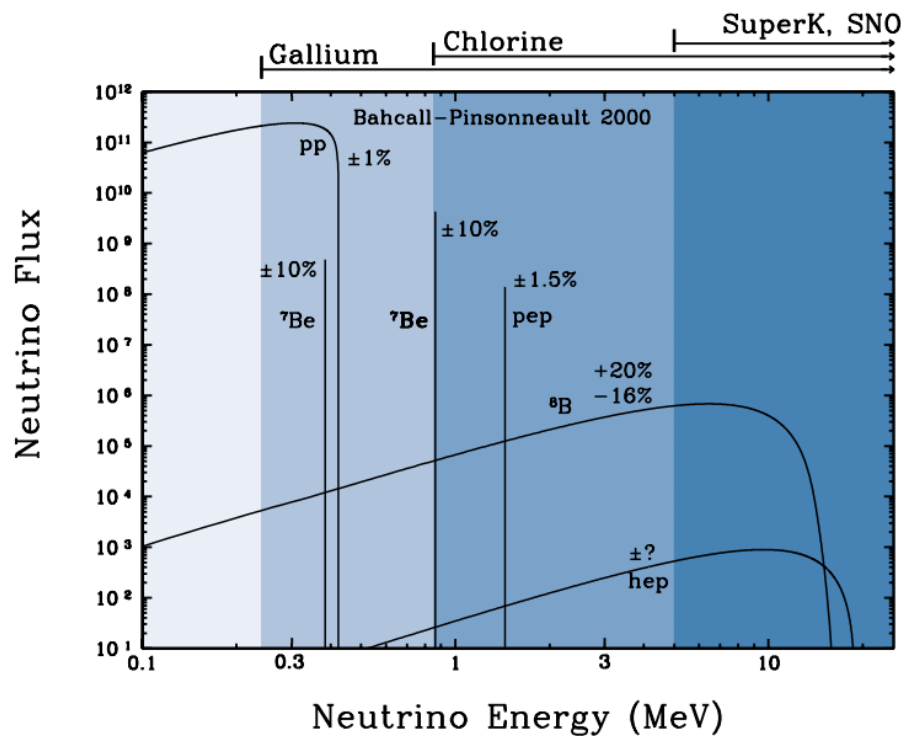


**Figure 2.2:** The solar neutrino flux as a function of neutrino energy for various fusion reactions and decay chains as predicted by the Standard Solar Model. Taken from [26].

<sup>293</sup> The first measurements of solar neutrinos observed a significant reduction in the  
<sup>294</sup> event rate compared to predictions from the Standard Solar Model [27, 28]. The  
<sup>295</sup> proposed solution to this “solar neutrino problem” was  $\nu_e \leftrightarrow \nu_\mu$  oscillations in a

<sup>296</sup> precursory version of the PMNS model [29]. The Kamiokande [30], Gallex [31] and  
<sup>297</sup> Sage [32] experiments confirmed the  $\sim 0.5$  factor deficit of solar neutrinos.

<sup>298</sup> The conclusive solution to this problem was determined by the SNO collaboration  
<sup>299</sup> [33]. Using a deuterium water target to observe  ${}^8B$  neutrinos, the event rate of charged  
<sup>300</sup> current (CC), neutral current (NC), and elastic scattering (ES) interactions (Given in  
<sup>301</sup> Equation 2.13) was simultaneously measured. CC events can only occur for electron  
<sup>302</sup> neutrinos, whereas the NC channel is agnostic to neutrino flavour, and the ES reaction  
<sup>303</sup> has a slight excess sensitivity to electron neutrino interactions. This meant that there  
<sup>304</sup> were direct measurements of the  $\nu_e$  and  $\nu_x$  neutrino flux. It was concluded that the  
<sup>305</sup> CC and ES interaction rates were consistent with the deficit previously observed.  
<sup>306</sup> Most importantly, the NC reaction rate was only consistent with the others under the  
<sup>307</sup> hypothesis of flavour transformation.



<sup>308</sup> Many experiments have since measured the neutrino flux of different interaction  
<sup>309</sup> chains within the sun [34–36]. The most recent measurement was that of CNO neutrinos  
<sup>310</sup> which were recently observed with  $5\sigma$  significance by the Borexino collaboration.  
<sup>311</sup> Future neutrino experiments aim to further these spectroscopic measurements of  
<sup>312</sup> different fusion chains within the Sun [37–39]. Solar neutrinos act as an irreducible  
<sup>313</sup> background for dark matter experiments like DARWIN but oscillation parameter  
<sup>314</sup> measurements can be made [40].

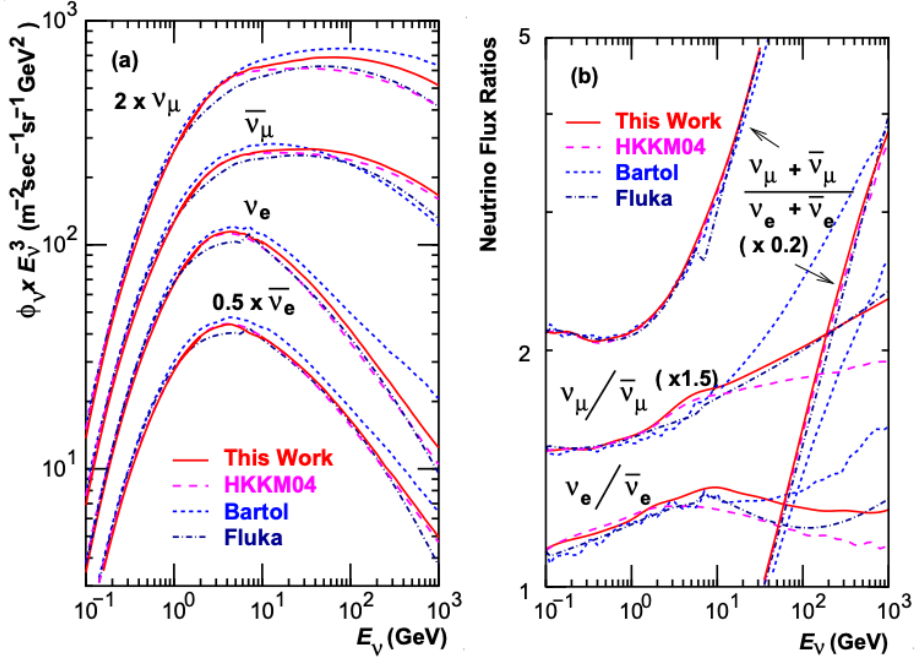
### <sup>315</sup> 2.3.2 Atmospheric Neutrinos

- <sup>316</sup> The interactions of primary cosmic ray protons in Earth's upper atmosphere generate  
<sup>317</sup> showers of energetic hadrons. These are mostly pions and kaons which when they  
<sup>318</sup> decay produce a natural source of neutrinos spanning energies of MeV to TeV [41].  
<sup>319</sup> The main decay is via

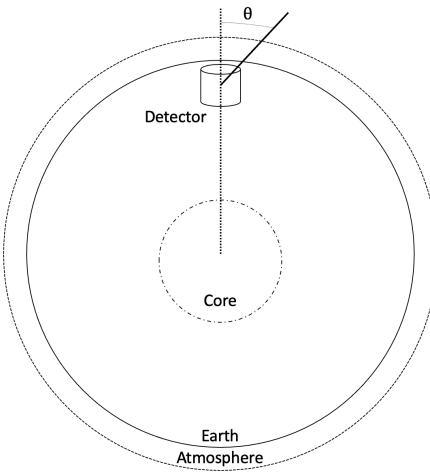
$$\begin{aligned} \pi^\pm &\rightarrow \mu^\pm + (\nu_\mu, \bar{\nu}_\mu) \\ \mu^\pm &\rightarrow e^\pm + (\nu_e, \bar{\nu}_e) + (\nu_\mu, \bar{\nu}_\mu) \end{aligned} \tag{2.14}$$

<sup>320</sup> such that for a single pion decay, three neutrinos are typically produced. The  
<sup>321</sup> atmospheric neutrino flux energy spectra as predicted by the Bartol [42], Honda  
<sup>322</sup> [43–45], and FLUKA [46] models are illustrated in Figure 2.3. The flux distribution  
<sup>323</sup> peaks at an energy of  $O(10)\text{GeV}$ . The uncertainties associated with these models  
<sup>324</sup> are dominated by the hadronic production of kaon and pions as well as the primary  
<sup>325</sup> cosmic flux.

<sup>326</sup> Unlike long-baseline experiments which have a fixed baseline, the distance at-  
<sup>327</sup> mospheric neutrinos propagate is dependent upon the zenith angle at which they  
<sup>328</sup> interact. This is illustrated in Figure 2.4. Neutrinos that are generated directly above  
<sup>329</sup> the detector ( $\cos(\theta) = 1.0$ ) have a baseline equivalent to the height of the atmosphere  
<sup>330</sup> whereas neutrinos that interact directly below the detector ( $\cos(\theta) = -1.0$ ) have to  
<sup>331</sup> travel a length equal to the diameter of the Earth. This means atmospheric neutrinos  
<sup>332</sup> have a baseline that varies from  $O(20)\text{km}$  to  $O(6 \times 10^3)\text{km}$ . Any neutrino generated  
<sup>333</sup> at or below the horizon will be subject to matter effects as they propagate through the  
<sup>334</sup> Earth.



**Figure 2.3:** Left panel: The atmospheric neutrino flux for different neutrino flavours as a function of neutrino energy as predicted by the 2007 Honda model (“This work”) [43], the 2004 Honda model (“HKKM04”) [44], the Bartol model [42] and the FLUKA model [46]. Right panel: The ratio of the muon to electron neutrino flux as predicted by all the quoted models. Both figures taken from [43].



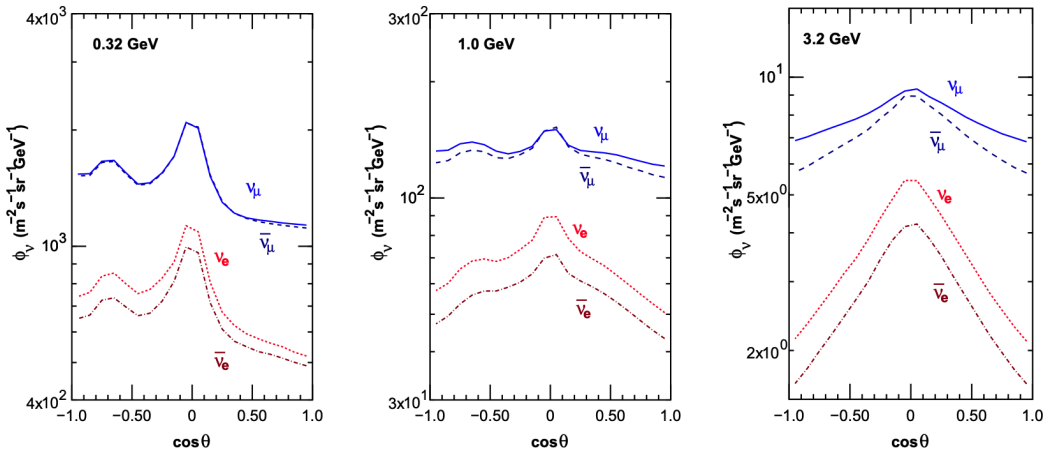
**Figure 2.4:** A diagram illustrating the definition of zenith angle as used in the Super Kamiokande experiment [47].

Figure 2.5 highlights the neutrino flux as a function of the zenith angle for different

slices of neutrino energy. For medium to high-energy neutrinos (and to a lesser degree

for low-energy neutrinos), the flux is approximately symmetric around  $\cos(\theta) = 0$ .

To the accuracy of this approximation, the systematic uncertainties associated with atmospheric flux for comparing upward-going and down-going neutrino cancels. This allows the down-going events, which are mostly insensitive to oscillation probabilities, to act as an unoscillated prediction (similar to a near detector in an accelerator neutrino experiment).



**Figure 2.5:** Prediction of  $\nu_e, \bar{\nu}_e, \nu_\mu, \bar{\nu}_\mu$  fluxes as a function of zenith angle as calculated by the HKKM model [45]. The left, middle and right panels represent three values of neutrino energy, 0.32GeV, 1.0GeV and 3.2GeV respectively. Predictions for other models including Bartol [42], Honda [43] and FLUKA [46] are given in [47].

Precursory hints of atmospheric neutrinos were observed in the mid-1960s searching for  $\nu_\mu + X \xrightarrow{(-)} X^* + \mu^\pm$  [48], although it was called an anomaly at the time of measurement. This was succeeded with the IMB-3 [49] and Kamiokande [50] experiments which measured the ratio of muon neutrinos compared to electron neutrinos  $R(\nu_\mu/\nu_e)$ . Both experiments were found to have a consistent deficit of muon neutrinos, with  $R(\nu_\mu/\nu_e) = 0.67 \pm 0.17$  and  $R(\nu_\mu/\nu_e) = 0.60^{+0.07}_{-0.06} \pm 0.05$ . Super-Kamiokande (SK) [47] extended this analysis by fitting oscillation parameters in  $P(\nu_\mu \rightarrow \nu_\tau)$  which found best fit parameters  $\sin^2(2\theta) > 0.92$  and  $1.5 \times 10^{-3} < \Delta m^2 < 3.4 \times 10^{-3}$ eV $^2$ .

Since then, atmospheric neutrino experiments have been making precision measurements of the  $\sin^2(\theta_{23})$  and  $\Delta m^2_{32}$  oscillation parameters. Atmospheric neutrino oscillation is dominated by  $P(\nu_\mu \rightarrow \nu_\tau)$ , where SK observed a  $4.6\sigma$  discovery of  $\nu_\tau$

<sup>354</sup> appearance [51]. Figure 2.6 illustrates the current estimates on the atmospheric mixing  
<sup>355</sup> parameters from a wide range of atmospheric and accelerator neutrino observatories.

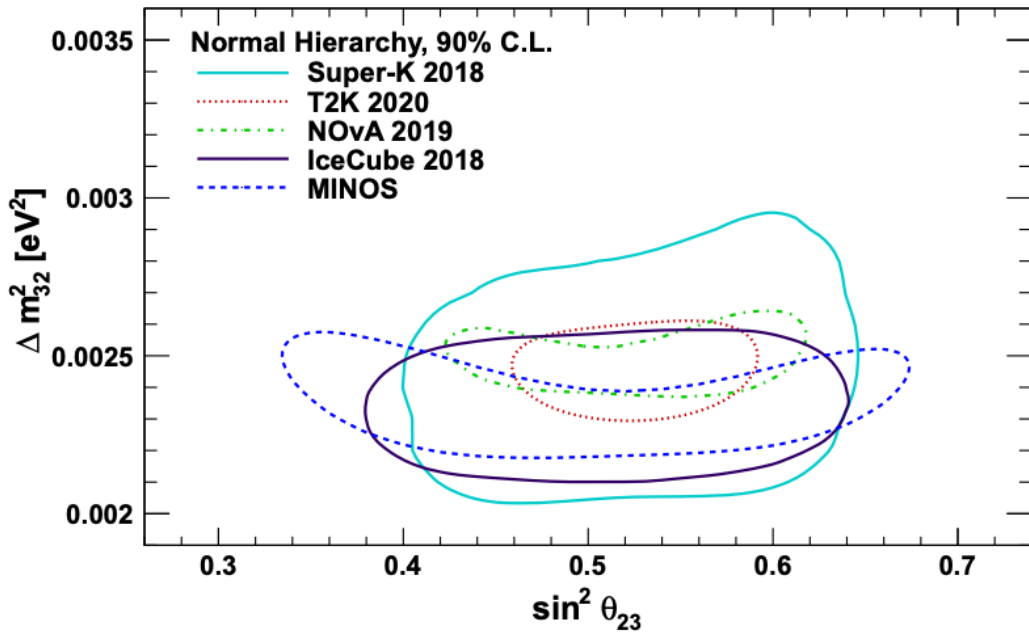


**Figure 2.6:** Constraints on the atmospheric oscillation parameters,  $\sin^2(\theta_{23})$  and  $\Delta m_{32}^2$ , from atmospheric and long baseline experiments: SK [52], T2K [53], NOvA [54], IceCube [55] and MINOS [56]. Figure taken from [57].

### <sup>356</sup> 2.3.3 Accelerator Neutrinos

<sup>357</sup> The concept of using a man-made “neutrino beam” was first realised in 1962 [58].  
<sup>358</sup> Since then, many experiments have followed which all use the same fundamental  
<sup>359</sup> concepts. Typically, a proton beam is aimed at a target producing charged mesons that  
<sup>360</sup> decay to neutrinos. The mesons can be sign-selected by the use of magnetic focusing  
<sup>361</sup> horns to generate a neutrino or antineutrino beam. Pions are the primary meson that  
<sup>362</sup> decay and depending on the orientation of the magnetic field, a muon (anti-)neutrino  
<sup>363</sup> beam is generated via  $\pi^+ \rightarrow \mu^+ + \nu_\mu$  or  $\pi^- \rightarrow \mu^- + \bar{\nu}_\mu$ . The decay of muons and  
<sup>364</sup> kaons does result in an irreducible intrinsic electron neutrino background. In T2K,  
<sup>365</sup> this background contamination is  $O(< 1\%)$  [59]. There is also an approximately  $\sim 5\%$

<sup>366</sup> “wrong-sign” neutrino background of  $\bar{\nu}_\mu$  generated via the same decays. As the beam is  
<sup>367</sup> generated by proton interactions (rather than anti-proton interactions), the wrong-sign  
<sup>368</sup> component in the antineutrino beam is larger when operating in neutrino mode.

<sup>369</sup> Tuning the proton energy in the beam and using beam focusing techniques allows  
<sup>370</sup> the neutrino energy to be set to a value that maximises the disappearance oscillation  
<sup>371</sup> probability in the  $L/E$  term in Equation 2.10. This means that accelerator experiments  
<sup>372</sup> are typically more sensitive to the mixing parameters as compared to a natural neutrino  
<sup>373</sup> source. However, the disadvantage compared to atmospheric neutrino experiments is  
<sup>374</sup> that the baseline has to be shorter due to the lower flux. Consequently, there is typically  
<sup>375</sup> less sensitivity to matter effects and the ordering of the neutrino mass eigenstates.

<sup>376</sup> A neutrino experiment measures

$$R(\vec{x}) = \Phi(E_\nu) \times \sigma(E_\nu) \times \epsilon(\vec{x}) \times P(\nu_\alpha \rightarrow \nu_\beta), \quad (2.15)$$

<sup>377</sup> where  $R(\vec{x})$  is the event rate of neutrinos at position  $\vec{x}$ ,  $\Phi(E_\nu)$  is the flux of neutrinos  
<sup>378</sup> with energy  $E_\nu$ ,  $\sigma(E_\nu)$  is the cross-section of the neutrino interaction and  $\epsilon(\vec{x})$  is the  
<sup>379</sup> efficiency and resolution of the detector. In order to leverage the most out of an  
<sup>380</sup> accelerator neutrino experiment, the flux and cross-section systematics need to be  
<sup>381</sup> constrained. This is typically done via the use of a “near detector”, situated at a baseline  
<sup>382</sup> of  $O(1)$ km. This detector observes the unoscillated neutrino flux and constrains the  
<sup>383</sup> parameters used within the flux and cross-section model.

<sup>384</sup> The first accelerator experiments to precisely measure oscillation parameters were  
<sup>385</sup> MINOS [60] and K2K [61]. These experiments confirmed the  $\nu_\mu$  disappearance seen in  
<sup>386</sup> atmospheric neutrino experiments by finding consistent parameter values for  $\sin^2(\theta_{23})$   
<sup>387</sup> and  $\Delta m_{23}^2$ . The current generation of accelerator neutrino experiments, T2K and NO $\nu$ A

388 extended this field by observing  $\bar{\nu}_\mu \rightarrow \bar{\nu}_e$  and lead the sensitivity to atmospheric mix-  
 389 ing parameters as seen in Figure 2.6 [62]. The two experiments differ in their peak  
 390 neutrino energy, baseline, and detection technique. The NO $\nu$ A experiment is situated  
 391 at a baseline of 810km from the NuMI beamline which delivers 2GeV neutrinos. The  
 392 T2K neutrino beam is peaked around 0.6GeV and propagates 295km. The NO $\nu$ A  
 393 experiment also uses functionally identical detectors (near and far) which allow the  
 394 approximate cancellation of detector systematics whereas T2K uses a plastic scintil-  
 395 lator technique at the near detector and a water Cherenkov far detector. The future  
 396 generation experiments DUNE [63] and Hyper-Kamiokande [64] will succeed these  
 397 experiments as the high-precision era of neutrino oscillation parameter measurements  
 398 develops.

399 Several anomalous results have been observed in the LSND [9] and MiniBooNE [10]  
 400 detectors which were designed with purposefully short baselines. Parts of the neu-  
 401 trino community attributed these results to oscillations induced by a fourth “sterile”  
 402 neutrino [65] but several searches in other experiments, MicroBooNE [66] and KAR-  
 403 MEN [67], found no hints of additional neutrino species. The solution to the anomalous  
 404 results is still being determined.

#### 405 2.3.4 Reactor Neutrinos

406 As illustrated in the first discovery of neutrinos (section 2.1), nuclear reactors are a very  
 407 useful man-made source of electron antineutrinos. For reactors that use low-enriched  
 408 uranium  $^{235}\text{U}$  as fuel, the antineutrino flux is dominated by the  $\beta$ -decay fission of  $^{235}\text{U}$ ,  
 409  $^{238}\text{U}$ ,  $^{239}\text{Pu}$  and  $^{241}\text{Pu}$  [68] as illustrated in Figure 2.7.

410 Due to their low energy, reactor electron antineutrinos predominantly interact  
 411 via the inverse  $\beta$ -decay (IBD) interaction. The typical signature contains two signals

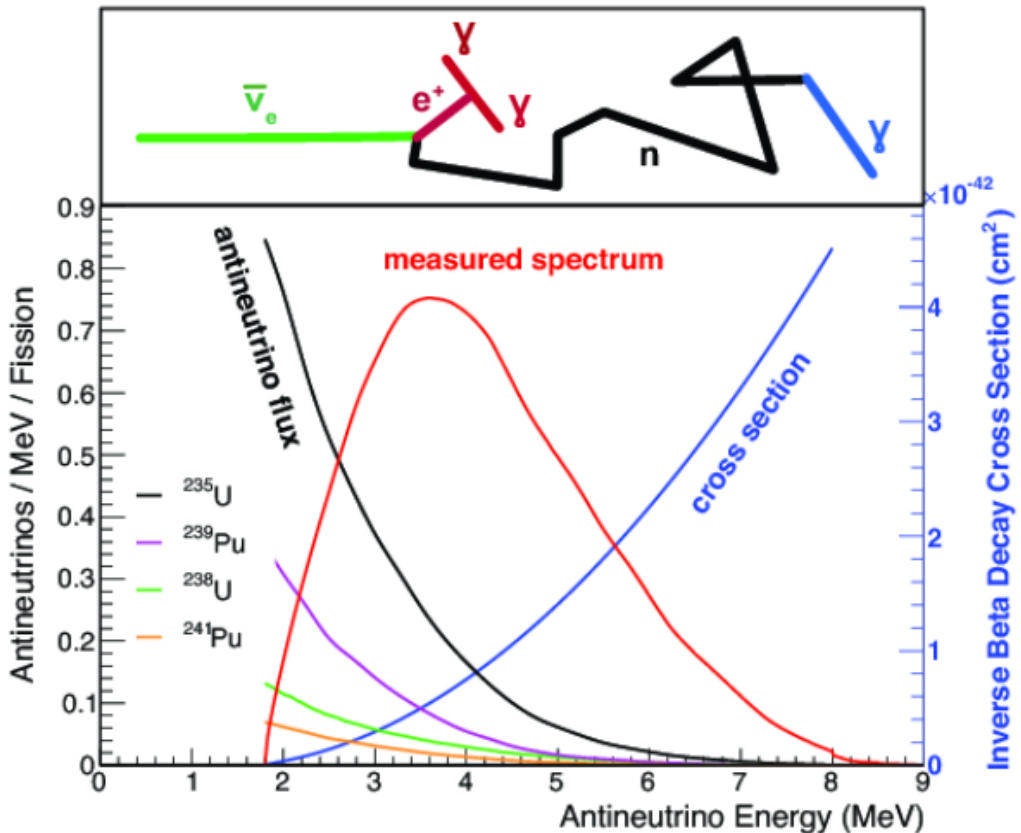


**Figure 2.7:** Reactor electron antineutrino fluxes for  $^{235}\text{U}$  (Black),  $^{238}\text{U}$  (Green),  $^{239}\text{Pu}$  (Purple), and  $^{241}\text{Pu}$  (Orange) isotopes. The inverse  $\beta$ -decay cross-section (Blue) and corresponding measurable neutrino spectrum (Red) are also given. Top panel: Schematic of Inverse  $\beta$ -decay interaction including the eventual capture of the emitted neutron. This capture emits a  $\gamma$ -ray which provides a second signal of the event. Taken from [69].

delayed by  $O(200)\mu\text{s}$ ; firstly the prompt photons from positron annihilation, and secondly the photons emitted ( $E_{tot}^\gamma = 2.2\text{MeV}$ ) from de-excitation after neutron capture on hydrogen. Searching for both signals improves the detector's ability to distinguish between background and signal events [70]. Recently, SK included gadolinium dopants into the ultra-pure water to increase the energy released from the photon cascade to  $\sim 8\text{MeV}$  and reduce the time of the delayed signal to  $\sim 28\mu\text{s}$ .

There are many short baseline experiments ( $L \sim O(1)\text{km}$ ) that have measured the  $\sin^2(\theta_{13})$  and  $\Delta m_{23}^2$  oscillation parameters. Daya Bay [71], RENO [72] and Double Chooz [73] have all provided precise measurements, with the first discovery of a

421 non-zero  $\theta_{13}$  made by Daya Bay and RENO (and complemented by T2K [73]). The  
422 constraints on  $\sin^2(\theta_{13})$  by the reactor experiments lead the field and are often used as  
423 external inputs to accelerator neutrino experiments to improve their sensitivity to  $\delta_{CP}$   
424 and mass hierarchy determination. JUNO-TAO [74], a small collaboration within the  
425 larger JUNO experiment, is a next-generation reactor experiment that aims to precisely  
426 measure the isotopic antineutrino yields from the different fission chains. Alongside  
427 this, it aims to explain the ‘5MeV excess’ [75–77] by conducting a search for sterile  
428 neutrinos with a mass scale of around 1eV.

429 Kamland [78] is the only experiment to have observed reactor neutrinos using a  
430 long baseline (flux weighted averaged baseline of  $L \sim 180\text{km}$ ) which allows it to have  
431 sensitivity to  $\Delta m_{12}^2$ . Combined with the SK solar neutrino experiment, the combined  
432 analysis puts the most stringent constraint on  $\Delta m_{12}^2$  [79].

## 433 2.4 Summary

434 Since observing the first evidence of neutrino oscillations in the late 1990’s, numerous  
435 measurements of the mixing parameters have been made. Many experiments use  
436 neutrinos as a tool for discovery of new physics (diffuse supernova background,  
437 neutrinoless double beta decay and others) so the PMNS parameters are summarised  
438 in the Particle Data Group (PDG) review tables. The analysis presented in this thesis  
439 focuses on the 2020 T2K oscillation analysis presented in [80] where the 2018 PDG  
440 constraints [81] were used. These constraints are outlined in Table 2.1.

441 The  $\sin^2(\theta_{13})$  measurement stems from the electron antineutrino disappearance,  
442  $P(\bar{\nu}_e \rightarrow \bar{\nu}_e)$ , and is take as the average best-fit from the combination of Daya Bay,  
443 Reno and Double Chooz. It is often used as a prior uncertainty within other neu-  
444 trino oscillation experiments, typically termed the reactor constraint. The  $\sin^2(\theta_{12})$

Parameter	2018 Constraint
$\sin^2(\theta_{12})$	$0.307 \pm 0.013$
$\Delta m_{21}^2$	$(7.53 \pm 0.18) \times 10^{-5} \text{ eV}^2$
$\sin^2(\theta_{13})$	$(2.12 \pm 0.08) \times 10^{-2}$
$\sin^2(\theta_{23})$ (I.H., Q1)	$0.421^{+0.033}_{-0.025}$
$\sin^2(\theta_{23})$ (I.H., Q2)	$0.592^{+0.023}_{-0.030}$
$\sin^2(\theta_{23})$ (N.H., Q1)	$0.417^{+0.025}_{-0.028}$
$\sin^2(\theta_{23})$ (N.H., Q2)	$0.597^{+0.024}_{-0.030}$
$\Delta m_{32}^2$ (I.H.)	$(-2.56 \pm 0.04) \times 10^{-3} \text{ eV}^2$
$\Delta m_{32}^2$ (N.H.)	$(2.51 \pm 0.05) \times 10^{-3} \text{ eV}^2$

**Table 2.1:** The 2018 Particle Data Group constraints of the oscillation parameters taken from [81]. The value of  $\Delta m_{23}^2$  is given for both normal hierarchy (N.H.) and inverted hierarchy (I.H.) and  $\sin^2(\theta_{23})$  is broken down by whether its value is below (Q1) or above (Q2) 0.5.

parameter is predominantly measured through electron neutrino disappearance,  $P(\nu_e \rightarrow \nu_{\mu,\tau})$ , in solar neutrino experiments. The long-baseline reactor neutrino experiment Kamland also has sensitivity to this parameter and is used in a joint fit to solar data from SNO and SK, using the reactor constraint. Measurements of  $\sin^2(\theta_{23})$  are made by long-baseline and atmospheric neutrino experiments. The PDG value is a joint fit of T2K, NOvA, MINOS and IceCube DeepCore experiments. The latest T2K-only measurement, provided at Neutrino2020 and is the basis of this thesis, is given as  $\sin^2(\theta_{23}) = 0.546^{+0.024}_{-0.046}$  [80]. The PDG constraint on  $\Delta m_{12}^2$  is provided by the KamLAND experiment using solar and geoneutrino data. This measurement utilised a  $\sin^2(\theta_{13})$  constraint from accelerator (T2K, MINOS) and reactor neutrino (Daya Bay, RENO, Double Chooz) experiments. Accelerator measurements make some of the most stringent constraints on  $\Delta m_{23}^2$  although atmospheric experiments have more sensitivity to the mass hierarchy determination. The PDG performs a joint fit of accelerator and atmospheric data, in both normal and inverted hierarchy separately. The latest T2K-only result is  $\Delta m_{32}^2 = 2.49^{+0.058}_{-0.082} \times 10^{-3} \text{ eV}^2$  favouring normal hierarchy [80]. The value of  $\delta_{CP}$  is largely undetermined. CP-conserving values of 0 and  $\pi$  were

<sup>461</sup> rejected with  $\sim 2\sigma$  intervals, as published in Nature, although more recent analysis  
<sup>462</sup> have reduced the rejection intervals to 90%. Since the 2018 PDG publication, there has  
<sup>463</sup> been a new measurement of  $\sin^2(\theta_{13}) = (2.20 \pm 0.07) \times 10^{-2}$  [82], alongside updated  
<sup>464</sup>  $\Delta m_{23}^2$  and  $\sin^2(\theta_{23})$  measurements.

<sup>465</sup> Throughout this thesis, several sample spectra predictions and contours are pre-  
<sup>466</sup> sented which require oscillation parameters to be assumed. Table 2.2 defines two sets  
<sup>467</sup> of oscillation parameters, with “Asimov A” set being close to the preferred values  
<sup>468</sup> from a previous T2K-only fit [83] and “Asimov B” being CP-conserving and further  
<sup>469</sup> from maximal  $\theta_{23}$  mixing.

Parameter	Asimov A	Asimov B
$\Delta m_{12}^2$	$7.53 \times 10^{-5} \text{ eV}^2$	
$\Delta m_{32}^2$	$2.509 \times 10^{-3} \text{ eV}^2$	
$\sin^2(\theta_{12})$	0.304	
$\sin^2(\theta_{13})$	0.0219	
$\sin^2(\theta_{23})$	0.528	0.45
$\delta_{CP}$	-1.601	0.0

**Table 2.2:** Reference values of the neutrino oscillation parameters for two different oscillation parameter sets.

470 **Chapter 3**

471 **T2K and SK Experiment Overview**

472 As the successor of the Kamiokande experiment, the Super-Kamiokande (SK) collaboration  
473 has been leading atmospheric neutrino oscillation analyses for over two decades.  
474 The detector has provided some of the strongest constraints on proton decay and the  
475 first precise measurements of the  $\Delta m_{23}^2$  and  $\sin^2(\theta_{23})$  neutrino oscillation parameters.  
476 The ability of the detector to low-energy neutrino events has been significantly im-  
477 proved with the recent gadolinium doping of the ultra-pure water target. The history,  
478 detection technique, and operation of the SK detector is described in section 3.1.

479 The Tokai-to-Kamioka (T2K) experiment was one of the first long-baseline ex-  
480 periments to use both neutrino and antineutrino beams to precisely measure the  
481 charge parity violation within the neutrino sector. With the SK detector observing  
482 the oscillated neutrino flux, the T2K experiment observed the first hints of a non-zero  
483  $\sin^2(\theta_{13})$  measurement and continues to lead the field with the constraints it provides  
484 on  $\sin^2(\theta_{13})$ ,  $\sin^2(\theta_{23})$ ,  $\Delta m_{23}^2$  and  $\delta_{CP}$ . The techniques which T2K uses in gener-  
485 ating its neutrino beam as well as the near-detector used to constrain the flux and  
486 cross-section parameters used in this analysis are documented in section 3.2.

487 **3.1 The Super-Kamiokande Experiment**

488 The SK experiment began taking data in 1996 [84] and has had many modifications  
489 throughout its lifespan. There have been seven defined periods of data taking as  
490 noted in Table 3.1. Data taking began in SK-I which ran for five years. Between the

491 SK-I and SK-II periods, a significant proportion of the PMTs were damaged during  
 492 maintenance. Those that survived were equally distributed throughout the detector  
 493 in the SK-II era, which resulted in a reduced photo-coverage. From SK-III onwards,  
 494 repairs to the detector meant the full suite of PMTs was operational. Before the  
 495 start of SK-IV, the data acquisition and electronic systems were upgraded. Between  
 496 SK-IV and SK-V, a significant effort was placed into tank open maintenance and  
 497 repair/replacement of defective PMTs, a task for which the author of this thesis was  
 498 required. Consequently, the detector conditions were significantly different between  
 499 the two operational periods. SK-VI saw the start of the 0.01% gadolinium doped water.  
 500 SK-VII, which started during the writing of this thesis, has increased the gadolinium  
 501 concentration to 0.03% for continued operation [85].

Period	Start Date	End Date	Live-time (days)
I	April 1996	July 2001	1489.19
II	October 2002	October 2005	798.59
III	July 2006	September 2008	518.08
IV	September 2008	May 2018	3244.4
V	January 2019	July 2020	461.02
VI	July 2020	May 2022	583.3
VII	May 2022	Ongoing	N/A

**Table 3.1:** The various SK periods and respective live-time. The SK-VI live-time is calculated until 1<sup>st</sup> April 2022. SK-VII started during the writing of this thesis.

### 502 3.1.1 The SK Detector

503 The basic structure of the Super-Kamiokande (SK) detector is a cylindrical tank with a  
 504 diameter 39.3m and height 41.1m filled with ultrapure water [86]. A diagram of the  
 505 significant components of the SK detector is given in Figure 3.1. The SK detector is  
 506 situated in the Kamioka mine in Gifu, Japan. The mine is underground with roughly  
 507 1km rock overburden (2.7km water equivalent overburden) [87]. At this depth, the

508 rate of cosmic ray muons is significantly decreased to a value of  $\sim 2\text{Hz}$ . The top of  
 509 the tank is covered with stainless steel which is designed as a working platform for  
 510 maintenance, calibration, and location for high voltage and data acquisition electronics.

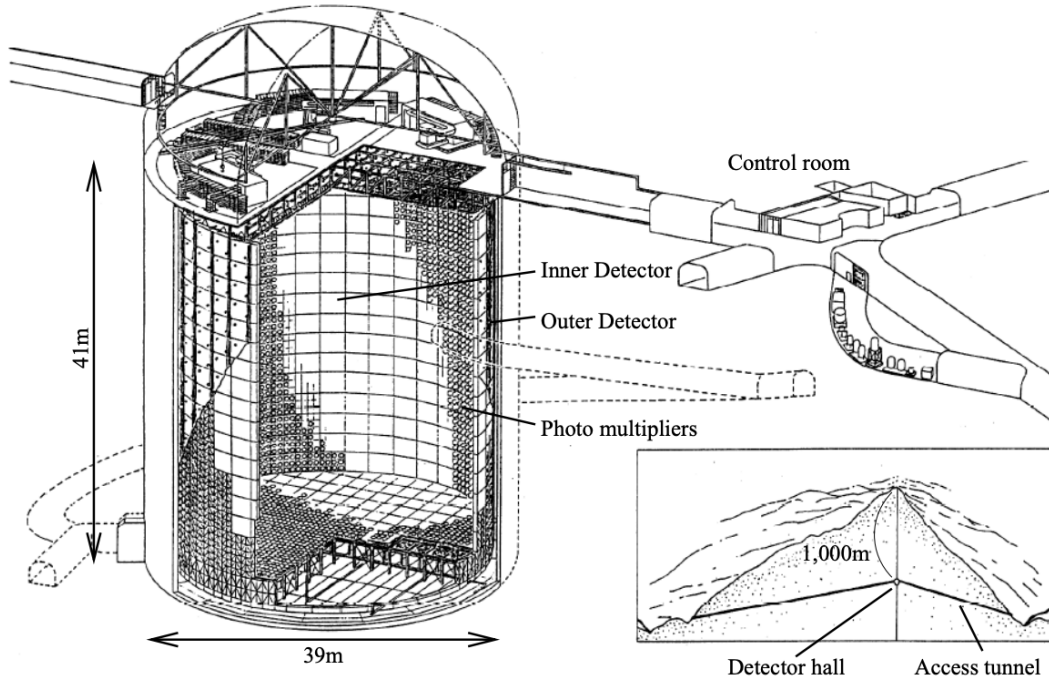


**Figure 3.1:** A schematic diagram of the Super-Kamiokande Detector. Taken from [88].

511 A smaller cylindrical structure (36.2m diameter, 33.8m height) is situated inside the  
 512 tank, with an approximate 2m gap between this structure and the outer tank wall. The  
 513 purpose of this structure is to support the photomultiplier tubes (PMTs). The volume  
 514 inside and outside the support structure is referred to as the inner detector (ID) and  
 515 outer detector (OD), respectively. In the SK-IV era, the ID and OD are instrumented  
 516 by 11,129 50cm and 1,885 20cm PMTs respectively [86]. The ID contains a 32kton  
 517 mass of water. Many analyses performed at SK use a “fiducial volume” defined by the  
 518 volume of water inside the ID excluding some distance to the ID wall. This reduces the  
 519 volume of the detector which is sensitive to neutrino events but reduces radioactive  
 520 backgrounds and allows for better reconstruction performance. The nominal fiducial

521 volume is defined as the area contained inside 2m from the ID wall for a total of  
522 22.5kton water [89].

523 The two regions of the detector (ID and OD) are optically separated with opaque  
524 black plastic. The purpose of this is to determine whether a track entered or exited  
525 the ID. This allows cosmic ray muons and partially contained events to be tagged and  
526 separated from neutrino events entirely contained within the ID. This black plastic is  
527 also used to cover the area between the ID PMTs to reduce photon reflection from the  
528 ID walls. Opposite to this, the OD is lined with a reflective material to allow photons to  
529 reflect around inside the OD until collected by one of the PMTs. Furthermore, each OD  
530 PMT is backed with  $50 \times 50\text{cm}$  plates of wavelength shifting acrylic which increases  
531 the efficiency of light collection [87].

532 In the SK-IV data-taking period, the photocathode coverage of the detector, or the  
533 fraction of the ID wall instrumented with PMTs, is  $\sim 40\%$  [87]. The PMTs have a  
534 quantum efficiency (the ratio of detected electrons to incident photons) of  $\sim 21\%$  for  
535 photons with wavelengths of  $360\text{nm} < \lambda < 390\text{nm}$ . The proportion of photoelectrons  
536 that produce a signal in the dynode of a PMT, termed the collection efficiency, is  
537  $> 70\%$  [87]. The PMTs used within SK are most sensitive to photons with wavelength  
538  $300\text{nm} \leq \lambda \leq 600\text{nm}$  [87]. One disadvantage of using PMTs as the detection media  
539 is that the Earth's geomagnetic field can modify its response. Therefore, a set of  
540 compensation coils is built around the inner surface of the detector to mitigate this  
541 effect [90].

542 As mentioned, the SK detector is filled with ultrapure water, which in a perfect  
543 world would contain no impurities. However, bacteria and organic compounds can  
544 significantly degrade the water quality. This decreases the attenuation length, which  
545 reduces the total number of photons that hit a PMT. To combat this, a sophisticated  
546 water treatment system has been developed [87, 91]. UV lights, mechanical filters,

547 and membrane degasifiers are used to reduce the bacteria, suspended particulates,  
548 and radioactive materials from the water. The flow of water within the tank is also  
549 critical as it can remove stagnant bacterial growth or build-up of dust on the surfaces  
550 within the tank. Gravity drifts impurities in the water towards the bottom of the  
551 tank which, if left uncontrolled, can create asymmetric water conditions between  
552 the top and bottom of the tank. Typically, the water entering the tank is cooled  
553 below the ambient temperature of the tank to control convection and inhibit bacteria  
554 growth. Furthermore, the rate of dark noise hits within PMTs is sensitive to the PMT  
555 temperature [92] so controlling the temperature gradients within the tank is beneficial  
556 for stable measurements.

557 SK-VI is the first phase of the SK experiment to use gadolinium dopants within  
558 the ultrapure water [85]. As such, the SK water system had to be replaced to avoid  
559 removing the gadolinium concentrate from the ultrapure water [93]. For an inverse  
560  $\beta$ -decay (IBD) interaction in a water target, the emitted neutron is thermally captured  
561 on hydrogen. This process releases 2.2MeV  $\gamma$  rays which are difficult to detect as  
562 the resulting Compton scattered electrons are very close to the Cherenkov threshold,  
563 limiting the number of photons produced. Thermal capture of neutrons on gadolin-  
564 ium generates  $\gamma$  rays with higher energy (8MeV [70]) meaning they are more easily  
565 detected. SK-VI has 0.01% Gd loading (0.02% gadolinium sulphate by mass) which  
566 causes  $\approx$  50% of neutrons emitted by IBD to be captured on gadolinium [94, 95].  
567 Whilst predominantly useful for low energy analyses, Gd loading allows better  $\nu/\bar{\nu}$   
568 separation for atmospheric neutrino event selections [96]. Efforts are currently in place  
569 to increase the gadolinium concentrate to 0.03% for  $\approx$  75% neutron capture efficiency  
570 on gadolinium [97]. The final stage of loading targets 0.1% concentrate.

### 571 3.1.2 Calibration

572 The calibration of the SK detector is documented in [86] and summarised below. The  
573 analysis presented within this thesis is dependent upon ‘high energy events’ (Charged  
574 particles with  $O(> 100)\text{MeV}$  momenta). These are events that are expected to generate  
575 a larger number of photons such that each PMT will be hit with multiple photons.  
576 The reconstruction of these events depends upon the charge deposited within each  
577 PMT and the timing response of each individual PMT. Therefore, the most relevant  
578 calibration techniques to this thesis are outlined.

579 Before installation, 420 PMTs were calibrated to have identical charge responses  
580 and then distributed throughout the tank in a cross-shape pattern (As illustrated by  
581 Figure 3.2). These are used as a standardised measure for the rest of the PMTs installed  
582 at similar geometric positions within SK to be calibrated against. To perform this  
583 calibration, a xenon lamp is located at the center of the SK tank which flashes uniform  
584 light at 1Hz. This allows for geometrical effects, water quality variation, and timing  
585 effects to be measured in-situ throughout normal data-taking periods.

586 When specifically performing calibration of the detector (in out-of-data taking  
587 mode), the water in the tank was circulated to avoid top/bottom asymmetric water  
588 quality. Any non-uniformity within the tank significantly affects the PMT hit proba-  
589 bility through scattering or absorption. This becomes a dominant effect for the very  
590 low-intensity light sources discussed later which are designed such that only one  
591 photon is incident upon a given PMT.

592 The “gain” of a PMT is defined as the ratio of the total charge of the signal produced  
593 compared to the charge of photoelectrons emitted by the photocathodes within the  
594 PMT. To calibrate the signal of each PMT, the “relative” and “absolute” gain values are

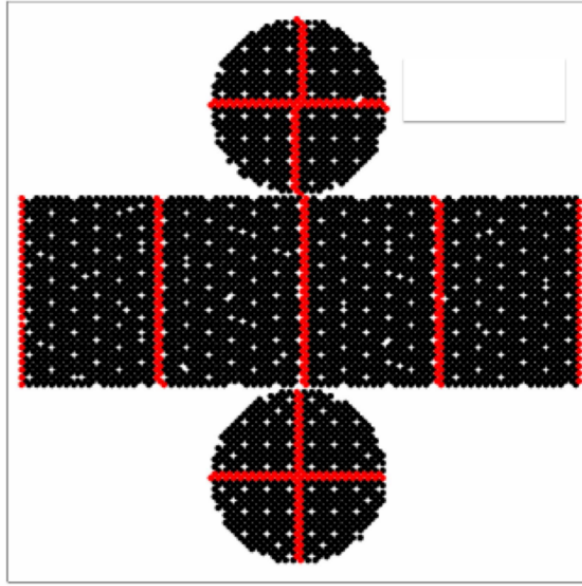


**Figure 3.2:** The location of “standard PMTs” (red) inside the SK detector. Taken from [86].

595 measured. The relative gain is the variation of gain among each of the PMTs whereas  
 596 the absolute gain is the average gain of all PMTs.

597 The relative gain is calibrated as follows. A laser is used to generate two measure-  
 598 ments: a high-intensity flash that illuminates every PMT with a sufficient number of  
 599 photons, and a low-intensity flash in which only a small number of PMTs collect light.  
 600 The first measurement creates an average charge,  $Q_{obs}(i)$  on PMT  $i$ , whereas the second  
 601 measurement ensures that each hit PMT only generates a single photoelectron. For the  
 602 low-intensity measurement, the number of times each PMT records a charge larger  
 603 than 1/4 photoelectrons,  $N_{obs}(i)$ , is counted. The values measured can be expressed as

$$\begin{aligned} Q_{obs}(i) &\propto I_H \times f(i) \times \epsilon(i) \times G(i), \\ N_{obs}(i) &\propto I_L \times f(i) \times \epsilon(i), \end{aligned} \tag{3.1}$$

604 Where  $I_H$  and  $I_L$  is the intensity of the high and low flashes,  $f(i)$  is the acceptance  
 605 efficiency of the  $i^{\text{th}}$  PMT,  $\epsilon(i)$  is the product of the quantum and collection efficiency

606 of the  $i^{\text{th}}$  PMT and  $G(i)$  is the gain of the  $i^{\text{th}}$  PMT. The relative gain for each PMT can  
 607 determined by taking the ratio of these quantities.

608 The absolute gain calibration is performed by observing fixed energy  $\gamma$ -rays of  
 609  $E_{\gamma} \sim 9\text{MeV}$  emitted isotropically from neutron capture on a NiCf source situated at  
 610 the center of the detector. This generates a photon yield of about 0.004 photoelec-  
 611 trons/PMT/event, meaning that  $> 99\%$  of PMT signals are generated from single  
 612 photoelectrons. A charge distribution is generated by performing this calibration over  
 613 all PMTs, and the average value of this distribution is taken to be the absolute gain  
 614 value.

615 As mentioned in subsection 3.1.1, the average quantum and collection efficiency  
 616 for the SK detector is  $\sim 21\%$  and  $> 70\%$  respectively. However, these values do differ  
 617 between each PMT and need to be calibrated accordingly. Consequently, the NiCf  
 618 source is also used to calibrate the “quantum  $\times$  collection” efficiency (denoted “QE”)  
 619 value of each PMT. The NiCf low-intensity source is used as the PMT hit probability  
 620 is proportional to the QE ( $N_{\text{obs}}(i) \propto \epsilon(i)$  in Equation 3.1). A Monte Carlo prediction  
 621 which includes photon absorption, scattering, and reflection is made to estimate the  
 622 number of photons incident on each PMT and the ratio of the number of predicted  
 623 to observed hits is calculated. The difference is attributed to the QE efficiency of that  
 624 PMT. This technique is extended to calculate the relative QE efficiency by normalizing  
 625 the average of all PMTs which removes the dependence on the light intensity.

626 Due to differing cable lengths and readout electronics, the timing response between  
 627 a photon hitting the PMT and the signal being captured by the data acquisition can be  
 628 different between each PMT. Due to threshold triggers (Described in subsection 3.1.3),  
 629 the time at which a pulse reaches a threshold is dependent upon the size of the pulse.  
 630 This is known as the ‘time-walk’ effect and also needs to be accounted for in each PMT.  
 631 To calibrate the timing response, a pulse of light with width 0.2ns is emitted into the

632 detector through a diffuser. Two-dimensional distributions of time and pulse height  
633 (or charge) are made for each PMT and are used to calibrate the timing response. This  
634 is performed in-situ during data taking with the light source pulsing at 0.03Hz.

635 The top/bottom water quality asymmetry is measured using the NiCf calibration  
636 data and cross-referencing these results to the “standard PMTs”. The water attenuation  
637 length is continuously measured by the rate of vertically-downgoing cosmic-ray  
638 muons which enter via the top of the tank.

639 Dark noise is the phenomenon where a PMT registers a pulse that is consistent  
640 with a single photoelectron emitted from photon detection despite the PMT being in  
641 complete darkness. This is predominately caused by two processes. Firstly there is  
642 intrinsic dark noise which is where photoelectrons gain enough thermal energy to be  
643 emitted from the photocathode, and secondly, the radioactive decay of contaminants  
644 inside the structure of the PMT. Typical dark noise rate for PMTs used within SK are  
645  $O(3)$ kHz [87]. This is lower than the expected number of photons generated for a ‘high  
646 energy event’ (As described in subsection 3.1.4) but instability in this value can cause  
647 biases in reconstruction. Dark noise is related to the gain of a PMT and is calibrated  
648 using hits inside a time window recorded before an event trigger [98].

### 649 3.1.3 Data Acquisition and Triggering

650 The analysis presented in this thesis only uses the SK-IV period of the SK experiment  
651 so this subsection focuses on the relevant points of the data acquisition and triggering  
652 systems to that SK period. The earlier data acquisition and triggering systems are  
653 documented in [99, 100].

654 Before the SK-IV period started, the existing front-end electronics were replaced  
655 with “QTC-Based Electrons with Ethernet, QBEE” systems [101]. When the QBEE

observes a signal above a 1/4 photoelectron threshold, the charge-to-time (QTC) converter generates a rectangular pulse. The start of the rectangular pulse indicates the time at which the analog photoelectron signal was received and the width of the pulse indicates the total charge integrated throughout the signal. This is then digitized by time-to-digital converters and sent to the “front-end” PCs. The digitized signal from every QBEE is then chronologically ordered and sent to the “merger” PCs. It is the merger PCs that apply the software trigger. Any triggered events are passed to the “organizer” PC. This sorts the data stream of multiple merger PCs into chronologically ordered events which are then saved to disk. The schematic of data flow from PMTs to disk is illustrated in Figure 3.3.

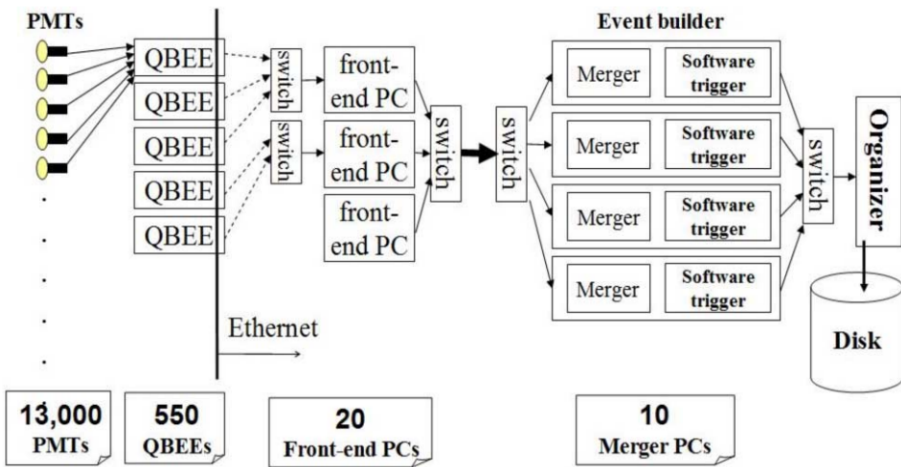


**Figure 3.3:** Schematic view of the data flow through the data acquisition and online system. Taken from [102].

The software trigger (described in [103]) operates by determining the number of PMT hits within a 200ns sliding window,  $N_{200}$ . This window coincides with the maximum time that a Cherenkov photon would take to traverse the length of the SK tank [100]. For lower energy events that generate fewer photons, this technique is useful for eliminating background processes like dark noise and radioactive decay which would be expected to separate in time. When the value of  $N_{200}$  exceeds some threshold, a software trigger is issued. There are several trigger thresholds used within

the SK-IV period which are detailed in Table 3.2. If one of these thresholds is met, the PMT hits within an extended time window are also read out and saved to disk. In the special case of an event that exceeds the SHE trigger but does not exceed the OD trigger, the AFT trigger looks for delayed coincidences of 2.2MeV gamma rays emitted from neutron capture in a  $535\mu\text{s}$  window after the SHE trigger. A similar but more complex “Wideband Intelligent Trigger (WIT)” has been deployed and is described in [104].

Trigger	Acronym	Condition	Extended time window ( $\mu\text{s}$ )
Super Low Energy	SLE	>34/31 hits	1.3
Low Energy	LE	>47 hits	40
High Energy	HE	>50 hits	40
Super High Energy	SHE	>70/58 hits	40
Outer Detector	OD	>22 hits in OD	N/A

**Table 3.2:** The trigger thresholds and extended time windows saved around an event which were utilised throughout the SK-IV period. The exact thresholds can change and the values listed here represent the thresholds at the start and end of the SK-IV period.

### 3.1.4 Cherenkov Radiation

Cherenkov light is emitted from any highly energetic charged particle traveling with relativistic velocity,  $\beta$ , greater than the local speed of light in a medium [105]. Cherenkov light is formed at the surface of a cone with characteristic pitch angle,

$$\cos(\theta) = \frac{1}{\beta n}. \quad (3.2)$$

684 where  $n$  is the refractive index of the medium. Consequently, the Cherenkov  
 685 momentum threshold,  $P_{thres}$ , is dependent upon the mass,  $m$ , of the charged particle  
 686 moving through the medium,

$$P_{thres} = \frac{m}{\sqrt{n^2 - 1}} \quad (3.3)$$

687 For water, where  $n = 1.33$ , the Cherenkov threshold momentum and energy for  
 688 various particles are given in Table 3.3. In contrast,  $\gamma$ -rays are detected indirectly via  
 689 the combination of photons generated by Compton scattering and pair production.  
 690 The threshold for detection in the SK detector is typically higher than the threshold  
 691 for photon production. This is due to the fact that the attenuation of photons in the  
 692 water means that typically  $\sim 75\%$  of Cherenkov photons reach the ID PMTs. Then the  
 693 collection and quantum efficiencies described in subsection 3.1.1 result in the number  
 694 of detected photons being lower than the number of photons which reach the PMTs.

Particle	Threshold Momentum (MeV)	Threshold Energy (MeV)
Electron	0.5828	0.7751
Muon	120.5	160.3
Pion	159.2	211.7
Proton	1070.0	1423.1

**Table 3.3:** The threshold momentum and energy for a particle to generate Cherenkov light in ultrapure water, as calculated in Equation 3.2 in ultrapure water which has refractive index  $n = 1.33$ .

695 The Frank-Tamm equation [106] describes the relationship between the number of  
 696 Cherenkov photons generated per unit length,  $dN/dx$ , the wavelength of the photons  
 697 generated,  $\lambda$ , and the relativistic velocity of the charged particle,

$$\frac{d^2N}{dxd\lambda} = 2\pi\alpha \left(1 - \frac{1}{n^2\beta^2}\right) \frac{1}{\lambda^2}. \quad (3.4)$$

698 where  $\alpha$  is the fine structure constant. For a 100MeV momentum electron, approx-  
 699 imately 330 photons will be produced per centimeter in the  $300\text{nm} \leq \lambda \leq 700\text{nm}$   
 700 region which the ID PMTs are most sensitive to [87].

## 701 3.2 The Tokai to Kamioka Experiment

702 The Tokai to Kamioka (T2K) experiment is a long-baseline neutrino oscillation exper-  
 703 iment located in Japan. Proposed in the early 2000s [107, 108] to replace K2K [109],  
 704 T2K was designed to observe electron neutrino appearance whilst precisely measuring  
 705 the oscillation parameters associated with muon neutrino disappearance [110]. The  
 706 experiment consists of a neutrino beam generated at the Japan Proton Accelerator  
 707 Research Complex (J-PARC), a suite of near detectors situated 280m from the beam  
 708 target, and the Super Kamiokande far detector positioned at a 295km baseline. The  
 709 cross-section view of the T2K experiment is drawn in Figure 3.4.

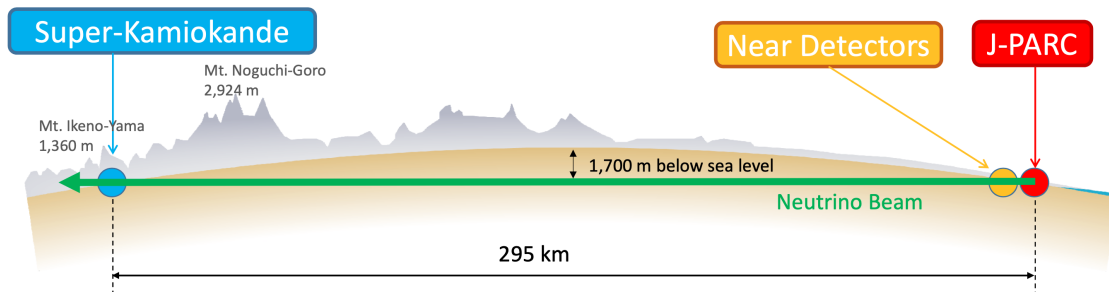


**Figure 3.4:** The cross-section view of the Tokai to Kamioka experiment illustrating the beam generation facility at J-PARC, the near detector situated at a baseline of 280m and the Super Kamiokande far detector situated 295km from the beam target.

The T2K collaboration makes world-leading measurements of the  $\sin^2(\theta_{23})$ ,  $\Delta m_{23}^2$ , and  $\delta_{CP}$  oscillation parameters. Improvements in the precision and accuracy of parameter estimates are still being made by including new data samples and developing the models which describe the neutrino interactions and detector responses [111]. Electron neutrino appearance was first observed at T2K in 2014 [112] with  $7.3\sigma$  significance.

The near detectors provide constraints on the beam flux and cross-section model

parameters used within the oscillation analysis by observing the unoscillated neutrino beam. There are a host of detectors situated in the near detector hall (As illustrated in Figure 3.5): ND280 (subsection 3.2.2), INGRID (subsection 3.2.3), NINJA [113], WAGASCI [114], and Baby-MIND [115]. The latter three are not currently used within the oscillation analysis presented within this thesis.

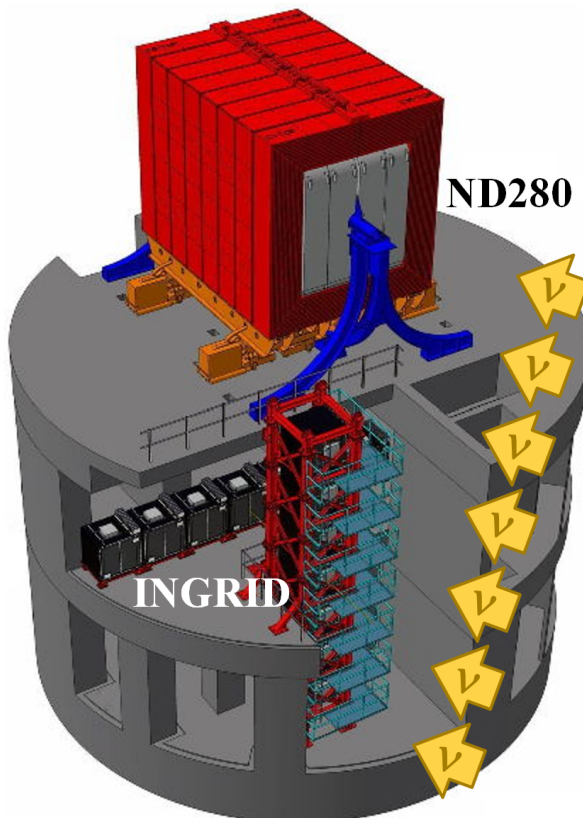


**Figure 3.5:** The near detector suite for the T2K experiment showing the ND280 and INGRID detectors. The distance between the detectors and the beam target is 280m.

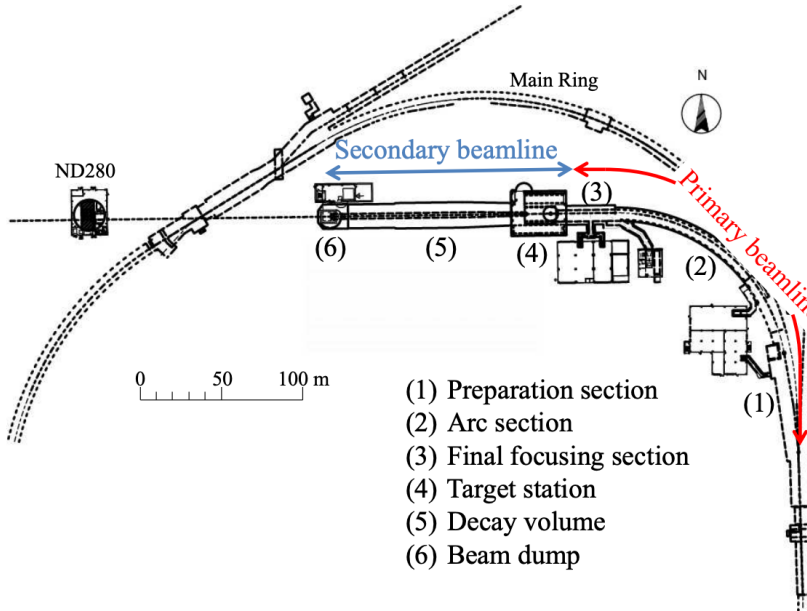
Whilst this thesis presents the ND280 in terms of its purpose for the oscillation analysis, the detector can also make many cross-section measurements at neutrino energies of  $O(1)$ GeV for the different targets within the detector [116, 117]. These measurements are of equal importance as they can lead the way in determining the model parameters used in the interaction models for the future high-precision era of neutrino physics.

DB: Discuss BANFF, PTheta, MaCh3 and covariance

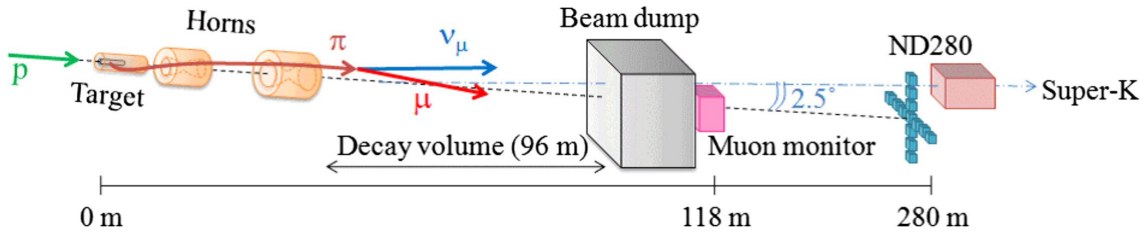
### 3.2.1 The Neutrino Beam

The neutrino beam used within the T2K experiment is described in [59, 118] and summarised below. The accelerating facility at J-PARC is composed of two sections; the primary and secondary beamlines. Figure 3.6 illustrates a schematic of the beamline, focusing mostly on the components of the secondary beamline. The primary beamline has three accelerators that progressively accelerate protons; a linear accelerator, a rapid-cycling synchrotron, and the main-ring (MR) synchrotron. Once fully accelerated by the MR, the protons have a kinetic energy of 30GeV. Eight bunches of these protons, separated by 500ns, are extracted per “spill” from the MR and directed towards a graphite target (a rod of length 91.4cm and diameter 2.6cm). Spills are extracted at 0.5Hz with  $\sim 3 \times 10^{14}$  protons contained per spill.

The secondary beamline consists of three main components: the target station, the decay volume, and the beam dump. The target station is comprised of the target, beam monitors, and three magnetic focusing horns. The proton beam interacts with the graphite target to form a secondary beam of mostly pions and kaons. The secondary beam travels through a 96m long decay volume, generating neutrinos through the following decays [59],



(a) Primary and secondary beamline



(b) Secondary beamline

**Figure 3.6:** Top panel: Bird's eye view of the most relevant part of primary and secondary beamline used within the T2K experiment. The primary beamline is the main-ring proton synchrotron, kicker magnet, and graphite target. The secondary beamline consists of the three focusing horns, decay volume, and beam dump. Figure taken from [118]. Bottom panel: The side-view of the secondary beamline including the focusing horns, beam dump and neutrino detectors. Figure taken from [119].

$$\begin{array}{ll}
 \pi^+ \rightarrow \mu^+ + \nu_\mu & \pi^- \rightarrow \mu^- + \bar{\nu}_\mu \\
 K^+ \rightarrow \mu^+ + \nu_\mu & K^- \rightarrow \mu^- + \bar{\nu}_\mu \\
 \rightarrow \pi^0 + e^+ + \nu_e & \rightarrow \pi^0 + e^- + \bar{\nu}_e \\
 \rightarrow \pi^0 + \mu^+ + \nu_\mu & \rightarrow \pi^0 + \mu^- + \bar{\nu}_\mu \\
 K_L^0 \rightarrow \pi^- + e^+ + \nu_e & K_L^0 \rightarrow \pi^+ + e^- + \bar{\nu}_e \\
 \rightarrow \pi^- + \mu^+ + \nu_\mu & \rightarrow \pi^+ + \mu^- + \bar{\nu}_\mu \\
 \mu^+ \rightarrow e^+ + \bar{\nu}_\mu + \nu_e & \mu^- \rightarrow e^- + \nu_\mu + \bar{\nu}_e
 \end{array}$$

The electrically charged component of the secondary beam is focused towards the far detector by the three magnetic horns. These horns direct charged particles of a particular polarity towards SK whilst defocusing the oppositely charged particles. This allows a mostly neutrino or mostly antineutrino beam to be used within the experiment, denoted as “forward horn current (FHC)” or “reverse horn current (RHC)” respectively.

Figure 3.7 illustrates the different contributions to the FHC and RHC neutrino flux.

The low energy flux is dominated by the decay of pions whereas kaon decay becomes the dominant source of neutrinos for  $E_\nu > 3\text{GeV}$ . The “wrong-sign” component, which is the  $\bar{\nu}_\mu$  background in a  $\nu_\mu$  beam, and the intrinsic irreducible  $\nu_e$  background, are predominantly due to muon decay for  $E_\nu < 2\text{GeV}$ . As the antineutrino production cross-section is smaller than the neutrino cross-section, the wrong-sign component is more dominant in the RHC beam as compared to that in the FHC beam.

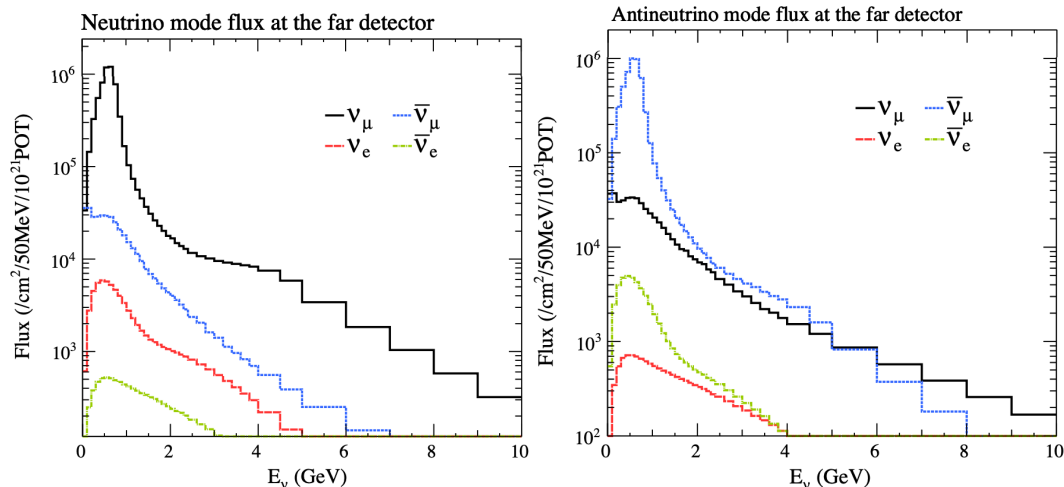


**Figure 3.7:** The Monte Carlo prediction of the energy spectrum for each flavour of neutrino ( $\nu_e$ ,  $\bar{\nu}_e$ ,  $\nu_\mu$  and  $\bar{\nu}_\mu$ ) in the neutrino dominated beam FHC mode (Left) and antineutrino dominated beam RHC mode (Right) expected at SK. Taken from [120].

The beam dump, situated at the end of the decay volume, stops all charged particles other than highly energetic muons ( $p_\mu > 5\text{GeV}$ ). The MuMon detector monitors the

<sup>761</sup> penetrating muons to determine the beam direction and intensity which is used to  
<sup>762</sup> constrain some of the beam flux systematics within the analysis [119, 121].

<sup>763</sup> The T2K experiment uses an off-axis beam to narrow the neutrino energy distribu-  
<sup>764</sup> tion. This was the first implementation of this technique in a long-baseline neutrino  
<sup>765</sup> oscillation experiment after its original proposal [122]. Pion decay,  $\pi \rightarrow \mu + \nu_\mu$ , is a  
<sup>766</sup> two-body decay. Consequently, the neutrino energy,  $E_\nu$ , can be determined based on  
<sup>767</sup> the pion energy,  $E_\pi$ , and the angle at which the neutrino is emitted,  $\theta$ ,

$$E_\nu = \frac{m_\pi^2 - m_\mu^2}{2(E_\pi - p_\pi \cos(\theta))}, \quad (3.5)$$

<sup>768</sup> where  $m_\pi$  and  $m_\mu$  are the mass of the pion and muon respectively. For a fixed  
<sup>769</sup> energy pion, the neutrino energy distribution is dependent upon the angle at which the  
<sup>770</sup> neutrinos are observed from the initial pion beam direction. For the 295km baseline at  
<sup>771</sup> T2K,  $E_\nu = 0.6\text{GeV}$  maximises the electron neutrino appearance probability,  $P(\nu_\mu \rightarrow \nu_e)$ ,  
<sup>772</sup> whilst minimising the muon disappearance probability,  $P(\nu_\mu \rightarrow \nu_\mu)$ . Figure 3.8  
<sup>773</sup> illustrates the neutrino energy distribution for a range of off-axis angles, as well as the  
<sup>774</sup> oscillation probabilities most relevant to T2K.

### <sup>775</sup> 3.2.2 The Near Detector at 280m

<sup>776</sup> Whilst all the near detectors are situated in the same “pit” located at 280m from the  
<sup>777</sup> beamline, the “ND280” detector is the off-axis detector which is situated at the same  
<sup>778</sup> off-axis angle as the Super-Kamiokande far detector. It has two primary functions;  
<sup>779</sup> firstly it measures the neutrino flux and secondly it counts the event rates of different  
<sup>780</sup> types of neutrino interactions. Both of these constrain the flux and cross-section

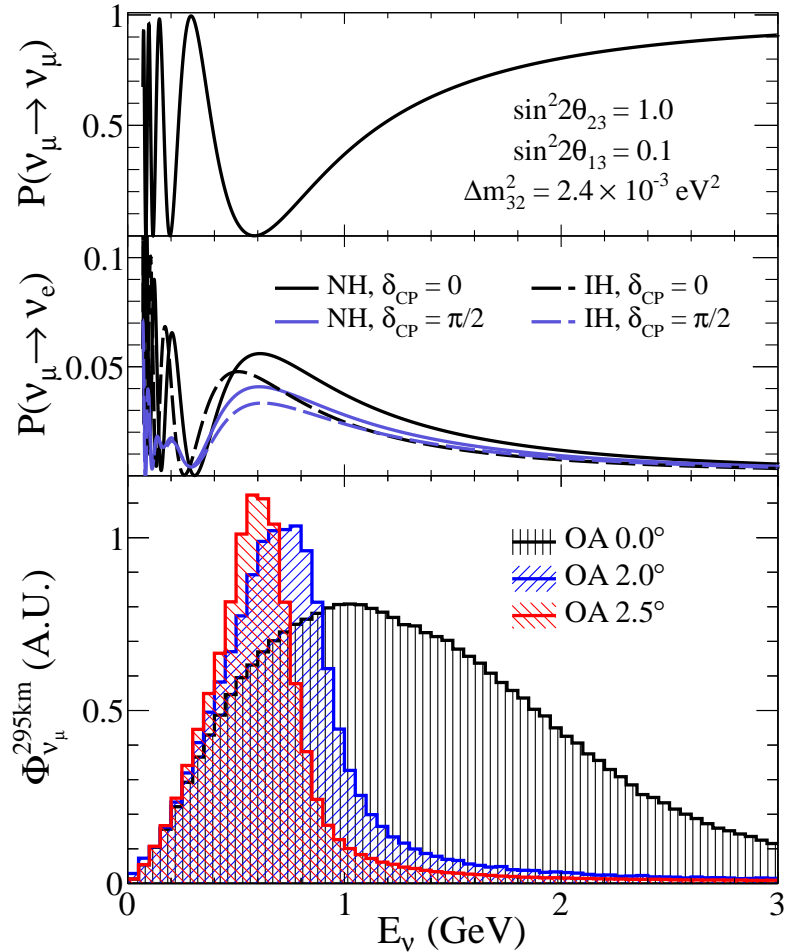


**Figure 3.8:** Top panel: T2K muon neutrino disappearance probability as a function of neutrino energy. Middle panel: T2K electron neutrino appearance probability as a function of neutrino energy. Bottom panel: The neutrino flux distribution for three different off-axis angles (Arbitrary units) as a function of neutrino energy.

781 systematics invoked within the model for a more accurate prediction of the expected  
 782 event rate at the far detector.

783 As illustrated in Figure 3.9, the ND280 detector consists of several sub-detectors.  
 784 The most important part of the detector for this analysis is the tracker region. This is  
 785 comprised of two time projection chambers (TPCs) sandwiched between three fine  
 786 grain detectors (FGDs). The FGDs contain both hydrocarbon plastics and water tar-  
 787 gets for neutrino interactions and provide track reconstruction near the interaction  
 788 vertex. The emitted charged particles can then propagate into the TPCs which pro-  
 789 vide particle identification and momentum reconstruction. The FGDs and TPCs are

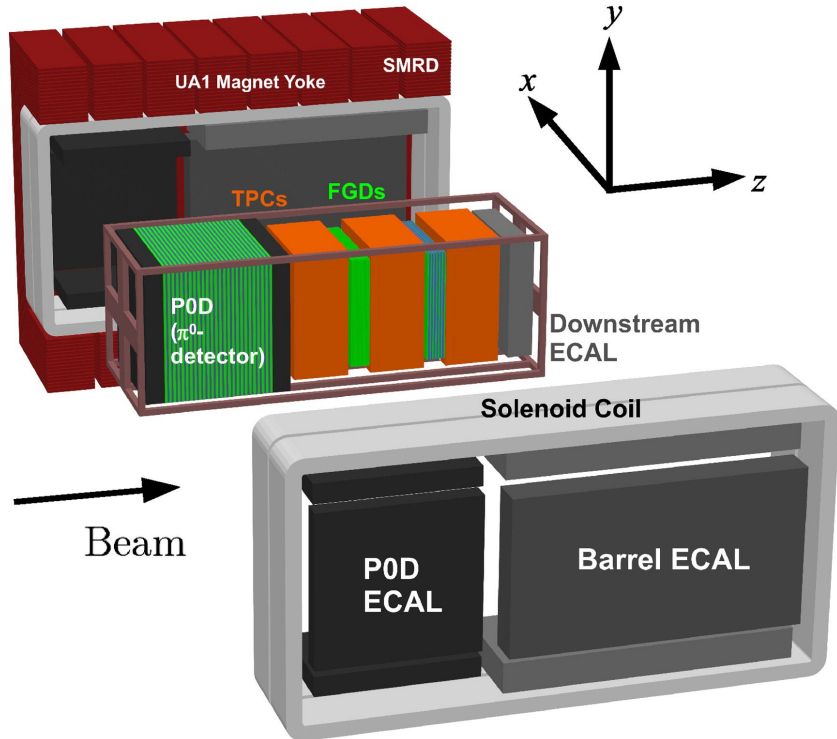


**Figure 3.9:** The components of the ND280 detector. The neutrino beam travels from left to right. Taken from [118].

790 further described in subsubsection 3.2.2.1 and subsubsection 3.2.2.2 respectively. The  
 791 electromagnetic calorimeter (ECAL) encapsulates the tracker region alongside the  $\pi^0$   
 792 detector (P0D). The ECAL measures the deposited energy from photons emitted from  
 793 interactions within the FGD. The P0D constrains the cross-section of neutral current  
 794 interactions which generate neutral pions, which is one of the largest backgrounds in  
 795 the electron neutrino appearance oscillation channel. The P0D and ECAL detectors  
 796 are detailed in subsubsection 3.2.2.3 and subsubsection 3.2.2.4 respectively. The entire  
 797 detector is located within a large yoke magnet which produces a 0.2T magnetic field.  
 798 This design of the magnet also includes a scintillating detector called the side muon  
 799 range detector (SMRD) which is used to track high-angle muons as well as acting as a  
 800 cosmic veto. The SMRD is described in subsubsection 3.2.2.5.

801    **3.2.2.1 Fine Grained Detectors**

802    The T2K tracker region is comprised of two fine grained detectors (FGD) and three  
803    Time Projection Chambers (TPC). A detailed description of the FGD design, construc-  
804    tion, and assembly is found in [123] and summarised below. The FGDs are the primary  
805    target for neutrino interactions with a mass of 1.1 tonnes per FGD. Alongside this,  
806    the FGDs are designed to be able to track short-range particles which do not exit the  
807    FGD. Typically, short-range particles are low momentum and are observed as tracks  
808    that deposit a large amount of energy per unit length. This means the FGD needs  
809    good granularity to resolve these particles. The FGDs have the best timing resolution  
810    ( $\sim 3\text{ns}$ ) of any of the sub-detectors of the ND280 detector. As such, the FGDs are  
811    used for time of flight measurements to distinguish forward going positively charged  
812    particles from backward going negatively charged particles. Finally, any tracks which  
813    pass through multiple sub-detectors are required to be track matched to the FGD.

814       Both FGDs are made from square scintillator planes of side length 186cm and  
815    width 2.02cm. Each plane consists of two layers of 192 scintillator bars in an X or Y  
816    orientation. A wavelength shifting fiber is threaded through the center of each bar and  
817    is read out by a multi-pixel photon counter (MPPC). FGD1 is the most upstream of  
818    the two FGDs and contains 15 planes of carbon plastic scintillator which is a common  
819    target in external neutrino scattering data. As the far detector is a pure water target, 7  
820    of the 15 scintillator planes in FGD2 have been replaced with a hybrid water-scintillator  
821    target. Due to the complexity of the nucleus, nuclear effects can not be extrapolated  
822    between different nuclei. Therefore having the ability to take data on one target which  
823    is the same as external data and another target which is the same as the far detector  
824    target is beneficial for reliable model parameter estimates.

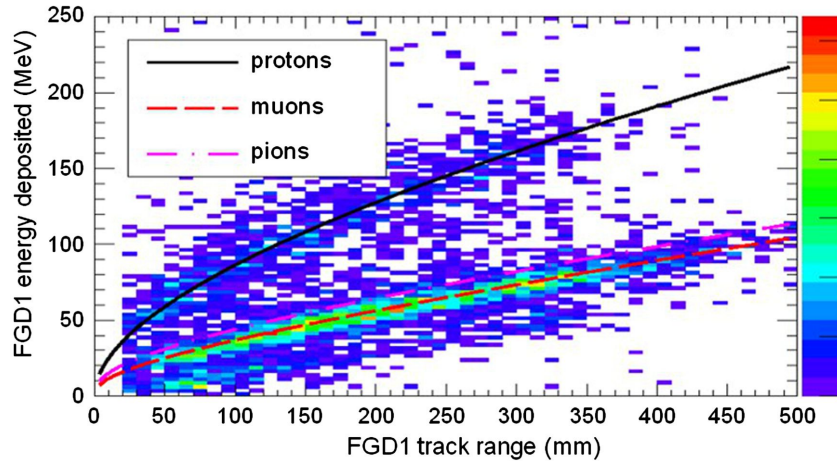


**Figure 3.10:** Comparison of data to Monte Carlo prediction of integrated deposited energy as a function of track length for particles that stopped in FGD1. Taken from [123].

The integrated deposited energy is used for particle identification. The FGD can distinguish protons from other charged particles by comparing the integrated deposited energy from data to Monte Carlo prediction as seen in Figure 3.10.

### 3.2.2.2 Time Projection Chambers

The majority of particle identification and momentum measurements within ND280 are provided by three Time Projection Chambers (TPCs) [124]. The TPCs are located on either side of the FGDs. They are located inside of the magnetic field meaning the momentum of a charged particle can be determined from the bending of the track.

Each TPC module consists of two gas-tight boxes, as shown in Figure 3.11, which are made of non-magnetic material. The outer box is filled with CO<sub>2</sub> which acts as an electrical insulator between the inner box and the ground. The inner box forms the field cage which produces a uniform electric drift field of  $\sim 275\text{V/cm}$  and is filled with an argon gas mixture. Charged particles moving through this gas mixture ionize the gas and the ionised charge is drifted towards micromegas detectors which measure the ionization charge. The time and position information in the readout allows a three-dimensional image of the neutrino interaction.

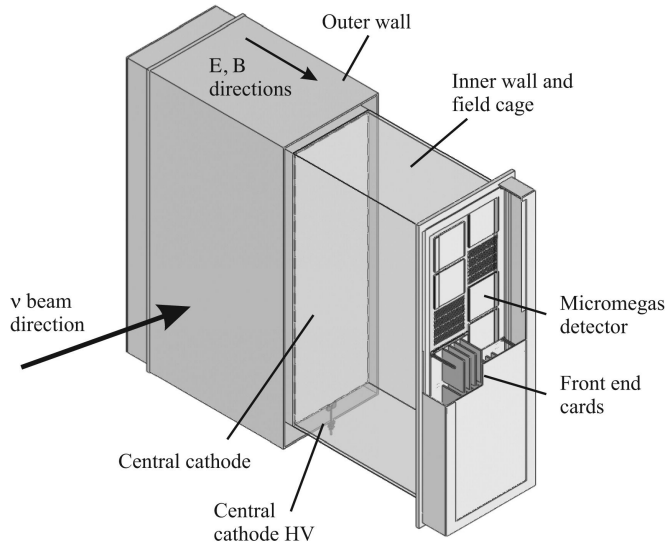


**Figure 3.11:** Schematic design of a Time Projection Chamber detector. Taken from [124].

The particle identification of tracks that pass through the TPCs is performed using  $dE/dx$  measurements. Figure 3.12 illustrates the data to Monte Carlo distributions of the energy lost by a charged particle passing through the TPC as a function of the reconstructed particle momentum. The resolution is  $7.8 \pm 0.2\%$  meaning that electrons and muons can be distinguished. This allows reliable measurements of the intrinsic  $\nu_e$  component of the beam.

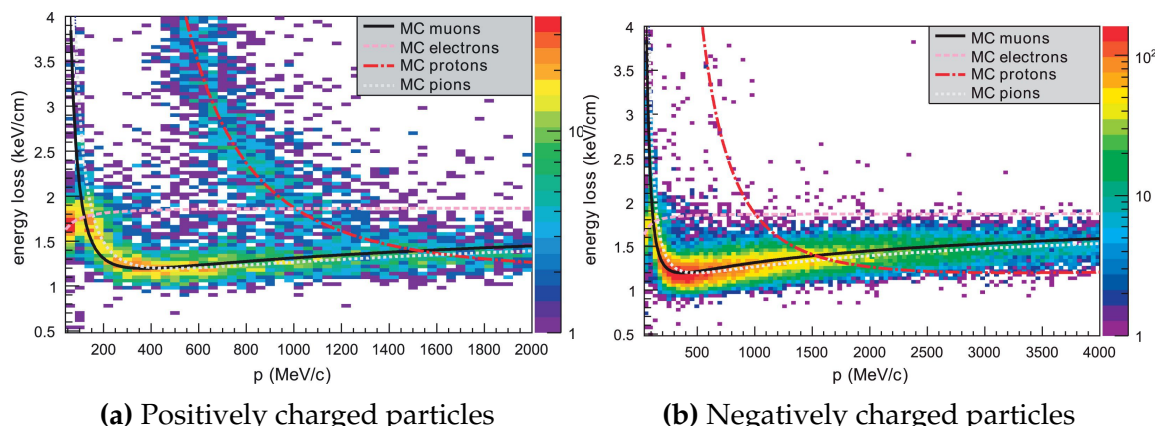


**Figure 3.12:** The distribution of energy loss as a function of reconstructed momentum for charged particles passing through the TPC, comparing data to Monte Carlo prediction. Taken from [124].

**<sup>847</sup> 3.2.2.3  $\pi^0$  Detector**

<sup>848</sup> If one of the  $\gamma$ -rays from a  $\pi^0 \rightarrow 2\gamma$  decay is missed at the far detector, the recon-  
<sup>849</sup> struction will determine that event to be a charge current  $\nu_e$ -like event. This is one of  
<sup>850</sup> the main backgrounds hindering the electron neutrino appearance searches. The  $\pi^0$   
<sup>851</sup> detector (P0D) measures the cross-section of the neutral current induced neutral pion  
<sup>852</sup> production on a water target to constrain this background.

<sup>853</sup> The P0D is a cube of approximately 2.5m length consisting of layers of scintillating  
<sup>854</sup> bars, brass and lead sheets, and water bags as illustrated in Figure 3.13. Two electro-  
<sup>855</sup> magnetic calorimeters are positioned at the most upstream and most downstream  
<sup>856</sup> position in the sub-detector and the water target is situated in between them. The  
<sup>857</sup> scintillator layers are built from two triangular bars orientated in opposite directions  
<sup>858</sup> to form a rectangular layer. Each triangular scintillator bar is threaded with optical  
<sup>859</sup> fiber which is read out by MPPCs. The high-Z brass and lead regions produce electron  
<sup>860</sup> showers from the photons emitted in  $\pi^0$  decay.

<sup>861</sup> The sub-detector can generate measurements of NC1 $\pi^0$  cross-sections on a water  
<sup>862</sup> target by measuring the event rate both with and without the water target, with the  
<sup>863</sup> cross-section on a water target being determined as the difference. The total active  
<sup>864</sup> mass is 16.1 tonnes when filled with water and 13.3 tonnes when empty.

**<sup>865</sup> 3.2.2.4 Electromagnetic Calorimeter**

<sup>866</sup> The electromagnetic calorimeter [126] (ECal) encapsulates the P0D and tracking sub-  
<sup>867</sup> detectors. Its primary purpose is to aid  $\pi^0$  reconstruction from any interaction in  
<sup>868</sup> the tracker. To do this, it measures the energy and direction of photon showers from  
<sup>869</sup>  $\pi^0 \rightarrow 2\gamma$  decay. It can also distinguish pion and muon tracks depending on the shape  
<sup>870</sup> of the photon shower deposited.

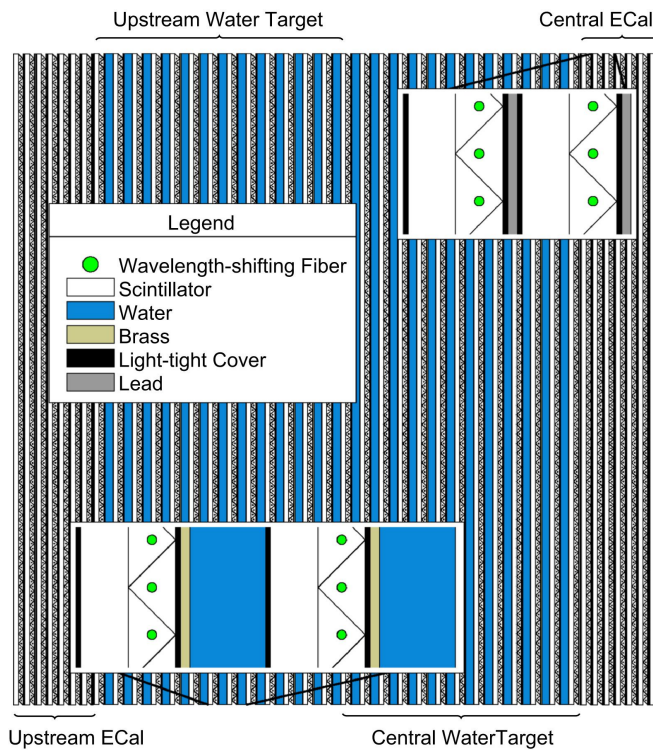


**Figure 3.13:** A schematic of the P0D side-view. Taken from [125].

871        The ECal is comprised of three sections; the P0D ECal which surrounds the P0D,  
 872        the barrel ECal which encompasses the tracking region, and the downstream ECal  
 873        which is situated downstream of the tracker region. The barrel and downstream  
 874        ECals are tracking calorimeters that focus on electromagnetic showers from high-angle  
 875        particles emitted from the tracking sub-detectors. Particularly in the TPC, high-angle  
 876        tracks (those which travel perpendicularly to the beam-axis) can travel along a single  
 877        scintillator bar resulting in very few hits. The width of the barrel and downstream  
 878        ECal corresponds to  $\sim 11$  electron radiation lengths to ensure a significant amount of  
 879        the  $\pi^0$  energy is contained. As the P0D has its own calorimetry which reconstructs  
 880        showers, the P0D ECal determines the energy which escapes the P0D.

881        Each ECal is constructed of multiple layers of scintillating bars sandwiched between  
 882        lead sheets. The scintillating bars are threaded with optical fiber and read out by  
 883        MPPCs. Each sequential layer of the scintillator is orientated perpendicular to the  
 884        previous which allows a three dimensional event reconstruction. The target mass

885 of the P0D ECal, barrel ECal, and downstream ECal are 1.50, 4.80 and 6.62 tonnes  
886 respectively.

887 **3.2.2.5 Side Muon Range Detector**

888 As illustrated in Figure 3.9, the ECal, FGDs, P0D, and TPCs are enclosed within the  
889 UA1 magnet. Originally designed for the NOMAD [127] experiment and reconditioned  
890 for use in the T2K experiment [128], the UA1 magnet provides a uniform horizontal  
891 magnetic field of 0.2T with an uncertainty of  $2 \times 10^{-4}$ T.

892 Built into the UA1 magnet, the side muon range detector (SMRD) [129] monitors  
893 high-energy muons which leave the tracking region and permeate through the ECal.  
894 It additionally acts as a cosmic muon veto and trigger.

895 **3.2.3 The Interactive Neutrino GRID**

896 The Interactive Neutrino GRID (INGRID) detector is situated within the same “pit” as  
897 the other near detectors. It is aligned with the beam in the “on-axis” position and mea-  
898 sures the beam direction, spread, and intensity. The detector was originally designed  
899 with 16 identical modules [118] (two modules have since been decommissioned) and a  
900 “proton” module. The design of the detector is cross-shaped with length and height  
901 10m × 10m as illustrated in Figure 3.14.

902 Each module is composed of iron sheets interlaced with eleven tracking scintillator  
903 planes for a total target mass of 7.1 tonnes per module. The scintillator design is an X-Y  
904 pattern of 24 bars in both orientations, where each bar contains wave-length shifting  
905 fibers which are connected to multi-pixel photon counters (MPPCs). Each module is  
906 encapsulated inside veto planes to aid the rejection of charged particles entering the  
907 module.

908     The proton module is different from the other modules in that it consists of entirely  
 909    scintillator planes with no iron target. The scintillator bars are also smaller than those  
 910    used in the other modules to increase the granularity of the detector and improve  
 911    tracking capabilities. The module sits in the center of the beamline and is designed to  
 912    give precise measurements of quasi-elastic charged current interactions to evaluate  
 913    the performance of the Monte Carlo simulation of the beamline.

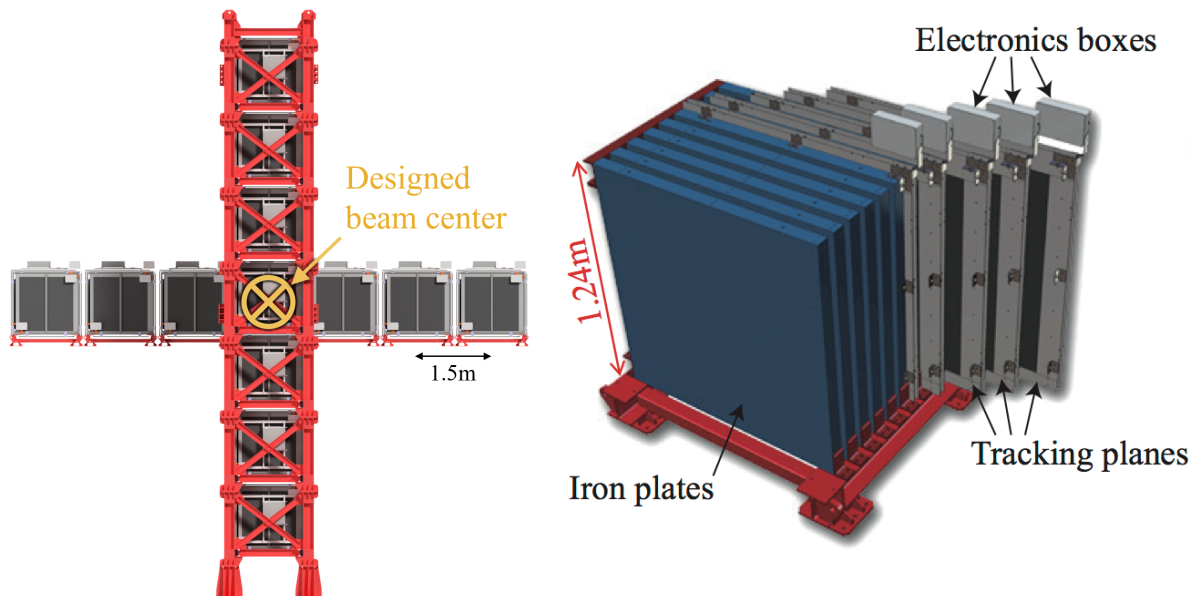


**Figure 3.14:** Left panel: The Interactive Neutrino GRID on-axis Detector. 14 modules are arranged in a cross-shape configuration, with the center modules being directly aligned with the on-axis beam. Right panel: The layout of a single module of the INGRID detector. Both figures are recreated from [118].

914     The INGRID detector can measure the beam direction to an uncertainty of 0.4mrad  
 915    and the beam center within a resolution of 10cm [118]. The beam direction in both the  
 916    vertical and horizontal directions is discussed in [130] and it is found to be in good  
 917    agreement with the MUMON monitor described in subsection 3.2.1.

<sub>918</sub> **Chapter 4**

<sub>919</sub> **Bayesian Statistics and Markov Chain**  
<sub>920</sub> **Monte Carlo Techniques**

<sub>921</sub> This thesis presents a Bayesian oscillation analysis. To extract the oscillation parameters,  
<sub>922</sub> a Markov Chain Monte Carlo (MCMC) method is used. This chapter explains  
<sub>923</sub> the theory of how parameter estimates can be determined using this technique and  
<sub>924</sub> condenses the material found in the literature [131–134].

<sub>925</sub> The oscillation parameter determination presented within this thesis is built upon  
<sub>926</sub> a simultaneous fit to neutrino beam data in the near detector, beam data at SK and  
<sub>927</sub> atmospheric data at SK. In total, there are four oscillation parameters of interest  
<sub>928</sub> ( $\sin^2(\theta_{23})$ ,  $\sin^2(\theta_{13})$ ,  $\Delta m_{23}^2$ , and  $\delta_{CP}$ ), two oscillation parameters to which this study  
<sub>929</sub> will not be sensitive ( $\sin^2(\theta_{12})$ ,  $\Delta m_{12}^2$ ) and many nuisance parameters that control the  
<sub>930</sub> systematic uncertainty models invoked within this study.

<sub>931</sub> The MCMC technique generates a multi-dimensional probability distribution across  
<sub>932</sub> all of the model parameters used in the fit. To determine the parameter estimate of a  
<sub>933</sub> single parameter, this multi-dimensional object is integrated over all other parameters.  
<sub>934</sub> This process is called Marginalisation and is further described in subsection 4.3.1.  
<sub>935</sub> Monte Carlo techniques approximate the probability distribution of each parameter  
<sub>936</sub> within the limit of generating infinite samples. As ever, generating a large number of  
<sub>937</sub> samples is time and resource-dependent. Therefore, an MCMC technique is utilised  
<sub>938</sub> within this analysis to reduce the required number of steps to sufficiently sample the  
<sub>939</sub> parameter space. This technique is described in further detail in subsection 4.2.1.

## 940 4.1 Bayesian Statistics

941 Bayesian inference treats observable data,  $D$ , and model parameters,  $\vec{\theta}$ , on equal  
942 footing such that a probability model of both data and parameters is required. This is  
943 the joint probability distribution  $P(D, \vec{\theta})$  and can be described by the prior distribution  
944 for model parameters  $P(\vec{\theta})$  and the likelihood of the data given the model parameters  
945  $P(D|\vec{\theta})$ ,

$$P(D, \vec{\theta}) = P(D|\vec{\theta})P(\vec{\theta}). \quad (4.1)$$

946 The prior distribution,  $P(\vec{\theta})$ , describes all previous knowledge about the parameters  
947 within the model. For example, if the risk of developing health problems is known  
948 to increase with age, the prior distribution would describe the increase. For the  
949 purpose of this analysis, the prior distribution is typically the best-fit values taken  
950 from external data measurements with a Gaussian uncertainty. The prior distribution  
951 can also contain correlations between model parameters. In an analysis using Monte  
952 Carlo techniques, the likelihood of measuring some data assuming some set of model  
953 parameters is calculated by comparing the Monte Carlo prediction generated at that  
954 particular set of model parameters to the data.

955 It is parameter estimation that is important for this analysis and as such, we apply  
956 Bayes' theorem [135] to calculate the probability for each parameter to have a certain  
957 value given the observed data,  $P(\vec{\theta}|D)$ , which is known as the posterior distribution  
958 (often termed the posterior). This can be expressed as

$$P(\vec{\theta}|D) = \frac{P(D|\vec{\theta})P(\vec{\theta})}{\int P(D|\vec{\theta})P(\vec{\theta})d\vec{\theta}}. \quad (4.2)$$

959 The denominator in Equation 4.2 is the integral of the joint probability distribution

960 over all values of all parameters used within the fit. For brevity, we say that the  
961 posterior distribution is

$$P(\vec{\theta}|D) \propto P(D|\vec{\theta})P(\vec{\theta}). \quad (4.3)$$

962 In subsection 4.3.1, we see that for the cases used within this analysis, it is reason-  
963 able to know the posterior to some normalisation constant.

## 964 4.2 Monte Carlo Simulation

965 Monte Carlo techniques are used to numerically solve a complex problem that does  
966 not necessarily have an analytical solution. These techniques rely on building a large  
967 ensemble of samples from an unknown distribution and then using the ensemble to  
968 approximate the properties of the distribution.

969 An example that uses Monte Carlo techniques is to calculate the area underneath  
970 a curve. For example, take the problem of calculating the area under a straight line  
971 with gradient  $M = 0.4$  and intercept  $C = 1.0$ . Analytically, one can calculate the area  
972 under the line is equal to 30 units for  $0 \leq x \leq 10$ . Using Monte Carlo techniques,  
973 one can calculate the area under this line by throwing many random values for the  $x$   
974 and  $y$  components of each sample and then calculating whether that point falls below

the line. The area can then be calculated by the ratio of points below the line to the total number of samples thrown multiplied by the total area in which samples were scattered. The study is shown in Figure 4.1 highlights this technique and finds the area under the curve to be 29.9 compared to an analytical solution of 30.0. The deviation of the numerical to analytical solution can be attributed to the number of samples used in the study. The accuracy of the approximation in which the properties of the Monte Carlo samples replicate those of the desired distribution is dependent on the number of samples used. Replicating this study with a differing number of Monte Carlo samples used in each study (As shown in Figure 4.2) highlights how the Monte Carlo techniques are only accurate within the limit of a high number of samples.

Whilst the above example has an analytical solution, these techniques are just as applicable to complex solutions. Clearly, any numerical solution is only as useful as its efficiency. As discussed, the accuracy of the Monte Carlo technique is dependent upon the number of samples generated to approximate the properties of the distribution. Furthermore, if the positions at which the samples are evaluated are not ‘cleverly’ picked, the efficiency of the Monte Carlo technique significantly drops. Given the example in Figure 4.1, if the region in which the samples are scattered significantly extends passed the region of interest, many calculations will be calculated but do not add to the ability of the Monte Carlo technique to achieve the correct result. For instance, any sample evaluated at a  $y \geq 5$  could be removed without affecting the final result. This does bring in an aspect of the ‘chicken and egg’ problem in that to achieve efficient sampling, one needs to know the distribution beforehand.

### 4.2.1 Markov Chain Monte Carlo

This analysis utilises a multi-dimensional probability distribution, with some dimensions being significantly more constrained than others. This could be from prior

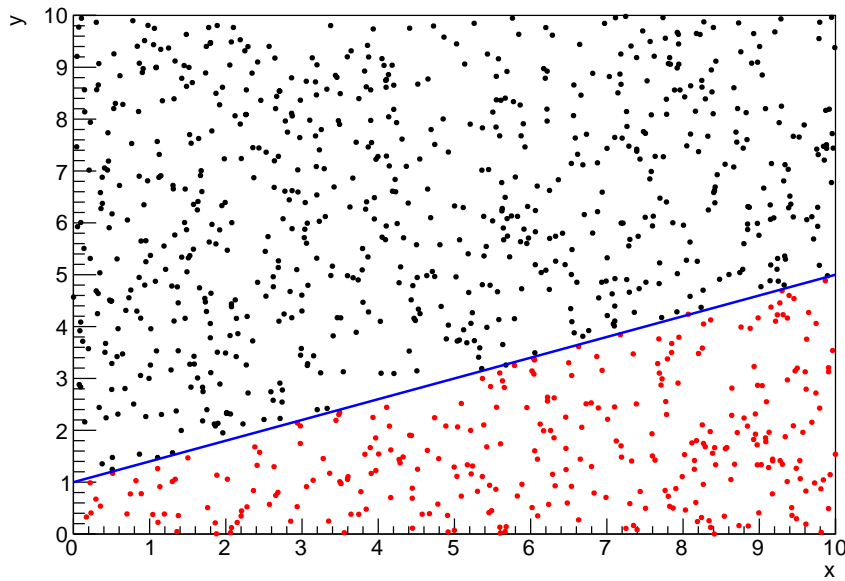


**Figure 4.1:** Example of using Monte Carlo techniques to find the area under the blue line. The gradient and intercept of the line are 0.4 and 1.0 respectively. The area found to be under the curve using one thousand samples is 29.9 units.

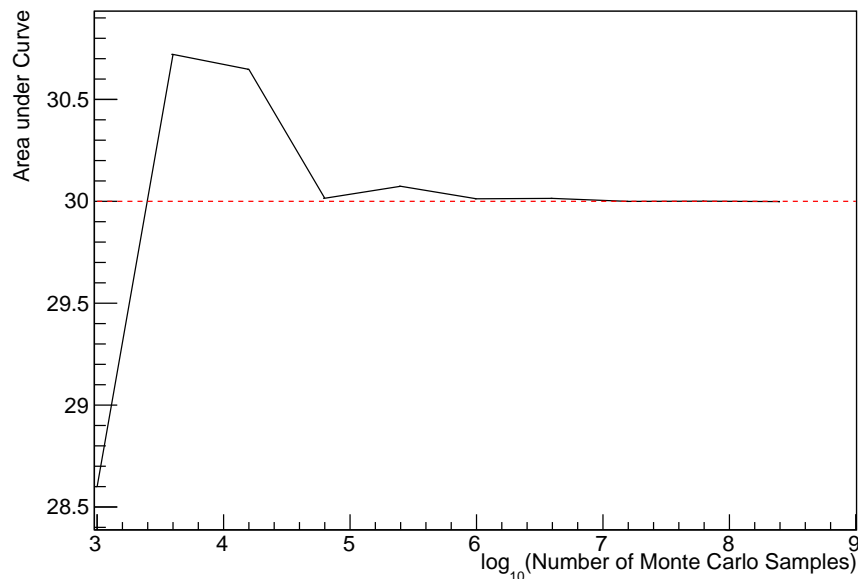


**Figure 4.2:** The area under a line of gradient 0.4 and intercept 1.0 for the range  $0 \leq x \leq 10$  as calculated using Monte Carlo techniques as a function of the number of samples used in each repetition. The analytical solution to the area is 30 units as given by the red line.

knowledge of parameter distributions from external data or un-physical regions in which parameters can not exist. Consequently, the Monte Carlo techniques used need to be as efficient as possible. For this analysis, the Markov Chain Monte Carlo (MCMC) technique is chosen. An MCMC technique is a Monte Carlo technique that uses a Markov chain to select which points at which to sample the parameter distribution. This technique performs a semi-random stochastic walk through the allowable parameter space. This builds a posterior distribution which has the property that the density of sampled points is proportional to the probability density of that parameter. This does mean that the samples produced by this technique are not statistically independent but they will cover the space of the distribution.

A Markov chain functions by selecting the position of step  $\vec{x}_{i+1}$  based on the position of  $\vec{x}_i$ . The space in which the Markov chain selects samples is dependent upon the total number of parameters utilised within the fit, where a discrete point in this space is described by the N-dimensional space  $\vec{x}$ . In a perfectly operating Markov chain, the position of the next step depends solely on the previous step and not on the further history of the chain ( $\vec{x}_0, \vec{x}_1$ , etc.). However, in solving the multi-dimensionality of the fit used within this analysis, each step becomes correlated with several of the steps preceding itself. This behaviour is further explained in subsection 4.2.3. Providing the MCMC chain is well optimised, it will begin to converge towards a unique stationary distribution. The period between the chain's initial starting point and the convergence to the unique stationary distribution is colloquially known as the burn-in period. This is discussed further in subsection 4.2.3. Once the chain reaches the stationary distribution, all points sampled after that point will look like samples from that distribution.

1024      Further details of the theories underpinning MCMC techniques are discussed  
1025    in [132] but can be summarised by the requirement that the chain satisfies the three  
1026    ‘regularity conditions’:

- 1027    • Irreducibility: From every position in the parameter space  $\vec{x}$ , there must exist a  
1028    non-zero probability for every other position in the parameter space to be reached.
- 1029    • Recurrence: Once the chain arrives at the stationary distribution, every step fol-  
1030    lowing from that position must be samples from the same stationary distribution.
- 1031    • Aperiodicity: The chain must not repeat the same sequence of steps at any point  
1032    throughout the sampling period.

1033    The output of the chain after burn-in (ie. the sampled points after the chain  
1034 has reached the stationary distribution) can be used to approximate the posterior  
1035 distribution and model parameters  $\vec{\theta}$ . To achieve the requirement that the unique  
1036 stationary distribution found by the chain be the posterior distribution, one can use  
1037 the Metropolis-Hastings algorithm. This guides the stochastic process depending on  
1038 the likelihood of the current proposed step compared to that of the previous step.  
1039 Implementation and other details of this technique are discussed in subsection 4.2.2.

#### 1040 4.2.2 Metropolis-Hastings Algorithm

1041 As a requirement for MCMCs, the Markov chain implemented in this technique must  
1042 have a unique stationary distribution that is equivalent to the posterior distribution.  
1043 To ensure this requirement and that the regularity conditions are met, this analysis  
1044 utilises the Metropolis-Hastings (MH) algorithm [136,137]. For the  $i^{th}$  step in the chain,  
1045 the MH algorithm determines the position in the parameter space to which the chain  
1046 moves to based on the current step,  $\vec{x}_i$ , and the proposed step,  $\vec{y}_{i+1}$ . The proposed step  
1047 is randomly selected from some proposal function  $f(\vec{x}_{i+1} | \vec{x}_i)$ , which depends solely

1048 on the current step (ie. not the further history of the chain). The next step in the chain  
 1049  $\vec{x}_{i+1}$  can be either the current step or the proposed step determined by whether the  
 1050 proposed step is accepted or rejected. To decide if the proposed step is selected, the  
 1051 acceptance probability,  $\alpha(\vec{x}_i, \vec{y}_i)$ , is calculated as

$$\alpha(\vec{x}_i, \vec{y}_{i+1}) = \min \left( 1, \frac{P(\vec{y}_{i+1}|D)f(\vec{x}_i|\vec{y}_{i+1})}{P(\vec{x}_i|D)f(\vec{y}_{i+1}|\vec{x}_i)} \right). \quad (4.4)$$

1052 Where  $P(\vec{y}_{i+1}|D)$  is the posterior distribution as introduced in section 4.1. To  
 1053 simplify this calculation, the proposal function is required to be symmetric such that  
 1054  $f(\vec{x}_i|\vec{y}_{i+1}) = f(\vec{y}_{i+1}|\vec{x}_i)$ . In practice, a multi-variate Gaussian distribution is used to  
 1055 throw parameter proposals from. This reduces Equation 4.4 to

$$\alpha(\vec{x}_i, \vec{y}_{i+1}) = \min \left( 1, \frac{P(\vec{y}_{i+1}|D)}{P(\vec{x}_i|D)} \right). \quad (4.5)$$

1056 After calculating this quantity, a random number,  $\beta$ , is generated uniformly be-  
 1057 tween 0 and 1. If  $\beta \leq \alpha(\vec{x}_i, \vec{y}_{i+1})$ , the proposed step is accepted. Otherwise, the chain  
 1058 sets the next step equal to the current step and this procedure is repeated. This can be  
 1059 interpreted as if the posterior probability of the proposed step is greater than that of  
 1060 the current step, ( $P(\vec{y}_{i+1}|D) \geq P(\vec{x}_i|D)$ ), the proposed step will always be accepted.  
 1061 If the opposite is true, ( $P(\vec{y}_{i+1}|D) \leq P(\vec{x}_i|D)$ ), the proposed step will be accepted  
 1062 with probability  $P(\vec{x}_i|D)/P(\vec{y}_{i+1}|D)$ . This ensures that the Markov chain does not get  
 1063 trapped in any local minima in the potentially non-Gaussian posterior distribution.  
 1064 The outcome of this technique is that the density of steps taken in a discrete region is  
 1065 directly proportional to the probability density in that region.

### 1066 4.2.3 MCMC Optimisation

1067 As discussed in subsection 4.2.2, the proposal function invoked within the MH algo-  
1068 rithm can take any form and the chain will still converge to the stationary distribution.  
1069 At each set of proposed parameter values, a prediction of the same spectra has to be  
1070 generated which requires significant computational resources. Therefore, the number  
1071 of steps taken before the unique stationary distribution is found should be minimised  
1072 as only steps after convergence add information to the oscillation analysis. Further-  
1073 more, the chain should entirely cover the allowable parameter space to ensure that all  
1074 values have been considered. Tuning the distance that the proposal function jumps  
1075 between steps on a parameter-by-parameter basis can both minimise the length of the  
1076 burn-in period and ensure that the correlation between step  $\vec{x}_i$  and  $\vec{x}_j$  is sufficiently  
1077 small.

1078 The effect of changing the width of the proposal function is highlighted in Figure 4.3.  
1079 Three scenarios, each with the same underlying stationary distribution (A Gaussian of  
1080 width 1.0 and mean 0.), are presented. The only difference between the three scenarios  
1081 is the width of the proposal function, colloquially known as the ‘step size  $\sigma$ ’. Each  
1082 scenario starts at an initial parameter value of 10.0 which would be considered an  
1083 extreme variation. For the case where  $\sigma = 0.1$ , it is clear to see that the chain takes  
1084 a long time to reach the expected region of the parameter. This indicates that this  
1085 chain would have a large burn-in period and does not converge to the stationary  
1086 distribution until step  $\sim 500$ . Furthermore, whilst the chain does move towards the  
1087 expected region, each step is significantly correlated with the previous. Considering  
1088 the case where  $\sigma = 5.0$ , the chain approaches the expected parameter region almost  
1089 instantly meaning that the burn-in period is not significant. However, there are clearly  
1090 large regions of steps where the chain does not move. This is likely due to the chain  
1091 proposing steps in the tails of the distribution which have a low probability of being

1092 accepted. Consequently, this chain would take a significant number of steps to fully  
 1093 span the allowable parameter region. For the final scenario, where  $\sigma = 0.5$ , you can see  
 1094 a relatively small burn-in period of approximately 100 steps. Once the chain reaches  
 1095 the stationary distribution, it moves throughout the expected region of parameter  
 1096 values many times, sufficiently sampling the full parameter region. This example is a  
 1097 single parameter varying across a continuous distribution and does not fully reflect  
 1098 the difficulties in the many-hundred multi-variate parameter distribution used within  
 1099 this analysis. However, it does give a conceptual idea of the importance of selecting  
 1100 the proposal function and associated step size.

1101 As discussed, step size tuning directly correlates to the average step acceptance  
 1102 rate. If the step size is too small, many steps will be accepted but the chain moves  
 1103 slowly. If the opposite is true, many steps will be rejected as the chain proposes steps  
 1104 in the tails of the distribution. Discussion in [138] suggests that the ‘ideal’ acceptance  
 1105 rate of a high dimension MCMC chain should be approximately  $\sim 25\%$ . An “ideal”  
 1106 step size [138] of

$$\sigma = \frac{2.4}{N_p}, \quad (4.6)$$

1107 where  $N_p$  is the number of parameters included in the MCMC fit. However, the  
 1108 complex correlations between systematics mean that some parameters have to be hand  
 1109 tuned and many efforts have been taken to select a set of parameter-by-parameter step  
 1110 sizes to approximately reach the ideal acceptance rate.

1111 Figure 4.3 highlights the likelihood as calculated by the fit in [DB: Link to AsimovA](#)  
 1112 **Sensitivity Section** as a function of the number of steps in each chain. In practice,  
 1113 many independent MCMC chains are run simultaneously to parallelise the task of

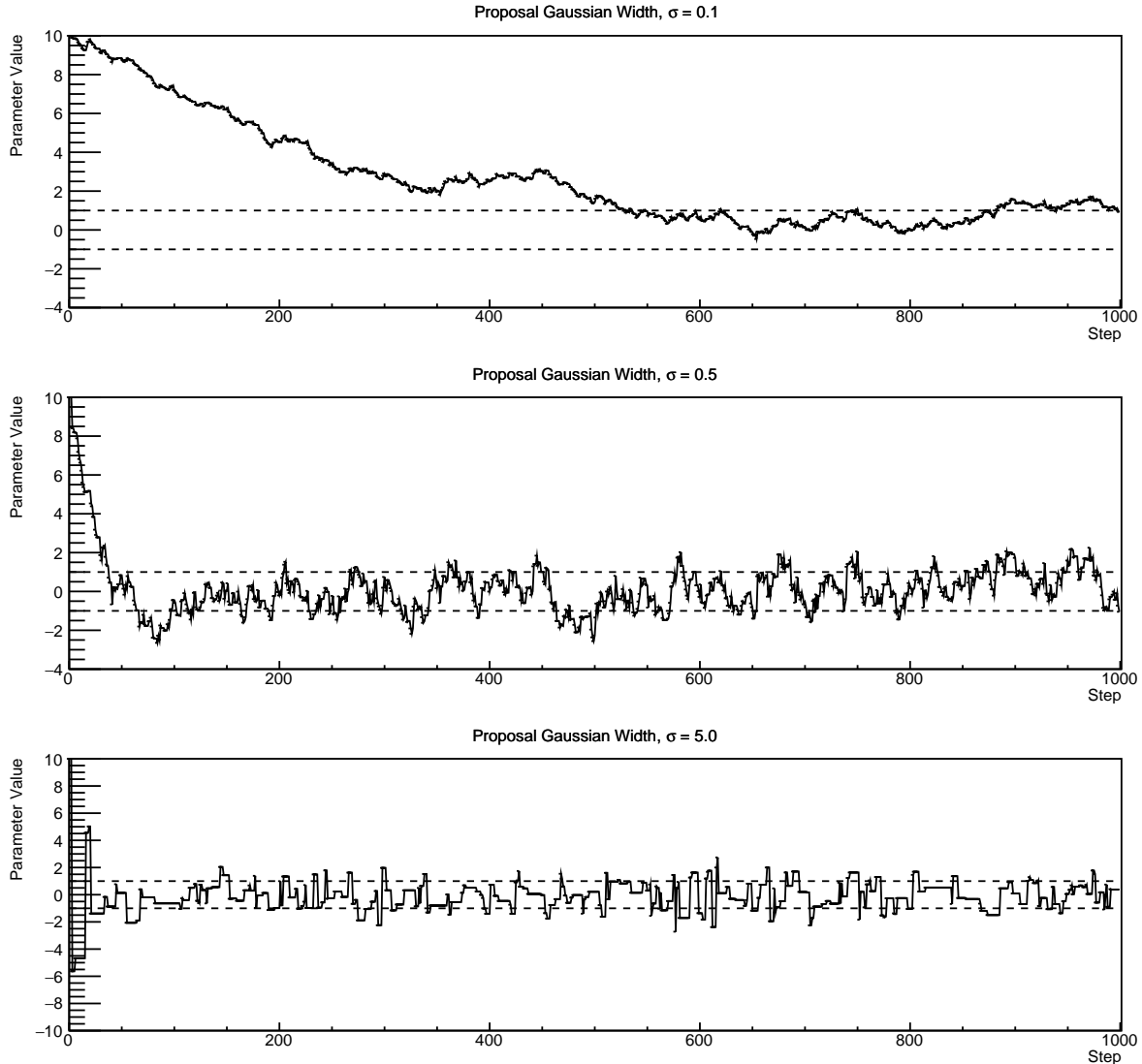


**Figure 4.3:** Three MCMC chains, each with a stationary distribution equal to a Gaussian centered at 0 and width 1 (As indicated by the black dotted lines). All of the chains use a Gaussian proposal function but have different widths (or ‘step size  $\sigma$ ’). The top panel has  $\sigma = 0.1$ , middle panel has  $\sigma = 0.5$  and the bottom panel has  $\sigma = 5.0$ .

1114 performing the fit. This figure overlays the distribution found in each chain. As seen,  
 1115 the likelihood decreases from its initial value and converges towards a stationary  
 1116 distribution after  $\sim 1 \times 10^5$  steps.

1117 Multiple configurations of this analysis have been performed throughout this thesis  
 1118 where different samples or systematics have been used. For all of these configurations,  
 1119 it was found that a burnin period of  $1 \times 10^5$  was sufficient in all cases.

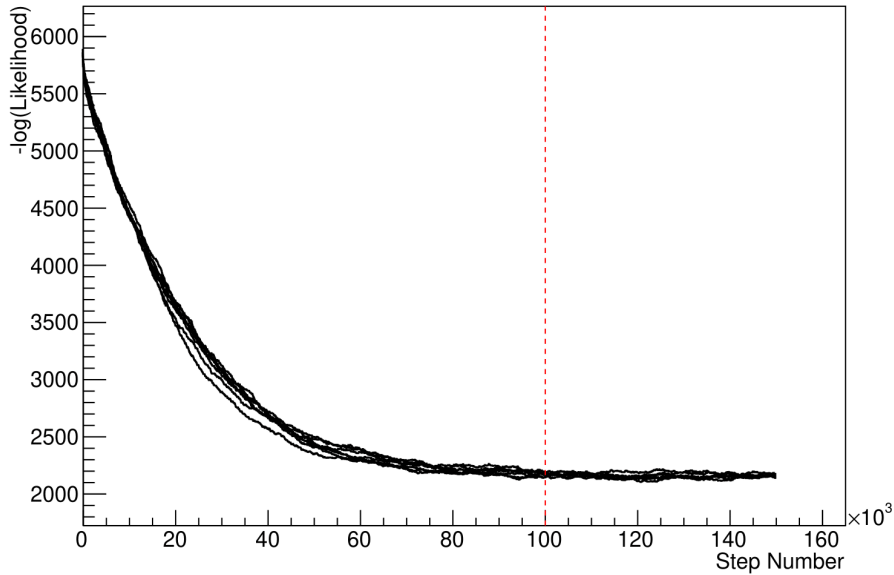


**Figure 4.4:** The log-likelihood from the fit detailed in DB: [Link to AsimovA Sensitivity Section](#) as a function of the number of steps accumulated in each fit. Many independent MCMC chains were run in parallel and overlaid on this plot. The red line indicates the  $1 \times 10^5$  step burn-in period after which the log-likelihood becomes stable.

## 1120 4.3 Understanding the MCMC Results

1121 The previous sections have described how to generate the posterior probability distri-  
 1122 bution using Bayesian MCMC techniques. However, this analysis focuses on oscillation  
 1123 parameter determination. The posterior distribution output from the chain is a high  
 1124 dimension object, with as many dimensions as there are parameters included in the os-  
 1125 cillation analysis. However, this multi-dimensional object is difficult to conceptualize  
 1126 so parameter estimations are often presented in one or two-dimensional projections  
 1127 of this probability distribution. To do this, we invoke the marginalisation technique  
 1128 highlighted in subsection 4.3.1.

---

### <sup>1129</sup> 4.3.1 Marginalisation

<sup>1130</sup> The output of the MCMC chain is a highly dimensional probability distribution  
<sup>1131</sup> which is very difficult to interpret. From the standpoint of an oscillation analysis  
<sup>1132</sup> experiment, the one or two-dimensional ‘projections’ of the oscillation parameters of  
<sup>1133</sup> interest are most relevant. Despite this, the best fit values and uncertainties on the  
<sup>1134</sup> oscillation parameters of interest should correctly encapsulate the correlations to the  
<sup>1135</sup> other systematic uncertainties (colloquially called ‘nuisance’ parameters). For this joint  
<sup>1136</sup> beam and atmospheric analysis, the oscillation parameters of interest are  $\sin^2(\theta_{23})$ ,  
<sup>1137</sup>  $\sin^2(\theta_{13})$ ,  $\Delta m_{23}^2$ , and  $\delta_{CP}$ . All other parameters (Including the oscillation parameter  
<sup>1138</sup> this fit is insensitive to) are deemed nuisance parameters. To generate these projections,  
<sup>1139</sup> we rely upon integrating the posterior distribution over all nuisance parameters. This  
<sup>1140</sup> is called marginalisation. A simple example of this technique is to imagine the scenario  
<sup>1141</sup> where two coins are flipped. To determine the probability that the first coin returned  
<sup>1142</sup> a ‘head’, the exact result of the second coin flip is disregarded and simply integrated  
<sup>1143</sup> over. For the parameters of interest,  $\vec{\theta}_i$ , we can calculate the marginalised posterior by  
<sup>1144</sup> integrating over the nuisance parameters,  $\vec{\theta}_n$ . In this case, Equation 4.2 becomes

$$P(\vec{\theta}_i|D) = \frac{\int P(D|\vec{\theta}_i, \vec{\theta}_n)P(\vec{\theta}_i, \vec{\theta}_n)d\vec{\theta}_n}{\int P(D|\vec{\theta})P(\vec{\theta})d\vec{\theta}} \quad (4.7)$$

<sup>1145</sup> Where  $P(\vec{\theta}_i, \vec{\theta}_n)$  encodes the prior knowledge about the uncertainty and correlations  
<sup>1146</sup> between the parameters of interest and the nuisance parameters. In practice, this  
<sup>1147</sup> is simply taking the one or two-dimensional projection of the multi-dimensional  
<sup>1148</sup> probability distribution.

Whilst in principle an easy solution to a complex problem, correlations between the interesting and nuisance parameters can bias the marginalised results. A similar effect is found when the parameters being marginalised over have non-Gaussian probability distributions. For example, Figure 4.5 highlights the marginalisation bias in the probability distribution found for a parameter when requiring a correlated parameter to have a positive parameter value. Due to the complex nature of this oscillation parameter fit presented in this thesis, there are correlations occurring between the oscillation parameters of interest and the other nuisance parameters included in the fit.

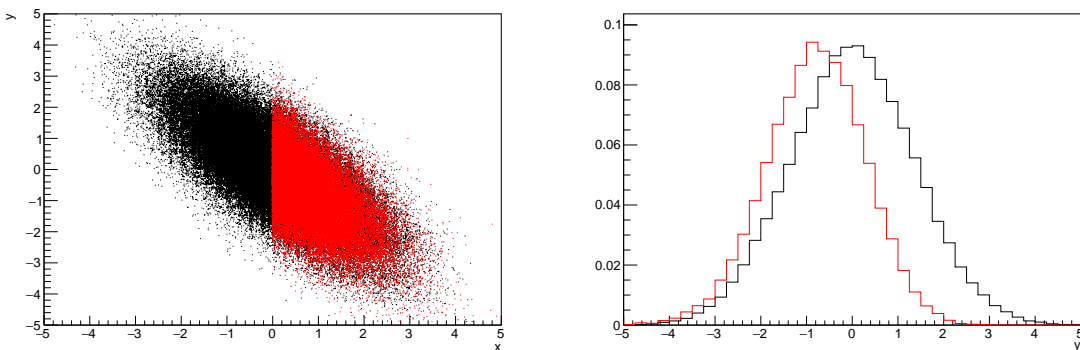


**Figure 4.5:** Left: The two dimensional probability distribution for two correlated parameters  $x$  and  $y$ . The red distribution shows the two dimensional probability distribution when  $0 \leq x \leq 5$ . Right: The marginalised probability distribution for the  $y$  parameter found when requiring the  $x$  to be bound between  $-5 \leq x \leq 5$  and  $0 \leq x \leq 5$  for the black and red distribution, respectively.

### 4.3.2 Parameter Estimation and Credible Intervals

The purpose of this analysis is to determine the best fit values for the oscillation parameters that the beam and atmospheric samples are sensitive to:  $\sin^2(\theta_{23})$ ,  $\sin^2(\theta_{13})$ ,  $\Delta m_{23}^2$ , and  $\delta_{CP}$ . Typically, the results presented take the form of one or two-dimension marginalised probability distributions for the appearance ( $\sin^2(\theta_{13})$  and  $\delta_{CP}$ ) and disappearance ( $\sin^2(\theta_{23})$  and  $\Delta m_{23}^2$ ) parameters. The posterior probability density

<sub>1164</sub> taken from the output MCMC chain is binned in these parameters. The parameter  
<sub>1165</sub> best-fit point is then taken to be the value that has the highest posterior probability.  
<sub>1166</sub> This is performed in both one and two-dimensional projections.

<sub>1167</sub> However, the single best-fit point in a given parameter is not of much use on its  
<sub>1168</sub> own. We would also like to determine the uncertainty, or credible interval, on that  
<sub>1169</sub> best-fit point. The definition of the  $1\sigma$  credible interval is that we have 68% belief that  
<sub>1170</sub> the parameter is within those bounds. For a more generalised definition, the credible  
<sub>1171</sub> interval is the region,  $R$ , of the posterior distribution that contains a specific fraction of  
<sub>1172</sub> the total probability, such that

$$\int_R P(\theta|D)d\theta = \alpha \quad (4.8)$$

<sub>1173</sub> Where  $\theta$  is the parameter on which we calculate the credible interval. This technique  
<sub>1174</sub> then calculates the  $\alpha \times 100\%$  credible interval.

<sub>1175</sub> In practice, this analysis uses the highest posterior density (HPD) credible intervals  
<sub>1176</sub> which are calculated through the following method. First, the probability distribution  
<sub>1177</sub> is area-normalised such that it has an integrated area equal to 1.0. The bins of proba-  
<sub>1178</sub> bility are then summed from the highest to lowest until the sum exceeds the  $1\sigma$  level  
<sub>1179</sub> (0.68 in this example). This process is repeated for a range of credible intervals, notably  
<sub>1180</sub> the  $1\sigma$ ,  $2\sigma$  and  $3\sigma$  along with other levels where the critical values for each level can  
<sub>1181</sub> be found in [139]. This process can be repeated for the two-dimensional probability  
<sub>1182</sub> distributions by creating two-dimensional contours of credible intervals rather than a  
<sub>1183</sub> one-dimensional result.

---

### <sup>1184</sup> 4.3.3 Bayesian Model Comparisons

<sup>1185</sup> Due to the matter resonance, this analysis has some sensitivity to the mass hierarchy  
<sup>1186</sup> of neutrino states (whether  $\Delta m_{23}^2$  is positive or negative) and the octant of  $\sin^2(\theta_{23})$   
<sup>1187</sup> . The Bayesian approach utilised within this analysis gives an intuitive method of  
<sup>1188</sup> model comparison by determining which hypothesis is most favourable. Taking the  
<sup>1189</sup> ratio of Equation 4.3 for the two hypotheses of normal hierarchy,  $NH$ , and inverted  
<sup>1190</sup> hierarchy,  $IH$ , gives

$$\frac{P(\vec{\theta}_{NH}|D)}{P(\vec{\theta}_{IH}|D)} = \frac{P(D|\vec{\theta}_{NH})}{P(D|\vec{\theta}_{IH})} \times \frac{P(\vec{\theta}_{NH})}{P(\vec{\theta}_{IH})}. \quad (4.9)$$

<sup>1191</sup> The middle term defines the Bayes factor which is a data-driven interpretation of  
<sup>1192</sup> how strong the data prefers one hierarchy to the other. For this analysis, equal priors  
<sup>1193</sup> on both mass hierarchy hypotheses are chosen ( $P(\vec{\theta}_{NH}) = P(\vec{\theta}_{IH}) = 0.5$ ). In practice,  
<sup>1194</sup> the MCMC chain proposes a value of  $|\Delta m_{23}^2|$  and then applies a 50% probability  
<sup>1195</sup> that the value is sign flipped. Consequently, the Bayes factor can be calculated from  
<sup>1196</sup> the ratio of the probability density in either hypothesis. This equates to counting the  
<sup>1197</sup> number of steps taken in the normal and inverted hierarchies and taking the ratio. The  
<sup>1198</sup> same approach can be taken to compare the upper octant (UO) compared to the lower  
<sup>1199</sup> octant (LO) hypothesis of  $\sin^2(\theta_{23})$ .

<sup>1200</sup> Whilst the value of the Bayes factor should always be shown, the Jeffreys scale [140]  
<sup>1201</sup> (highlighted in Table 4.1) gives an indication of the strength of preference for one model  
<sup>1202</sup> compared to the other. Other interpretations of the strength of preference of a model  
<sup>1203</sup> exist, e.g. the Kass and Raferty Scale [141].

$\log_{10}(B_{AB})$	$B_{AB}$	Strength of Preference
< 0.0	< 1	No preference for hypothesis A (Supports hypothesis B)
0.0 – 0.5	1.0 – 3.16	Preference for hypothesis A is weak
0.5 – 1.0	3.16 – 10.0	Preference for hypothesis A is substantial
1.0 – 1.5	10.0 – 31.6	Preference for hypothesis A is strong
1.5 – 2.0	31.6 – 100.0	Preference for hypothesis A is very strong
> 2.0	> 100.0	Decisive preference for hypothesis A

**Table 4.1:** Jeffreys scale for strength of preference for two models  $A$  and  $B$  as a function of the calculated Bayes factor ( $B_{AB} = B(A/B)$ ) between the two models [140]. The original scale is given in terms of  $\log_{10}(B(A/B))$  but converted to linear scale for easy comparison throughout this thesis.

#### <sup>1204</sup> 4.3.4 Comparison of MCMC Output to Expectation

<sup>1205</sup> To ensure the fit is performing well, a best-fit spectrum is produced using the pos-  
<sup>1206</sup> terior probability distribution and compared with the data, allowing easy by-eye  
<sup>1207</sup> comparisons to be made. A simple method of doing this is to perform a comparison  
<sup>1208</sup> in the fitting parameters (For instance, the reconstructed neutrino energy and lepton  
<sup>1209</sup> direction for T2K far detector beam samples) of the spectra generated by the MCMC  
<sup>1210</sup> chain to ‘data’. This ‘data’ could be true data or some variation of Monte Carlo predic-  
<sup>1211</sup> tion. This allows easy comparison of the MCMC probability distribution to the data.  
<sup>1212</sup> To perform this,  $N$  steps from the post burn-in MCMC chain are randomly selected  
<sup>1213</sup> (Where for all plots of this style in this thesis,  $N = 3000$ ). From these, the Monte Carlo  
<sup>1214</sup> prediction at each step is generated by reweighting the model parameters to the values  
<sup>1215</sup> specified at that step. Due to the probability density being directly correlated with  
<sup>1216</sup> the density of steps in a certain region, parameter values close to the best fit value are  
<sup>1217</sup> most likely to be selected.

<sup>1218</sup> In practice, for each bin of the fitting parameters has a probability distribution  
<sup>1219</sup> of event rates, with one entry per sampled MCMC step. This distribution is binned  
<sup>1220</sup> where the bin with the highest probability is selected as the mean and an error on

1221 the width of this probability distribution is calculated using the approach highlighted  
1222 in subsection 4.3.2. Consequently, the best fit distribution in the fit parameter is not  
1223 necessarily that which would be attained by reweighting the Monte Carlo prediction  
1224 to the most probable parameter values.

1225 A similar study can be performed to illustrate the freedom of the model parameter  
1226 space prior to the fit. This can be done by throwing parameter values from the prior  
1227 uncertainty of each parameter. This becomes troublesome for parameters with no  
1228 prior uncertainty as the range is technically infinite. Where applicable solutions to  
1229 remove these have been addressed.

1230 **Chapter 5**

1231 **Simulation, Reconstruction, and Event  
Reduction**

1233 As a crucial part of the oscillation analysis, an accurate prediction of the expected  
1234 neutrino spectrum at the far detector is required. This includes modeling the flux  
1235 generation, neutrino interactions, and detector effects. All of the simulation packages  
1236 required to do this are briefly described in section 5.1. The reconstruction of neutrino  
1237 events inside the far detector, including the `fitQun` algorithm, is documented in  
1238 section 5.2. This also includes data quality checks of the SK-V data which the author  
1239 performed for the T2K oscillation analysis presented at Neutrino 2020 [80]. Finally,  
1240 section 5.3 describes the steps taken in the SK detector to trigger on events of interest  
1241 whilst removing the comparatively large rate of cosmic ray muon events.

1242 **5.1 Simulation**

1243 In order to generate a Monte Carlo prediction of the expected event rate at the far  
1244 detector, all the processes in the beam and atmospheric flux, neutrino interaction, and  
1245 detector need to be modeled. Each of these parts is individually modeled and each of  
1246 them is detailed below.

1247 The beamline simulation consists of three distinct parts: the initial hadron inter-  
1248 action modeled by FLUKA [142], the target station geometry and particle tracking

performed by JNUBEAM, [143, 144] and any hadronic re-interactions simulated by GCALOR [145]. The primary hadronic interactions are  $O(10)\text{GeV}$ , where FLUKA matches external cross-section data better than GCALOR [146]. However, FLUKA is not very adaptable so a small simulation is built to model the interactions in the target and the output is then passed to JNUBEAM and GCALOR for propagation. The hadronic interactions are tuned to data from the NA61/SHINE [147–149] and HARP [150] experiments. The tuning is done by reweighting the FLUKA and GCALOR predictions to match the external data multiplicity and cross-section measurements, based on final state particle kinematics [146]. The culmination of this simulation package generates the predicted flux for neutrino and antineutrino beam modes which are illustrated in Figure 3.7.

The atmospheric neutrino flux **predictions are is** simulated by the HKKM model [43, 45]. The primary cosmic ray flux is tuned to AMS [151] and BESS [152] data assuming the US-standard atmosphere '76 [153] density profile and includes geomagnetic field effects. The primary cosmic rays interact to generate pions and muons. The interaction of these secondary particles to generate neutrinos is handled by DPMJET-III [154] for energies above 32GeV and JAM [45, 155] for energies below that value **DB: Question for Giles: Why different generators for above/below 32GeV?**. These hadronic interactions are tuned to BESS and L3 data [156, 157] using the same methodology as the tuning of the beamline simulation. The energy and cosine zenith predictions of  $\nu_e, \bar{\nu}_e, \nu_\mu, \bar{\nu}_\mu$  flux are given in Figure 2.3 and Figure 2.5, respectively. The flux is approximately symmetrical and peaked around the horizon ( $\cos(\theta_Z) = 0.0$ ). This is because horizontally-going pions and kaons can travel further than their vertically-going counterparts resulting in a larger probability of decaying to neutrinos. The symmetry is broken in lower-energy neutrinos due to geomagnetic effects, which modify the track of the primary cosmic rays. Updates to the HKKM model are currently ongoing [158].

Once a flux prediction has been made for all three detectors, NEUT 5.4.0 [159, 160] models the interactions of the neutrinos in the detectors. For the purposes of this analysis, quasi-elastic (QE), meson exchange (MEC), single meson production (PROD), coherent pion production (COH), and deep inelastic scattering (DIS) interactions are simulated. These interaction categories can be further broken down by whether they were propagated via a  $W^\pm$  boson in Charged Current (CC) interactions or via a  $Z^0$  boson in Neutral Current (NC) interactions. CC interactions have a charged lepton in the final state, which can be flavour-tagged in reconstruction to determine the flavour of the neutrino. In contrast, NC interactions have a neutrino in the final state so no flavour information can be determined from the observables left in the detector after an interaction. ~~This is the reason why NC events~~ ~~This is the reason why neutrinos which interact through NC modes~~ are assumed to not oscillate within this analysis. Both CC and NC interactions are modeled for all the above interaction categories, other than MEC interactions which are only modeled for CC events. ~~As the SK detector is only sensitive to charged particles above Cherenkov threshold, all charged current interactions are simulated whilst only neutral current processes that can produce charged particles (NCDIS, NCCOH, and NCPROD including  $\pi^0$  production) are modeled. NC MEC interactions can only produce charged particles through secondary re-interactions which is a low cross-section process.~~

As illustrated in Figure 5.1, CCQE interactions dominate the ~~low-energy~~ cross-section of neutrino interactions ~~around  $E_\nu \sim 0.5\text{GeV}$~~ . The NEUT implementation adopts the Llewellyn Smith [161] model for neutrino-nucleus interactions, where the nuclear ground state of any bound nucleons (neutrino-oxygen interactions) is approximated by a spectral-function [162] model that simulates the effects of Fermi momentum and Pauli blocking. The cross-section of QE interactions ~~are is~~ controlled by vector and axial-vector form factors parameterised by the BBBA05 [163] model and a dipole form factor with  $M_A^{QE} = 1.21\text{GeV}$  fit to external data [164], respectively. NEUT

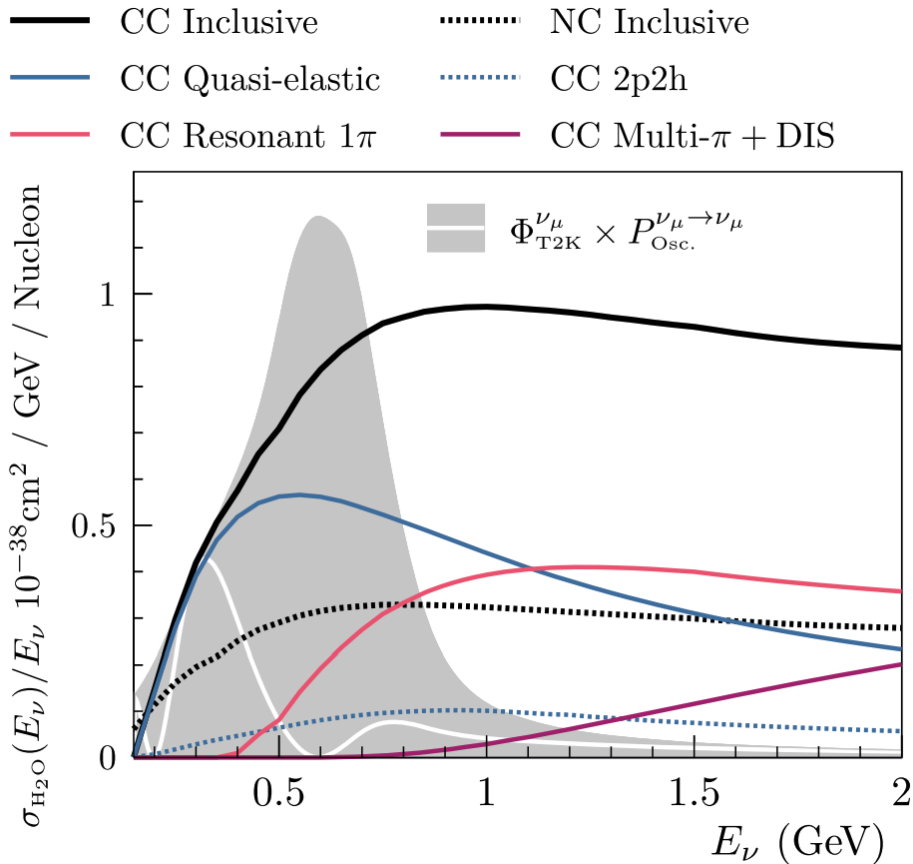


**Figure 5.1:** The NEUT prediction of the  $\nu_\mu$ -H<sub>2</sub>O cross-section overlaid on the T2K  $\nu_\mu$  flux. The charged current (black, solid) and neutral current (black, dashed) inclusive, charged current quasi-elastic (blue, solid), charged current 2p2h (blue, dashed), charged current single pion production (pink), and charged current multi- $\pi$  and DIS (Purple) cross-sections are illustrated. Figure taken from [159].

1302 implements the Valencia [165] model to simulate MEC events, where two nucleons  
 1303 and two holes in the nuclear target are produced (Often called 2p2h interactions).

1304 For neutrinos of energy  $O(1)$ GeV, PROD interactions become dominant. These  
 1305 predominantly produce charged and neutral pions although  $\gamma$ , kaon, and  $\eta$  production  
 1306 is also considered. To simulate these interactions, the Berger-Sehgal [166] model is  
 1307 implemented within NEUT. It simulates the excitation of a nucleon from a neutrino  
 1308 interaction, production of an intermediate baryon, and the **consequential subsequent**  
 1309 decay to a single meson or  $\gamma$ . Pions can also be produced through COH interactions,  
 1310 which occur when the incoming neutrino interacts with the entire oxygen **nuclei**

1311 target nucleus leaving a single pion outside of the nucleus. NEUT utilises the Berger-  
1312 Sehgal [167] model to simulate these COH interactions.

1313 DIS and multi- $\pi$  producing interactions become the most dominant for energies  
1314  $> O(5)\text{GeV}$ . PYTHIA [168] is used to simulate any interaction with invariant mass  
1315  $W > 2\text{GeV}/c^2$ , which produces at least one meson. For any interaction which produces  
1316 at least two mesons but has  $W < 2\text{GeV}/c^2$ , the Bronner model is **invoked used** [169].  
1317 Both of these models use parton distribution functions based on the Bodek-Yang  
1318 model [170–172].

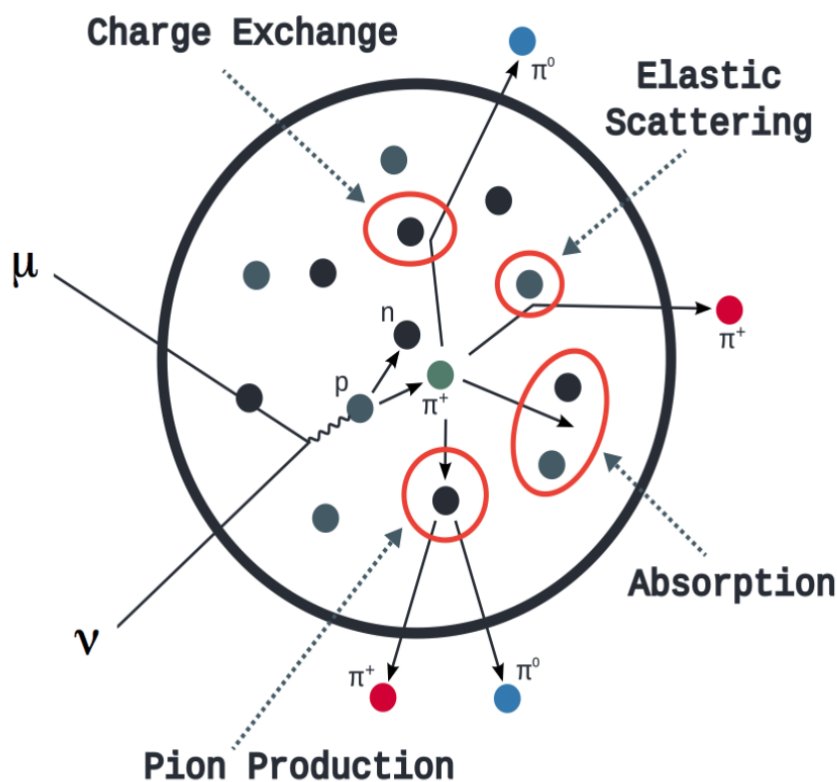


**Figure 5.2:** Illustration of the various processes which a pion can undergo before exiting the nucleus. Taken from [173].

1319 Any pion which is produced within the nucleus can re-interact through final state  
1320 interactions before it exits, as illustrated by the scattering, absorption, production, and  
1321 exchange interactions in Figure 5.2. These re-interactions alter the observable particles

1322 within the detector. For instance, if the charged pion from a CC PROD interaction is  
1323 absorbed, the observables would mimic a CC QE interaction. To simulate these effects,  
1324 NEUT uses a semi-classical intranuclear cascade model [159]. This cascade functions by  
1325 stepping the pion through the nucleus in fixed-length steps equivalent to  $dx = R_N/100$ ,  
1326 where  $R_N$  is the radius of the nucleus. At each step, the simulation allows the pion  
1327 to interact through scattering, charged exchange, absorption, or production with an  
1328 interaction-dependent probability calculated from a fit to external data [174]. This  
1329 cascade continues until the pion is absorbed or exits the nucleus.

1330 Once the final state particle kinematics have been determined **from by** NEUT, they  
1331 are passed into the detector simulation. The near detectors, ND280 and INGRID, are  
1332 simulated using a GEANT4 package [118,175] to simulate the detector geometry, particle  
1333 tracking, and energy deposition. The response of the detectors is simulated using  
1334 the elecSim package [118]. The far detector simulation is based upon the original  
1335 Kamiokande experiment software which uses the GEANT3-based SKDETSIM [118,176]  
1336 package. This **controls simulates** the interactions of particles in the water as well as  
1337 Cherenkov light production. The water quality and PMT calibration measurements  
1338 detailed in subsection 3.1.2 are also used within this simulation to make accurate  
1339 predictions of the detector response.

## 1340 5.2 Event Reconstruction at SK

1341 **Any above Cherenkov threshold event which Any event which generates optical**  
1342 **photons that** occurs in SK will be **recorded observed** by the PMT array, where each  
1343 PMT records the time and accumulated charge. This recorded information is shown  
1344 in event displays similar to those illustrated in Figure 5.3. To be useful for physics  
1345 analyses, this series of PMT hit information needs to be reconstructed to determine

the particle's identity and kinematics (or track parameters): four-vertex, direction, and momenta. ~~This is because The reconstruction uses the fact that~~ the charge and timing distribution of photons generated by a particular particle in an event is dependent upon its initial kinematics. ~~The concept of distinguishing electron and muon events is from the “fuzziness” of the ring.~~ Electron and muon rings are distinguished by their “fuzziness”. Muons are heavier and less affected by scattering or showering meaning they typically produce “crisp” rings. Electrons are more likely to interact via electromagnetic showering or scattering which results in larger variations of their direction from the initial direction. Consequently, electrons typically produce “fuzzier” rings compared to muons.

**1356      The below paragraph has been reordered**

For the purposes of this analysis, the `fitQun` reconstruction algorithm is utilised. Its core function is to compare a prediction of the accumulated charged and timing distribution from each PMT, generated for a particular particle identity and track parameters, to that observed in the neutrino event. It determines the preferred values by minimising a likelihood function which includes information from PMTs which were hit and those that were not hit. `fitQun` performs a simultaneous fit of particle kinematics and identity, improving both the accuracy of the fit parameters and the rejection of neutral current  $\pi^0$  events [177, 178]. The `fitQun` algorithm is based on the key concepts of the MiniBooNE reconstruction algorithm [179] and is described in [180] which is summarised below. The `fitQun` algorithm improves upon the APFit reconstruction algorithm which has been used for many previous SK analyses. APFit fits the vertex from timing information and then fits the momentum and direction of the particle from PMT hits within a 43 deg Cherenkov cone (which assumes an ultra-relativistic particle). It then fits the particle identity once the track parameters have been fit.

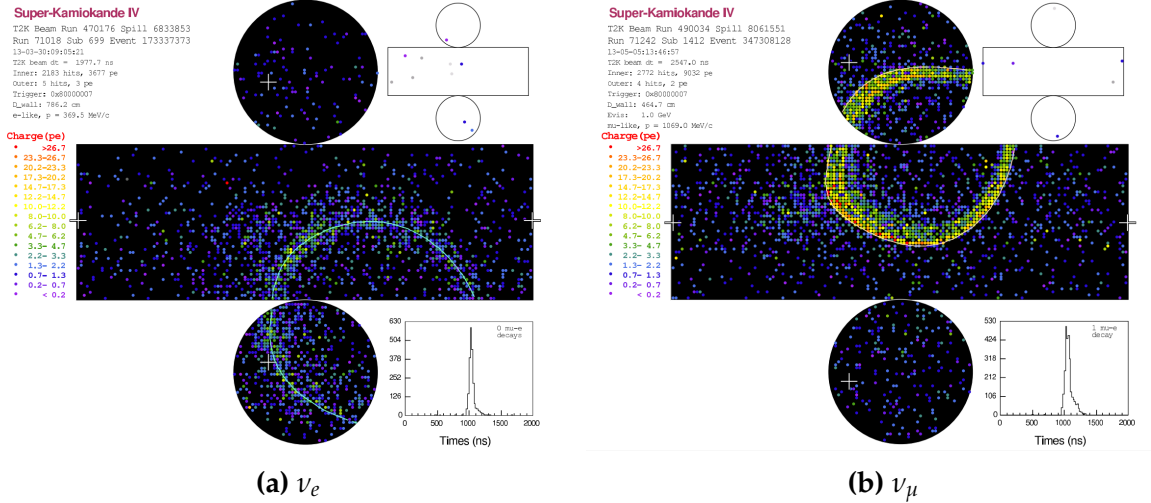


**Figure 5.3:** Event displays from Super Kamiokande illustrating the “crisp” ring from a muon and the typically “fuzzy” electron ring. Each pixel represents a PMT and the color scheme denotes the accumulated charge deposited on that PMT. Figures taken from [181].

1372     The below has been added as an overview of fiTQun

1373     The fiTQun reconstruction algorithm proceeds by:

- 1374     • **Vertex pre-fitting:** An estimate of the vertex is made using a goodness-of-fit  
1375       metric
- 1376     • **Peak finding:** The initial time of the event is determined by clustering events by  
1377       time residuals
- 1378     • **Single-ring fits:** Given the pre-fit vertex and estimated time of interaction, a  
1379       maximum likelihood technique searches for a single particle generating light
- 1380     • **Multi-ring fits:** Seeded from the single-ring fits, hypotheses with multiple light-  
1381       producing particles are considered using the same maximum likelihood technique

1382     **An event in SK can consist of a primary and decay particles. An event in SK can**  
 1383     **consist of multiple particles.** For example, a charge current muon neutrino interaction  
 1384     can generate two particles that have the potential of generating Cherenkov photons:  
 1385     the primary muon, and the secondary decay-electron from the muon. To ensure both

1386 particle are reconstructed separately, each event is divided into time clusters which  
 1387 are called “subevents”. The number of subevents is equal to the number of decay  
 1388 electrons plus one (the primary event). To find all the subevents in an event, a vertex  
 1389 goodness metric is calculated for some vertex position  $\vec{x}$  and time  $t$ ,

$$G(\vec{x}, t) = \sum_i^{\text{hit PMTs}} \exp \left( -\frac{1}{2} \left( \frac{T_{Res}^i(\vec{x}, t)}{\sigma} \right)^2 \right) \quad (5.1)$$

1390 where

$$T_{Res}^i(\vec{x}, t) = t^i - t - |R_{PMT}^i - \vec{x}| / c_n \quad (5.2)$$

1391 is the residual hit time. It is the difference in time between the PMT hit time,  $t^i$ ,  
 1392 of the  $i^{th}$  PMT and the expected time of the PMT hit if the photon was emitted at  
 1393 the start of the vertex.  $R_{PMT}^i$  is the position of the  $i^{th}$  PMT,  $c_n$  is the speed of light in  
 1394 water and  $\sigma = 4\text{ns}$  which is comparable to the time resolution of the PMT. When the  
 1395 proposed fit values of time and vertex are close to the true values,  $T_{Res}^i(\vec{x}, t)$  tends to  
 1396 zero resulting in subevents appearing as spikes in the goodness metric. The proposed  
 1397 fit vertex and time are grid-scanned, and the values which maximise the goodness  
 1398 metric are selected as the “pre-fit vertex”. Whilst this predicts a vertex for use in  
 1399 the clustering algorithm, the final vertex is fit using the higher-precision maximum  
 1400 likelihood method described below.

1401 Once the pre-fit vertex has been determined, the goodness metric is scanned as  
 1402 a function of  $t$  to determine the number of subevents. A peak-finding algorithm is  
 1403 then used on the goodness metric, requiring the goodness metric to exceed some

1404 threshold and drop below a reduced threshold before any subsequent additional  
1405 peaks are considered. The thresholds are set such that the rate of false peak finding  
1406 is minimised while still attaining good data to Monte Carlo agreement. To improve  
1407 performance, the pre-fit vertex for each delayed subevent is re-calculated after PMT  
1408 hits from the previous subevent are masked. This improves the decay-electron tagging  
1409 performance. Once all subevents have been determined, the time window around  
1410 each subevent is then defined by the earliest and latest time which satisfies  $-180 <$   
1411  $T_{Res}^i < 800\text{ns}$ . The subevents and associated time windows are then used as seeds for  
1412 further reconstruction.

1413 For a given subevent, the `fitQun` algorithm constructs a likelihood based on the  
1414 accumulated charge  $q_i$  and time information  $t_i$  from the  $i^{th}$  PMT,

$$L(\Gamma, \vec{\theta}) = \prod_j^{\text{unhit}} P_j(\text{unhit}|\Gamma, \vec{\theta}) \prod_i^{\text{hit}} \{1 - P_i(\text{unhit}|\Gamma, \vec{\theta})\} f_q(q_i|\Gamma, \vec{\theta}) f_t(t_i|\Gamma, \vec{\theta}), \quad (5.3)$$

1415 where  $\vec{\theta}$  defines the track parameters; vertex position, direction vector and mo-  
1416 ments, and  $\Gamma$  represents the particle hypothesis.  $P_i(\text{unhit}|\Gamma, \vec{\theta})$  is the probability of the  
1417  $i^{th}$  tube to not register a hit given the track parameters and particle hypothesis. The  
1418 charge likelihood,  $f_q(q_i|\Gamma, \vec{\theta})$ , and time likelihood,  $f_t(t_i|\Gamma, \vec{\theta})$ , represents the probability  
1419 density function of observing charge  $q_i$  and time  $t_i$  on the  $i^{th}$  PMT given the specified  
1420 track parameters and particle hypothesis.

1421 **I don't think the below paragraph is actually needed?**

1422 As the generation and propagation of the optical photons are independent of the  
1423 PMT and electronics response, it is natural to split the calculation into two. This split  
1424 was also performed to . Firstly, the expected number of photoelectrons (or predicted

charge),  $\mu_i = \mu_i(\vec{\theta}, \Gamma)$ , at the  $i^{th}$  PMT is calculated. This value is then substituted into the likelihood function. This allows the charge likelihood density  $f_q(q_i|\mu_i)$  and unhit probability  $P_i(\text{unhit}|\mu_i)$  to be expressed via quantities that are only dependent on the response of the PMT.

The predicted charge is calculated based on contributions from both the direct light and the scattered light. The direct light contribution is determined based on the integration of the Cherenkov photon profile along the track. PMT angular acceptance, water quality, and calibration measurements discussed in subsection 3.1.2 are included to accurately predict the charge probability density at each PMT. The scattered light is calculated in a similar way, although it includes a scattering function that depends on the vertex of the particle and the position of the PMT. The charge likelihood is calculated by comparing the prediction to the observed charge in the PMT.

The time likelihood is approximated to depend on the vertex  $\vec{x}$ , direction  $\vec{d}$ , and time  $t$  of the track **parameters** as well as the particle hypothesis. The expected time for PMT hits is calculated by assuming unscattered photons being emitted from the midpoint of the track,  $S_{mid}$ ,

$$t_{exp}^i = t + S_{mid}/c + |R_{PMT}^i - \vec{x} - S_{mid}\vec{d}|/c_n, \quad (5.4)$$

where  $c$  is the speed of light in a vacuum. The time likelihood is then expressed in terms of the residual difference between the PMT hit time and the expected hit time,  $t_{Res}^i = t^i - t_{exp}^i$ . The particle hypothesis and momentum also affect the Cherenkov photon distribution. These parameters modify the shape of the time likelihood density since in reality not all photons are emitted at the midpoint of the track. As with the charge likelihood, the contributions from both the direct and scattered light to the time

<sup>1447</sup> likelihood density are calculated separately, which are both calculated from particle  
<sup>1448</sup> gun studies.

<sup>1449</sup> **Below paragraphs, figures and equations are changed**

<sup>1450</sup> The track parameters and particle identity which maximise  $L(\Gamma, \vec{\theta})$  are defined as  
<sup>1451</sup> the best-fit parameters. In practice MINUIT [182] is used to minimise the value of  
<sup>1452</sup>  $-\ln L(\Gamma, \vec{\theta})$ . The `fitQun` algorithm considers an electron-like, muon-like, and charged  
<sup>1453</sup> pion-like hypothesis for events with a single final state particle, denoted “single-ring  
<sup>1454</sup> events”. The particle’s identity is determined by taking the ratio of the likelihood  
<sup>1455</sup> of each of the hypotheses. For instance, electrons and muons are distinguished by  
<sup>1456</sup> considering the value of  $\ln(L(e, \vec{\theta}_e)/L(\mu, \vec{\theta}_\mu))$  in comparison to the reconstructed  
<sup>1457</sup> momentum of the electron hypothesis, as illustrated by Figure 5.4. The coefficients  
<sup>1458</sup> of the discriminator between electron-like and muon-like events is determined from  
<sup>1459</sup> Monte Carlo studies [180]. Similar distributions exist for distinguishing electron-like  
<sup>1460</sup> events from  $\pi^0$ -like events, and muon-like events from pion-like events. They are  
<sup>1461</sup> defined as,

$$\begin{aligned} \text{Electron/Muon} &: \ln(L_e/L_\mu) > 0.2 \times p_e^{rec} [\text{MeV}], \\ \text{Electron}/\pi^0 &: \ln(L_e/L_{\pi^0}) < 175 - 0.875 \times m_{\gamma\gamma} [\text{MeV}], \\ \text{Muon/Pion} &: \ln(L_\mu/L_{\pi^\pm}) < 0.15 \times p_\mu^{rec} [\text{MeV}], \end{aligned} \quad (5.5)$$

<sup>1462</sup> as taken from [183], where  $p_e^{rec}$  and  $p_\mu^{rec}$  are the reconstructed momentum of the  
<sup>1463</sup> single-ring electron and muon fits, respectively.  $m_{\gamma\gamma}$  represents the reconstructed  
<sup>1464</sup> invariant mass of the two photons emitted from  $\pi^0$  decay. Typically, the distance  
<sup>1465</sup> between a particular entry in these two-dimensional distributions and the cut-line is  
<sup>1466</sup> termed the PID parameter and is illustrated in Figure 5.5.

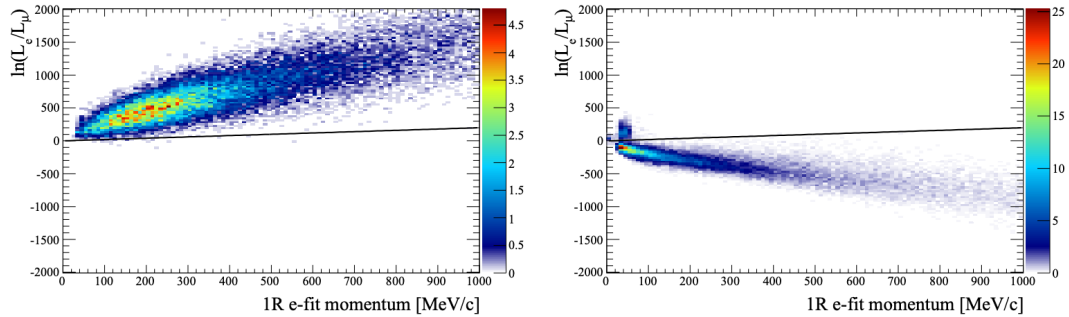


**Figure 5.4:** The difference of the electron-like and muon-like log-likelihood compared to the reconstructed single-ring fit momentum for atmospheric  $\nu_e$  (left) and  $\nu_\mu$  (right) samples. The black line represents the cut used to discriminate electron-like and muon-like events, which coefficients obtained from Monte Carlo studies. Figures taken from [180].

1467

### Review stop

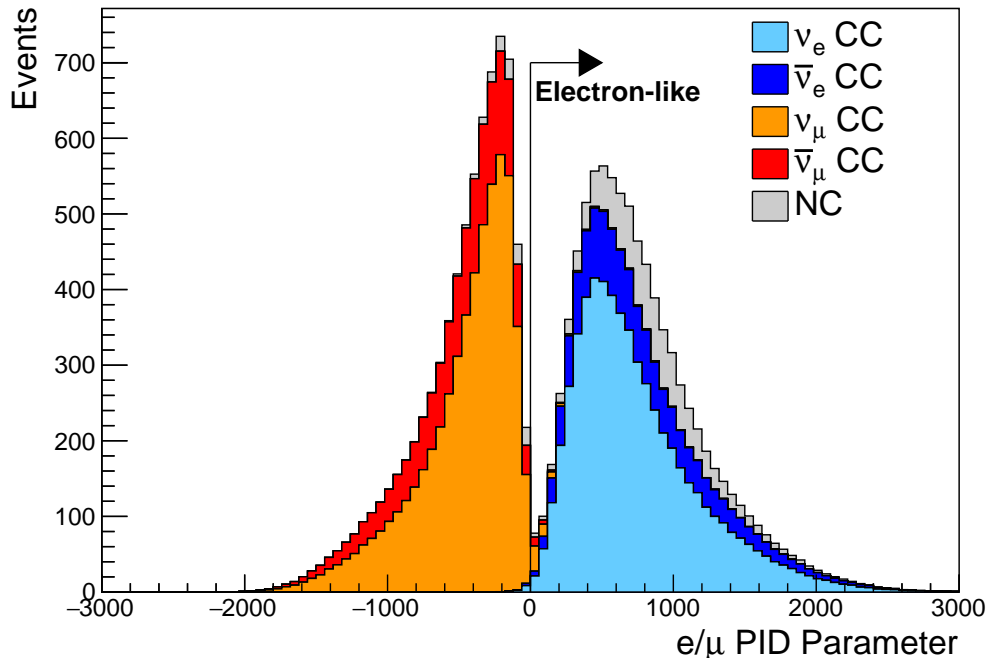


**Figure 5.5:** The electron/muon PID separation parameter for all sub-GeV single-ring events in SK-IV. The charged current (CC) component is broken down in four flavours of neutrino ( $\nu_\mu$ ,  $\bar{\nu}_\mu$ ,  $\nu_e$  and  $\bar{\nu}_e$ ). Events with positive values of the parameter are determined to be electron-like.

1468

The `fitQun` algorithm also considers a  $\pi^0$  hypothesis. To do this, it performs a fit looking for two standard electron-hypothesis tracks which point to the same

1469

1470 four-vertex. This assumes the electron tracks are generated from photon-conversion so  
1471 the electron tracks actually appear offset from the proposed  $\pi^0$  vertex. For these fits,  
1472 the conversion length, direction, and momentum of each photon are also considered  
1473 as track parameters which are then fit in the same methodology as the standard  
1474 single-ring hypotheses.

1475 Whilst lower energy events are predominately single-ring events, higher energy  
1476 neutrino events can generate final states with multiple particles which generate  
1477 Cherenkov photons. These “multi-ring” hypotheses are also considered in the `fitQun`  
1478 algorithm. When calculating the charge likelihood density, the predicted charge asso-  
1479 ciated with each ring is calculated separately and then summed to calculate the total  
1480 accumulated charge on each PMT. Similarly, the time likelihood for the multi-ring  
1481 hypothesis is calculated assuming each ring is independent. Each track is time-ordered  
1482 based on the time of flight from the center of the track to the PMT and the direct light  
1483 from any ring incident on the PMT is assumed to arrive before any scattered light. To  
1484 reduce computational resource [usage](#), the multi-ring fits only consider electron-like  
1485 and charged pion-like rings as the pion fit can be used as a proxy for a muon fit due to  
1486 their similar mass.

1487 Multi-ring fits proceed by proposing another ring to the previous fit and then  
1488 fitting the parameters in the method described above. Typically, multi-ring fits have  
1489 the largest likelihood because of the additional degrees of freedom introduced. **A**  
1490 [likelihood value is calculated for the  \$n\$ -ring and  \$\(n + 1\)\$ -ring hypotheses, where](#)  
1491 [the additional ring is only included if the likelihood value is above 9.35, based](#)  
1492 [on Monte Carlo studies in \[184\]. Consequently, the additional ring is only added](#)  
1493 [if the ratio of likelihoods passes a criterion, which is determined by Monte Carlo](#)  
1494 [studies.](#)

### <sup>1495</sup> 5.2.1 Validation of Reconstruction in SK-V

<sup>1496</sup> As an example of how the reconstruction depends on the detector conditions, the  
<sup>1497</sup> author of this thesis assessed the quality of event reconstruction for SK-V data. The  
<sup>1498</sup> detector systematics ~~invoked-within used in~~ the T2K-only oscillation analysis are  
<sup>1499</sup> determined using data-to-Monte Carlo comparisons of the SK-IV data [185]. Due to  
<sup>1500</sup> tank-open maintenance occurring between SK-IV and SK-V, the dark rate of each PMT  
<sup>1501</sup> was observed to increase in SK-V due to light exposure for a significant time during  
<sup>1502</sup> the repairs. This increase can be seen in Figure 5.6. Run-10 of the T2K experiment was  
<sup>1503</sup> conducted in the SK-V period, so the consistency of SK-IV and SK-V data needs to  
<sup>1504</sup> be studied to determine whether the SK-IV-defined systematics can be applied to the  
<sup>1505</sup> run-10 data. This comparison study was performed using the stopping muon data set  
<sup>1506</sup> for both the SK-IV and SK-V periods. This data sample is used due to the high rate of  
<sup>1507</sup> interactions ( $O(200)$  events per hour) as well as having similar energies to muons from  
<sup>1508</sup> CCQE  $\nu_\mu$  interactions from beam interactions. The rate of cosmic muons does depend  
<sup>1509</sup> on the solar activity cycle [186] but has been neglected in this comparison study. This  
<sup>1510</sup> is because the shape of the distributions is most important for the purposes of being  
<sup>1511</sup> compared to the detector systematics. The SK-IV and SK-V data samples consist of  
<sup>1512</sup> 2398.42 and 626.719 hours of data which equates to 686k and 192k events respectively.

<sup>1513</sup> The predicted charge calculated in the `fitQun` ~~charge-likelihood prediction al-~~  
<sup>1514</sup> ~~gorithm~~ includes a contribution from the photoelectron emission due to dark noise.  
<sup>1515</sup> Therefore, the increase in the SK-V dark rate needs to be accounted for. In practice, the  
<sup>1516</sup> average dark rate in each SK period is calculated and used as an input in the reconstruc-  
<sup>1517</sup> tion. This is calculated by averaging the dark rate per run for each period separately,  
<sup>1518</sup> using the calibration measurements detailed in subsection 3.1.2. The average dark  
<sup>1519</sup> rate from SK-IV and SK-V were found to be 4.57kHz and 6.30kHz, respectively. The  
<sup>1520</sup> ~~associated-charge charges associated~~ with the muon and decay electron subevents

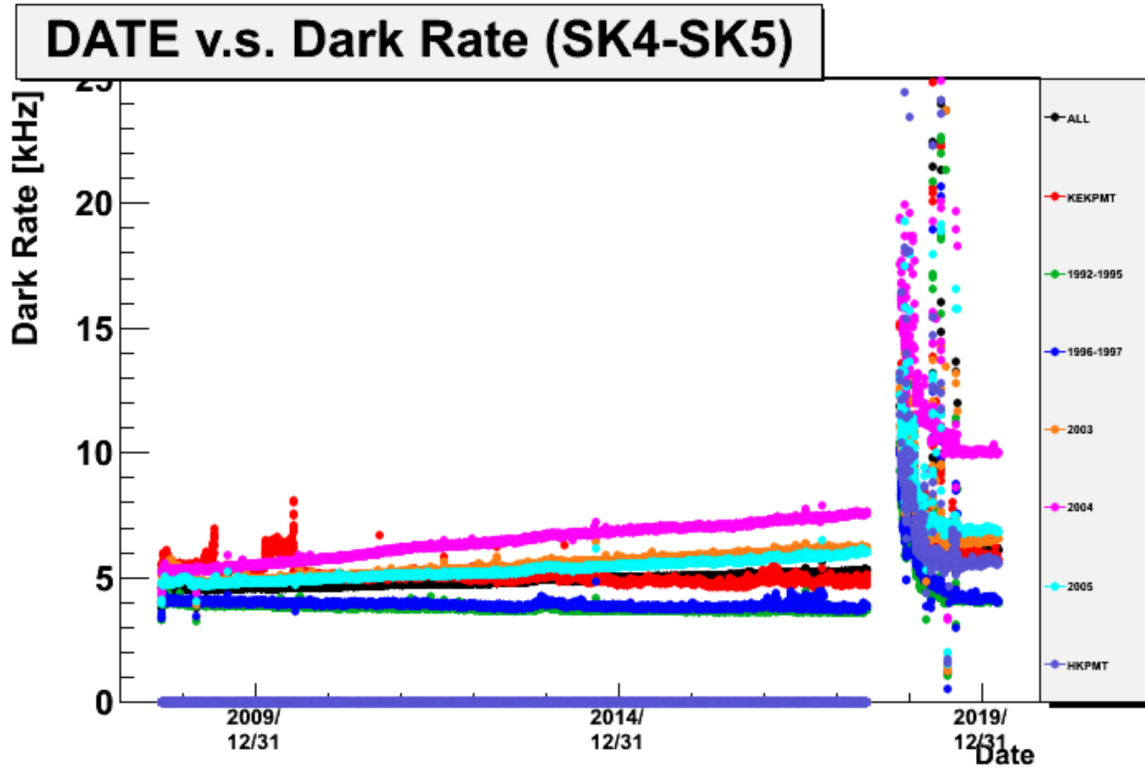


**Figure 5.6:** The variation of the measured dark rate as a function of date, broken down by PMT type. The SK-IV and SK-V periods span September 2008 to May 2018 and January 2019 to July 2020, respectively. The break in measurement in 2018 corresponds to the period of tank repair and refurbishment. Figure adapted from [185].

are illustrated in Figure 5.7. The photoelectron emission from dark noise ~~will be more noticeable is more significant~~ for events that have lower energy. This is because this contribution becomes more comparable to the number of photoelectrons emitted from incident photons in lower-energy events. This behaviour is observed in the data, where the charge deposited by the muon subevent is mostly unaffected by the increase in dark rate, whilst the charge associated with the decay-electron is clearly affected.

~~The energy scale systematic for the SK-IV period was determined to be 2.1%. It is defined to be equal to the difference between data and Monte Carlo prediction in the stopping muon data sample. The energy scale systematic is estimated from data-to-Monte Carlo differences in the stopping muon sample in [187] and found to be 2.1%.~~ To determine the consistency of SK-IV and SK-V with respect to the energy

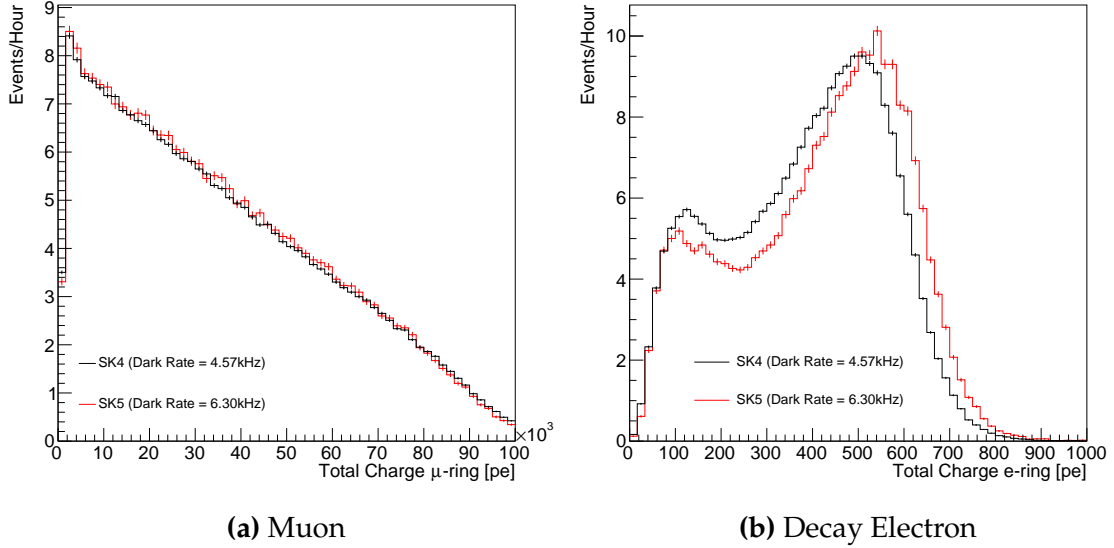


**Figure 5.7:** Comparison of the measured raw charge deposited per event from the stopping muon data samples between SK-IV (Blue) and SK-V (Red), split by the primary muon subevent and the associated decay electron subevent.

scale systematic, the muon momentum distribution is compared between the two SK periods. As the total number of Cherenkov photons is integrated across the track length, the reconstructed momentum divided by track length (or range) is compared between SK-IV and SK-V as illustrated in Figure 5.8.

The consistency between these distributions has been computed in two ways. Firstly, a Gaussian is fit to *the peak of* each distribution separately, whose *mean* *of* which is found to be  $(2.272 \pm 0.003)\text{MeV/cm}$  and  $(2.267 \pm 0.006)\text{MeV/cm}$  for SK-IV and SK-V respectively. The ratio of these is equal to  $1.002 \pm 0.003$ . The means of the Gaussian fits are consistent with the expected stopping power of a minimum ionising muon for a target material (water) with  $Z/A \sim 0.5$  [188]. The second consistency check is performed by introducing a nuisance parameter,  $\alpha$ , which modifies the SK-V distribution. The value of  $\alpha$  which minimises the  $\chi^2$  value between the SK-IV and SK-V is determined by scanning across a range of values. This is repeated by applying the nuisance parameter as both a multiplicative factor and an additive shift. The  $\chi^2$  distributions for different values of  $\alpha$  is illustrated in Figure 5.9. The

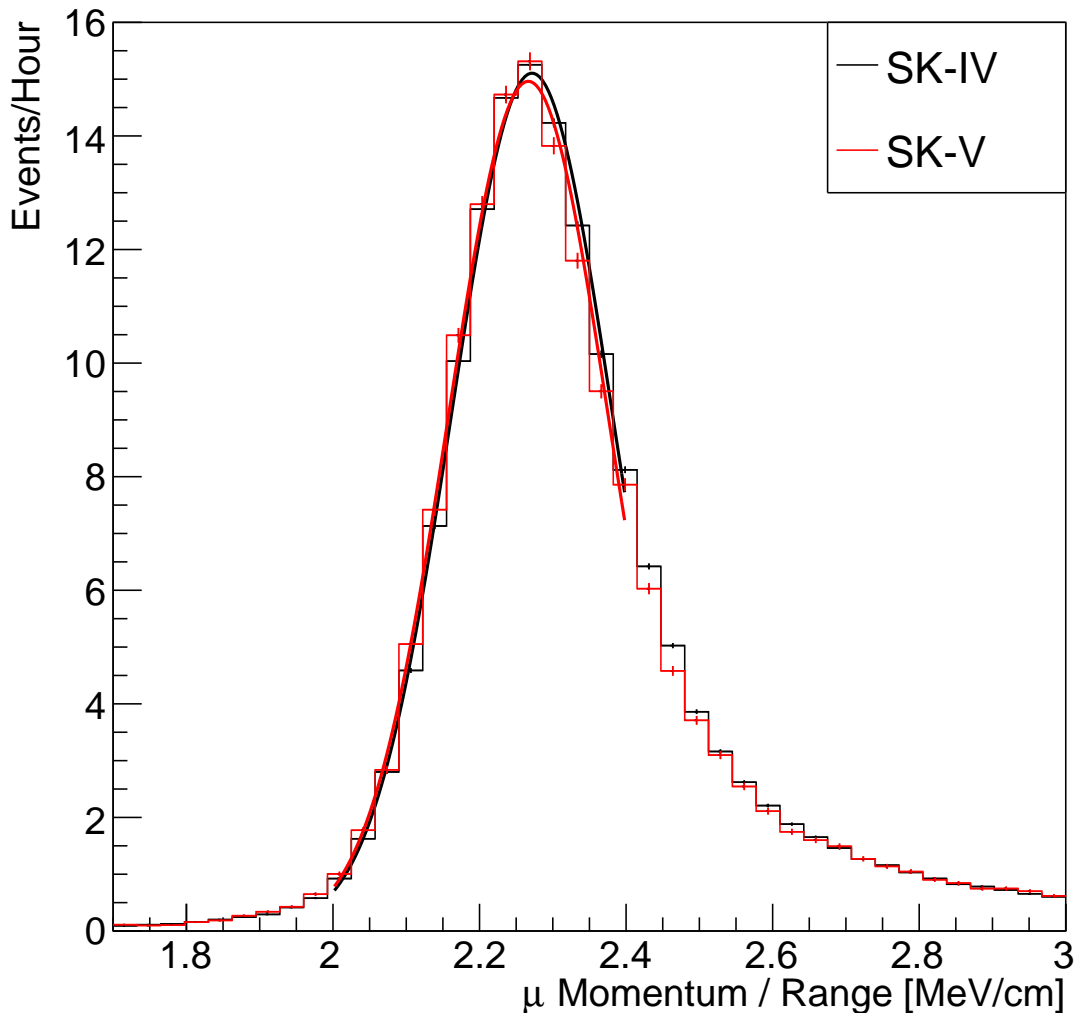


**Figure 5.8:** The distribution of the reconstructed momentum from the muon ring divided by the distance between the reconstructed muon and decay electron vertices as found in the stopping muon data sets of SK-IV (Black) and SK-IV (Red). Only events with one tagged decay electron are considered. A Gaussian fit is considered in the range [2.0, 2.4] MeV/cm and illustrated as the solid curve.

<sub>1547</sub> values which minimise the  $\chi^2$  are found to be 0.0052 and 1.0024 for the additive and  
<sub>1548</sub> multiplicative implementations, respectively. No evidence of shifts larger than the  
<sub>1549</sub> 2.1% uncertainty on the energy scale systematic has been found in the reconstructed  
<sub>1550</sub> momentum distribution of SK-IV and SK-V.

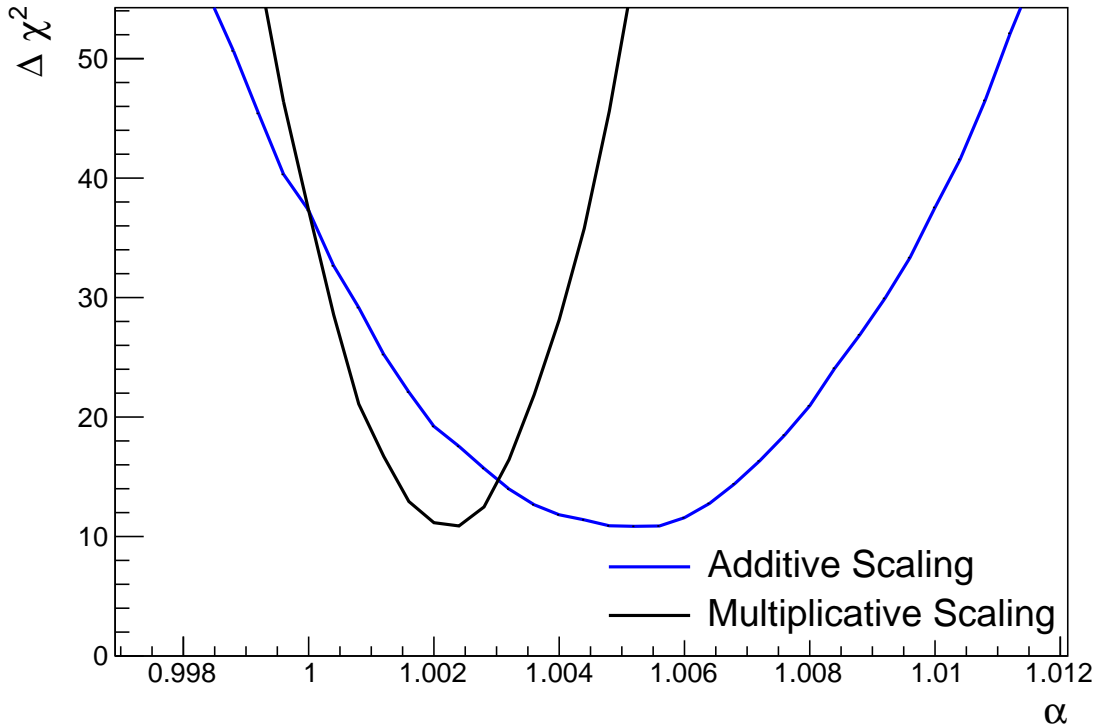


**Figure 5.9:** The  $\chi^2$  difference between the SK-IV and SK-V reconstructed muon momentum divided by range when the SK-V is modified by the scaling parameter  $\alpha$ . Both additive (Blue) and multiplicative (Black) scaling factors have been considered. In practice, the additive scaling factor actually uses the value of  $(\alpha - 1.0)$  but is illustrated like this so the results can be shown on the same axis range.

### 1551 5.3 Event Reduction at SK

1552 Atmospheric neutrino events observed in the SK detector are categorised into three  
 1553 different types of samples: fully contained (FC), partially contained (PC) and up-going  
 1554 muon (Up- $\mu$ ), using PMT hit signatures in the inner and outer detector (ID and OD,  
 1555 respectively). To identify FC neutrino events, it is required that the neutrino interacts  
 1556 inside the fiducial volume of the ID and that no significant OD activity is observed. For  
 1557 this analysis, an event is defined to be in the fiducial volume provided the event vertex  
 1558 is at least 0.5m away from the ID walls. PC events have the same ID requirements  
 1559 but can have a larger signal present inside the OD. **Typically these events are higher**

1560 **energy muon interactions that penetrate the ID walls** Typically, only high energy  
 1561 **muons from  $\nu_\mu$  interactions can penetrate the ID wall.** The Up- $\mu$  sample contains  
 1562 events where muons are created from neutrino interactions in the OD water or rock  
 1563 below the tank. They then propagate upwards through the detector. Downward-going  
 1564 muons generated from neutrino interactions above the tank are neglected is because of  
 1565 the difficulty in separating their signature from the cosmic muon shower background.  
 1566 The sample categories are visually depicted in Figure 5.10.

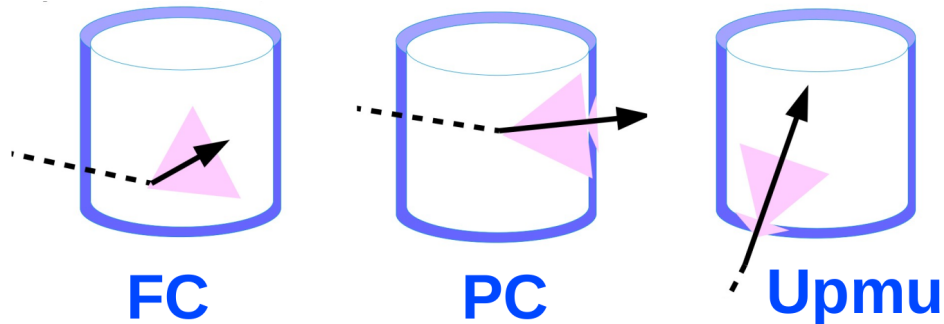


**Figure 5.10:** A depiction of the topology patterns for fully-contained (FC), partially-contained (PC) and up-going muon (Up- $\mu$ ) samples included in this analysis.

1567 Based on the event characteristics, as defined by the `fitQun` event reconstruction  
 1568 software, the FC events are categorised by

- 1569 • **Visible Energy:** equal to the sum of the reconstructed kinetic energy of particles  
 1570 above the Cerenkov threshold for all rings present in the event. The purpose is to  
 1571 separate events into sub-GeV and multi-GeV categories.
- 1572 • **Number of observed Cerenkov rings.** The purpose is to separate single-ring and  
 1573 multi-ring events, where single-ring events predominantly consist of quasi-elastic  
 1574 interactions and multi-ring events are typically resonant pion production or deep  
 1575 inelastic scattering events.

- 1576     • **Particle identification parameter of the most energetic ring:** A value deter-  
 1577         mined from the maximum likelihood value based on `fitQun`'s electron, muon, or  
 1578         pion hypothesis. The purpose is to separate electron-like and muon-like events.
  
- 1579     • **Number of decay electrons:** The purpose is to separate quasi-elastic events  
 1580         (which have one decay electron emitted from the muon decay) and resonant pion  
 1581         production events (which have two decay electrons emitted from the muon and  
 1582         pion).

1583     The PC and Up- $\mu$  categories are broken down into “through-going” and “stopping”  
 1584     samples depending on whether the muon leaves the detector. This is because the **PC**  
 1585     stopping events deposit the entire energy of the interaction into the detector, resulting  
 1586     in better reconstruction. The energy of events that exit the detector has to be estimated,  
 1587     **with typically worse resolution**, which introduces much larger systematic uncertain-  
 1588     ties. Through-going Up- $\mu$  samples are further broken down by whether any hadronic  
 1589     showering was observed in the event which typically indicates DIS interactions. The  
 1590     expected neutrino energy for the different categories is given in Figure 5.11. FC sub-  
 1591     GeV and multi-GeV events peak around 0.7GeV and 3GeV respectively, with slightly  
 1592     different peak energies for  $\nu_e$  and  $n\nu_\mu$  oscillation channels. PC and Up- $\mu$  are almost  
 1593     entirely comprised of  $\nu_\mu$  events and peak around 7GeV and 100GeV, respectively.

1594     In normal data-taking operations, the SK detector observes many background  
 1595     events alongside the beam and atmospheric neutrino signal events of physics inter-  
 1596     est **for this thesis**. Cosmic ray muons and flasher events, which are the spontaneous  
 1597     discharge of a given PMT, contribute the largest amount of background events in the en-  
 1598     ergy range relevant to **any analysis searching for neutrino events this thesis**. Lower  
 1599     energy analyses like DSNB searches are also subject to radioactive backgrounds [189].  
 1600     Therefore the data recorded is reduced with the aim of removing these background  
 1601     events. The reduction process is detailed in [47, 89] and briefly summarised below.

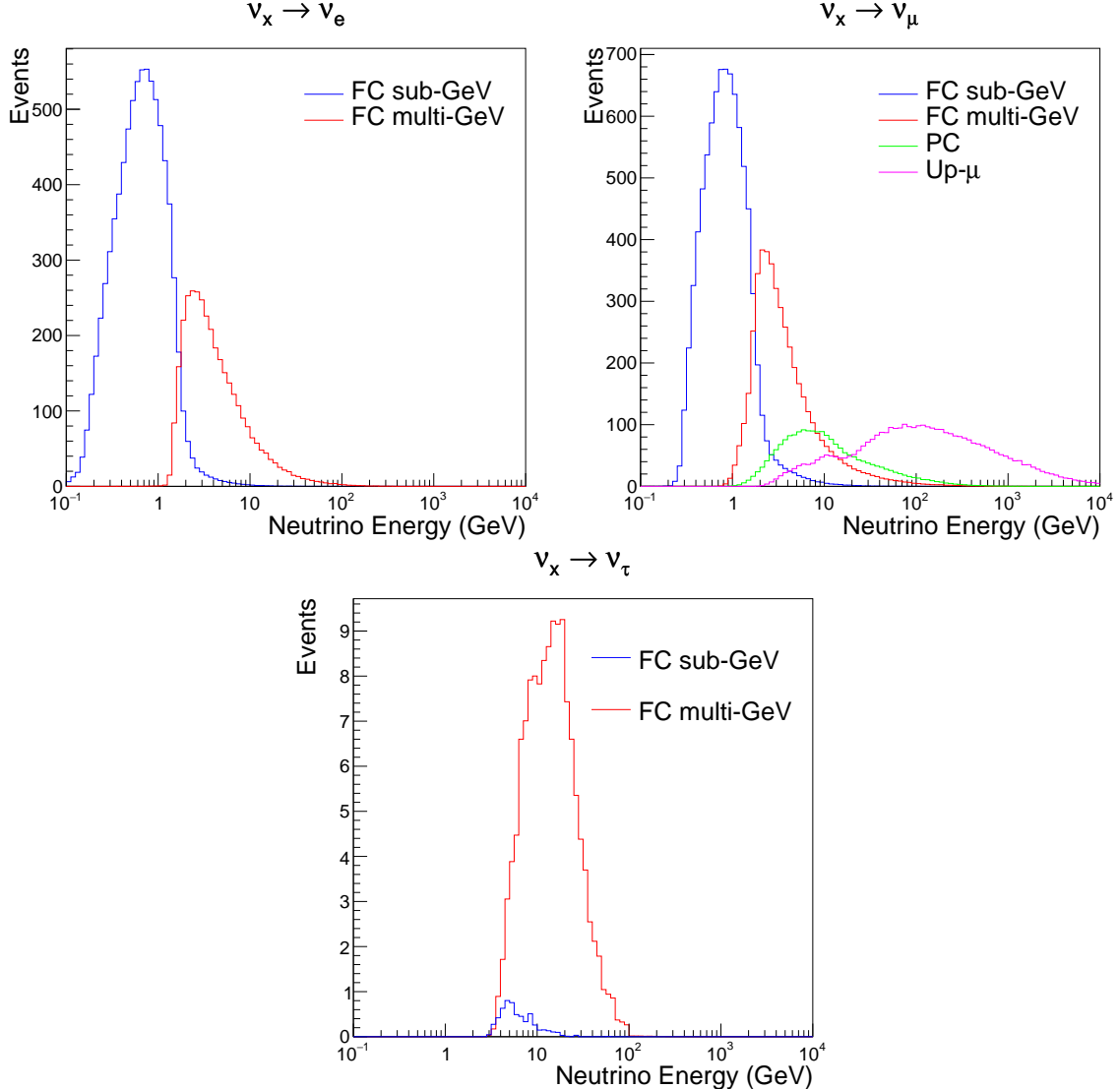


**Figure 5.11:** The predicted neutrino flux of the fully contained (FC) sub-GeV and multi-GeV, partially contained (PC), and upward-going muon (Up- $\mu$ ) events. The prediction is broken down by the  $\nu_x \rightarrow \nu_e$  prediction (top left),  $\nu_x \rightarrow \nu_\mu$  prediction (top right) and  $\nu_x \rightarrow \nu_\tau$  prediction (bottom). Asimov A oscillation parameters are assumed (given in Table 2.2).

1602        The first two steps in the FC reconstruction remove the majority of cosmic ray  
 1603        muons by requiring a significant amount of ID activity compared to that measured in  
 1604        the OD. Events that pass this cut are typically very high momentum muons or events  
 1605        that leave very little activity in the OD. Consequently, a third reduction step is then  
 1606        applied to select cosmic-ray muons that pass the initial reduction step. A purpose-built  
 1607        cosmic muon fitter is used to determine the entrance (or exit) position of the muon and

1608 a cut is applied to OD activity contained within 8m of this position. Flasher events are  
 1609 removed in the fourth reduction step which is based on the close proximity of PMT  
 1610 hits surrounding the PMT producing the flash. Events that pass all these reduction  
 1611 steps are reconstructed with the APFit algorithm. The fifth step of the reduction uses  
 1612 information from the more precise fitter to repeat the previous two steps with tighter  
 1613 cuts. Muons below the Cherenkov threshold can not generate optical photons in the  
 1614 ID but the associated decay electron can due to its lower mass. These are the types of  
 1615 events targeted in the fifth reduction step. The final cuts require the event vertex to be  
 1616 within the fiducial volume (0.5m from the wall although the nominal distance is 2.0m),  
 1617 visible energy  $E_{vis} > 30\text{MeV}$  and fewer than 16 hits within the higher energy OD  
 1618 cluster. The culmination of the fully contained reduction results in 8.09 events/day in  
 1619 the nominal fiducial volume [190]. The uncertainty in the reconstruction is calculated  
 1620 by comparing Monte Carlo prediction to data. The largest discrepancy is found to be  
 1621 1.3% in the fourth reduction step.

1622 The PC and Up- $\mu$  events are processed through their own reduction processes  
 1623 detailed in [47]. Both of these samples are reconstructed with the APFit algorithm  
 1624 rather than fitQun. This is because the efficiency of reconstructing events that leave  
 1625 the detector has not been sufficiently studied for reliable systematic uncertainties wth  
 1626 fitQun. The PC and Up- $\mu$  samples acquire events at approximately 0.66 and 1.44  
 1627 events/day.

1628 Events due to beam neutrinos undergo the same reduction steps as FC events and  
 1629 are then subject to further cuts [191]. The GPS system which links the timing between  
 1630 the beam facility and SK needs to be operating correctly and there should be no activity  
 1631 within the detector in the previous  $100\mu\text{s}$  before the trigger. The events then need to  
 1632 triggered between  $-2\mu\text{s}$  and  $10\mu\text{s}$  of the expected spill timing.

1633 Due to the lower energy beam neutrinos, the T2K samples are not dependent  
 1634 upon the visible energy neutrino as the range of neutrino energies are smaller than  
 1635 that found in atmospheric neutrinos. Furthermore, the 2020 T2K-only oscillation  
 1636 analysis only considers events which contain a single ring. Similar to atmospheric  
 1637 event selection, the number of decay electrons is used as a proxy for distinguishing  
 1638 CCQE and CCRES events. The expected neutrino energy, broken down by number  
 1639 of decay electrons, is given in ???. The beam neutrinos samples are not split by  
 1640 visible energy since their energy range is smaller than the atmospheric neutrino  
 1641 events. Following the T2K analysis in [80], only single-ring beam neutrino events  
 1642 are considered. Similar to atmospheric event selection, the number of decay electrons  
 1643 is used as a proxy for distinguishing CCQE and CCRES events. The expected neutrino  
 1644 energy, broken down by number of decay electrons, is given in Figure 5.12.

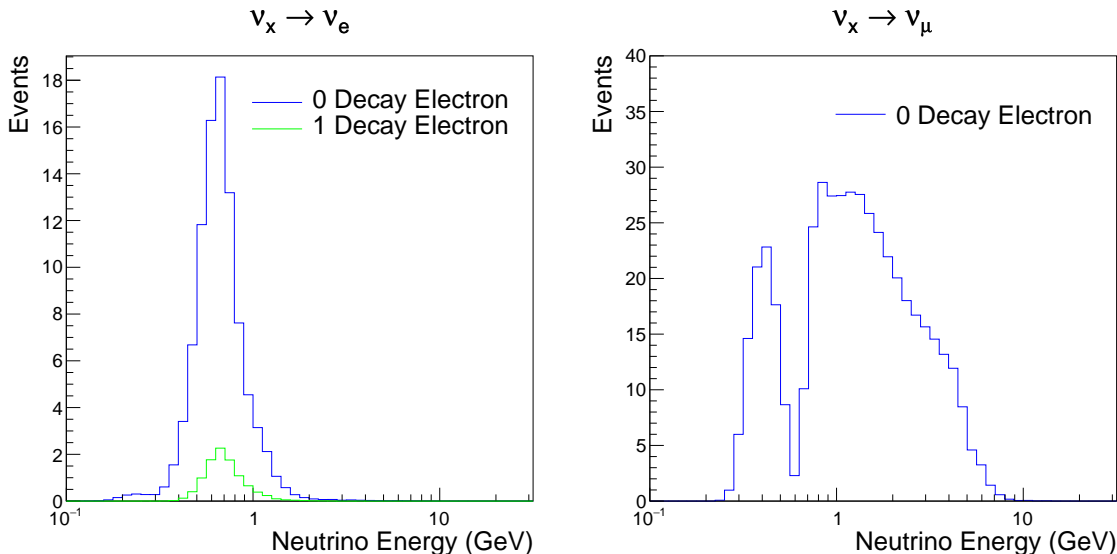


**Figure 5.12:** The predicted flux of beam neutrinos, as a function of neutrino energy. The predictions are broken down by the number of decay electrons associated with the particular events. Asimov A oscillation parameters are assumed (given in Table 2.2).

1645 **Chapter 6**

1646 **Sample Selections and Systematics**

1647 The oscillation analysis presented within this thesis is built upon a simultaneous  
1648 fit to atmospheric data at SK, neutrino beam data in the near detector, and beam  
1649 data measured at SK. The definitions of these samples are documented in section 6.1,  
1650 section 6.2, and section 6.3, respectively. The data collected and used within this  
1651 analysis is detailed in Table 6.1. The near and far detector data corresponds to T2K  
1652 runs 2-9 and runs 1-10, respectively. The accumulated POT and beam power for runs  
1653 1 – 10 are illustrated in Figure 6.1.

Data Type	Total
Near Detector FHC	$1.15 \times 10^{21}$ POT
Near Detector RHC	$8.34 \times 10^{20}$ POT
Far Detector FHC	$1.97 \times 10^{21}$ POT
Far Detector RHC	$1.63 \times 10^{21}$ POT
Atmospheric SK-IV	3244.4 days

**Table 6.1:** The amount of data collected in each detector used within this analysis. The data collected at the near and far detector, for both neutrino beam (FHC) and antineutrino beam (RHC), is measured as the number of protons on target (POT).

1654 The difference in POT recorded at the near and far detector is due to the difference  
1655 in downtime of the respective detector. The SK detector is very stable with almost 100%  
1656 of data recorded during beam operation. Due to various technical and operational  
1657 issues, the downtime of the near detector is significantly higher due to its more  
1658 complex design and operating requirements.

1659     The systematic parameters invoked within the flux, detector, and interaction models  
 1660    used within this analysis are documented in section 6.4. The standard configuration of  
 1661    the joint beam and atmospheric data fit utilises far detector systematics provided in  
 1662    the official inputs from the two experiments. Additionally, a correlated detector model  
 1663    which fits the parameters used in sample selections to data has been developed and  
 1664    documented in subsection 6.4.5.

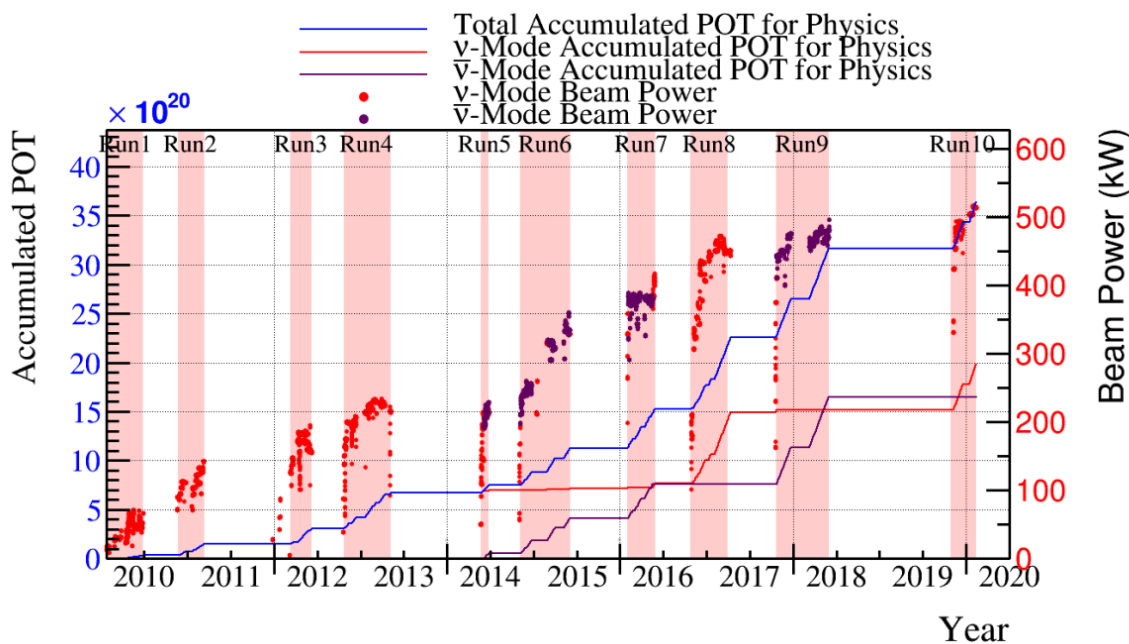


**Figure 6.1:** The accumulated beam data, measured as the number of protons on target (POT). The total data (blue) is given which comprises of the neutrino beam (red) and antineutrino (purple) components. The beam power for neutrino and antineutrino beams is given as the markers using the same colour scheme. The timescale runs from Run 1 which started in January 2010 until Run 10 which ended in February 2020. The ratio of accumulated data in neutrino and antineutrino beam is 54.7% : 45.3%.

## 1665 6.1 Atmospheric Samples

1666 The atmospheric event selection follows the official SK-IV analysis presented in [89]  
1667 and is documented below. The Monte Carlo prediction used within this analysis  
1668 corresponds to 500 years worth of neutrino events, which is scaled down to match the  
1669 SK-IV livetime of 3244.4 days.

1670 The fully contained (FC), partially contained (PC), and upward going muon events  
1671 ( $\text{up-}\mu$ ) which pass the reduction cuts discussed in section 5.3 are further broken down  
1672 into different samples based on reconstruction information. This section details the  
1673 samples used within this oscillation analysis, alongside the chosen binning, used  
1674 within the fit.

1675 FC events are first separated by the visible energy deposited within the detector.  
1676 This is calculated as the sum of the reconstructed kinetic energy above the Cherenkov  
1677 threshold for all rings present in the event. Events are separated by whether they were  
1678 above or below  $E_{\text{vis}} = 1.33\text{GeV}$ . This separates “subGeV” and “multiGeV” events.  
1679 Typically, lower energy events consist of charge current quasi-elastic (CCQE) inter-  
1680 actions which are better understood and simpler to reconstruct resulting in smaller  
1681 systematic uncertainties. Events are further separated by the number of rings as-  
1682 sociated with the event due to similar reasoning. As the oscillation probability is  
1683 dependent upon the flavour of neutrino, electron and muon events are separated  
1684 using a similar likelihood method to that discussed in section 5.2. To reduce computa-  
1685 tional resources required for the reconstruction, only electron and pion hypotheses are  
1686 considered so this separation cut depends on the ratio of the electron to pion likeli-  
1687 hoods,  $\log(L_e/L_\pi)$ . Finally, the number of decay electrons is used to classify events.  
1688 Charged current resonant pion production (CCRES) interactions generate a final-state  
1689 pion. This can decay, mostly likely through a muon, into a decay electron. Therefore

- any electron-like event with one decay electron or muon-like event with two decay electrons was most likely produced by a CCRES interaction. Consequently, the number of decay electrons can be used to distinguish CCQE and CCRES interaction modes. Ultimately, FC subGeV events are separated into the samples listed in Table 6.2.

Sample Name	Description
SubGeV-e-like-0dcy	Single ring $e$ -like events with zero decay electrons
SubGeV-e-like-1dcy	Single ring $e$ -like events with one or more decay electrons
SubGeV-mulike-0dcy	Single ring $\mu$ -like events with zero decay electrons
SubGeV-mulike-1dcy	Single ring $\mu$ -like events with one decay electrons
SubGeV-mulike-2dcy	Single ring $\mu$ -like events with two or more decay electrons
SubGeV-pi0like	Two $e$ -like ring events with zero decay electrons and reconstructed $\pi^0$ mass $85 \leq m_{\pi^0} < 215\text{MeV}$

**Table 6.2:** The fully contained subGeV samples, defined as events with visible energy  $E_{vis} < 1.33\text{GeV}$ , used within this oscillation analysis.

- In addition to the cuts discussed above, multiGeV samples also have additional cuts to separate samples which target neutrino and antineutrino separation. As discussed in section 7.1, the matter resonance only occurs for neutrinos in normal hierarchy and antineutrinos in an inverted mass hierarchy. Therefore, having flavour-enriched samples aids in the determination of the mass hierarchy. For a CCRES interaction,

$$\begin{aligned}
 \bar{\nu}_e + N &\rightarrow e^+ + N' + \pi^-, \\
 \nu_e + N &\rightarrow e^- + N' + \pi^+ \\
 &\quad \downarrow \mu^+ + \nu_\mu \\
 &\quad \downarrow e^+ + \nu_e + \bar{\nu}_\mu.
 \end{aligned} \tag{6.1}$$

- The  $\pi^-$  emitted from a  $\bar{\nu}_e$  interaction is more likely to be absorbed within the oxygen nucleus compared to the  $\pi^+$  from  $\nu_e$  interactions [192]. These pions then

1701 decay, mostly through muons, to electrons. Therefore the number of tagged decay  
 1702 electrons associated with an event gives an indication of whether the interaction  
 1703 was due to a neutrino or antineutrino: zero for  $\bar{\nu}_e$  events, and one for  $\nu_e$  events.  
 1704 The ability to separate neutrino from antineutrino events is illustrated in Table 6.4,  
 1705 where the MultiGeV-*e*like-nue has 78% purity of neutrino interactions with only 7%  
 1706 antineutrino background in that sample and the rest of the sample comprising of  
 1707 neutral current backgrounds.

1708 This relatively simple discriminator works reasonably well for single-ring events.  
 1709 However, this is not the case for multi-ring events. A multiGeV multiring separation  
 1710 (MME) likelihood cut which specifically targets multiGeV multiRing electron-like  
 1711 events was introduced in [193, 194]. This is a two-stage likelihood selection cut. Four  
 1712 observables are used within the first likelihood cut to distinguish CC $\nu_e$  and CC $\bar{\nu}_e$   
 1713 events from background:

- 1714     • The number of decay electrons
- 1715     • The maximum distance between the vertex of the neutrino and the decay electrons
- 1716     • The energy deposited by the leading energy ring
- 1717     • The reconstructed particle identification of that highest energy ring

1718 Background events consist of CC $\nu_\mu$  and NC interactions. Typically these produce  
 1719 events where the majority of the energy is carried by the hadronic system. Additionally,  
 1720 muons tend to travel further than the pions from CC $\nu_e$  before decaying. Consequently,  
 1721 the parameters used within the likelihood cut target the typical background interaction  
 1722 kinematics.

1723 Neutrino and antineutrino events are then separated by a second likelihood method  
 1724 ( $\nu/\bar{\nu}$  separation) detailed in [52]. This uses the number of decay electrons, the number  
 1725 of reconstructed rings, and the event's transverse momentum. The last two parameters

Sample Name	Description
MultiGeV- <i>e</i> -like-nue	Single ring <i>e</i> -like events with zero decay electrons
MultiGeV- <i>e</i> -like-nuebar	Single ring <i>e</i> -like events with one or more decay electrons
MultiGeV- <i>μ</i> -like	Single ring <i>μ</i> -like events
MultiRing- <i>e</i> -like-nue	Two or more ring events with leading energy <i>e</i> -like ring and passed both MME and $\nu/\bar{\nu}$ separation cuts
MultiRing- <i>e</i> -like-nuebar	Two or more ring events with leading energy <i>e</i> -like ring and passed MME and failed $\nu/\bar{\nu}$ separation cuts
MultiRing- <i>μ</i> -like	Two or more ring events with leading energy <i>μ</i> -like ring and only requires $E_{vis} > 0.6\text{GeV}$ <b>DB: Why is this not }1.33\text{GeV? N</b>
MultiRing-Other1	Two or more ring events with leading energy <i>e</i> -like ring and failed the MME likelihood cut

**Table 6.3:** The fully contained multiGeV samples used within this oscillation analysis. Both the sample name and description are given.

1726 are used because higher-energy samples tend to have more pions produced above  
 1727 the Cherenkov threshold which results in more rings compared to an antineutrino  
 1728 interaction. Furthermore, the angular distribution also tends to be more forward  
 1729 peaked in antineutrino interactions as compared to neutrino interactions [89]. These  
 1730 FC multiGeV sample definitions are detailed in Table 6.3.

1731 The PC and up- $\mu$  events are split by the amount of energy deposited within the  
 1732 outer detector, into “stopping” and “through-going” samples. This is because the  
 1733 momentum of events leaving the detector has to be approximated, which increases the  
 1734 systematic uncertainty. This estimate is particularly poor for very high-energy events.  
 1735 This is why up- $\mu$  through-going events are not binned in reconstructed momentum.  
 1736 If an event leaves the detector, the energy it takes with it has to be estimated which  
 1737 increases the systematic uncertainty compared to events entirely contained within the  
 1738 inner detector. The through-going up- $\mu$  are further separated by the presence of any  
 1739 electromagnetic showering in the event, as the assumption of non-showering muon

<sub>1740</sub> does not give reliable reconstruction for these types of events [47]. In total, 13 FC, 2  
<sub>1741</sub> PC, and 3 up- $\mu$  atmospheric samples are included within this analysis.

Sample	CC $\nu_e$	CC $\bar{\nu}_e$	CC( $\nu_\mu + \bar{\nu}_\mu$ )	CC( $\nu_\tau + \bar{\nu}_\tau$ )	NC
SubGeV-elike-0dcy	72.17	23.3	0.724	0.033	3.77
SubGeV-elike-1dcy	86.81	1.773	7.002	0.062	4.351
SubGeV-mulike-0dcy	1.003	0.380	90.07	0.036	8.511
SubGeV-mulike-1dcy	0.023	0.	98.46	0.029	1.484
SubGeV-mulike-2dcy	0.012	0.	99.25	0.030	0.711
SubGeV-pi0like	6.923	2.368	0.928	0.011	89.77
MultiGeV-elike-nue	78.18	7.041	3.439	1.886	9.451
MultiGeV-elike-nuebar	56.68	37.81	0.174	0.614	4.718
MultiGeV-mulike	0.024	0.005	99.67	0.245	0.058
MultiRing-elike-nue	59.32	12.39	4.906	3.385	20
MultiRing-elike-nuebar	52.39	31.03	1.854	1.585	13.14
MultiRing-mulike	0.673	0.080	97.33	0.342	1.578
MultiRingOther-1	27.98	2.366	34.93	4.946	29.78
PCStop	8.216	3.118	84.45	0.	4.214
PCThrus	0.564	0.207	98.65	0.	0.576
UpStop-mu	0.829	0.370	98.51	0.	0.289
UpThruNonShower-mu	0.206	0.073	99.62	0.	0.103
UpThruShower-mu	0.128	0.054	99.69	0.	0.132

**Table 6.4:** The purity of each atmospheric sample used within this analysis, broken down by charged current (CC) and neutral current (NC) interactions and which neutrino flavour interacted within the detector. Asimov A oscillation parameter sets are assumed (given in Table 2.2). Electron neutrino and antineutrino events are separated to illustrate the ability of the separation likelihood cuts used within the multiGeV and multiring sample selections.

<sub>1742</sub> The atmospheric samples are binned in direct observables: reconstructed lepton  
<sub>1743</sub> momentum and direction, as given by Table 6.5. The distribution of the reconstructed  
<sub>1744</sub> lepton momentum (for samples that only have one bin reconstructed zenith angle)  
<sub>1745</sub> and reconstructed direction for each atmospheric sample used within this analysis is  
<sub>1746</sub> illustrated in Figure 6.2.

Sample	$\cos(\theta_Z)$ Bins	Momentum Bin Edges ( $\log_{10}(P)$ MeV)
SubGeV- <i>e</i> like-0dcy	10	2.0, 2.4, 2.6, 2.8, 3.0, 3.2
SubGeV- <i>e</i> like-1dcy	1	2.0, 2.4, 2.6, 2.8, 3.0, 3.2
SubGeV- <i>m</i> ulike-0dcy	10	2.0, 2.4, 2.6, 2.8, 3.0, 3.2
SubGeV- <i>m</i> ulike-1dcy	10	2.0, 2.4, 2.6, 2.8, 3.0, 3.2
SubGeV- <i>m</i> ulike-2dcy	1	2.0, 2.4, 2.6, 2.8, 3.0, 3.2
SubGeV- <i>p</i> i0like	1	2.0, 2.2, 2.4, 2.6, 2.8, 3.2
MultiGeV- <i>e</i> like-nue	10	3.0, 3.4, 3.7, 4.0, 5.0
MultiGeV- <i>e</i> like-nuebar	10	3.0, 3.4, 3.7, 4.0, 5.0
MultiGeV- <i>m</i> ulike	10	3.0, 3.4, 5.0
MultiRing- <i>e</i> like-nue	10	3.0, 3.4, 3.7, 5.0
MultiRing- <i>e</i> like-nuebar	10	3.0, 3.4, 3.7, 5.0
MultiRing- <i>m</i> ulike	10	2.0, 3.124, 3.4, 3.7, 5.0
MultiRing- <i>O</i> ther1	10	3.0, 3.4, 3.7, 4.0, 5.0
PC-Stop	10	2.0, 3.4, 5.0
PC-Through	10	2.0, 3.124, 3.4, 3.7, 5.0
Upmu-Stop	10	3.2, 3.4, 3.7, 8.0
Upmu-Through-Showering	10	2.0, 8.0
Upmu-Through-NonShowering	10	2.0, 8.0

**Table 6.5:** The reconstructed cosine zenith and lepton momentum binning assigned to the atmospheric samples. The “ $\cos(\theta_Z)$  Bins” column illustrates the number of bins uniformly distributed over the  $-1.0 \leq \cos(\theta_Z) \leq 1.0$  region for fully and partially contained samples and  $-1.0 \leq \cos(\theta_Z) \leq 0.0$  region for up- $\mu$  samples. **DB: Does this belong in the appendix?**

1747

**DB: By-mode spectra of each sample needed? ie. Figure 6.3 for atmospherics?**

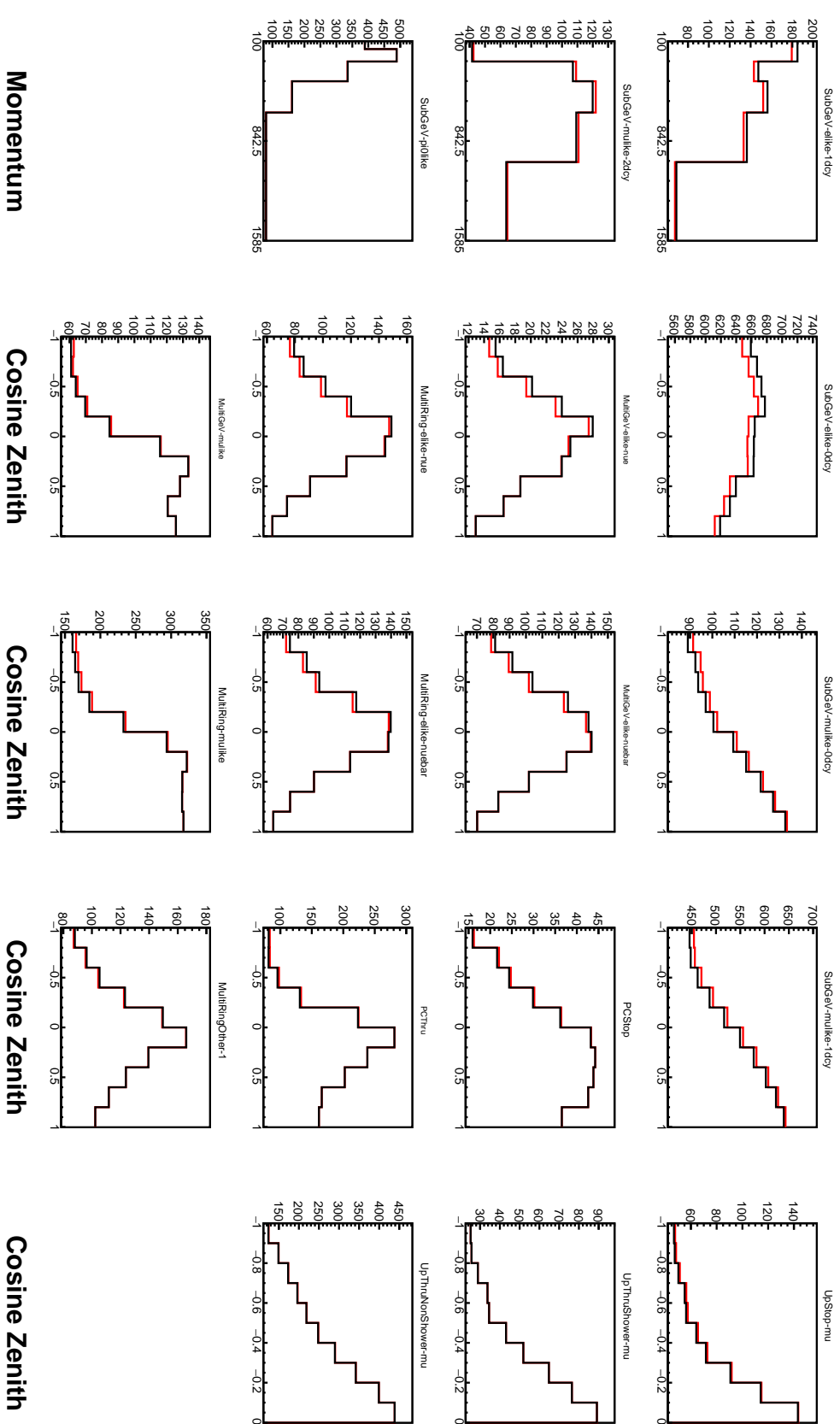


**Figure 6.2:** Comparison of the SK-IV atmospheric samples between predictions made with the CP-violating Asimov A (Black) and CP-conserving Asimov B (Red) oscillation parameter sets (given in Table 2.2). The subGeV samples CCRES and  $\pi^0$ -like samples are given in their reconstructed lepton momentum. All other samples are presented in their reconstructed zenith angle projection.

## <sup>1748</sup> 6.2 Near Detector Beam Samples

<sup>1749</sup> The near detector sample selections are documented in detail within [195] and sum-  
<sup>1750</sup> marised below. Samples are selected based upon the particular FGD in which the  
<sup>1751</sup> vertex of the neutrino interaction is in as well as the operating mode of the beam:  
<sup>1752</sup> FHC or RHC. For additional constraints on model parameters, wrong-sign neutrino  
<sup>1753</sup> samples are also considered when the beam is operating in RHC mode. Samples  
<sup>1754</sup> from the wrong-sign component of the FHC beam mode are not included as they are  
<sup>1755</sup> statistically insignificant compared to those samples already listed.

<sup>1756</sup> Before being assigned a sample, all events must undergo CC-inclusive cuts, as  
<sup>1757</sup> defined in [196]:

- <sup>1758</sup> • Event Timing: The DAQ must be operational and the event must occur within  
<sup>1759</sup> the expected beam time window
- <sup>1760</sup> • TPC Requirement: The track path must intercept one or more TPCs
- <sup>1761</sup> • Fiducial volume: The event must originate from within the fiducial volume. The  
<sup>1762</sup> fiducial volumes are defined as a region within each sub-detector [197].
- <sup>1763</sup> • Upstream Background: Remove events that have muons tracks that originate  
<sup>1764</sup> upstream of the FGDs by requiring no high-momentum tracks within 150mm  
<sup>1765</sup> upstream of the candidate vertex. Additionally, events that occur within the  
<sup>1766</sup> downstream FGD are vetoed if a secondary track starts within the upstream FGD
- <sup>1767</sup> • Broken track removal: All candidates where the muon candidate is broken in two  
<sup>1768</sup> are removed
- <sup>1769</sup> • Muon PID: Measurements of  $dE/dx$  in a TPC are used to distinguish muon-like  
<sup>1770</sup> events using a likelihood cut

<sub>1771</sub> In addition to these cuts, RHC neutrino events also have to undergo the following  
<sub>1772</sub> cuts to aid in the separation of neutrino and antineutrino [198]:

- <sub>1773</sub> • TPC Requirement: The track path must intercept TPC2
- <sub>1774</sub> • Positive Track: The highest momentum track must be positive
- <sub>1775</sub> • TPC1 Veto: Remove any events originating upstream of TPC1

<sub>1776</sub> Once all CC-inclusive events have been determined, they are further segregated  
<sub>1777</sub> into sub-samples that target the constraints on interaction modes most relevant at  
<sub>1778</sub> the far detector. They are split by pion multiplicity: CC0 $\pi$ , CC1 $\pi$ , and CCOther.  
<sub>1779</sub> These target specific interaction modes CCQE, CCRES, and other CC background  
<sub>1780</sub> interactions, respectively. Pions in the TPCs and FGDs are selected by requiring a  
<sub>1781</sub> second track to be observed, which is separate from the muon track and is in the same  
<sub>1782</sub> beam spill window and sub-detector. If the pion originated within a FGD, it must also  
<sub>1783</sub> pass through the sequential downstream TPC (TPC2 for FGD1, TPC3 for FGD2).

<sub>1784</sub> CC0 $\pi$ , CC1 $\pi$ , and CCOther samples are defined with the following cuts:

- <sub>1785</sub> •  $\nu_\mu$ CC0 $\pi$  Selection: No electrons in TPC and no charged pions or decay electrons  
<sub>1786</sub> within the TPC or FGD
- <sub>1787</sub> •  $\nu_\mu$ CC1 $\pi$  Selection: Exactly one charged pion in either the TPC or FGD, where  
<sub>1788</sub> the number of charged pions in the FGD is equal to the number of decay electrons
- <sub>1789</sub> •  $\nu_\mu$ CCOther Selection: All events which are not classified into the above two  
<sub>1790</sub> selections.

<sub>1791</sub> Counting the three selections for each FGD in FHC and RHC running, including  
<sub>1792</sub> the wrong-sign background in RHC, 18 near detector samples are used within this  
<sub>1793</sub> analysis. These samples are binned in reconstructed lepton momentum (illustrated in  
<sub>1794</sub> Figure 6.3) and direction with respect to the beam. The binning is chosen such that

each event has at least 20 Monte Carlo events in each bin [197]. This is to ensure that the bins are coarse enough to ensure the reduction of statistical errors, whilst also being fine enough to sample the high-resolution peak regions. The exact binning is detailed in [197].

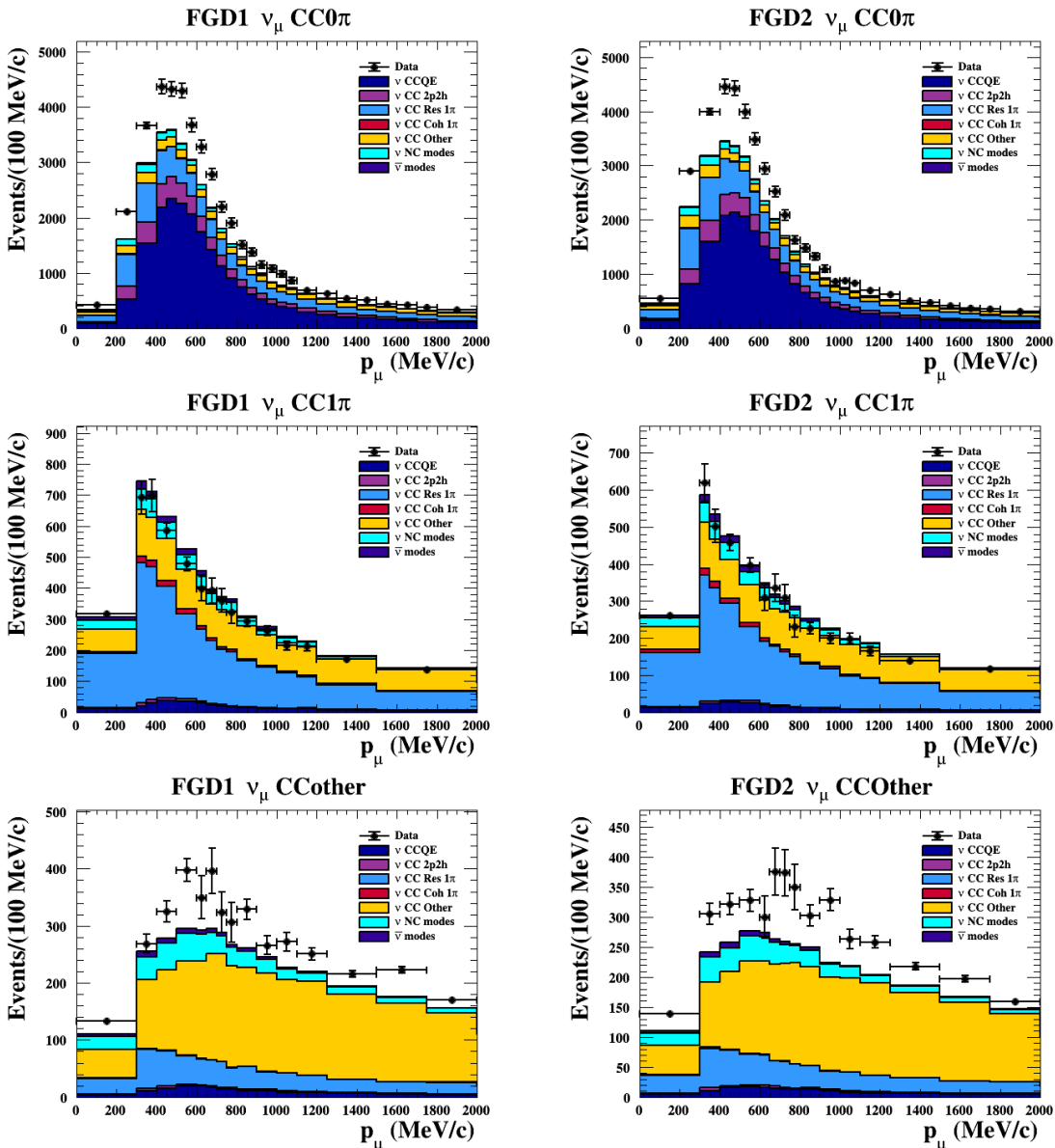


**Figure 6.3:** The nominal Monte Carlo predictions for the FGD1 and FGD2 samples in neutrino beam mode, broken down into the  $CC\nu_\mu 0\pi$ ,  $CC\nu_\mu 1\pi$  and  $CC\nu_\mu$  Other categories. Figures taken from [195].

## <sup>1799</sup> 6.3 Far Detector Beam Samples

<sup>1800</sup> The beam neutrino events which occur at the SK detector, which pass the reduction cuts  
<sup>1801</sup> detailed in section 5.3, are separated depending on whether the beam was operating  
<sup>1802</sup> in FH or RHC mode. The events are then separated into three samples: electron-like  
<sup>1803</sup> ( $1Re$ ), muon-like ( $1R\mu$ ), and CC $1\pi^+$ -like ( $1Re1de$ ) which are observed as electron-like  
<sup>1804</sup> events with an associated decay electron [185]. As discussed in section 6.1, positively  
<sup>1805</sup> charged pions emitted from neutrino interactions are more likely to produce decay  
<sup>1806</sup> electrons than negatively charged pions. Consequently, the CC $1\pi^+$ -like sample is only  
<sup>1807</sup> selected when the beam is operating in FHC mode. Therefore, five beam samples  
<sup>1808</sup> measured at SK are used in this analysis.

<sup>1809</sup> The fiducial volume definition for beam samples is slightly different from that used  
<sup>1810</sup> within the atmospheric samples. It uses both the distance to the closest wall ( $d_{Wall}$ )  
<sup>1811</sup> and the distance to the wall along the trajectory of the particle ( $to_{Wall}$ ). This allows  
<sup>1812</sup> events that originate close to the wall but are facing into the tank to be included within  
<sup>1813</sup> the analysis, which would have otherwise been removed. These additional events are  
<sup>1814</sup> beneficial for a statistics-limited experiment. The exact cut values for both  $d_{Wall}$  and  
<sup>1815</sup>  $to_{Wall}$  are different for each of the three types of sample and are optimised based on  
<sup>1816</sup> T2K sensitivity to  $\delta_{CP}$  [183, 199]. They are:

<sup>1817</sup> DB: Diagram of  $d_{Wall}$  and  $to_{Wall}$  needed?

<sup>1818</sup> **1Re event selection** For an event to be classified as a  $1Re$ -like, the event must follow:

- <sup>1819</sup> • Fully-contained and within  $d_{Wall} > 80\text{cm}$  and  $to_{Wall} > 170\text{cm}$
- <sup>1820</sup> • Total of one ring which is reconstructed as electron-like with reconstructed mo-  
<sup>1821</sup> mentum  $P_e > 100\text{MeV}$

- 1822     • Zero decay electrons are associated with the event  
1823     • Passes  $\pi^0$  rejection cut discussed in section 5.2

1824     The zero decay electron cut specifically targets CCQE interactions. Whereas, the  $\pi^0$   
1825     rejection cut is designed to remove neutral current  $\pi^0$  background events which can  
1826     be easily reconstructed as 1Re-like events.

1827     **CC1 $\pi^+$  event selection** This event selection is very similar to that of the 1Re sample.  
1828     The only difference is that the dWall and toWall criteria are changed to  $> 50\text{cm}$  and  
1829      $> 270\text{cm}$ , respectively. Furthermore, exactly one decay electron is required from the  
1830      $\pi^+$  decay.

1831     **1R $\mu$  event selection** A 1R $\mu$ -like event is determined by the following cuts:

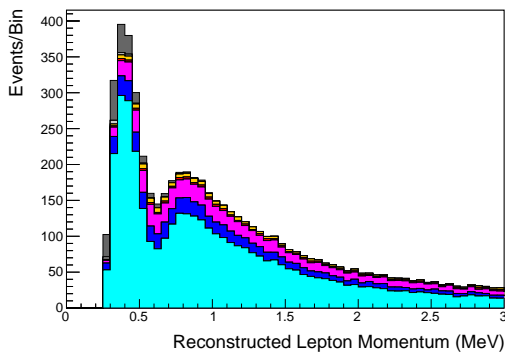
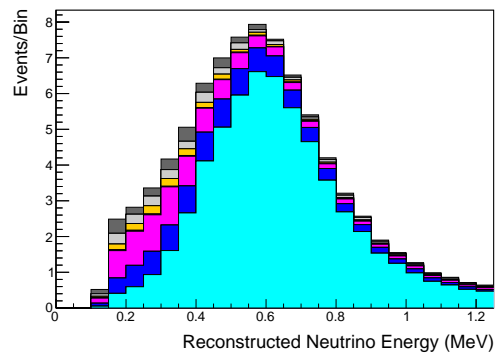
- 1832     • Fully-contained and within  $\text{dWall} > 50\text{cm}$  and  $\text{toWall} > 250\text{cm}$   
1833     • Total of one ring which is reconstructed as muon-like with reconstructed momen-  
1834     tum  $P_\mu > 200\text{MeV}$   
1835     • Fewer than two decay electrons are associated with the event  
1836     • Passes  $\pi^+$  rejection cut discussed in section 5.2

1837     As pions and muons have similar masses, the Cherenkov rings they generate have  
1838     similar opening angles. To enhance the purity, the events have to pass the  $\pi^+$  rejection  
1839     cut which is specifically optimised to separate the two types of events.

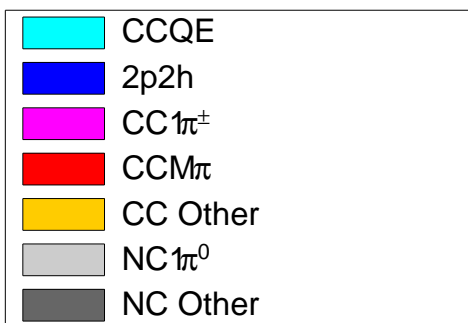
1840     All of these samples are binned in reconstructed neutrino energy. This is possible  
1841     as the direction from the source is known extremely well. This value is calculated for  
1842     the 1Re-like and 1R $\mu$ -like samples assuming CCQE interactions,

$$E_\nu^{rec} = \frac{(M_N - V_{nuc})E_l - m_l^2/2 + M_N V_{nuc} - V_{nuc}^2/2 + (M_P^2 + M_N^2)/2}{M_N - V_{nuc} - E_l + P_l \cos(\theta_{beam})} \quad (6.2)$$

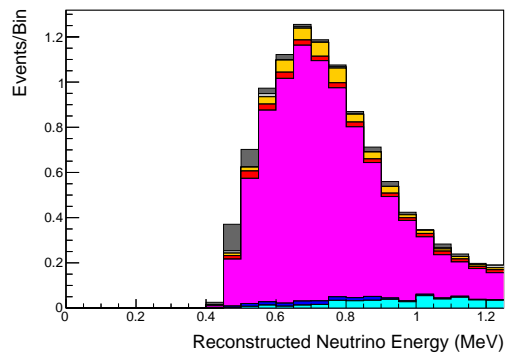
Where  $M_N$ ,  $M_P$  and  $m_l$  are the masses of the neutron, proton and outgoing lepton, respectively.  $V_{nuc} = 27\text{MeV}$  is the binding energy of the oxygen nuclei [185],  $\theta_{beam}$  is the angle between the beam and the direction of the outgoing lepton, and  $E_l$  and  $P_l$  are the energy and momentum of that outgoing lepton.

(a) FHC 1R $\mu$ 

(b) FHC 1Re



(c)

(d) FHC CC1 $\pi^+$ 

**Figure 6.4:** The reconstructed neutrino energy, as defined by Equation 6.2 and Equation 6.3, for the 1R $\mu$ -like, 1Re-like and CC1 $\pi^+$ -like samples. Asimov A oscillation parameter sets are assumed (given in Table 2.2). These samples are the FHC mode samples. For ease of viewing, the 1R $\mu$  sample only shows the  $0. \leq E_\nu^{rec} < 3.0\text{GeV}$  but the binning extends to 30.0GeV.

<sup>1847</sup> The reconstructed neutrino energy of the CC1 $\pi^+$ -like events is modified to include  
<sup>1848</sup> the delta resonance produced within the interaction,

$$E_\nu^{rec} = \frac{2M_N E_l + M_{\Delta^{++}}^2 - M_N^2 - m_l^2}{2(M_N - E_l + P_l \cos(\theta_{beam}))} \quad (6.3)$$

<sup>1849</sup> Where  $M_{\Delta^{++}}$  is the mass of the delta baryon. Binding energy effects are not  
<sup>1850</sup> considered as a two-body process with the delta baryon is assumed. This follows  
<sup>1851</sup> the T2K oscillation analysis presented in [80], although recent developments of the  
<sup>1852</sup> interaction model in the latest T2K oscillation analysis do include effects from binding  
<sup>1853</sup> energy in this calculation [200].

<sup>1854</sup> The reconstructed neutrino energy for the FHC samples is illustrated in Figure 6.4.  
<sup>1855</sup> As expected, the 1R $\mu$ -like and 1Re-like samples are heavily dominated by CCQE in-  
<sup>1856</sup> teractions, with smaller contributions from 2p2h meson exchange and resonant pion  
<sup>1857</sup> production interactions. The CC1 $\pi^+$ -like sample predominantly consists of charged  
<sup>1858</sup> current resonant pion production interactions. The 1Re-like and CC1 $\pi^+$ -like samples  
<sup>1859</sup> are also binned by the angle between the neutrino beam and the reconstructed lepton  
<sup>1860</sup> momentum. This is to aid in charged current and neutral current separation, as indi-  
<sup>1861</sup> cated in Figure 6.5. This is because the neutral current backgrounds are predominantly  
<sup>1862</sup> due to  $\pi^0$ -decays, where the opening angle of the two gammas alongside the different  
<sup>1863</sup> final state kinematics produces a slightly broader angular distribution compared to  
<sup>1864</sup> the final state particles originating from charged current  $\nu_e$  interactions.

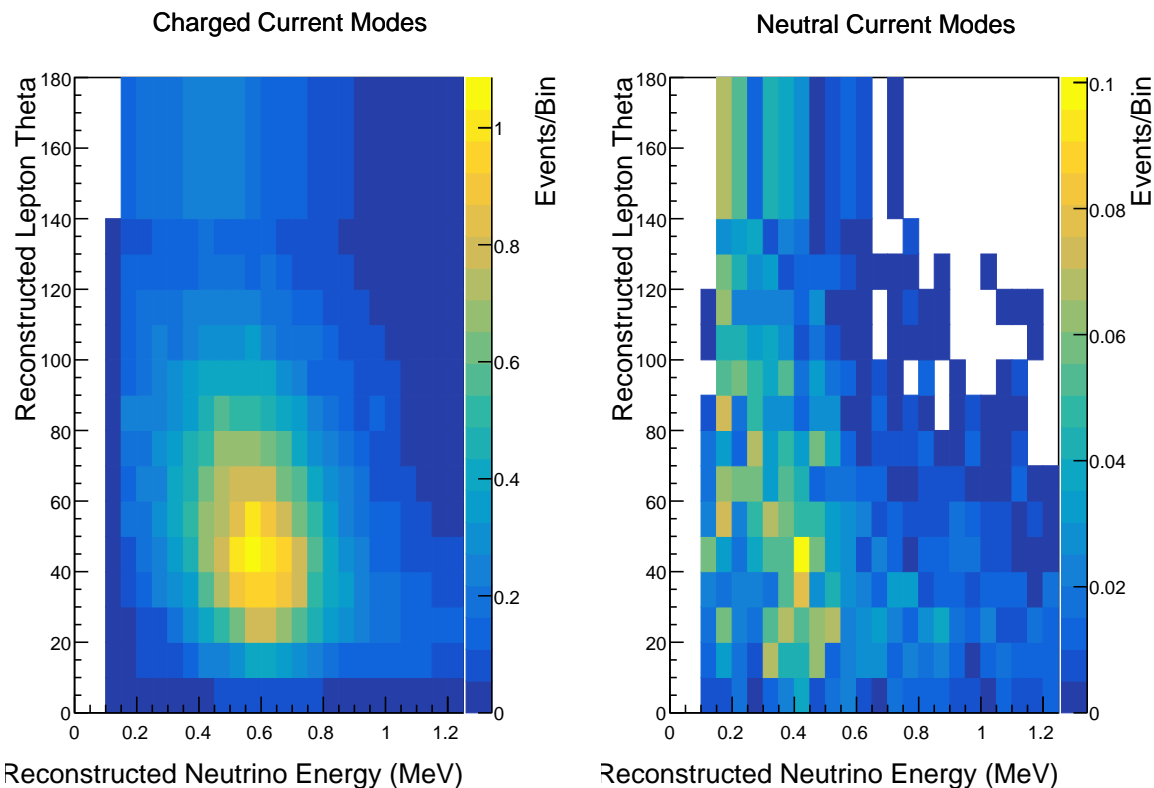


**Figure 6.5:** The distribution of the angle between the neutrino beam direction and the reconstructed final state lepton, for the FHC 1Re-like sample. The distribution is broken down by neutrino interaction mode into charged current (left) and neutral current (right) components. Asimov A oscillation parameter sets are assumed (given in Table 2.2). DB: Is this needed or will it just bring up more questions?

## 1865 6.4 Systematic Uncertainties

1866 The systematic model parameters for this analysis are split into groups, or blocks,  
1867 depending on their purpose. They consist of flux uncertainties, neutrino-matter  
1868 interaction systematics, and detector efficiencies. There are also uncertainties on the  
1869 oscillation parameters which this analysis will not be sensitive to,  $\Delta m_{12}^2$  and  $\sin^2(\theta_{12})$ .  
1870 These uncertainties are taken from the 2018 PDG measurements [81]. As described in  
1871 chapter 4, each model parameter used within this analysis requires a prior uncertainty.  
1872 This is provided via separate covariance matrices for each block. The covariance  
1873 matrices can include prior correlations between parameters within a single block, but  
1874 the separate treatment means prior uncertainties can not be included for parameters  
1875 in different groups. Some parameters in these models have no reasonably motivated  
1876 uncertainties and are assigned flat priors which do not modify the likelihood penalty.  
1877 The flux, neutrino interaction, and detector modeling simulations have already been  
1878 discussed in section 5.1 and section 5.2. The uncertainties invoked within each of these  
1879 models are described below.

### 1880 6.4.1 Beam Flux

1881 The neutrino beam flux systematics is based upon the uncertainty in the modeling of  
1882 the components of the beam. This includes the hadron production model and their re-  
1883 interactions, the shape, intensity, and alignment of the beam with respect to the target,  
1884 and the uniformity of the magnetic field produced by the horn, alongside other effects.  
1885 The uncertainty, as a function of neutrino energy, is illustrated in Figure 6.6 which  
1886 includes a depiction of the total uncertainty as well as the contribution from individual  
1887 components. The uncertainty around the peak of the energy distribution ( $E_\nu \sim 0.6\text{GeV}$ )

1888 is dominated by the measurements of the beam profile and alignment. Outside of this  
1889 region, the uncertainties within hadron production dominate the uncertainty.

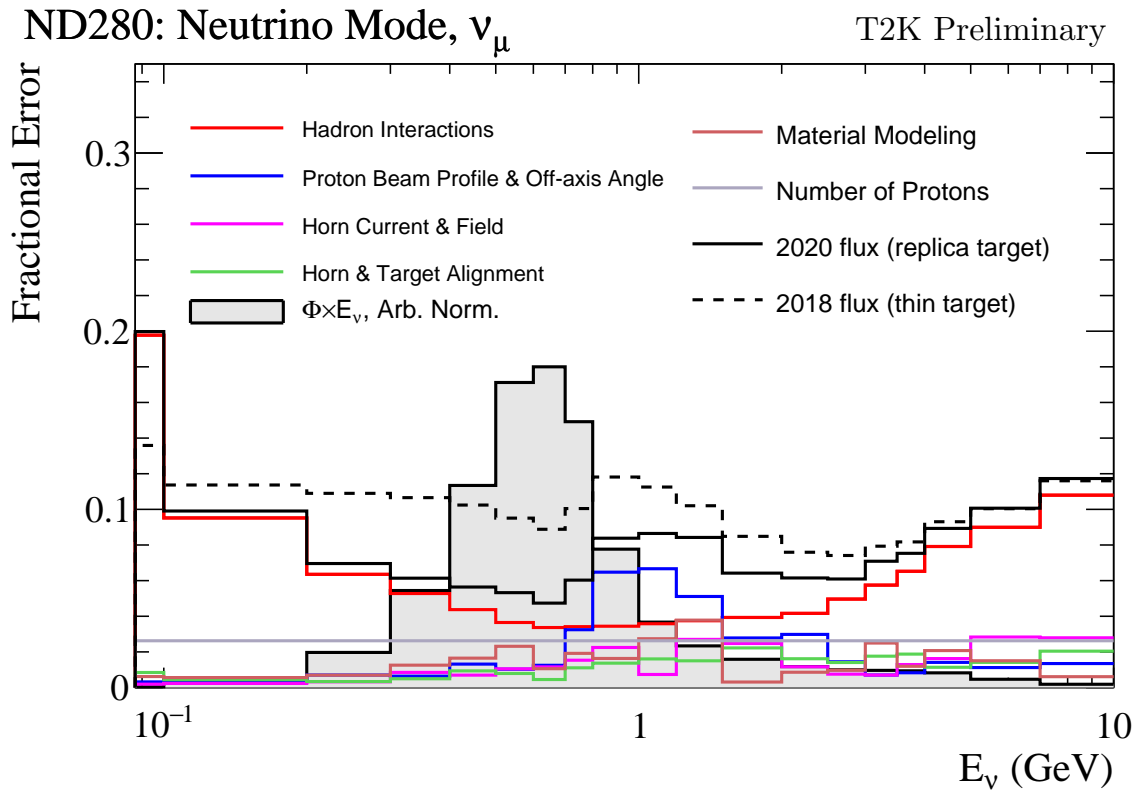


**Figure 6.6:** The total uncertainty evaluated on the near detector  $\nu_\mu$  flux prediction constrained by the replica-target data, illustrated as a function of neutrino energy. The solid(dashed) line indicates the uncertainty used within this analysis(the T2K 2018 analysis [201]). The solid histogram indicates the neutrino flux as a function of energy. Figure taken from [202].

1890 The beam flux uncertainties are described by one hundred parameters. They are  
1891 split between the ND280 and SK detectors and binned by neutrino flavour:  $\nu_\mu$ ,  $\bar{\nu}_\mu$ ,  $\nu_e$   
1892 and  $\bar{\nu}_e$ . The response is then broken down as a function of neutrino energy. The bin  
1893 density in the neutrino energy is the same for the  $\nu_\mu$  in FHC and  $\bar{\nu}_\mu$  in RHC beams,  
1894 and narrows for neutrino energies close to the oscillation maxima of  $E_\nu = 0.6\text{GeV}$ .  
1895 This binning is specified in Table 6.6. All of these systematic uncertainties are applied  
1896 as normalisation parameters with Gaussian priors centered at 1.0 and error specified  
1897 from a covariance matrix provided by the T2K beam group [202].

Neutrino Flavour	Sign	Neutrino Energy Bin Edges (GeV)
$\mu$	Right	0., 0.4, 0.5, 0.6, 0.7, 1., 1.5, 2.5, 3.5, 5., 7., 30.
$\mu$	Wrong	0., 0.7, 1., 1.5, 2.5, 30.
$e$	Right	0., 0.5, 0.7, 0.8, 1.5, 2.5, 4., 30.
$e$	Wrong	0., 2.5, 30.

**Table 6.6:** The neutrino energy binning for the different neutrino flavours. “Right” sign indicates neutrinos in the FHC beam and antineutrinos in the RHC beam. “Wrong” sign indicates antineutrinos in the FHC beam and neutrinos in the RHC beam. The binning of the detector response is identical for the FHC and RHC modes as well as at ND280 and SK.

## 1898 6.4.2 Atmospheric Flux

1899 The atmospheric neutrino flux is modeled by the HKKM model [43]. 16 systematic  
 1900 uncertainties are applied to control the normalisation of each neutrino flavour, energy,  
 1901 and direction. All of the parameters are given Gaussian priors centered at 0 and width  
 1902 equal to one. They are summarised below:

- 1903 • **Absolute Normalisation:** The overall normalisation of each neutrino flavour is  
 1904 controlled by two independent systematic uncertainties, for  $E_\nu < 1\text{GeV}$  and  $E_\nu >$   
 1905  $1\text{GeV}$ , respectively. This is driven mostly by hadronic interaction uncertainties for  
 1906 the production of pions and kaons [43]. The strength of the response is dependent  
 1907 upon the neutrino energy.
- 1908 • **Relative Normalisation:** Uncertainties on the ratio of  $(\nu_\mu + \bar{\nu}_\mu) / (\nu_e + \bar{\nu}_e)$  are  
 1909 controlled by the difference between the HKKM model [43], FLUKA [46] and  
 1910 Bartol models [42]. Three independent parameters are applied in the energy  
 1911 ranges:  $E_\nu < 1\text{GeV}$ ,  $1\text{GeV} < E_\nu < 10\text{GeV}$ , and  $E_\nu > 10\text{GeV}$ .
- 1912 •  **$\nu/\bar{\nu}$  Normalisation:** The uncertainties in the  $\pi^+/\pi^-$  (and kaon equivalent) pro-  
 1913 duction uncertainties in the flux of  $\nu/\bar{\nu}$ . The response is applied using the same  
 1914 methodology as the relative normalisation parameters.

1915 • **Up/Down and Vertical/Horizontal Ratio:** Similar to the above two systematics,  
1916 the difference between the HKKM, FLUKA, and Bartol model predictions, as a  
1917 function of  $\cos(\theta_Z)$ , is used to control the normalisation of events as a function of  
1918 zenith angle.

1919 •  **$K/\pi$  Ratio:** Higher energy neutrinos ( $E_\nu > 10\text{GeV}$ ) become dependent upon  
1920 kaon decay as the dominant source of neutrinos. Measurements of the ratio of  
1921  $K/\pi$  [203] are used to control the systematic uncertainty of the expected ratio of  
1922 pion and kaon production.

1923 • **Solar Activity:** As the 11-year solar cycle can affect the Earth's magnetic field,  
1924 the flux of primary cosmic rays varies across the same period. The uncertainty is  
1925 calculated by taking a  $\pm 1$  year variation, equating to a 10% uncertainty for the  
1926 SK-IV period.

1927 • **Atmospheric Density:** The height of the interaction of the primary cosmic rays is  
1928 dependent upon the atmospheric density. The HKKM assumes the US standard  
1929 1976 [153] profile. This systematic controls the uncertainty in that model.

1930 Updates to the HKKM and Bartol models are underway [158] to use a similar  
1931 tuning technique to that used in the beam flux predictions. After those updates, it may  
1932 be possible to include correlations in the hadron production uncertainty systematics  
1933 for beam and atmospheric flux predictions.

### 1934 6.4.3 Neutrino Interaction

1935 The neutrino interactions which occur within all the detectors are modeled by NEUT.  
1936 The two independent oscillation analyses, T2K-only [204] and the SK-only [52], have  
1937 developed separate interaction models. To leverage the most sensitivity out of this  
1938 simultaneous beam and atmospheric analysis, a correlated interaction model has been

1939 defined. Where applicable, correlations allow the systematic uncertainties applied to  
1940 the atmospheric samples to be constrained by measurements of the near detector in  
1941 the beam experiment. This can lead to stronger sensitivity to oscillation parameters as  
1942 compared to an uncorrelated model.

1943 The low energy T2K systematic model has a more sophisticated treatment of CCQE,  
1944 CCMEC, and CCRES uncertainties which is due to the purpose-made cross-section  
1945 measurements made by the near detector. Furthermore, extensive comparisons of this  
1946 model have been performed to external data [204]. However, the model is not designed  
1947 for high-energy atmospheric events, like those illustrated in Figure 5.11. Therefore  
1948 the high energy systematic model from the SK-only analysis is implemented for the  
1949 relevant multiGeV, PC, and up- $\mu$  samples. The CCQE systematic parameters invoked  
1950 within the SK high energy model are actually contained within T2K's CCQE model.  
1951 Consequently, the more sophisticated CCQE and CCMEC T2K model parameters  
1952 have been incorporated into the high energy model but are uncorrelated from the low  
1953 energy counterparts.

1954 The high energy systematic model includes parameters developed from com-  
1955 parisons of Nieves and Rein-Seghal models which affect resonant pion producing  
1956 interactions, comparisons of the GRV98 and CKMT models which control DIS interac-  
1957 tions, and hadron multiplicity measurements which modulate the normalisation of  
1958 multi-pion producing events. The uncertainty of the  $\nu_\tau$  cross-section is particularly  
1959 large and is controlled by a 25% normalisation uncertainty. These parameters are  
1960 applied via normalisation or shape parameters. The former linearly scales the weight  
1961 of all affected Monte-Carlo events, whereas the latter can increase or decrease a partic-  
1962 ular event's weight depending on its neutrino energy and mode of interaction. The  
1963 response of the shape parameters is defined by third-order polynomial splines which  
1964 return a weight for a particular neutrino energy. To reduce computational resources

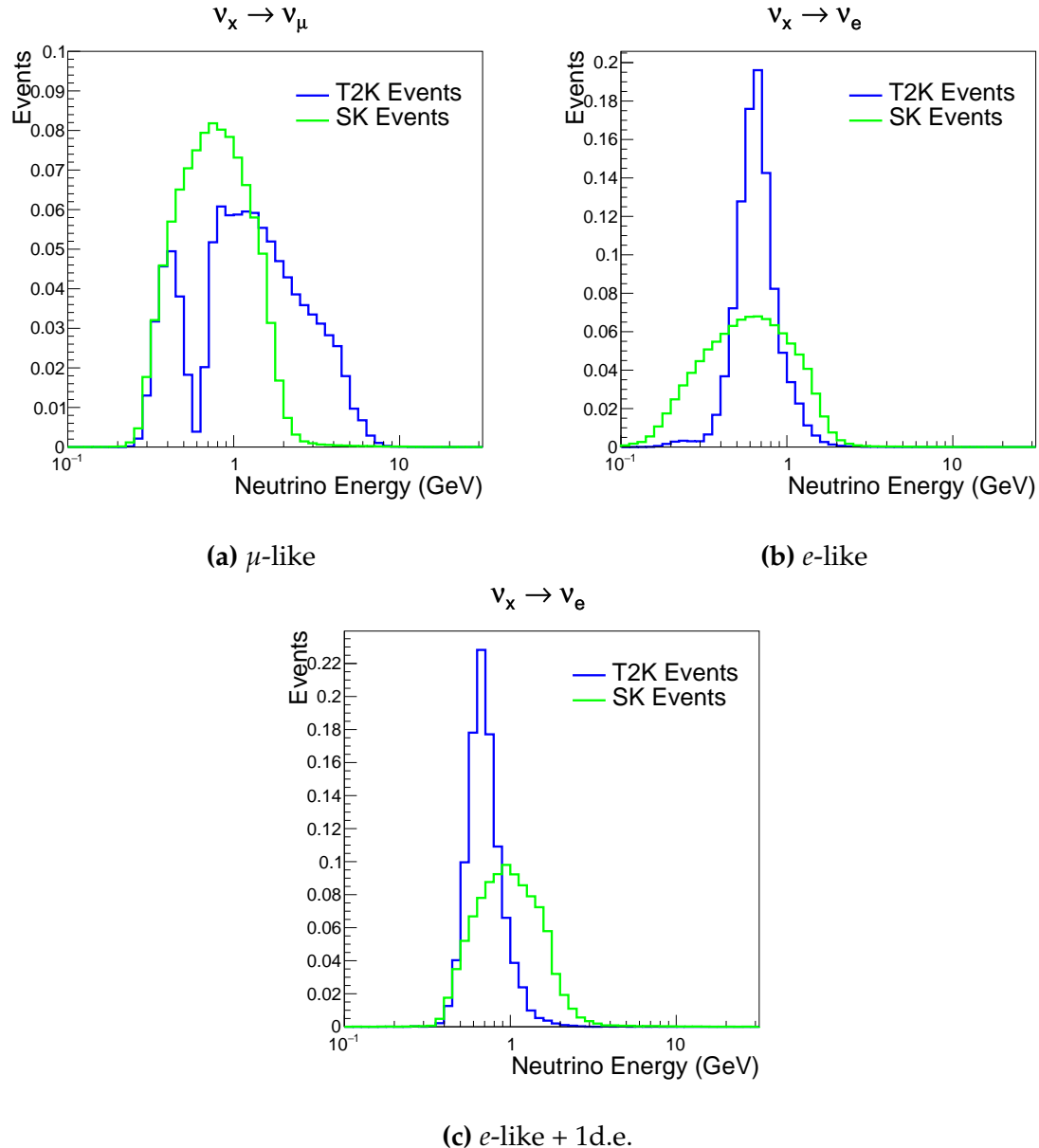
for the far detector fit, the response is binned by neutrino energy and sample binning: lepton momentum and cosine zenith binning for atmospheric splined responses and reconstructed neutrino energy and direction binning for beam samples. In total, 17 normalisation and 15 shape parameters are included in the high-energy model within this analysis.

Figure 6.7 indicates the predicted neutrino energy distribution for both beam and subGeV atmospheric samples. There is clearly significant overlap in neutrino energy between the subGeV atmospheric and beam samples, allowing similar kinematics in the final state particles. Figure 6.8 illustrates the fractional contribution of the different interaction modes per sample.

Comparing beam and atmospheric samples which target CCQE interactions (S.G. e-like 0de, S.G.  $\mu$ -like [0,1]de, [FHC,RHC] 1R  $\mu$ -like and [FHC,RHC] 1R e-like samples), there is a very similar contribution of CCQE, CC 2p2h, and CC1 $\pi^\pm$  interactions. The samples which target CC1 $\pi^\pm$  interactions, (S.G. e-like 0de, S.G.  $\mu$ -like 2de and FHC 1R+1d.e e-like) also consist of very similar mode interactions.

As a consequence of the similarity in energy and mode contributions, correlating the systematic model between the beam and subGeV atmospheric samples ensures that this analysis attains the largest sensitivity to oscillation parameters while still ensuring neutrino interaction systematics are correctly accounted for. Due to its more sophisticated CCQE and 2p2h model, the T2K systematic model was chosen as the basis of the correlated model.

The T2K systematic model [204] is applied in a similar methodology to the SK model parameters. It consists of 19 shape parameters and 24 normalisation parameters. Four additional parameters, which model the uncertainty in the binding energy, are applied in a way to shift the momentum of the lepton emitted from a nucleus. This controls the uncertainty specified on the 27MeV binding energy assumed within Equation 6.2.



**Figure 6.7:** The predicted neutrino energy distribution for subGeV atmospheric and beam samples. FHC and RHC beam samples are summed together Asimov A oscillation parameters are assumed (given in Table 2.2). Beam and atmospheric samples with similar cuts are compared against one another.

<sup>1991</sup> The majority of these parameters are assigned a Gaussian prior uncertainty. Those  
<sup>1992</sup> that have no reasonably motivated uncertainty, or those which have not been fit to  
<sup>1993</sup> external data, are assigned a flat prior which does not affect the penalty term.

<sup>1994</sup> There are three particular tunes of the T2K flux and low energy cross section model  
<sup>1995</sup> typically considered. Firstly, the “generated” tune which is the set of dial values with

	CC QE	CC 2p2h	CC $1\pi^\pm$	CC $M\pi$	CC Other	NC $\pi^0$	NC $1\pi^\pm$	NC $M\pi$	NC Coh.	NC Other
FHC 1R+1d.e. e-like	<b>0.04</b>	<b>0.02</b>	<b>0.83</b>	<b>0.03</b>	<b>0.04</b>	<b>0.01</b>	<b>0.01</b>	<b>0.01</b>	<b>0.00</b>	<b>0.01</b>
RHC 1R e-like	<b>0.62</b>	<b>0.12</b>	<b>0.11</b>	<b>0.01</b>	<b>0.02</b>	<b>0.06</b>	<b>0.01</b>	<b>0.01</b>	<b>0.01</b>	<b>0.04</b>
FHC 1R e-like	<b>0.68</b>	<b>0.12</b>	<b>0.10</b>	<b>0.00</b>	<b>0.02</b>	<b>0.04</b>	<b>0.01</b>	<b>0.00</b>	<b>0.00</b>	<b>0.02</b>
RHC 1R $\mu$ -like	<b>0.62</b>	<b>0.13</b>	<b>0.17</b>	<b>0.02</b>	<b>0.03</b>	<b>0.00</b>	<b>0.02</b>	<b>0.00</b>	<b>0.00</b>	<b>0.00</b>
FHC 1R $\mu$ -like	<b>0.62</b>	<b>0.12</b>	<b>0.16</b>	<b>0.02</b>	<b>0.03</b>	<b>0.00</b>	<b>0.03</b>	<b>0.00</b>	<b>0.00</b>	<b>0.00</b>
S.G. $\pi^0$ -like	<b>0.05</b>	<b>0.01</b>	<b>0.02</b>	<b>0.00</b>	<b>0.01</b>	<b>0.68</b>	<b>0.06</b>	<b>0.07</b>	<b>0.06</b>	<b>0.04</b>
S.G. $\mu$ -like 2de	<b>0.04</b>	<b>0.01</b>	<b>0.80</b>	<b>0.10</b>	<b>0.04</b>	<b>0.00</b>	<b>0.00</b>	<b>0.00</b>	<b>0.00</b>	<b>0.00</b>
S.G. $\mu$ -like 1de	<b>0.72</b>	<b>0.11</b>	<b>0.12</b>	<b>0.01</b>	<b>0.02</b>	<b>0.00</b>	<b>0.01</b>	<b>0.00</b>	<b>0.00</b>	<b>0.00</b>
S.G. $\mu$ -like 0de	<b>0.68</b>	<b>0.11</b>	<b>0.10</b>	<b>0.01</b>	<b>0.02</b>	<b>0.01</b>	<b>0.05</b>	<b>0.01</b>	<b>0.00</b>	<b>0.02</b>
S.G. e-like 1de	<b>0.05</b>	<b>0.01</b>	<b>0.75</b>	<b>0.10</b>	<b>0.05</b>	<b>0.00</b>	<b>0.01</b>	<b>0.02</b>	<b>0.00</b>	<b>0.01</b>
S.G. e-like 0de	<b>0.73</b>	<b>0.11</b>	<b>0.10</b>	<b>0.01</b>	<b>0.02</b>	<b>0.02</b>	<b>0.00</b>	<b>0.00</b>	<b>0.00</b>	<b>0.00</b>

**Figure 6.8:** The interaction mode contribution of each sample given as a fraction of the total event rate in that sample. Asimov A oscillation parameters are assumed (given in Table 2.2). The Charged Current (CC) modes are broken into quasi-elastic (QE), 2p2h, resonant charged pion production ( $1\pi^\pm$ ), multi-pion production ( $M\pi$ ), and other interaction categories. Neutral Current (NC) interaction modes are given in interaction mode categories:  $\pi^0$  production, resonant charged pion production, multi-pion production, and others.

which the Monte Carlo was generated. Secondly, the set of dial values which are taken from external data measurements and used as inputs. These are the “pre-fit” dial values. The reason these two sets of dial values are different is that the external data measurements are continually updated but it is very computationally intensive to regenerate a Monte Carlo prediction after each update. The final tune is the “post-fit”, “post-ND fit” or “post-BANFF” dial values. These are the values taken from a fit to the beam near detector data. This fit is performed by two independent fitting frameworks, MaCh3 and BANFF, which ensures reliable measurements. The output of each fitter is converted into a covariance matrix to describe the error and correlations between all the flux and cross-section parameters. This is then propagated to the far-detector

2006 oscillation analysis group for use in the P-Theta fitting framework. As MaCh3 can  
2007 perform a near detector fit, it is included within the simultaneous fit of the far-detector  
2008 beam and atmospheric oscillation analysis. This is because this technique does not  
2009 require any assumption of Gaussian posterior distributions which is required in the  
2010 covariance matrix methodology.

2011 On top of the combination of the SK and T2K interaction models, several other  
2012 parameters have been specifically developed for the joint oscillation analysis. The  
2013 majority of the atmospheric samples'  $\delta_{CP}$  sensitivity comes from the normalisation  
2014 of subGeV electron-like events. These are modeled using a spectral function model  
2015 to approximate the nuclear ground state. However, the near detector is not able to  
2016 constrain the model. Therefore, an additional systematic is introduced which models  
2017 an alternative Continous Random Phase Approximation (CRPA) nuclear ground  
2018 state. The reasoning is documented in [205]. As the near detector can not sufficiently  
2019 constrain the model, this dial approximates the event weights if a CRPA model had  
2020 been assumed rather than a spectral function. This dial only effects  $\nu_e$  and  $\bar{\nu}_e$  and is  
2021 applied as a shape parameter.

2022 Further additions to the model have been introduced due to the inclusion of the  
2023 subGeV  $\pi^0$  atmospheric sample. This particularly targets charged current and neutral  
2024 current  $\pi^0$  producing interactions to help constrain the systematic uncertainties. There  
2025 is no analogous sample in the T2K beam-only analysis so no significant effort has  
2026 been placed into building a sufficient uncertainty model. Therefore, an uncertainty  
2027 that affects neutral current resonant  $\pi^0$  production is incorporated into this analysis.  
2028 Comparisons of NEUT's NC resonant pion production predictions have been made to  
2029 MiniBooNE [206] data and a consistent 16% to 21% underprediction is observed [205].  
2030 Consequently, a conservative 30% normalisation parameter is invoked.

2031 Down-going events are mostly insensitive to oscillation parameters and can act  
 2032 similar to the near detector within an accelerator experiment (Details will be dis-  
 2033 cussed in chapter 7). This region of phase space can act as a sideband and allows the  
 2034 cross-section model and near detector constraint to be studied. The distribution of  
 2035 events in this region is calculated using the technique outlined in subsection 4.3.4. For  
 2036 CCQE-targeting samples, the application of the near detector constraint is well within  
 2037 the statistical fluctuation of the down-going data such that no significant tension is  
 2038 observed between the data and the Monte Carlo prediction after the near detector  
 2039 constraint is applied. This is not the case for samples with target CCRES interac-  
 2040 tions. The electron-like data is consistent with the constrained prediction at high  
 2041 reconstructed momenta but diverges at lower momentum, whereas the muon-like  
 2042 sample is under-predicted throughout the range of momenta. To combat this disagree-  
 2043 ment, an additional cross-section systematic dial, specifically designed to inflate the  
 2044 low pion momentum systematics was developed in [205]. This is a shape parameter  
 2045 implemented through a splined response.

#### 2046 6.4.4 Near Detector

2047 The systematics applied due to uncertainties arising from the response of the near  
 2048 detector is documented in [133]. The response is described by 574 normalisation param-  
 2049 eters binned in the selected sample as well as momentum and angle,  $P_\mu$  and  $\cos(\theta_\mu)$ ,  
 2050 of the final-state muon. These are applied via a covariance matrix with each parameter  
 2051 being assigned a Gaussian prior from that covariance matrix. These normalisation  
 2052 parameters are built from underlying systematics, e.g. pion secondary interaction  
 2053 systematics, which are randomly thrown and the variation in each  $P_\mu \times \cos(\theta_\mu)$  bin is  
 2054 determined. Two thousand throws are evaluated and a covariance matrix response is  
 2055 created. This allows significant correlations between FGD1 and FGD2 samples, as well

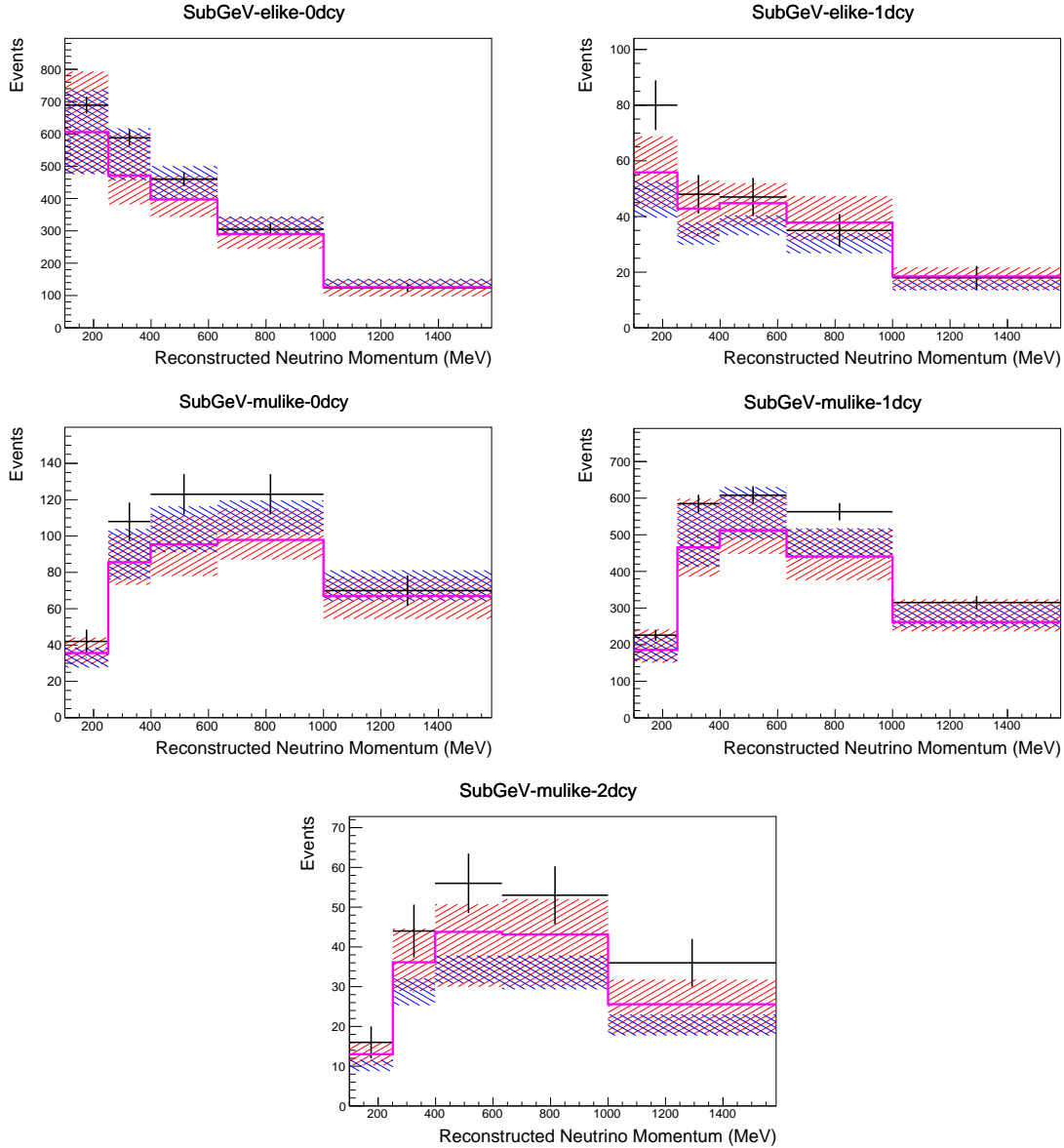


**Figure 6.9:** Down-going atmospheric subGeV single-ring samples comparing the mean and error of the pre-fit and post-fit Monte Carlo predictions in red and blue, respectively. The magenta histogram illustrates the Monte Carlo prediction using the generated dial values. The black points illustrate the down-going data with statistical errors given. The mean and errors of the Monte Carlo predictions are calculated by the techniques documented in subsection 4.3.4. The pre-fit spectrum is calculated by throwing the cross-section and atmospheric flux dial values from the pre-fit covariance matrix. The post-fit spectrum is calculated by sampling the cross-section dial values from an ND fit MCMC chain, whilst still throwing the atmospheric flux dials from the pre-fit covariance.

as adjacent  $P_\mu \times \cos(\theta_\mu)$  bins. Statistical uncertainties are accounted for by including fluctuations of each event's weight from a Poisson distribution.

2058 Similar to the cross-section systematics, MaCh3 and BANFF are used to constrain  
2059 the uncertainty of these systematics through independent validations. Each fitter  
2060 generates a post-fit covariance matrix which is compared and passed to the far-detector  
2061 oscillation analysis working group. As the analysis presented within this thesis uses  
2062 the MaCh3 framework, a joint oscillation analysis fit of all three sets of samples and  
2063 their respective systematics is performed.

2064 **6.4.5 Far Detector**

2065 Two configurations of the far detector systematic model implementation have been  
2066 considered. Firstly, the far detector systematic uncertainties for beam and atmospheric  
2067 samples are taken from their respective analysis inputs, denoted “official inputs” anal-  
2068 ysis. Consequently, no correlations are assumed between the beam and atmospheric  
2069 samples. The generation of the beam- and atmospheric-specific inputs are documented  
2070 in subsubsection 6.4.5.1 and subsubsection 6.4.5.2. Secondly, a correlated detector  
2071 model has been developed. Here, the distribution of parameters used for applying  
2072 event cuts (e.g. electron-muon PID separation) is modified within the fit. It follows  
2073 a similar methodology to the beam far detector systematics implementation but per-  
2074 forms a joint fit of the beam and atmospheric data. This alternative implementation is  
2075 detailed in subsubsection 6.4.5.3.

2076 **6.4.5.1 Beam Samples**

2077 There are 45 systematics which describe the response of the far detector to beam  
2078 events [185], split into 44 normalisation parameters and one energy scale systematic.  
2079 The energy scale systematic is applied as a multiplicative scaling of the reconstructed  
2080 neutrino energy. It is described by a Gaussian, centered at one with equal to the

2081 difference in Monte Carlo to data comparisons performed in [187]. The normalisation  
 2082 parameters are assigned a Gaussian error centralised at one with width taken from a  
 2083 covariance matrix. A detailed breakdown of the generation of the covariance matrix  
 2084 is found in [199]. To build the covariance matrix, a fit is performed on atmospheric  
 2085 data which has been selected using beam sample selection cuts. These cuts use the  
 2086 variables,  $L^i$ , where the index  $i$  is detailed in Table 6.7. Each  $L^i$  is a smear,  $\alpha$ , and shift,  
 2087  $\beta$  parameter such that,

$$L_j^i \rightarrow \bar{L}_j^i = \alpha_j^i L + \beta_j^i \quad (6.4)$$

2088 Where  $L_j^i$  ( $\bar{L}_j^i$ ) correspond to nominal(varied) PID cut parameters given in Table 6.7.  
 2089 The shift and smear parameters are binned by final-state topology,  $j$ , where the binning  
 2090 is given in Table 6.8. The final-state topology binning is because the detector will  
 2091 respond differently to events that have one or multiple rings. For example, the detector  
 2092 will be able to distinguish single-ring events better than two overlapping ring events,  
 2093 resulting in smaller systematic uncertainty for one-ring events compared to two-ring  
 2094 events. This approach is used to allow the cut parameter distributions to be modified  
 2095 within the fit, allowing for better data to Monte Carlo agreement. Only the shape  
 2096 of each of the cut variables is used within this fit, such that physics effects are not  
 2097 considered.

Cut Variable	Parameter Name
0	<code>fitQun e/mu PID</code>
1	<code>fitQun e/pi0 PID</code>
2	<code>fitQun mu/pi PID</code>
3	<code>fitQun Ring-Counting Parameter</code>

**Table 6.7:** List of cut variables that are included within the shift/smear fit documented in [199].

Category	Description
$1e$	Only one electron above Cherenkov threshold in the final state
$1\mu$	Only one muon above Cherenkov threshold in the final state
$1e+other$	One electron and one or more other charged particles above Cherenkov threshold in the final state
$1\mu+other$	One muon and one or more other charged particles above Cherenkov threshold in the final state
$1\pi^0$	Only one $\pi^0$ in the final state
$1\pi^\pm$ or $1p$	Only one hadron (typically charged pion or proton) in the final state
Other	Any other final state

**Table 6.8:** Reconstructed event topology categories on which the SK detector systematics [199] are based.

2098 Beyond the uncertainty on the PID cut criteria, the mis-modeling of  $\pi^0$  events  
 2099 is also considered. If one of the two rings from a  $\pi^0$  event is missed, this will be  
 2100 reconstructed as a  $CC\nu_e$ -like event. This is one of the largest systematics hindering the  
 2101 electron neutrino appearance analyses. Consequently, additional systematics has been  
 2102 introduced to constrain the mis-modeling of  $\pi^0$  events in SK, binned by reconstructed  
 2103 neutrino energy. To evaluate this systematic uncertainty, a set of “hybrid- $\pi^0$ ” samples  
 2104 is constructed. These events are built by overlaying one electron-like ring from the  
 2105 SK atmospheric neutrino samples or decay electron ring from a stopping cosmic ray  
 2106 muon with one simulated photon ring. Both rings are chosen so that momenta and  
 2107 opening angle follow the decay kinematics of NC  $\pi^0$  events from the T2K-MC. Hybrid-  
 2108  $\pi^0$  Monte Carlo samples with both rings from the SK Monte Carlo are produced  
 2109 to compare with the hybrid- $\pi^0$  data samples and the difference in the fraction of  
 2110 events that pass the  $\nu_e$  selection criteria is used to assign the systematic errors. In  
 2111 order to investigate any data to Monte Carlo differences that may originate from  
 2112 either the higher energy ring or lower energy ring, two samples are built; a sample  
 2113 in which the electron constitutes the higher energy ring from the  $\pi^0$  decay called the  
 2114 primary sample and another one in which it constitutes the lower energy ring called

2115 the secondary sample. The standard T2K  $\nu_e$  fiTQun event selection criteria are used to  
2116 select events.

2117 Final contributions to the covariance matrix are determined by supplementary  
2118 uncertainties attained by comparing stopping muon data to Monte Carlo prediction,  
2119 as first introduced in section 5.2. The efficiency of tagging decay electrons is estimated  
2120 by the stopping muon data to Monte Carlo differences by comparing the number  
2121 of one decay electron events to the number of events with one or fewer decay elec-  
2122 trons. Similarly, the rate at which fake decay electrons are reconstructed by fiTQun  
2123 is estimated by comparing the number of two decay electron events to the number  
2124 of events with one or two reconstructed decay electrons. The two sources of sys-  
2125 tematics are added in quadrature weighted by the number of events with one true  
2126 decay electron yielding a 0.2% systematic uncertainty. A fiducial volume systematic of  
2127  $\pm 2.5\text{cm}$  which corresponds to a 0.5% shift in the normalisation of events. Additional  
2128 normalisation uncertainties based on neutrino flavour and interaction mode are also  
2129 defined in [185, 207, 208].

2130 Two additional sources of uncertainty are included: secondary and photo-nuclear  
2131 interactions. These are estimated by varying the underlying parameters are building a  
2132 distribution of sample event rates. These contributions are then added in quadrature  
2133 to the above covariance matrix.

#### 2134 6.4.5.2 Atmospheric Samples

2135 The systematic parameters which control the detector systematics for atmospheric  
2136 samples, documented in [89], are split into two sub-groups. Those which are related  
2137 to particle identification and ring counting systematics and those which are related to  
2138 calibration, separation, and reduction uncertainties.

2139     The particle identification systematics consist of five parameters. The ring separation systematic enforces an anti-correlated response between the single-ring and  
 2140 multi-ring samples. This is implemented as a fractional increase/decrease in the overall normalisation of each sample, depending on the distance to the nearest wall  
 2141 from an event's vertex. The coefficients of the normalisation are estimated prior to the fit and depend on the particular atmospheric sample. The single-ring and multi-ring  
 2142 PID systematics encode the detector's ability to separate electron-like and muon-like  
 2143 events and are implemented in a similar way to the ring separation systematic.

2147     The multi-ring electron-like separation likelihood, discussed in section 6.1, encodes  
 2148 the ability of the detector to separate neutrino from anti-neutrino events. As an important  
 2149 systematic in the mass hierarchy determination, systematic uncertainties control  
 2150 the relative normalisations of the  $\nu_e$  and  $\bar{\nu}_e$  enriched samples. Two normalisation  
 2151 parameters are implemented which vary the event rate of each multi-ring sample,  
 2152 whilst ensuring the total event rate is conserved.

2153     There are 22 systematics related to calibration measurements, including effects  
 2154 from backgrounds, reduction, and showering effects. They are documented in [89] and  
 2155 briefly summarised in Table 6.9. They are applied via normalisation parameters, with  
 2156 the separation systematics requiring the conservation of event rate across all samples.

#### 2157     6.4.5.3 Correlated Detector Model

2158     A complete uncertainty model of the SK detector would be able to determine the  
 2159 systematic shift on the sample spectra for a variation of the underlying parameters,  
 2160 e.g. PMT angular acceptance. However, this is computationally intensive, requiring  
 2161 Monte Carlo predictions to be made for each plausible variation. Consequently, an  
 2162 effective parameter model has been utilised for a correlated detector model following  
 2163 from the T2K-only model implementation documented in subsubsection 6.4.5.1. The

**Table 6.9:** Sources of systematic errors specified within the grouped into the “calibration” systematics model.

Index	Description
0	Partially contained reduction
1	Fully contained reduction
2	Separation of fully contained and partially contained events
3	Separation of stopping and through-going partially contained events in top of detector
4	Separation of stopping and through-going partially contained events in barrel of detector
5	Separation of stopping and through-going partially contained events in bottom of detector
6	Background due to cosmic rays
7	Background due to flasher events
8	Vertex systematic moving events into and out of fiducial volume
9	Upward going muon event reduction
10	Separation of stopping and through-going in upward going muon events
11	Energy systematic in upward going muon events
12	Reconstruction of the path length of upward going muon events
13	Separation of showering and non-showering upward going muon events
14	Background of stopping upward going muon events
15	Background of non-showering through-going upward going muon events
16	Background of showering through-going upward going muon events
17	Efficiency of tagging two rings from $\pi^0$ decay
18	Efficiency of decay electron tagging
19	Background from downgoing cosmic muons
20	Asymmetry of energy deposition in tank
21	Energy scale deposition

<sup>2164</sup> implementation performs a simultaneous fit of detector and oscillation parameters,  
<sup>2165</sup> for the detector parameters given in Table 6.7.

<sup>2166</sup> The correlated detector model utilises the same smear and shift parameters docu-  
<sup>2167</sup> mented in subsubsection 6.4.5.1, split by final state topology. Beyond this, the shift  
<sup>2168</sup> and smear parameters are split by visible energy deposited within the detector, with

2169 binning specified in Table 6.10. This is because atmospheric events are categorised  
2170 by subGeV and multiGeV events based on visible energy, so this splitting is required  
2171 when correlating the systematic model for beam and atmospheric events. Alongside  
2172 the technical requirement, higher energy events will be better reconstructed due to  
2173 fractionally less noise within the detector. This implementation correlates the detector  
2174 systematics between the far-detector beam and subGeV atmospheric samples due  
2175 to their similar energies and interaction types. As a result of the inclusion of visible  
2176 energy binning, Equation 6.4 becomes

$$L_{jk}^i \rightarrow \bar{L}_{jk}^i = \alpha_{jk}^i L + \beta_{jk}^i, \quad (6.5)$$

2177 where  $k$  is the visible energy bin. As there are no equivalent beam samples, the  
2178 multiGeV, multiring, PC, and Up- $\mu$  samples will be subject to the ATMPD particle  
2179 identification systematics implementation as described in subsubsection 6.4.5.2 rather  
2180 than using this correlated detector model. The calibration systematics also described  
2181 in the aforementioned chapter still apply to all atmospheric samples.

Index	Range (MeV)
0	$30 \geq x > 300$
1	$300 \geq x > 700$
2	$700 \geq x > 1330$
3	$1330 \geq x$

**Table 6.10:** Visible energy binning for which the correlated SK detector systematics are based

2182 The implementation of this systematic model takes the events reconstructed values  
2183 of the cut parameters, modifies them by the particular shift and smear parameter for  
2184 that event, and then re-applies event selection. This invokes event migration, which is

2185 a new feature incorporated into the MaCh3 framework which is only achievable due  
2186 to the event-by-event reweighting scheme.

2187 Particular care has to be taken when varying the ring counting parameter. This  
2188 is because the number of rings is a finite value (one-ring, two-rings, etc.) which can  
2189 not be continuously varied through this shift and smear technique. Consequently a  
2190 ring counting parameter,  $RC_i$ , is calculated for the  $i^{th}$  event, following the definition  
2191 in [184]. The likelihood from all considered one-ring ( $L_{1R}$ ) and two-ring ( $L_{2R}$ ) fits  
2192 are compared to determine the preferred hypothesis. The difference is computed as  
2193  $\Delta_{LLH} = \log(L_{1R}) - \log(L_{2R})$ . The ring counting parameter is then defined as,

$$RC_i = \text{sgn}(\Delta_{LLH}) \times \sqrt{|\Delta_{LLH}|}, \quad (6.6)$$

2194 where  $\text{sgn}(x) = x/|x|$ . This ring counting parameter corresponds to an intermedi-  
2195 ate likelihood value used within the `fitQun` algorithm to decide the number of rings  
2196 associated with a particular event. However, fake-ring merging algorithms are applied  
2197 after this likelihood value is used. Consequently, this ring counting parameter does  
2198 not always exactly correspond to the number of reconstructed rings. This can be seen  
2199 in Figure 6.10.

2200 As the `fitQun` algorithm does not provide a likelihood value after the fake-ring  
2201 algorithms have been applied, the ring counting parameter distribution is correlated to  
2202 the final number of reconstructed rings through “maps”. These are two-dimensional  
2203 distributions of the ring counting parameter and the final number of reconstructed  
2204 rings. An example is illustrated in Figure 6.11. In principle, the `fitQun` reconstruction  
2205 algorithm should be re-run after the variation in the ring counting parameter. However,

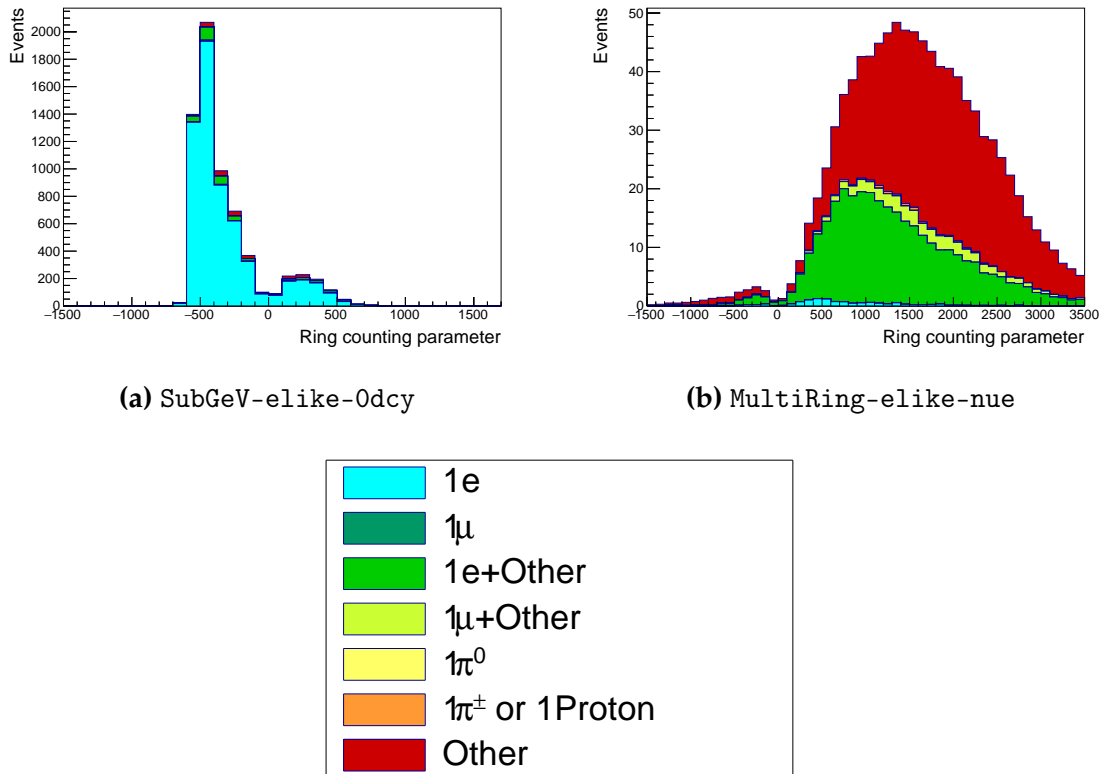


**Figure 6.10:** The ring counting parameter as defined in Equation 6.6 for the SubGeV-*elike*-0dcy and MultiRing-*elike*-*nue* samples.

<sup>2206</sup> this is not computationally viable. Therefore the “maps” are used as a reweighting  
<sup>2207</sup> template.

The maps are split by final state topology and true neutrino flavour and all fitQun  
 -reconstructed Monte Carlo events are used to fill them. The maps are row-normalised  
 to represent the probability of X number of rings for a given  $RC_i$  value. Prior to the  
 fit, an event's nominal weight is calculated as  $W^i(N_{Rings}^i, L_{jk}^i)$ , where  $N_{Rings}^i$  is the  
 reconstructed number of rings for the  $i^{th}$  event and  $W^i(x, y)$  is the bin content in map  
 associated with the  $i^{th}$  event, where  $x$  number of rings and  $y$  is ring counting parameter.  
 Then during the fit, the value of  $R = W^i(N_{Rings}^i, \bar{L}_{jk}^i) / W^i(N_{Rings}^i, L_{jk}^i)$  is calculated as  
 the event weight for the  $i^{th}$  event. This is the only cut variable that uses a reweighting  
 scheme rather than event migration.

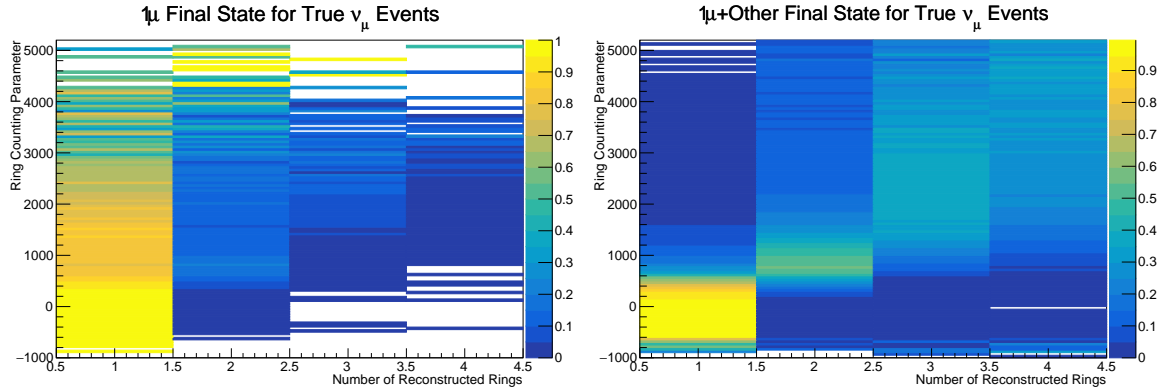


**Figure 6.11:** The ring counting parameter, defined in Equation 6.6, as a function of the number of reconstructed rings as found by the `fitQun` reconstruction algorithm. Left: true  $\nu_\mu$  events with only one muon above the Cherenkov threshold in the final state. Right: true  $\nu_\mu$  events with one muon and at least one other charged particle above the Cherenkov threshold in the final state.

2217     The  $\pi^0$  systematics introduced in subsection 6.4.4 are applied via a covariance  
 2218     matrix. This is not possible in the alternative model as no covariance matrix is used.  
 2219     Thus, the implementation of the  $\pi^0$  systematics has been modified. The inputs from  
 2220     the hybrid  $\pi^0$  sample is included via the use of “ $\chi^2$  maps”, which are two-dimensional  
 2221     histograms in  $\alpha_{jk}^i$  and  $\beta_{jk}^i$  parameters over some range. Illustrative examples of the  $\chi^2$   
 2222     maps are given in Figure 6.12. Due to their nature, the shift and smear parameters are  
 2223     typically very correlated. A map is produced for each cut parameter given in Table 6.7  
 2224     and for each visible energy bin given in Table 6.10.

2225     The maps are filled through the  $\chi^2$  comparison of the hybrid  $\pi^0$  Monte Carlo and  
 2226     data in the particle identification parameters documented in Table 6.7. The Monte  
 2227     Carlo distribution is modified by the  $\alpha_{jk}^i$  and  $\beta_{jk}^i$  scaling, whilst cross-section and flux  
 2228     nuisance parameters are thrown from their prior uncertainties. The  $\chi^2$  between the  
 2229     scaled Monte Carlo and data is calculated and the relevant point in the  $\chi^2$  map is filled.

2230     The implementation within this alternative detector model is to add the bin contents  
 2231     of the maps, for the relevant values of the  $\alpha_{jk}^i$  and  $\beta_{jk}^i$  parameters, to the likelihood  
 2232     penalty. Only  $1\pi^0$  final state topology shift and smear parameters use this prior  
 2233     uncertainty.

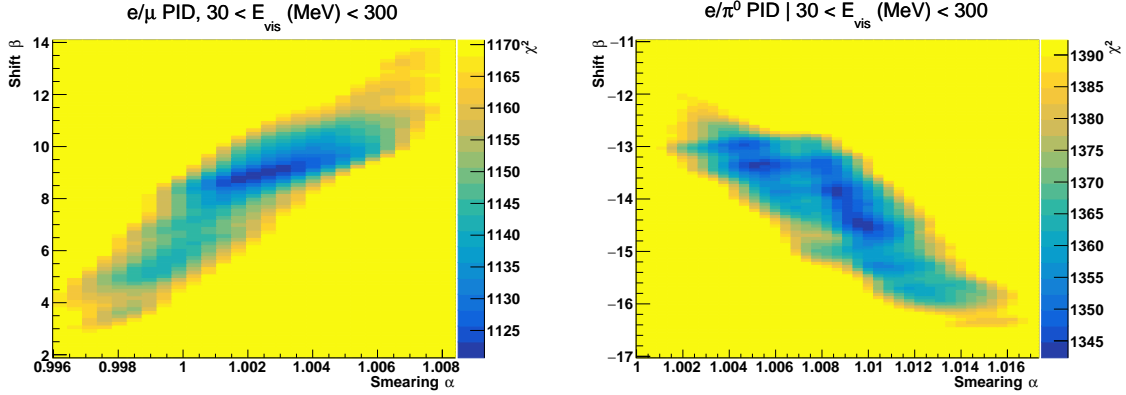


**Figure 6.12:** The  $\chi^2$  between the hybrid- $\pi^0$  Monte Carlo and data samples, as a function of smear ( $\alpha$ ) and shift ( $\beta$ ) parameters, for events which have  $1\pi^0$  final state topology. Left: Electron-muon separation PID parameter for events with  $30 \geq E_{vis}(\text{MeV}) < 300$ . Right: Electron- $\pi^0$  separation PID parameter for events with  $30 \geq E_{vis}(\text{MeV}) < 300$ .

2234 Similarly, the implementation of the supplementary systematics documented in  
 2235 subsubsection 6.4.5.1 needs to be modified. A new framework [209] was built in  
 2236 tandem with the T2K-SK working group [185] so the additional parameters can be  
 2237 incorporated into the MaCh3 framework. These are applied as normalisation parame-  
 2238 ters, depending on the particular interaction mode, number of tagged decay electrons,  
 2239 and whether the primary particle generated Cherenkov light. They are assigned  
 2240 Gaussian uncertainties with widths described by a covariance matrix. Furthermore,  
 2241 the secondary interaction and photo-nuclear effects need to be accounted for in this  
 2242 detector model using a different implementation than that in subsubsection 6.4.5.1.  
 2243 This was done by including a shape parameter for each of the secondary interactions  
 2244 and the photo-nuclear systematic parameters.

2245 There are a total of 224  $\alpha_{jk}^i$  and  $\beta_{jk}^i$  parameters, of which 32 have prior constraints  
 2246 from the hybrid  $\pi^0$  samples.

2247 One final complexity of this correlated detector model is that the two sets of sam-  
 2248 ples, beam and subGeV atmospheric, use slightly different parameters to distinguish  
 2249 electron and muon-like events. The T2K samples use the value of  $\log(L_e/L_\mu)$  whereas  
 2250 the atmospheric samples use the value of  $\log(L_e/L_\pi)$ , where  $L_X$  is the likelihood for

2251 hypothesis X. This is because the T2K fits use single-ring `fitQun` fitting techniques,  
 2252 whereas multi-ring fits are applied to the atmospheric samples where only the electron  
 2253 and pion hypothesis are considered. The correlation between the two likelihood ratios  
 2254 is illustrated in Figure 6.13. As discussed in section 5.2, the pion hypothesis is a very  
 2255 good approximation of the muon hypothesis due to their similar mass. Consequently,  
 2256 using the same shift and smear parameters correlated between the beam and subGeV  
 2257 atmospheric samples is deemed a good approximation.

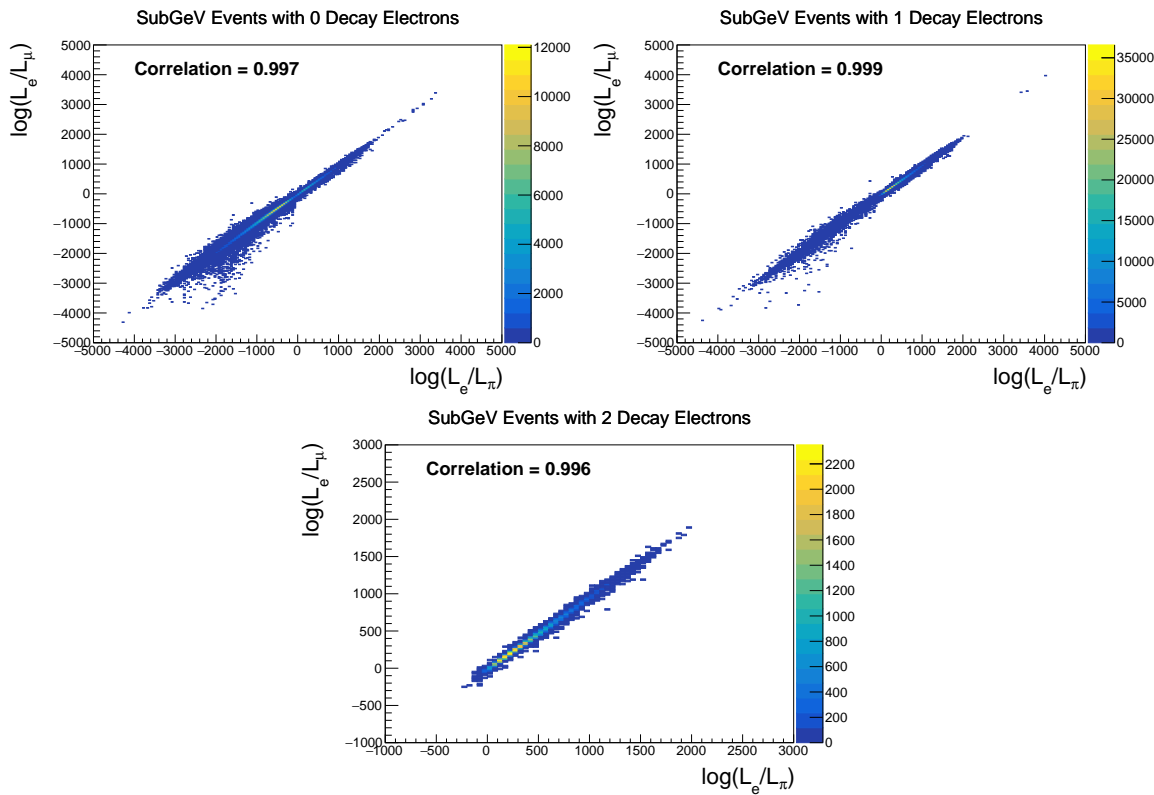


**Figure 6.13:** The distribution of  $\log(L_e/L_\mu)$  compared to  $\log(L_e/L_\pi)$  for subGeV events with zero (top left), one (top right) or two (bottom) decay electrons. The correlation in the distribution is calculated as 0.997, 0.999 and 0.996, respectively.

2258

# Chapter 7

2259

## Oscillation Probability Calculation

2260 It is important to understand how and where the sensitivity to the oscillation pa-  
2261 rameters comes from for both atmospheric and beam samples. An overview of how  
2262 these samples observe changes in  $\delta_{CP}$ ,  $\Delta m_{23}^2$ , and  $\sin^2(\theta_{23})$  is given in section 7.1. It  
2263 also explains the additional complexities involved when performing an atmospheric  
2264 neutrino analysis as compared to a beam-only analysis.

2265 Without additional techniques, atmospheric sub-GeV upward-going neutrinos  
2266 ( $E_\nu < 1.33\text{GeV}, \cos(\theta_Z) < 0.$ ) can artificially inflate the sensitivity to  $\delta_{CP}$  due to the  
2267 quickly varying oscillation probability in this region. Therefore, a “sub-sampling”  
2268 approach has been developed to reduce these biases ensuring accurate and reliable  
2269 sensitivity measurements. This technique ensures that small-scale unresolvable fea-  
2270 tures of the oscillation probability have been averaged over whilst the large-scale  
2271 features in the oscillation probability are unaffected. The documentation and valida-  
2272 tion of this technique are found in section 7.2. The oscillation probability calculation is  
2273 computationally intensive due to the large number of matrix multiplications needed.  
2274 Consequently, the CUDAProb3 implementation choice made within the fitting frame-  
2275 work, as detailed in section 7.3, ensures that the analysis can be done in a timely  
2276 manner.

2277 Whilst the beam neutrinos are assumed to propagate through a constant density  
2278 slab of material, the density variations through the Earth result in more complex  
2279 oscillation patterns. Furthermore, the uncertainty in the electron density can modify  
2280 the oscillation probability for the denser core layers of the Earth. The model of the

2281 Earth used within this analysis is detailed in section 7.4. This includes information  
2282 about the official SK-only methodology as well as improvements that can be made  
2283 to remove some of the approximations made in that analysis. Another complexity of  
2284 atmospheric neutrinos oscillation studies is that the height of production in the atmo-  
2285 sphere is not known on an event-by-event basis. An analytical averaging technique  
2286 that approximates the uncertainty of the oscillation probability has been followed,  
2287 with the author of this thesis being responsible for the implementation and validation.  
2288 This implementation of an external technique is illustrated in section 7.5.

## 2289 7.1 Overview

2290 DB: Should this be moved into an earlier chapter? The selections chapter references  
2291 the matter resonance which has not yet been explained at that point

2292 The analysis presented within this thesis focuses on the determination of oscillation  
2293 parameters from atmospheric and beam neutrinos. Whilst subject to the same oscil-  
2294 lation formalism, the way in which the two samples have sensitivity to the different  
2295 oscillation parameters differs quite significantly.

2296 Atmospheric neutrinos have a varying baseline, or “path length”,  $L$ , such that  
2297 the distance each neutrino travels before interacting is dependent upon the zenith  
2298 angle,  $\theta_Z$ . As primary cosmic rays can interact anywhere between the Earth’s surface  
2299 and  $\sim 50\text{km}$  above that, the height,  $h$ , in the atmosphere at which the neutrino was  
2300 generated also affects the path length,

$$L = \sqrt{(R_E + h)^2 - R_E^2 (1 - \cos^2(\theta_Z))} - R_E \cos(\theta_Z). \quad (7.1)$$

2301 Where  $R_E = 6,371\text{km}$  is the Earth's radius. Consequently, the oscillation probability  
2302 is dependent upon two parameters,  $\cos(\theta_Z)$  and  $E_\nu$ .

2303 The oscillation probability used within this analysis is based on [21]. The neutrino  
2304 wavefunction in the vacuum Hamiltonian evolves in each layer of constant matter  
2305 density via

$$i \frac{d\psi_j(t)}{dt} = \frac{m_j^2}{2E_\nu} \psi_j(t) - \sum_k \sqrt{2} G_F N_e U_{ej} U_{ke}^\dagger \psi_k(t), \quad (7.2)$$

2306 where  $m_j^2$  is the square of the  $j^{th}$  vacuum eigenstate mass,  $E_\nu$  is the neutrino  
2307 energy,  $G_F$  is Fermi's constant,  $N_e$  is the electron number density and  $U$  is the PMNS  
2308 matrix. The transformation  $N_e \rightarrow -N_e$  and  $\delta_{CP} \rightarrow -\delta_{CP}$  is applied for antineutrino  
2309 propagation. Thus, a model of the Earth's density is required for atmospheric neutrino  
2310 propagation. Following the official SK-only methodology [210], this analysis uses the  
2311 Preliminary Reference Earth Model (PREM) [211]. This model provides piecewise cubic  
2312 polynomials as a function of the Earth's radius which results in the density profile  
2313 illustrated in Figure 7.1. As discussed, the propagator requires layers of constant  
2314 density. The SK methodology approximates the PREM model by using four layers of  
2315 constant density [210]. The details of these layers are detailed in Table 7.1.

Layer	Outer Radius [km]	Density [ $\text{g}/\text{cm}^3$ ]	Chemical composition (Z/A)
Inner Core	1220	13	$0.468 \pm 0.029$
Outer Core	3480	11.3	$0.468 \pm 0.029$
Lower Mantle	5701	5.0	0.496
Transition Zone	6371	3.3	0.496

**Table 7.1:** Description of the four layers of the Earth invoked within the constant density approximation of the PREM model [211].

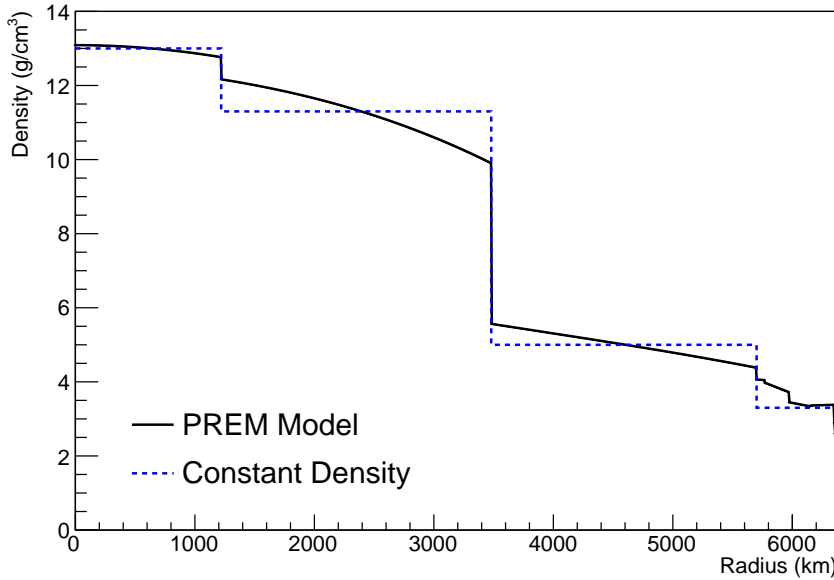


**Figure 7.1:** The density of the Earth given as a function of the radius, as given by the PREM model (Black), and the constant density four-layer approximation (Blue), as used in the official SK-only analysis.

2316        The atmospheric neutrino oscillation probabilities can be presented as two dimen-  
 2317        sional “oscillograms” as illustrated in Figure 7.2. The distinct discontinuities, as a  
 2318        function of  $\cos(\theta_Z)$ , are due to the discrete change in density invoked within the PREM  
 2319        model.

2320        Atmospheric neutrinos do have sensitivity to  $\delta_{CP}$  through a normalisation term.  
 2321        Figure 7.3 illustrates the difference in oscillation probability between CP-conserving  
 2322        ( $\delta_{CP} = 0$ ) and a CP-violating ( $\delta_{CP} = -1.601$ ) value taken from Asimov A oscillation  
 2323        parameter set (Table 2.2). The result is a complicated oscillation pattern in the appear-  
 2324        ance probability for sub-GeV upgoing neutrinos. The detector does not have sufficient  
 2325        resolution to resolve these individual patterns so the sensitivity to  $\delta_{CP}$  for atmospheric  
 2326        neutrinos comes via the overall normalisation of these events.

2327        The presence of matter means that the effect  $\delta_{CP}$  has on the oscillation probability  
 2328        is not equal between neutrinos and antineutrinos, which would be expected when  
 2329        propagating through a vacuum. This is further extenuated by the fact that SK can

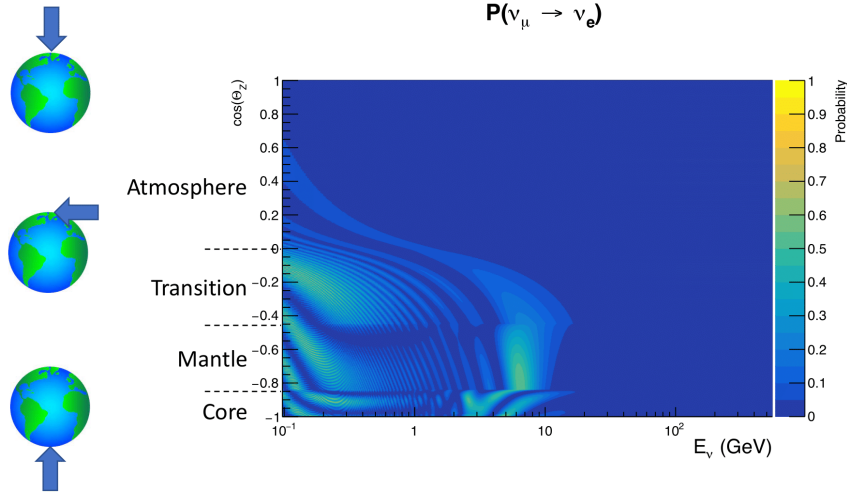


**Figure 7.2:** An “oscillogram” that depicts the  $P(\nu_\mu \rightarrow \nu_e)$  oscillation probability as a function of neutrino energy and cosine of the zenith angle. The zenith angle is defined such that  $\cos(\theta_Z) = 1.0$  represents neutrinos that travel from directly above the detector. The four-layer constant density PREM model approximation is used and Asimov A oscillation parameters are assumed (Table 2.2).

not distinguish neutrinos and antineutrinos well and that the cross-section neutrino interaction is larger than that for antineutrinos. Finally, sample selections (discussed in section 6.1) targeting different neutrino interaction modes result in an imbalance in the percentage of neutrinos to anti-neutrinos. This is because negatively charged pions from antineutrino interactions are more likely to be captured by a nucleus compared to a positively charged pion. All of these effects lead to a difference in the number of neutrinos detected compared to antineutrinos. This changes how the  $\delta_{CP}$  normalisation term is observed, resulting in a very complex sensitivity to  $\delta_{CP}$ .

Atmospheric neutrinos are subject to matter effects as they travel through the dense matter in the Earth. The vacuum and matter oscillation probabilities for  $P(\nu_e \rightarrow \nu_e)$  and  $P(\bar{\nu}_e \rightarrow \bar{\nu}_e)$  are presented in Figure 7.4, where the PREM model has been assumed. The oscillation probability for both neutrinos and antineutrinos is affected in the presence of matter. However, the resonance effects around  $O(5)\text{GeV}$  only occur for neutrinos in normal mass hierarchy and antineutrinos in inverse mass hierarchy. The

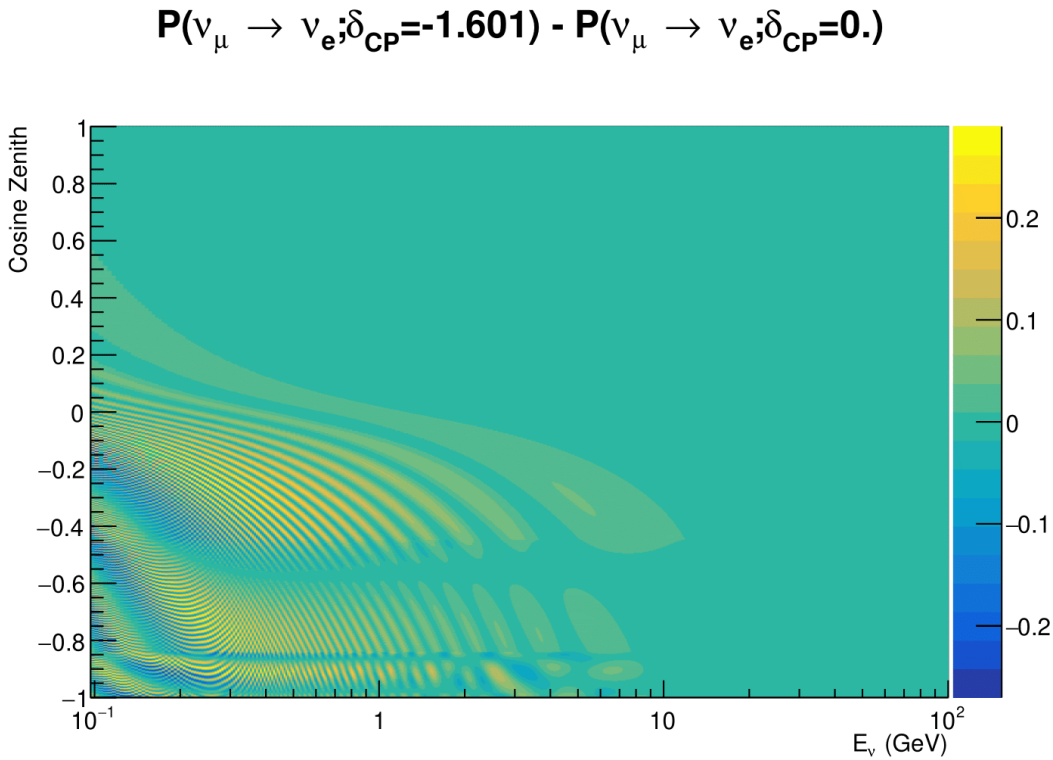


**Figure 7.3:** The effect of  $\delta_{CP}$  for atmospheric neutrinos given in terms of the neutrino energy and zenith angle. This oscillogram compares the  $P(\nu_\mu \rightarrow \nu_e)$  oscillation probability for a CP conserving ( $\delta_{CP} = 0.0$ ) and a CP violating ( $\delta_{CP} = -1.601$ ) value taken from the Asimov A parameter set. The other oscillation parameters assume the Asimov A oscillation parameter set given in Table 2.2.

<sup>2344</sup> exact position and amplitude of the resonance depend on  $\sin^2(\theta_{23})$  meaning that the  
<sup>2345</sup> atmospheric neutrinos have sensitivity to  $\sin^2(\theta_{23})$ .

<sup>2346</sup> As the T2K beam flux is centered at the first oscillation maximum ( $E_\nu = 0.6\text{GeV}$ ),  
<sup>2347</sup> the sensitivity to  $\delta_{CP}$  is predominantly observed as a change in the event-rate of e-like  
<sup>2348</sup> samples in  $\nu/\bar{\nu}$  modes. Figure 7.5 illustrates the  $P(\nu_\mu \rightarrow \nu_e)$  oscillation probability  
<sup>2349</sup> for a range of  $\delta_{CP}$  values. A circular modulation of the first oscillation peak (in both  
<sup>2350</sup> magnitude and position) is observed when varying throughout the allowable values  
<sup>2351</sup> of  $\delta_{CP}$ . The CP-conserving values of  $\delta_{CP} = 0, \pi$  have a lower(higher) oscillation  
<sup>2352</sup> maximum than the CP-violating values of  $\delta_{CP} = -\pi/2(\delta_{CP} = \pi/2)$ . A sub-dominant

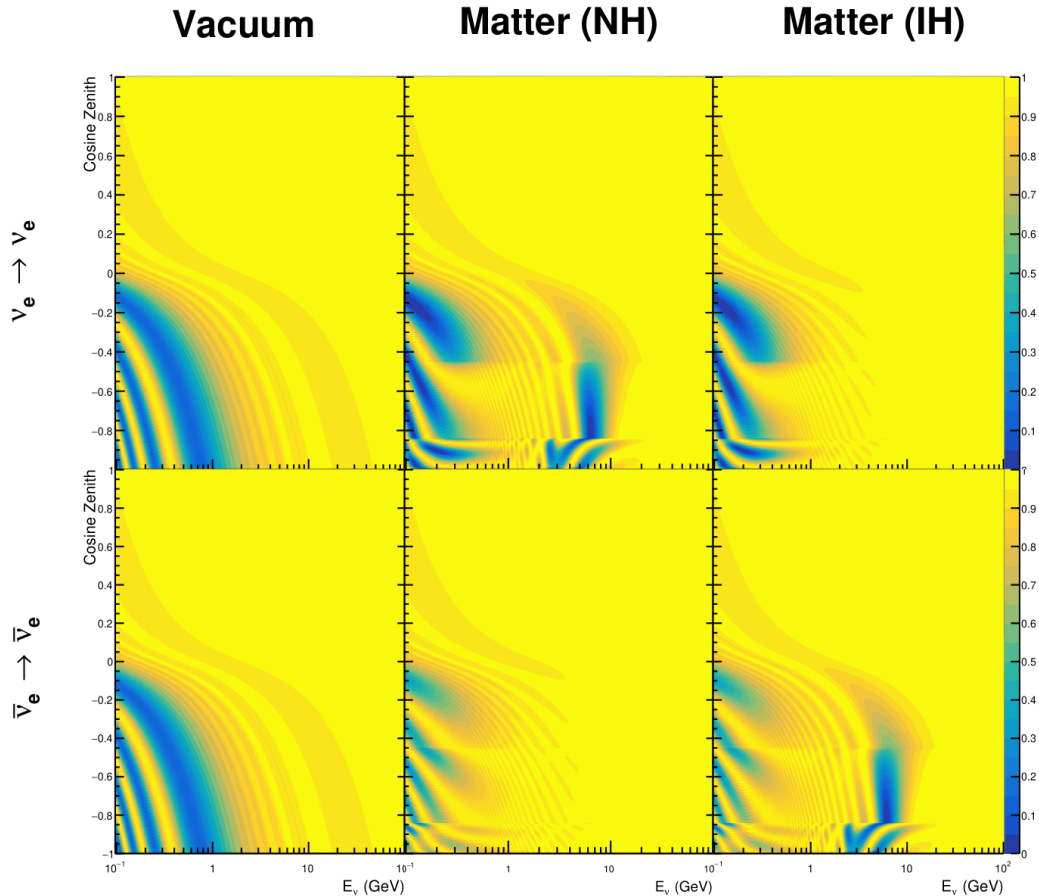


**Figure 7.4:** An illustration of the matter-induced effects on the oscillation probability, given as a function of neutrino energy and zenith angle. The top row of panels gives the  $P(\nu_e \rightarrow \nu_e)$  oscillation probability and the bottom row illustrates the  $P(\bar{\nu}_e \rightarrow \bar{\nu}_e)$  oscillation probability. The left column highlights the oscillation probability in a vacuum, whereas the middle and right column represents the oscillation probabilities when the four-layer fixed density PREM model is assumed. All oscillation probabilities assume the “Asimov A” set given in Table 2.2, but importantly, the right column sets an inverted mass hierarchy. The “matter resonance” effects at  $E_\nu \sim 5\text{GeV}$  can be seen in the  $P(\nu_e \rightarrow \nu_e)$  for normal mass hierarchy and  $P(\bar{\nu}_e \rightarrow \bar{\nu}_e)$  for inverted hierarchy.

shift in the energy of the oscillation peak is also present to aid in separating the two  
 CP-conserving values of  $\delta_{CP}$ .

T2K’s sensitivity to the  $\sin^2(\theta_{23})$  and  $\Delta m_{23}^2$  is observed as a shape-based variation  
 of the muon-like samples, as illustrated in Figure 7.5. The value of  $\Delta m_{32}^2$  laterally shifts  
 the position of the oscillation dip (around  $E_\nu \sim 0.6\text{GeV}$ ) in the  $P(\nu_\mu \rightarrow \nu_\mu)$  oscillation

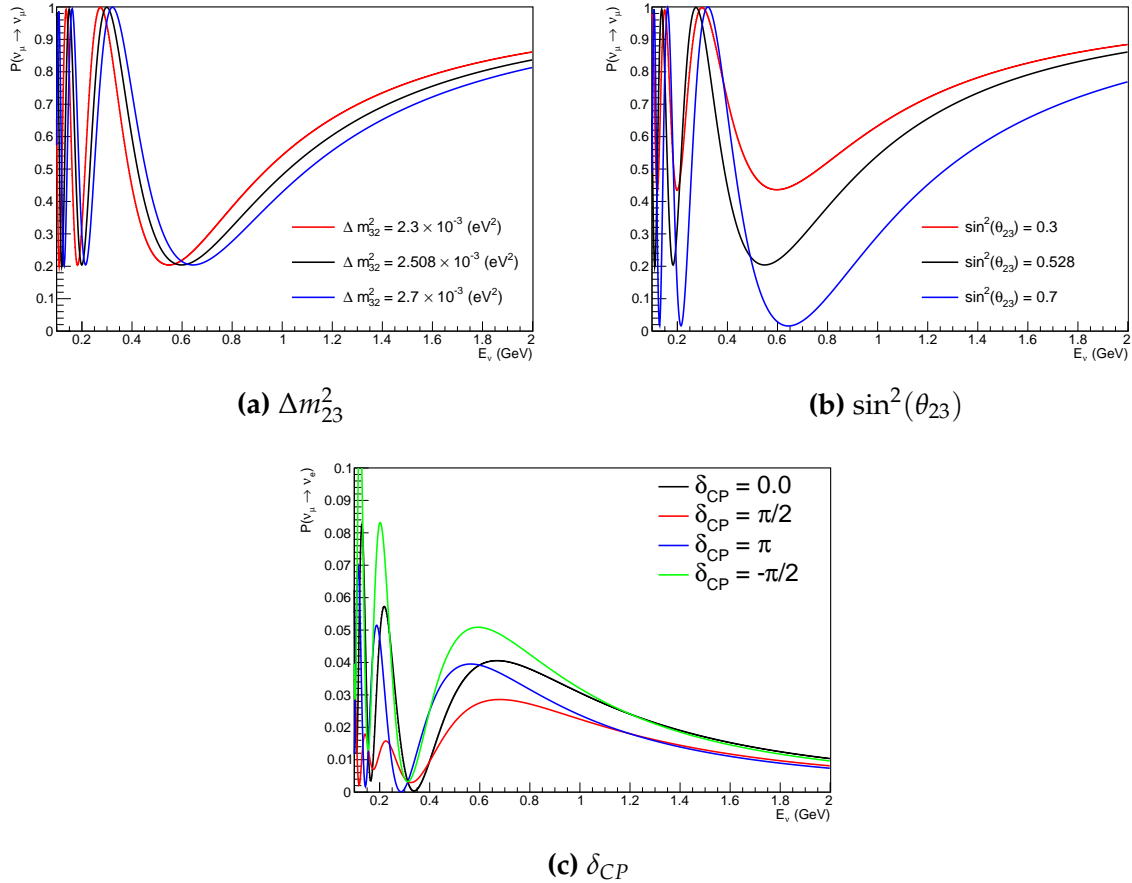


**Figure 7.5:** The oscillation probability for beam neutrino events given as a function of neutrino energy. All oscillation parameters assume the “Asimov A” set given in Table 2.2 unless otherwise stated. Each panel represents a change in one of the oscillation parameters whilst keeping the remaining parameters fixed.

probability. A variation of  $\sin^2(\theta_{23})$  is predominantly observed as a vertical shift of the oscillation dip with second-order horizontal shifts being due to matter effects. The beam neutrinos have limited sensitivity to matter effects due to the relatively shorter baseline as well as the Earth’s mantle being a relatively low-density material (as compared to the Earth’s core). For some values of  $\delta_{CP}$ , the degeneracy in the number of e-like events allows the mass hierarchy to be resolved. This leads to a  $\delta_{CP}$ -dependent mass hierarchy sensitivity which can be seen in Figure 7.6.

Whilst all oscillation channels should be included for completeness, the computational resources required to run a fit are limited and any reasonable approximations

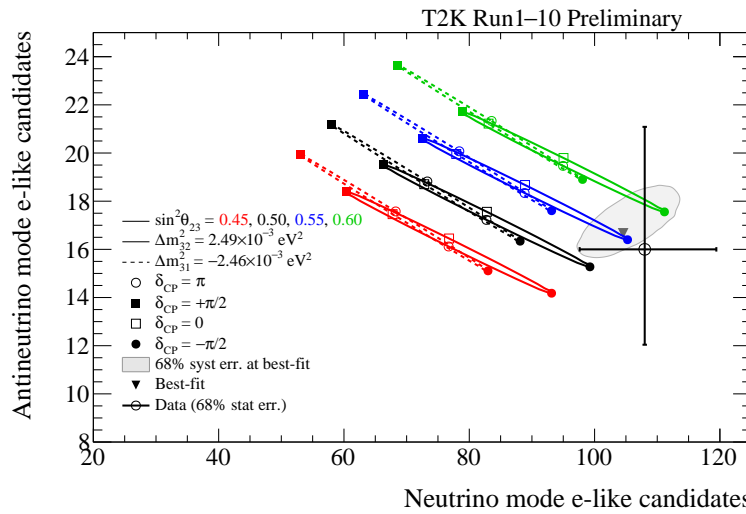


**Figure 7.6:** The number of electron-like events in the FHC and RHC operating mode of the beam, as a function of the oscillation probabilities. Both normal hierarchy (Solid) and inverse hierarchy (Dashed) values of  $\Delta m_{23}^2$  are given.

which reduce the number of oscillation probability calculations that need to be made should be applied. The  $\nu_e \rightarrow \nu_{e,\mu,\tau}$  (and antineutrino equivalent) oscillations can be ignored for beam neutrinos as the  $\nu_e/\bar{\nu}_e$  fluxes are approximately two orders of magnitude smaller than the corresponding  $\nu_\mu/\bar{\nu}_\mu$  flux. Furthermore, as the peak neutrino energy of the beam is well below the threshold for charged current tau production ( $E_\nu = 3.5\text{GeV}$  [51], only a small proportion of the neutrinos produced in the beam have the required energy. For the few neutrinos that have sufficient energy, the oscillation probability is very small due to the short baseline. Whilst these approximations can be made for the beam neutrinos, the atmospheric flux of  $\nu_e$  is of the same order of magnitude as the  $\nu_\mu$  flux and the energy distribution of atmospheric neutrinos extends well above the tau production threshold.

## 2378 7.2 Treatment of Fast Oscillations

2379 As shown in Figure 7.7, atmospheric neutrino oscillations have a significantly more  
2380 complex structure for upgoing neutrinos with energy below 1GeV. This is because the  
2381  $L/E$  dependence of the oscillation probability in this region induces rapid variations  
2382 for small changes in  $L$  or  $E$ . As discussed in section 7.1, this is also the region in which  
2383 atmospheric neutrinos have sensitivity to  $\delta_{CP}$ . In practice, the direction of the neutrino  
2384 is inferred from the direction of the final state particles traveling in the detector, which  
2385 can be poor for low-energy neutrino interactions. This creates a distinct difference  
2386 from the beam neutrinos where the position of the source is very precisely known.

2387 As a consequence of the unresolvable structure, an average oscillation probability  
2388 is observed in the subGeV upgoing region. This creates a computational problem; A  
2389 significantly large amount of Monte Carlo statistics would be required to accurately  
2390 predict the number of events if Monte Carlo averaging was the only technique used.  
2391 This section describes the ‘sub-sampling’ approach developed for this analysis and  
2392 compares it to the methodology used within the SK-only analysis.

2393 The official SK-only analysis uses the osc3++ oscillation parameter fitter [210].  
2394 To perform the fast oscillation averaging, it uses a ‘nearest-neighbour’ technique.  
2395 For a given neutrino event, the nearest twenty neighbours in reconstructed lepton  
2396 momentum and zenith angle are found and a distribution of their neutrino energies is  
2397 built. The RMS,  $\sigma$ , of this distribution is then used to compute an average oscillation  
2398 probability for the given neutrino Monte Carlo event.

2399 For the  $i^{th}$  event, the oscillation weight is calculated as

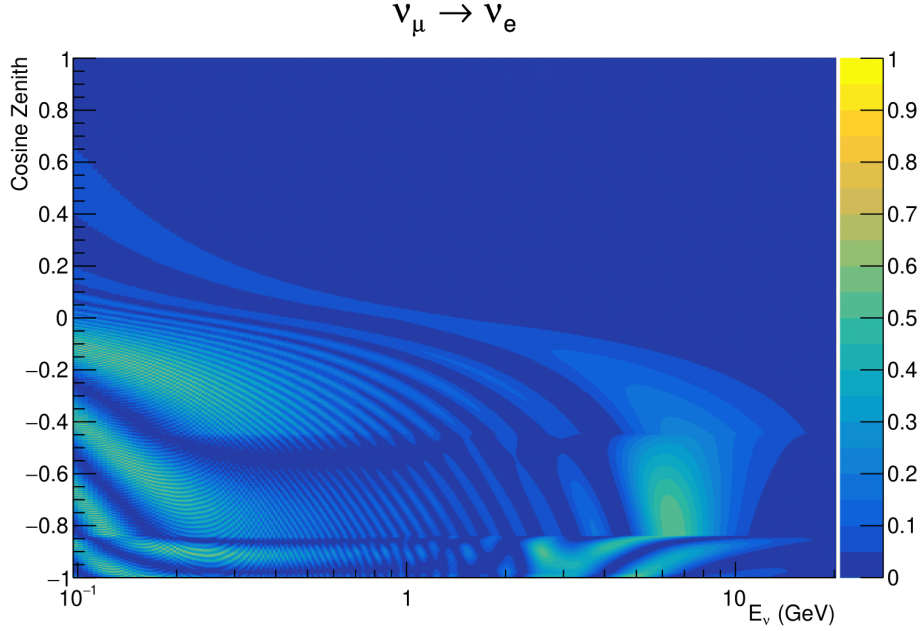


**Figure 7.7:** The oscillation probability  $P(\nu_\mu \rightarrow \nu_e)$ , given as a function of neutrino energy and zenith angle, which highlights an example of the “fast” oscillations in the sub-GeV upgoing region.

$$W_i = \frac{1}{5}P(E_i, \bar{L}_i) + \frac{1}{5} \sum_{\beta=-1,-0.5,0.5,1} P(E_i + \beta\sigma_i, L_\beta), \quad (7.3)$$

where  $P(E, L)$  is the oscillation probability calculation for neutrino energy  $E$  and path length  $L$  and the two path lengths,  $\bar{L}_i$  and  $L_\beta$  are discussed below. All of the oscillation probability calculations are performed with a fixed zenith angle such that the same density profile is used.

The uncertainty in the production height is controlled by using an “average” production height,  $\bar{L}_i$ , which represents the average path length computed using twenty production heights taken from the Honda flux model’s prediction [45]. For a given event, the production heights are sampled in steps of 5% of their cumulative distribution function.  $L_\beta$  values are similarly calculated but instead use different combinations of four production heights,

$$\begin{aligned}
 L_{-1.0} &= \frac{1}{4}L(45, 50, 55, 60), \\
 L_{-0.5} &= \frac{1}{4}L(35, 40, 65, 70), \\
 L_{+0.5} &= \frac{1}{4}L(25, 30, 75, 68), \\
 L_{+1.0} &= \frac{1}{4}L(15, 20, 85, 89).
 \end{aligned} \tag{7.4}$$

2410 This averaging technique works because of the inference between the zenith angle  
 2411 and the reconstructed direction of final state particles in the detector. For low-energy  
 2412 neutrinos, where the resolution of the true neutrino direction is poor,  $\sigma_i$  will be large,  
 2413 resulting in significant averaging effects. Contrary to this, the inferred direction of  
 2414 high-energy neutrinos will be much closer to the true value, meaning that  $\sigma_i$  will be  
 2415 smaller, culminating in small averaging effects.

2416 In practice, this technique is performed before the fit in order to deal with the  
 2417 computational cost. This is possible as the Osc3++ framework uses binned oscillation  
 2418 parameters rather than continuous so the oscillation parameters used in the fit are  
 2419 known prior to run-time. The framework used in this analysis uses continuous  
 2420 oscillation parameters, and due to the MCMC fitting technique, there is no way to  
 2421 know which oscillation parameter values will be selected *a priori*. Therefore, the  
 2422 oscillation parameter calculation has to be performed at run-time. Computing five  
 2423 oscillation probabilities per event would require far too many computational resources  
 2424 to be viable. Therefore SK technique can not be used within this analysis. However,  
 2425 the concept of the averaging technique can be taken from it.

2426 To perform a similar averaging as the SK analysis, a sub-sampling approach using  
 2427 binned oscillograms has been devised. The technique can be explained by considering  
 2428 a “fine” and “coarse” oscillogram. The fine oscillograms are used to define the array of

2429  $\cos(\theta_Z)$  and  $E_\nu$  used in the oscillation engine. The coarse oscillograms cover the same  
2430 phase-space but have fewer bins, where the value of a particular coarse bin is taken  
2431 as the linear average (flat prior in  $E_\nu$  and  $\cos(\theta_Z)$ ) of all fine bins which falls into it.  
2432 The coarse oscillogram is then used for determining the oscillation weight for a given  
2433 event. The binning which is used to calculate the oscillation probabilities, known as  
2434 the ‘fine’ binning, has  $N \times N$  subdivisions per coarse bin. Figure 7.8 illustrates the  
2435  $N = 2$  example where the assigned value to a coarse bin is the average of the four fine  
2436 bins which fall in that coarse bin. Whilst the coarse bin edges do not have to be linear  
2437 on either axis, the sub-division of the fine bins is linear over the range of a coarse bin.

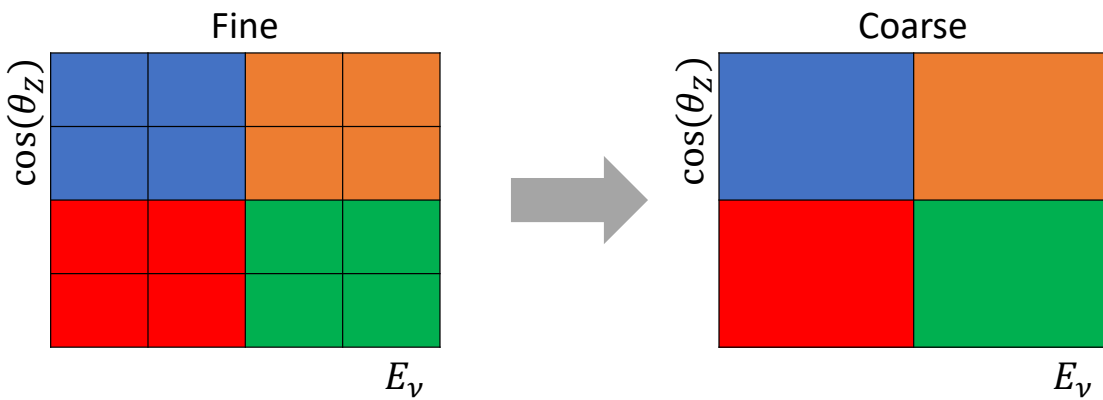


**Figure 7.8:** Illustration of the averaging procedure for  $N = 2$ . The oscillation probabilities calculated on the finer left binning are averaged to obtain the oscillation probabilities in the coarser right binning. These averaged oscillation probabilities with the coarser binning are then applied to each event during the fit.

2438 The coarse binning is defined with  $67 \times 52$  bins in true neutrino energy  $\times$  cosine  
2439 zenith. It is picked to be identical to that provided in [212]. In general, the binning is  
2440 logarithmically spaced in neutrino energy but has some hand-picked bin edges. Firstly,  
2441 the bin density around the matter resonance is smoothly increased around the matter  
2442 resonance region. This is to avoid smearing this region which can be well sampled by  
2443 the Monte Carlo. Secondly, bin edges are selected to hit  $0.4, 0.6, 1, 10, 30, 50, 100\text{GeV}$ .  
2444 This is to ensure that the Coulomb correction systematic and the atmospheric flux  
2445 systematics definitions in neutrino energy can be hit. The cosine zenith binning is

2446 approximately linearly spaced across the allowable range but the values of layer  
2447 transitions are hit precisely:  $-0.8376$  (core-mantle) and  $-0.4464$  (mantle/transition  
2448 zone). Bins are spread further apart for downgoing events as this is a region unaffected  
2449 by the fast oscillation wavelengths and reduces the total number of calculations  
2450 required to perform the calculation.

2451 The choice of  $N$  is justified based on two studies. Firstly, the variation of event rates  
2452 of each sample is studied as a function of  $N$ . For a given set of oscillation parameters  
2453 thrown from the PDG prior constraints (detailed in Table 2.1), the oscillation probabili-  
2454 ties are calculated using a given value of  $N$ . Each sample is re-weighted and the event  
2455 rate is stored. The value of  $N$  is scanned from 1, which corresponds to no averaging, to  
2456 24, which corresponds to the largest computationally viable subdivision binning. The  
2457 event rate of each sample at large  $N$  is expected to converge to a stationary value due  
2458 to the fine binning fully sampling the small-scale structure. Figure 7.9 illustrates this  
2459 behaviour for the SubGeV\_elike\_0dcy sample for 30 different throws of the oscillation  
2460 parameters.

2461 Denoting the event rate for one sample for a given throw  $t$  at each  $N$  by  $\lambda_t^N$ , the  
2462 average over all considered  $N$  values ( $\bar{\lambda}_t = \frac{1}{24} \sum_{N=1}^{24} \lambda_t^N$ ) is computed. The variance in  
2463 the event rate at each  $N$  is then calculated as

$$\text{Var}[\lambda^N] = \frac{1}{N_{\text{throws}}} \sum_{t=1}^{N_{\text{throws}}} (\lambda_t^N - \bar{\lambda}_t)^2 - \left[ \frac{1}{N_{\text{throws}}} \sum_{t=1}^{N_{\text{throws}}} (\lambda_t^N - \bar{\lambda}_t) \right]^2. \quad (7.5)$$

2464 The aim of the study is to find the lowest value of  $N$  such that this variance is  
2465 below 0.001. This is the typical threshold used by T2K fitters to validate systematic  
2466 implementation so has been set as the same criteria. The results of this study for  
2467 each atmospheric sample used within this thesis are illustrated in Figure 7.10 for

### SubGeV-elike-0dcy

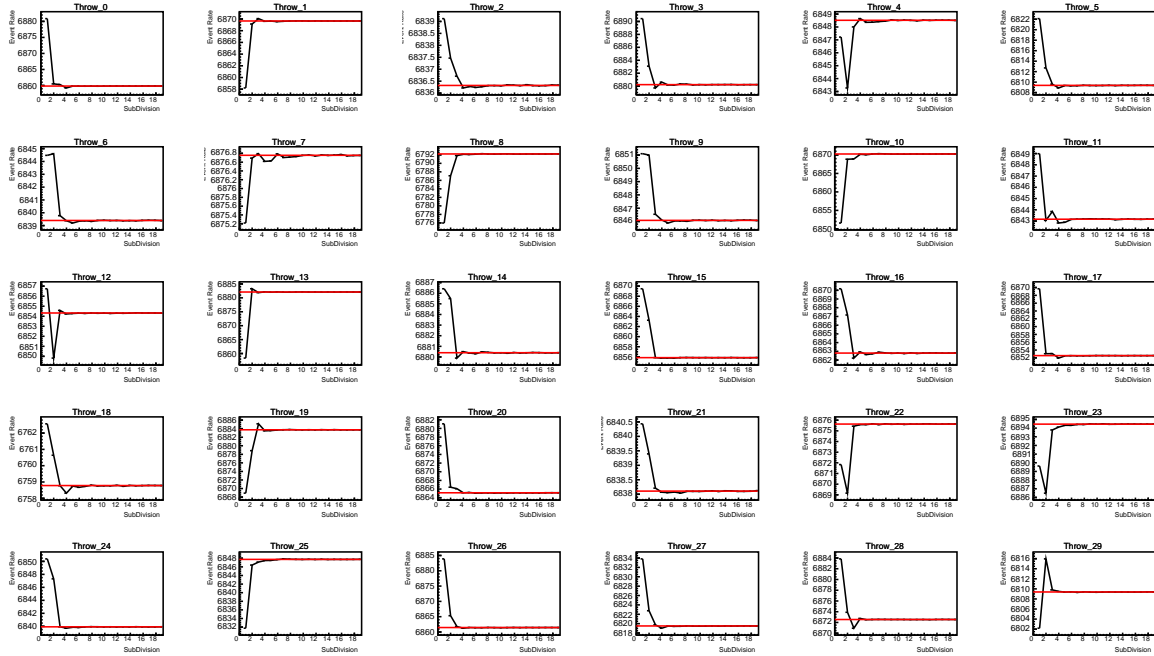


**Figure 7.9:** Event rate of the SubGeV\_elike\_0dcy sample as a function of the number of subdivisions per coarse bin. Each subplot represents the event rate of the sample at a different oscillation parameter set thrown from the PDG priors detailed in Table 2.1. The red line in each subplot represents the mean of the event rate over the different values of sub-divisions for that particular oscillation parameter throw.

2468 2000 throws of the oscillation parameters. As can be seen, the variance is below  
 2469 the threshold at  $N = 10$ , and is driven primarily by the SubGeV\_mulike\_1dcy and  
 2470 SubGeV\_elike\_0dcy samples.

2471 The second study to determine the value of  $N$  is as follows. The likelihood for each  
 2472 sample is computed against an Asimov data set created with Asimov A oscillation  
 2473 parameters (Table 2.2). Following Equation 7.5, the variance of the log-likelihood over  
 2474 all considered  $N$  is computed. The results are shown in Figure 7.11.

2475 A choice of  $N = 10$  sub-divisions per coarse bin has a variance in both event rate  
 2476 and log-likelihood residuals less than the required threshold of 0.001. The largest  
 2477 value of the likelihood variance is of order  $10^{-7}$ , corresponding to an error on the log-

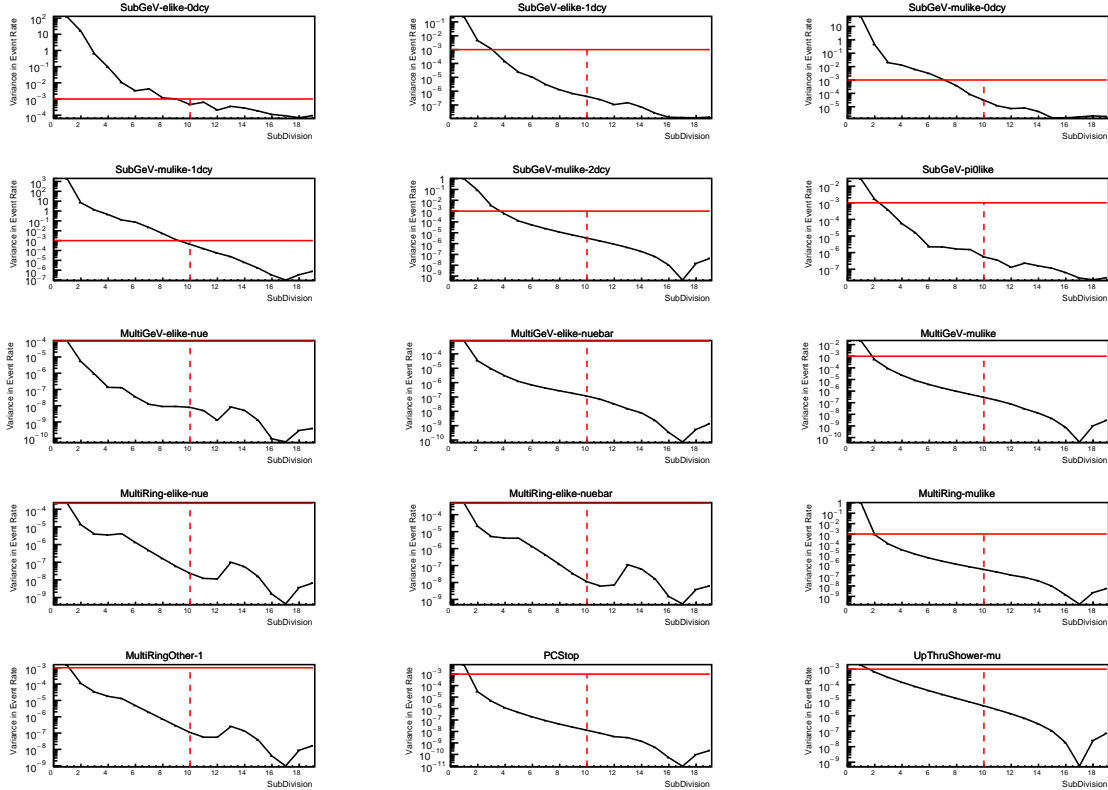


**Figure 7.10:** Variance of event rate for each atmospheric sample as a function of the number of sub-divisions per coarse bin. The solid red line indicates the 0.1% threshold and the dashed red line indicates the variance at a sub-division  $N = 10$ .

2478 likelihood of about  $3 \times 10^{-4}$  which is small enough to be negligible for the oscillation  
 2479 analysis.

2480 Figure 7.12 illustrates the effect of the smearing using  $N = 10$ . The fast oscillations  
 2481 in the sub-GeV upgoing region have been replaced with a normalisation effect whilst  
 2482 the large matter resonance structure remains.

### 2483 7.3 Calculation Engine

2484 As previously discussed in section 7.2, the calculation of oscillation probabilities is per-  
 2485 formed at run-time due to utilising continuous oscillation parameters. Consequently,  
 2486 the time per calculation is crucial for fit performance. The initial fitting framework

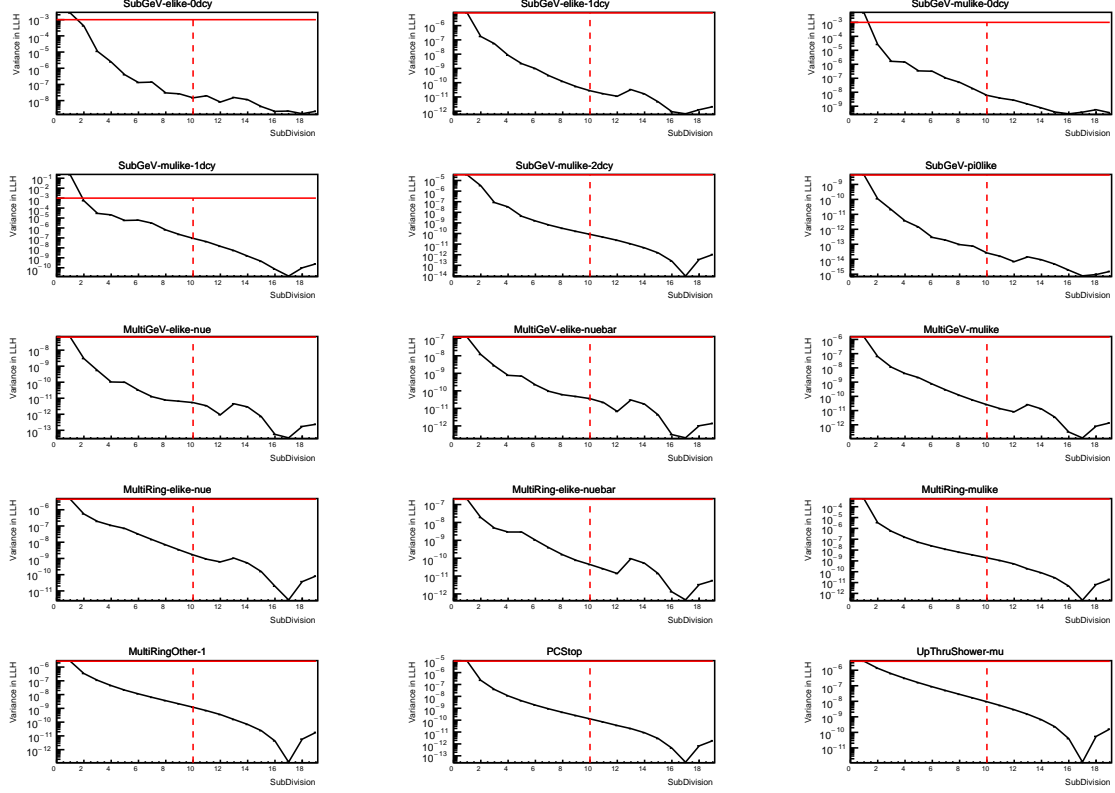


**Figure 7.11:** Variance of sample likelihood, when compared to ‘Asimov data’ set at Asimov A, for each atmospheric sample as a function of the number of sub-divisions per coarse bin. The solid red line indicates the 0.1% threshold and the dashed red line is a graphical indication of the variance at a sub-division  $N = 10$ .

used for this analysis was developed with ProbGPU [213]. This is a GPU-only implementation of the prob3 engine [214]. It is primarily designed for neutrino propagation in a beam experiment (single layer of constant density) with the atmospheric propagation code not being used prior to the analysis in this thesis.

Another engine, CUDAProb3 [215], has been implemented within the fitting framework used in this analysis. It has been specifically optimised for atmospheric neutrino oscillation calculation so does not contain the code to replace the beam oscillation calculation. The engine utilises object-orientated techniques as compared to the functional implementation of ProbGPU. This allows the energy and cosine zenith arrays to be kept on GPU memory, rather than having to load these arrays onto GPU memory for each calculation. General memory interfacing is one of the slowest tasks which

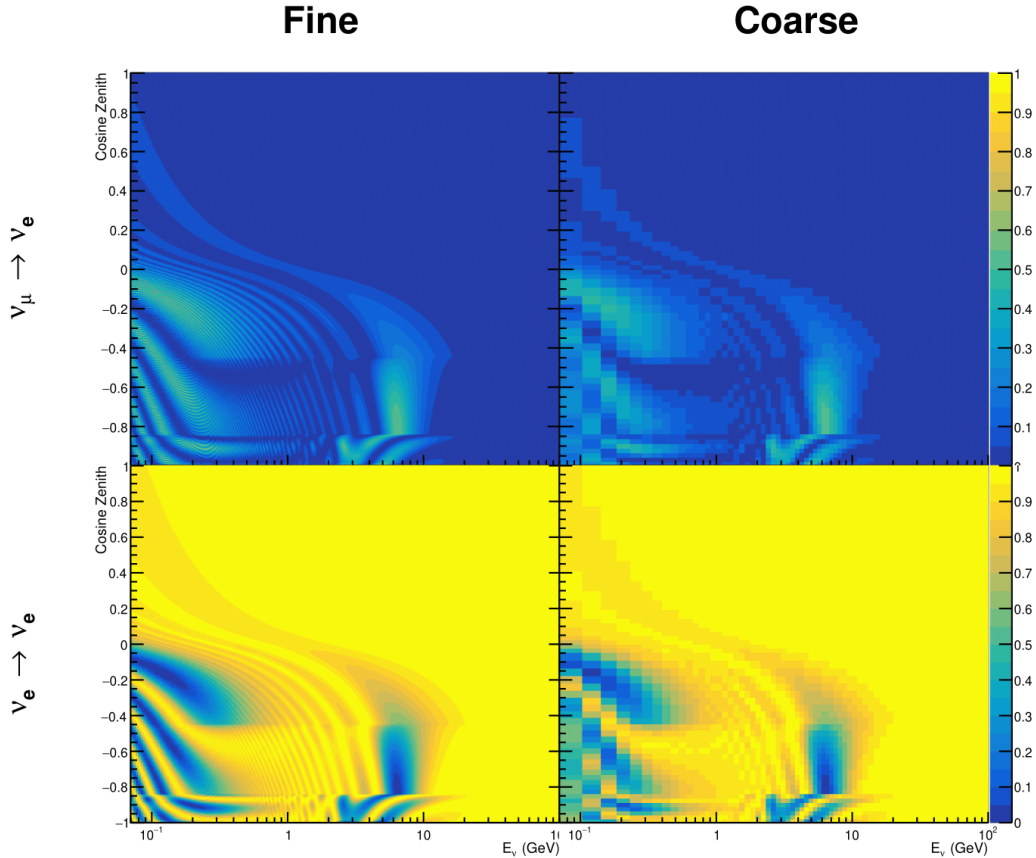


**Figure 7.12:** The oscillation probability,  $P(\nu_\mu \rightarrow \nu_e)$  (top row) and  $P(\nu_e \rightarrow \nu_\mu)$  (bottom row), given as a function of neutrino energy and zenith angle. The left column gives the “fine” binning used to calculate the oscillation probabilities and the right column illustrates the “coarse” binning used to reweight the Monte Carlo events. The fine binning choice is given with  $N = 10$ , which was determined to be below the threshold from Figure 7.10 and Figure 7.11.

2498    GPUs can do, so being able to eliminate this significantly reduces the time required  
 2499    for calculation. This can be seen in Figure 7.13, where the GPU implementation of  
 2500    CUDAProb3 is approximately three times faster than the ProbGPU engine.

2501    Another significant advantage of CUDAProb3 is that it contains a CPU multithreaded  
 2502    implementation which is not possible with the ProbGPU or prob3 engines. This elimi-  
 2503    nates the requirement for GPU resources when submitting jobs to batch systems. As  
 2504    illustrated in Figure 7.13, the calculation speed depends on the number of available

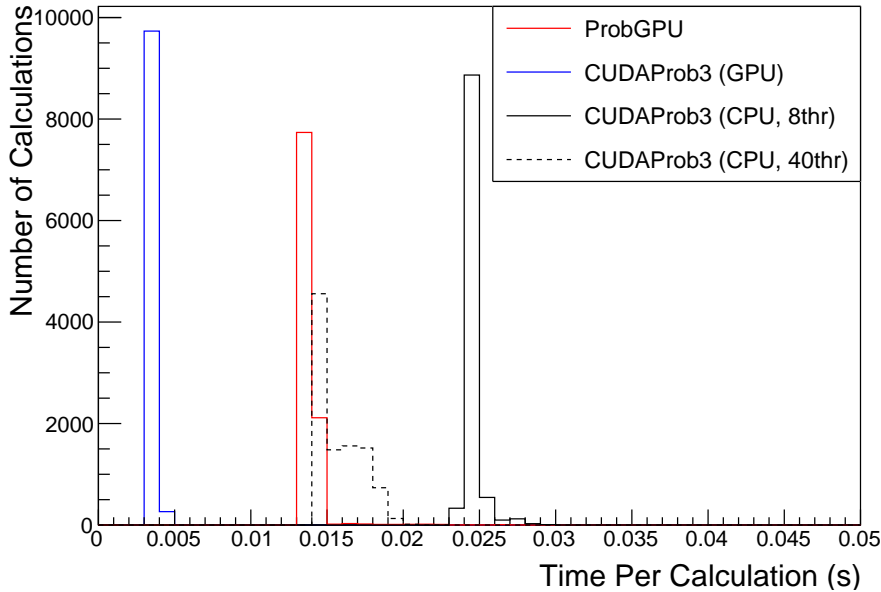


**Figure 7.13:** The calculation time taken to both calculate the oscillation probabilities and fill the “coarse” oscillograms, following the technique given in section 7.2, for the CUDAProb3 and ProbGPU (Red) calculation engines. CUDAProb3 has both a GPU (Blue) and CPU (Black) implementation, where the CPU implementation is multithreaded. Therefore, 8-threads (solid) and 40-threads (dashed) configurations have been tested. Prob3, which is a CPU single-thread implementation has a mean step time of 1.142s.

2505 threads. Using 8 threads (which is typical of the batch systems being used) is ap-  
 2506 proximately twice as slow as the ProbGPU engine implementation, but would allow  
 2507 the fitting framework to be run on many more resources. This fact is utilised for any  
 2508 SK-only fits but GPU resources are required for any fits which include beam samples  
 2509 due to the ProbGPU requirement. Based on the benefits shown by the implementa-  
 2510 tion in this section, efforts are being placed into including linear propagation for beam  
 2511 neutrino propagation into the engine [216].

## 2512 7.4 Matter Density Profile

2513 For an experiment observing atmospheric neutrinos propagating through the Earth, a  
 2514 model of the Earth’s density profile is required. The model used within this analysis is

2515 the Preliminary Reference Earth Model (PREM) [211], as illustrated in Figure 7.1. As  
2516 discussed in section 7.1, the propagator used within the calculation engine requires  
2517 constant density layers. To follow the official SK-only analysis [210], the average  
2518 density of each layer has been taken from the PREM model. Table 7.1 documents  
2519 the density and radii of the layers used within this approximation. The density  
2520 measurements provided in the PREM model are provided in terms of mass density,  
2521 whereas neutrino oscillations are sensitive to the electron number density. This value  
2522 can be computed as the product of the chemical composition, or the  $Z/A$  value, and  
2523 the mass density of each layer. Currently, the only way to calculate the chemical  
2524 composition value for layers close to the Earth’s core is through neutrino oscillations.  
2525 The chemical composition of the upper layers of the Earth’s Mantle and the Transition  
2526 zone is well known due to it being predominantly pyrolite which has a chemical  
2527 composition value of 0.496 [217]. The components of the Earth’s core region are less  
2528 well known. Consequently, the chemical composition dial for the core layers is set to a  
2529 value of 0.468, as calculated in [218]. This value is assigned a Gaussian error with a  
2530 standard deviation equivalent to the difference in chemical composition in core and  
2531 mantle layers. Figure 7.14 illustrates the effect of moving from the  $Z/A = 0.5$  method  
2532 which is used in the official SK-only analysis [210] to these more precise values.

2533 The beam oscillation probability in this thesis uses a baseline of 295km, density  
2534  $2.6\text{g/cm}^3$ , and chemical composition 0.5 as is done by the official T2K-only analysis  
2535 [219].

2536 Whilst the propagator requires a fixed density layer model of the Earth, the density  
2537 only has to be fixed for a specific  $E_\nu \times \cos(\theta_Z)$  bin in a given layer. As the density is a  
2538 function of radius, which is a function of the direction in which a neutrino propagates,  
2539 a better approximation of the PREM model can be made if a  $\cos(\theta_Z)$ -specific density is  
2540 calculated.

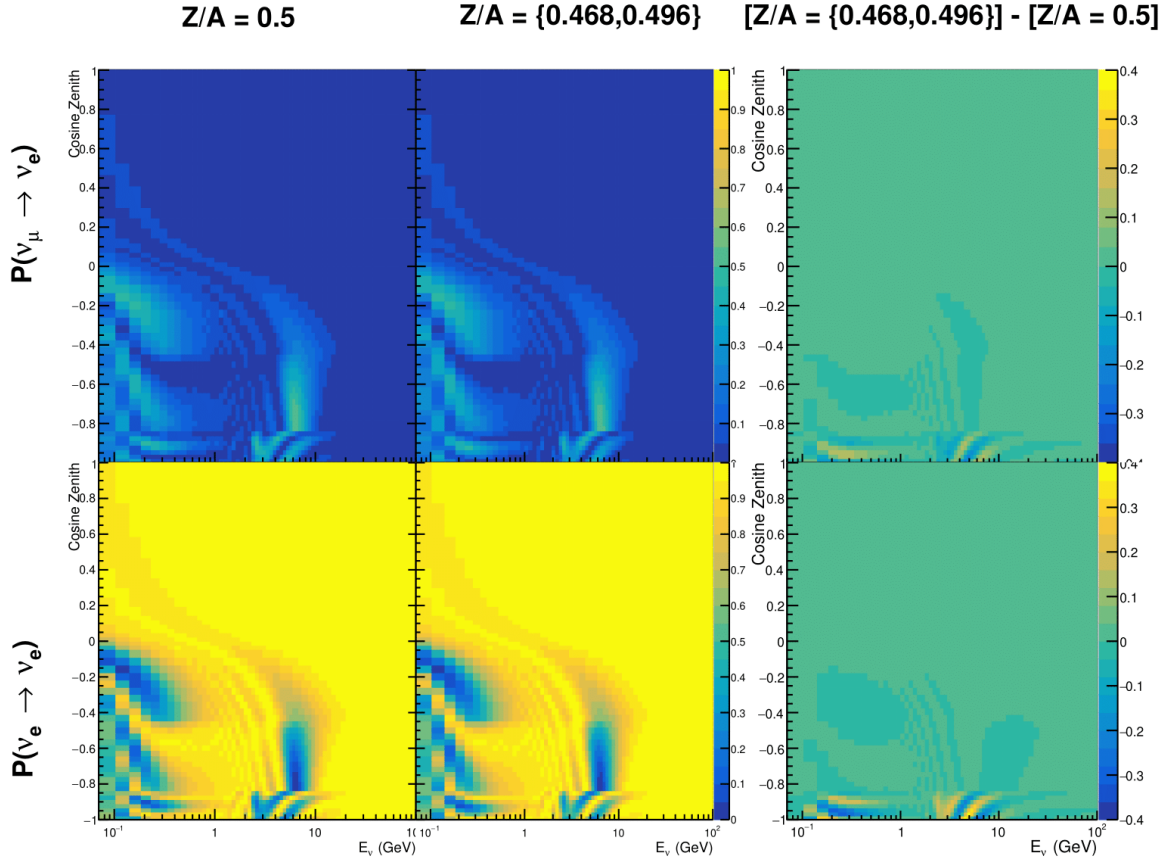


**Figure 7.14:** The oscillation probability,  $P(\nu_\mu \rightarrow \nu_e)$  (top row) and  $P(\nu_e \rightarrow \nu_e)$  (bottom row), given as a function of neutrino energy and zenith angle. The left column gives probabilities where the constant  $Z/A = 0.5$  approximation which is used in the official SK-only analysis. The middle column gives the probabilities where  $Z/A = [0.468, 0.498]$  values are used, as given in Table 7.1. The right column illustrates the difference in oscillation probability between the two different techniques.

2541 To achieve this, the average density,  $\langle \rho \rangle_i$ , in the  $i^{th}$  layer, is calculated as the density,  
 2542  $\rho(t)$ , integrated over the track a given  $\cos(\theta_Z)$ ,

$$\langle \rho \rangle_i = \frac{1}{t_{i+1} - t_i} \int_{t_i}^{t_{i+1}} \rho(t) dt \quad (7.6)$$

2543 where  $t_i$  are the intersection points between each layer and  $t$  is the path length of  
 2544 the trajectory across the layer.

2545 The oscillation probability calculation speed is approximately linear in the number  
 2546 of layers invoked within the Earth model. Therefore a four-layer model is still utilized  
 2547 with the only difference to the official SK-only analysis being that the four-layer model  
 2548 used for each value of  $\cos(\theta_Z)$  is different. Following the method outlined in [220],  
 2549 a four-layer piecewise quadratic polynomial is fit to the PREM model for the four  
 2550 layers defined in Table 7.1. This fit was not performed by the author of the thesis  
 2551 and is documented in [212]. The coefficients of the quadratic fit to each layer are  
 2552 given in Table 7.2 with the final distribution illustrated in Figure 7.15. The quadratic  
 2553 approximation is clearly much closer to the PREM model as compared to the constant  
 2554 density approximation.

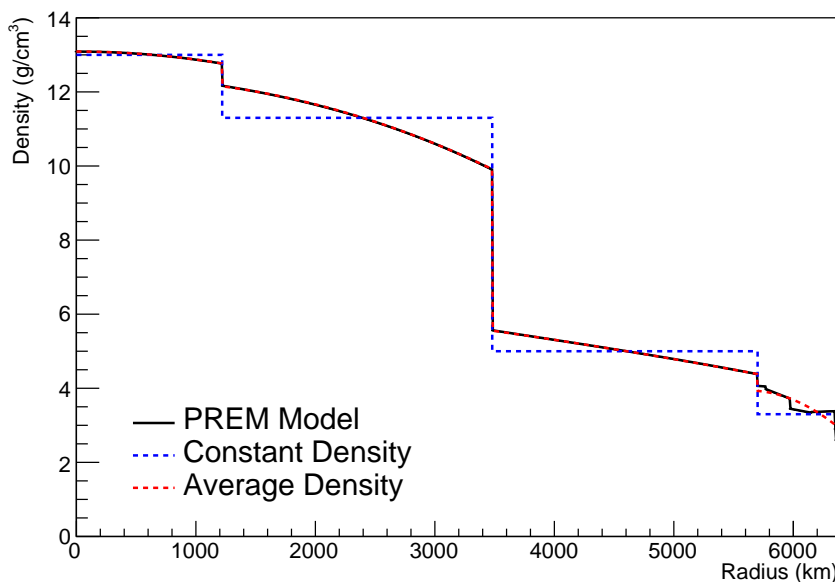


**Figure 7.15:** The density of the Earth given as a function of the radius, as given by the PREM model (Black), the constant density four-layer approximation (Blue), as used in the official SK-only analysis, and the quadratic approximation of the PREM model (Red).

Layer	Outer Radius [km]	Density [g/cm <sup>3</sup> ]
Inner Core	1220	$13.09 - 8.84x^2$
Outer Core	3480	$12.31 + 1.09x - 10.02x^2$
Lower Mantle	5701	$6.78 - 1.56x - 1.25x^2$
Transition Zone	6371	$-50.42 + 123.33x - 69.95x^2$

**Table 7.2:** The quadratic polynomial fits to the PREM model for four assumed layers of the PREM model. The fit to calculate the coefficients is given in [212], where  $x = R/R_{Earth}$ .

The effect of using the quadratic density per  $\cos(\theta_Z)$  model is highlighted in Figure 7.16. The slight discontinuity in the oscillation probability around  $\cos(\theta_Z) \sim -0.45$  in the fixed density model, which is due to the transition to mantle layer boundary, has been reduced. This is expected as the difference in the density across this boundary is significantly smaller in the quadratic density model as compared to the constant density model. Whilst the difference in density across the other layer transitions is reduced, there is still a significant difference. This means the discontinuities in the oscillation probabilities remain but are significantly reduced. However, as the quadratic density approximation matches the PREM model well in this region, these discontinuities are due to the Earth model rather than an artifact of the oscillation calculation.

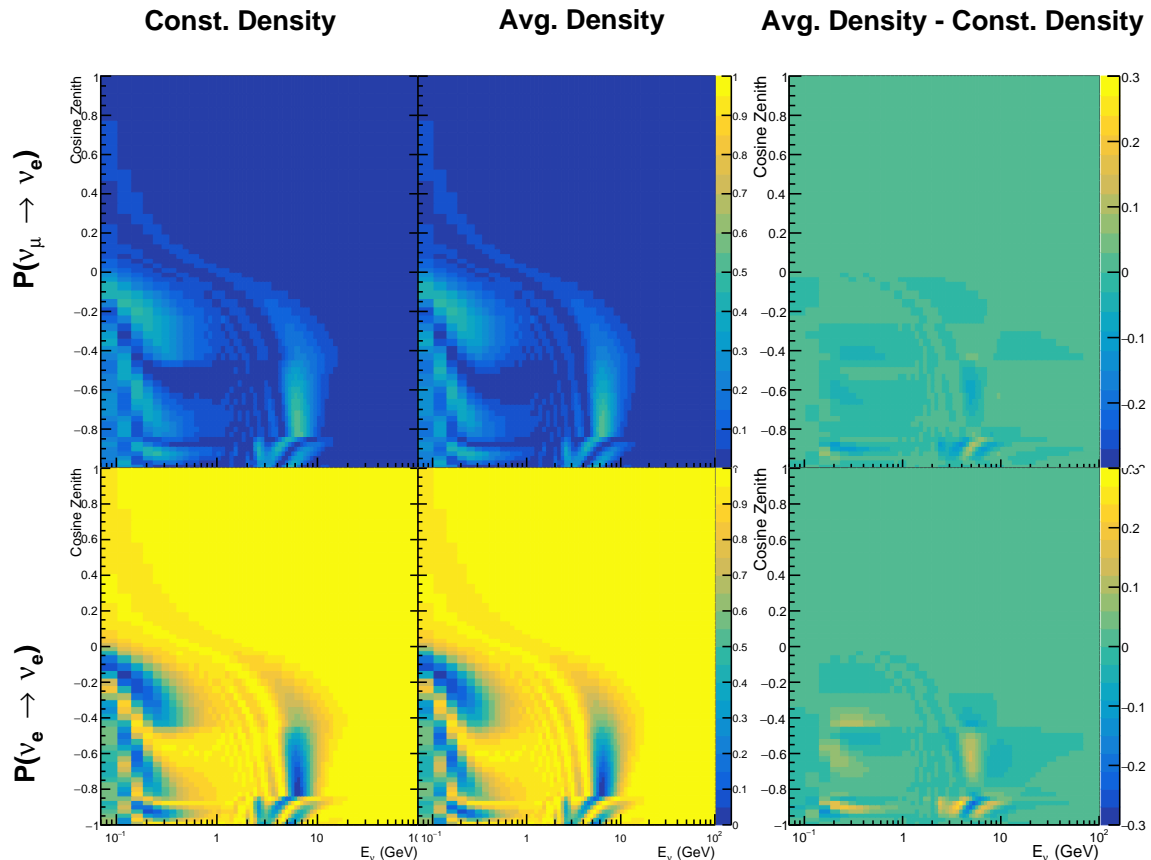


**Figure 7.16:** The oscillation probability,  $P(\nu_\mu \rightarrow \nu_e)$  (top row) and  $P(\nu_e \rightarrow \nu_e)$  (bottom row), given as a function of neutrino energy and zenith angle. The left column gives probabilities where the four-layer constant density approximation is used. The middle column gives the probabilities where the density is integrated over the trajectory, using the quadratic PREM approximation, for each  $\cos(\theta_Z)$  is used. The right column illustrates the difference in oscillation probability between the two different techniques.

## 2566 7.5 Production Height Averaging

2567 As discussed in section 7.1, the height at which the cosmic ray flux interacts in the  
2568 atmosphere is not known on an event-by-event basis. The production height can vary  
2569 from the Earth’s surface to  $\sim 50\text{km}$  above that. The SK-only analysis methodology  
2570 (described in section 7.2) for including the uncertainty on the production height is  
2571 to include variations from the Honda model when pre-calculating the oscillation  
2572 probabilities prior to the fit. This technique is not possible for this analysis which  
2573 uses continuous oscillation parameters that can not be known prior to the fit. Conse-  
2574 quently, an analytical averaging technique was developed in [212]. The author of this  
2575 thesis was not responsible for the derivation of the technique but has performed the  
2576 implementation and validation of the technique for this analysis alone.

2577 Using the 20 production heights per Monte Carlo neutrino event, provided as 5%  
2578 percentiles from the Honda flux model, a production height distribution  $p_j(h|E_\nu, \cos\theta_Z)$   
2579 is built for each neutrino flavour  $j = \nu_e, \bar{\nu}_e, \nu_\mu, \bar{\nu}_\mu$ . In practice, a histogram is filled with  
2580 20 evenly spaced bins in production height  $h$  between 0 and 50km. The neutrino energy  
2581 and cosine zenith binning of the histogram is the same as that provided in section 7.2.  
2582 The average production height,  $\bar{h} = \int dh \frac{1}{4} \sum_j p_j(h|E_\nu, \cos(\theta_Z))$ , is calculated. The  
2583 production height binning of this histogram is then translated into  $\delta t(h) = t(\bar{h}) - t(h)$ ,  
2584 where  $t(h)$  is the distance travelled along the trajectory.

2585 For the  $i^{\text{th}}$  traversed layer, the transition amplitude,  $D_i(t_{i+1}, t_i)$ , is computed. The  
2586 time-ordered product of these is then used as the overall transition amplitude via

$$A(t_{n+1}, t_0) = D_n(t_{n+1}, t_n) \dots D_1(t_2, t_1) D_0(t_1, t_0), \quad (7.7)$$

2587

where,

$$\begin{aligned} D_n(t_{n+1}, t_n) &= \exp[-iH_n(t_{n+1} - t_n)] \\ &= \sum_{k=1}^3 C_k \exp[ia_k(t_{n+1} - t_n)] \end{aligned} \quad (7.8)$$

2588

is expressed as a diagonalised time-dependent solution to the Schrodinger equation.

2589

The  $0^{th}$  layer is the propagation through the atmosphere and is the only term that depends on the production height. Using the substitution  $t_0 = t(\bar{h}) - \delta t(h)$ , it can be shown that

2591

$$D_0(t_1, t_0) = D_0(t_1, \bar{h})D_0(\delta t). \quad (7.9)$$

2592

Thus Equation 7.7 becomes

$$\begin{aligned} A(t_{n+1}, t_0) &= D_n(t_{n+1}, t_n) \dots D_1(t_2, t_1) D_0(t_1, \bar{h}) D(\delta t) \\ &= A(t_{n+1}, \bar{h}) \sum_{k=1}^3 C_k \exp[ia_k \delta t], \\ &= \sum_{k=1}^3 B_k \exp[ia_k \delta t]. \end{aligned} \quad (7.10)$$

2593

The oscillation probability averaged over production height is then calculated as

$$\begin{aligned}
 \bar{P}(\nu_j \rightarrow \nu_i) &= \int d(\delta t) p_j(\delta t | E_\nu, \cos \theta_Z) P(\nu_j \rightarrow \nu_i) \\
 &= \int d(\delta t) p_j(\delta t | E_\nu, \cos \theta_Z) A(t_{n+1}, t_0) A^*(t_{n+1}, t_0) \\
 &= \sum_{km} (B_k)_{ij} (B_m)_{ij}^* \int d(\delta t) p_j(\delta t | E_\nu, \cos \theta_Z) \exp[i(a_k - a_m)\delta t]
 \end{aligned} \tag{7.11}$$

2594 In practice, implementation in CUDAProb3 [215] is relatively straightforward as  
 2595 the majority of these terms are already calculated in the standard oscillation calculation.  
 2596 Figure 7.17 illustrates the results of the production height averaging. As expected,  
 2597 the main effect is observed in the low-energy downward-going and horizontal-going  
 2598 events. Upward-going events have to travel the radius of the Earth,  $R_E = 6371\text{km}$ ,  
 2599 where the production height uncertainty is a small fraction of the total path length.

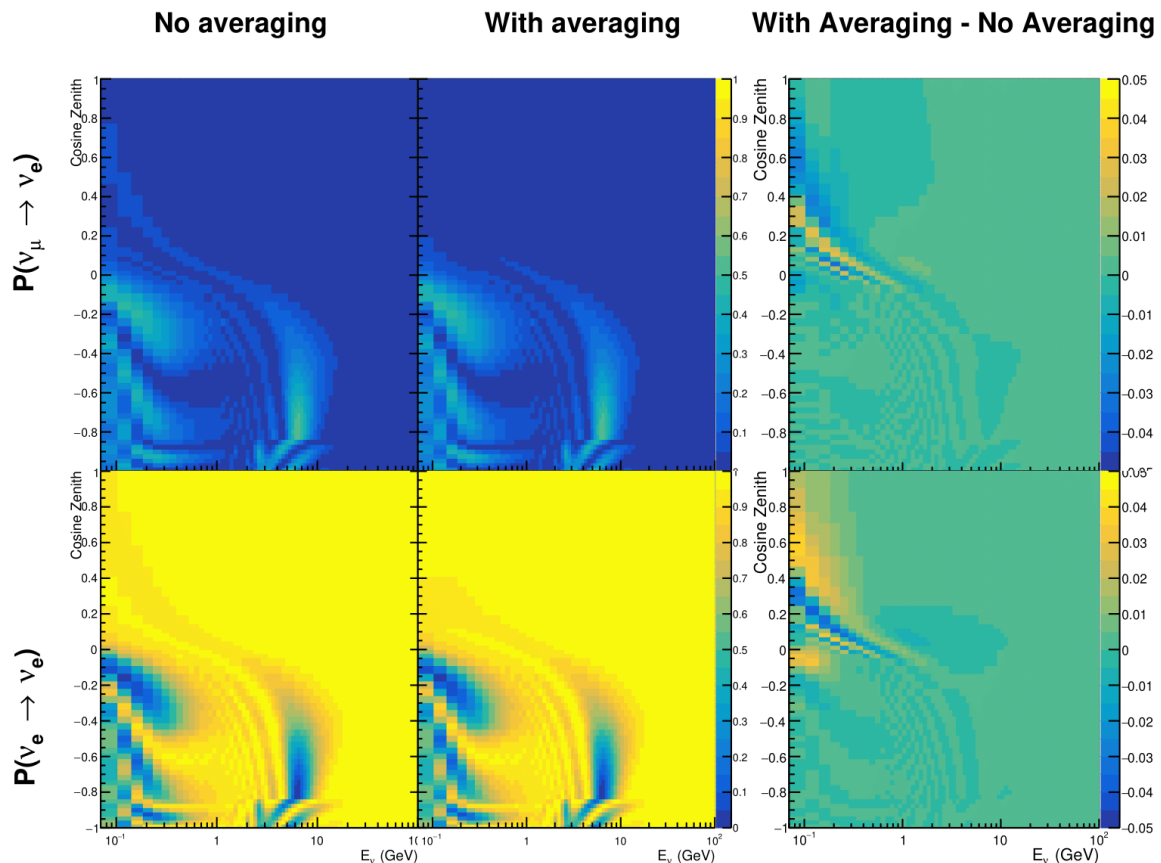


**Figure 7.17:** The oscillation probability,  $P(\nu_\mu \rightarrow \nu_e)$  (top row) and  $P(\nu_e \rightarrow \nu_e)$  (bottom row), given as a function of neutrino energy and zenith angle. The left column gives probabilities where a fixed production height of 25km is used. The middle column gives the probabilities where the production height is analytically averaged. The right column illustrates the difference in oscillation probability between the two different techniques.

2600 **Chapter 8**

2601 **Oscillation Analysis**

2602 **8.1 Likelihood Calculation**

2603 This analysis performs a joint oscillation parameter fit of the ND280, and the SK  
2604 atmospheric samples.

2605 Once the Monte Carlo predictions of each beam and atmospheric sample has been  
2606 built, following from chapter 6, a likelihood needs to be constructed. This is done  
2607 by comparing the Monte Carlo prediction to “data”. The data can consist of either  
2608 an Asmiov Monte Carlo prediction, which is typically used for sensitivity studies,  
2609 or real data. The Monte Carlo prediction is calculated at a particular point,  $\vec{\theta}$ , in the  
2610 model parameter space,  $N_i^{MC} = N_i^{MC}(\vec{\theta})$ . Both the data and Monte Carlo spectra are  
2611 binned, where the  $i^{th}$  bin content is represented by  $N_i^D$  and  $N_i^{MC}$ , respectively. The bin  
2612 contents for the beam near detector, beam far detector and atmospheric samples are  
2613 denoted with *ND*, *FD* and *Atm*, respectively. The binning index,  $i$ , runs over all the  
2614 bins within the sample and all samples with that set. Taking the beam far detector  
2615 samples as example, it would run over all the reconstructed neutrino energy bins in all  
2616 samples (FHC1R $\mu$ , RHC1R $\mu$ , etc.). The likelihood calculation between data and Monte  
2617 Carlo for a particular bin follows a Poisson distribution, where the data is treated as a  
2618 fluctuation of the simulation.

2619 Following the T2K analysis presented in [80], the likelihood contribution from the  
2620 near detector also includes a Monte Carlo statistical uncertainty term, derived from

the Barlow and Beeston statistical treatment [221, 222]. In addition to treating the data as a fluctuation of the Monte Carlo prediction, it includes a contribution from the likelihood that the generated simulation is a statistical fluctuation of the actual true simulation assuming infinite statistics. The technical implementation of this additional likelihood term is documented in [195]. The term is defined as,

$$\frac{(\beta_i - 1)^2}{2\sigma_{\beta_i}^2}, \quad (8.1)$$

where  $\beta_i$  represents a scaling parameter for each bin  $i$ , which is a value based on the amount of Monte Carlo statistics in a bin [195].  $\sigma_{\beta_i} = \sqrt{\sum_i w_i^2 / N_i^{MC}}$ , and  $\sqrt{\sum_i w_i^2}$  represents the sum of the square of the weights of the Monte Carlo events which fall into bin  $i$ .

Additional contributions to the likelihood come from the variation of the systematic model parameters. For those parameters with well-motivated uncertainty estimates, a covariance matrix,  $V$  describes the prior knowledge of each parameter as well as any correlations between the parameters. Due to the technical implementation, a single covariance matrix describes each “block” of model parameters, e.g. beam flux systematics. For simplicity, the covariance matrix associated with the  $k^{th}$  block is denoted  $V^k$ . This substitution results in  $\vec{\theta} = \sum_k^{N_b} \vec{\theta}^k$  and  $V = \sum_k^{N_b} V^k$ , for  $N_b$  number of blocks describing: oscillation parameters, beam flux, atmospheric flux, neutrino interaction, near detector, beam far detector and atmospheric far detector systematics detailed in section 6.4. The number of parameters in the  $k^{th}$  block is defined as  $n(k)$ .

The final likelihood term is defined as,

$$\begin{aligned}
& -\ln(\mathcal{L}) = & (8.2) \\
& \sum_i^{\text{NDbins}} N_i^{\text{ND},MC}(\vec{\theta}) - N_i^{\text{ND},D} + N_i^{\text{ND},D} \times \ln \left[ N_i^{\text{ND},D} / N_i^{\text{ND},MC}(\vec{\theta}) \right] + \frac{(\beta_i - 1)^2}{2\sigma_{\beta_i}^2} \\
& + \sum_i^{\text{FDbins}} N_i^{\text{FD},MC}(\vec{\theta}) - N_i^{\text{FD},D} + N_i^{\text{FD},D} \times \ln \left[ N_i^{\text{FD},D} / N_i^{\text{FD},MC}(\vec{\theta}) \right] \\
& + \sum_i^{\text{Atmbins}} N_i^{\text{Atm},MC}(\vec{\theta}) - N_i^{\text{Atm},D} + N_i^{\text{Atm},D} \times \ln \left[ N_i^{\text{Atm},D} / N_i^{\text{Atm},MC}(\vec{\theta}) \right] \\
& + \frac{1}{2} \sum_k^{N_b} \sum_i^{n(k)} \sum_j^{n(k)} (\vec{\theta}^k)_i (V^k)_{ij}^{-1} (\vec{\theta}^k)_j.
\end{aligned}$$

2641 This is the value determined at each step of the MCMC to build the posterior  
 2642 distribution, as discussed in chapter 4.

2643

2644 **Bibliography**

- 2645 [1] J. Chadwick, Verhandl. Dtsc. Phys. Ges. **16**, 383 (1914).
- 2646 [2] C. D. Ellis and W. A. Wooster, Proc. R. Soc. Lond. A Math. Phys. Sci. **117**, 109  
2647 (1927).
- 2648 [3] W. Pauli, Phys. Today **31N9**, 27 (1978).
- 2649 [4] E. Fermi, Z. Phys. **88**, 161 (1934).
- 2650 [5] F. Reines and C. L. Cowan, Phys. Rev. **92**, 830 (1953).
- 2651 [6] C. L. Cowan, F. Reines, F. B. Harrison, H. W. Kruse, and A. D. McGuire, Science  
2652 **124**, 103 (1956), <http://science.sciencemag.org/content/124/3212/103.full.pdf>.
- 2653 [7] G. Danby *et al.*, Phys. Rev. Lett. **9**, 36 (1962).
- 2654 [8] K. Kodama *et al.*, Physics Letters B **504**, 218 (2001).
- 2655 [9] LSND, A. Aguilar-Arevalo *et al.*, Phys. Rev. **D64**, 112007 (2001), hep-ex/0104049.
- 2656 [10] MiniBooNE Collaboration, A. A. Aguilar-Arevalo *et al.*, Phys. Rev. Lett. **110**,  
2657 161801 (2013).
- 2658 [11] Planck Collaboration *et al.*, aap **641** (2020).
- 2659 [12] The ALEPH Collaboration, The Delphi Collaboration, The L3 Collaboration, The  
2660 SLD Collaboration, The LEP Electroweak Working Group, The SLD Electroweak  
2661 and Heavy Flavour Groups, J. A. Bagger *et al.*, Physics Reports **427**, 257 (2006).
- 2662 [13] B. Pontecorvo, Sov. Phys. JETP **26**, 984 (1968), [Zh. Eksp. Teor. Fiz. 53, 1717 (1967)].
- 2663 [14] B. Pontecorvo, Sov. Phys. JETP **7**, 172 (1958), [Zh. Eksp. Teor. Fiz. 34, 247 (1957)].
- 2664 [15] M. Kobayashi and T. Maskawa, Progress of Theoretical Physics **49**, 652 (1973).
- 2665 [16] N. Cabibbo, Phys. Rev. Lett. **10**, 531 (1963).
- 2666 [17] A. M. and, Journal of Physics: Conference Series **587**, 012030 (2015).
- 2667 [18] A. Y. Smirnov, (2003).
- 2668 [19] S. Mikheyev and A. Smirnov, Soviet Journal of Nuclear Physics **42**, 913 (1985).

- 2669 [20] L. Wolfenstein, Phys. Rev. D **17**, 2369 (1978).
- 2670 [21] V. D. Barger, K. Whisnant, S. Pakvasa, and R. J. N. Phillips, Phys. Rev. D **22**, 2718  
2671 (1980).
- 2672 [22] The Super-Kamiokande Collaboration, Y. Ashie *et al.*, Phys. Rev. Lett. **93**, 101801  
2673 (2004).
- 2674 [23] SNO Collaboration, Q. R. Ahmad *et al.*, Phys. Rev. Lett. **89**, 011301 (2002).
- 2675 [24] 2015 Nobel prize in Physics as listed by Nobelprize.org, [https://www.](https://www.nobelprize.org/nobel_prizes/physics/laureates/2015/)  
2676 [nobelprize.org/nobel\\_prizes/physics/laureates/2015/](https://www.nobelprize.org/nobel_prizes/physics/laureates/2015/), Accessed: 22-06-  
2677 2022.
- 2678 [25] J. A. Formaggio and G. P. Zeller, Rev. Mod. Phys. **84**, 1307 (2012), 1305.7513.
- 2679 [26] A. Bellerive, Int. J. Mod. Phys. A **19**, 1167 (2004).
- 2680 [27] R. Davis, D. S. Harmer, and K. C. Hoffman, Phys. Rev. Lett. **20**, 1205 (1968).
- 2681 [28] N. Vinyoles *et al.*, Astrophys. J. **835**, 202 (2017).
- 2682 [29] V. Gribov and B. Pontecorvo, Phys. Lett. B **28**, 493 (1969).
- 2683 [30] K. S. Hirata *et al.*, Phys. Rev. Lett. **63**, 16 (1989).
- 2684 [31] W. Hampel *et al.*, Phys. Lett. B **447**, 127 (1999).
- 2685 [32] SAGE Collaboration, J. N. Abdurashitov *et al.*, Phys. Rev. C **60**, 055801 (1999).
- 2686 [33] Q. R. Ahmad *et al.*, Phys. Rev. Lett. **89** (2002).
- 2687 [34] Borexino Collaboration, Nature **562**, 505 (2018).
- 2688 [35] B. Aharmim *et al.*, Astrophys. J. **653**, 1545 (2006).
- 2689 [36] M. Agostini *et al.*, (2020).
- 2690 [37] S. Andringa *et al.*, Adv. High Energy Phys. **2016**, 1 (2016).
- 2691 [38] J. F. Beacom *et al.*, Chin. phys. C **41**, 023002 (2017).
- 2692 [39] F. An *et al.*, J. Phys. G Nucl. Part. Phys. **43**, 030401 (2016).
- 2693 [40] J. Aalbers *et al.*, (2020), 2006.03114.
- 2694 [41] T. K. Gaisser and M. Honda, (2002).

- 2695 [42] G. D. Barr, T. K. Gaisser, P. Lipari, S. Robbins, and T. Stanev, Physical Review D  
2696 **70** (2004).
- 2697 [43] M. Honda, T. Kajita, K. Kasahara, S. Midorikawa, and T. Sanuki, Physical Review  
2698 D **75** (2007).
- 2699 [44] M. Honda, T. Kajita, K. Kasahara, and S. Midorikawa, Phys. Rev. D **70**, 043008  
2700 (2004).
- 2701 [45] M. Honda, T. Kajita, K. Kasahara, and S. Midorikawa, Phys. Rev. D **83**, 123001  
2702 (2011).
- 2703 [46] A. Fasso, A. Ferrari, P. R. Sala, and J. Ranft, (2001).
- 2704 [47] Y. Ashie *et al.*, Physical Review D **71** (2005).
- 2705 [48] F. Reines *et al.*, Phys. Rev. Lett. **15**, 429 (1965).
- 2706 [49] D. Casper *et al.*, Phys. Rev. Lett. **66**, 2561 (1991).
- 2707 [50] K. S. Hirata *et al.*, Phys. Lett. B **280**, 146 (1992).
- 2708 [51] Z. Li *et al.*, Physical Review D **98** (2018).
- 2709 [52] Kamiokande Collaboration *et al.*, (2017).
- 2710 [53] T2K Collaboration, Nature **580**, 339 (2020).
- 2711 [54] M. A. Acero *et al.*, Phys. Rev. Lett. **123**, 151803 (2019).
- 2712 [55] M. G. Aartsen *et al.*, Phys. Rev. Lett. **120** (2018).
- 2713 [56] P. Adamson *et al.*, Phys. Rev. Lett. **112** (2014).
- 2714 [57] M. S. Athar *et al.*, Progress in Particle and Nuclear Physics **124**, 103947 (2022).
- 2715 [58] G. Danby *et al.*, Phys. Rev. Lett. **9**, 36 (1962).
- 2716 [59] K. Abe *et al.*, Physical Review D **87** (2013).
- 2717 [60] MINOS Collaboration, D. G. Michael *et al.*, Phys. Rev. Lett. **97**, 191801 (2006).
- 2718 [61] G. Danby *et al.*, Phys. Rev. Lett. **9**, 36 (1962).
- 2719 [62] NOvA Collaboration, M. A. Acero *et al.*, Phys. Rev. Lett. **123**, 151803 (2019).
- 2720 [63] B. Abi, R. Acciarri, M. A. Acero, and G. e. a. Adamov, Eur. Phys. J. C Part. Fields

- 2721       **80** (2020).
- 2722       [64] Hyper-Kamiokande Proto-Collaboration *et al.*, Prog. Theor. Exp. Phys. **2015**,  
2723       53C02 (2015).
- 2724       [65] C. Blanco, D. Hooper, and P. Machado, Physical Review D **101** (2020).
- 2725       [66] MicroBooNE Collaboration *et al.*, Search for an Excess of Electron Neutrino  
2726       Interactions in MicroBooNE Using Multiple Final State Topologies, 2021.
- 2727       [67] KARMEN Collaboration, B. Armbruster *et al.*, Phys. Rev. D **65**, 112001 (2002).
- 2728       [68] S.-B. Kim, T. Lasserre, and Y. Wang, Adv. High Energy Phys. **2013**, 1 (2013).
- 2729       [69] M. Sajjad Athar *et al.*, Prog. Part. Nucl. Phys. **124**, 103947 (2022), 2111.07586.
- 2730       [70] K. Abe *et al.*, Nucl. Instrum. Methods Phys. Res. A **1027**, 166248 (2022).
- 2731       [71] F. P. An *et al.*, Phys. Rev. Lett. **108**, 171803 (2012).
- 2732       [72] RENO Collaboration, J. K. Ahn *et al.*, Phys. Rev. Lett. **108**, 191802 (2012).
- 2733       [73] Double Chooz Collaboration, Y. Abe *et al.*, Phys. Rev. Lett. **108**, 131801 (2012).
- 2734       [74] J. Collaboration *et al.*, TAO Conceptual Design Report: A Precision Measurement  
2735       of the Reactor Antineutrino Spectrum with Sub-percent Energy Resolution, 2020,  
2736       2005.08745.
- 2737       [75] for the RENO Collaboration, New results from RENO and the 5 MeV excess,  
2738       AIP Publishing LLC, 2015.
- 2739       [76] Y. Abe *et al.*, Journal of High Energy Physics **2014** (2014).
- 2740       [77] Daya Bay Collaboration, D. Adey *et al.*, Phys. Rev. Lett. **123**, 111801 (2019).
- 2741       [78] M. P. Decowski, Nucl. Phys. B. **908**, 52 (2016).
- 2742       [79] The KamLAND Collaboration, A. Gando *et al.*, Phys. Rev. D **83**, 052002 (2011).
- 2743       [80] P. Dunne, Latest Neutrino oscillation results from T2K, 2020.
- 2744       [81] M. Tanabashi *et al.*, Phys. Rev. D. **98** (2018).
- 2745       [82] Particle Data Group, R. L. Workman and Others, PTEP **2022**, 083C01 (2022).
- 2746       [83] T2K Collaboration, K. Abe *et al.*, Phys. Rev. Lett. **112**, 181801 (2014).

- [84] Y. Fukuda *et al.*, Phys. Rev. Lett. **81**, 1562 (1998).
- [85] Linyan Wan, (2022).
- [86] K. Abe *et al.*, Nuclear Instruments and Methods in Physics Research Section A: Accelerators, Spectrometers, Detectors and Associated Equipment **737**, 253 (2014).
- [87] S. Fukuda *et al.*, Nucl. Instrum. Methods Phys. Res. A **501**, 418 (2003).
- [88] Y. Itow *et al.*, (2001).
- [89] M. Jiang *et al.*, Prog. Theor. Exp. Phys. **2019** (2019).
- [90] S. Fukuda *et al.*, Nuclear Instruments and Methods in Physics Research Section A: Accelerators, Spectrometers, Detectors and Associated Equipment **501**, 418 (2003), <http://www.sciencedirect.com/science/article/pii/S016890020300425X>.
- [91] Y. Nakano *et al.*, Nucl. Instrum. Methods Phys. Res. A **977**, 164297 (2020).
- [92] Hamamatsu, Hamamatsu Photonics Photomultiplier Tubes Handbook.
- [93] K. Abe *et al.*, Nucl. Instrum. Methods Phys. Res. A **1027**, 166248 (2022).
- [94] J. F. Beacom and M. R. Vagins, Phys. Rev. Lett. **93**, 171101 (2004).
- [95] L. Marti *et al.*, Nucl. Instrum. Methods Phys. Res. A **959**, 163549 (2020).
- [96] L. Marti *et al.*, (2019).
- [97] M. Vagins, Solar/DSNB Neutrino\_SK-Gd, 2022.
- [98] J. Focht, PhD thesis, Massachusetts Institute of Technology, 2004.
- [99] T. Tanimori *et al.*, IEEE Transactions on Nuclear Science **36**, 497 (1989).
- [100] Super-Kamiokande Collaboration, J. Hosaka *et al.*, Phys. Rev. D **73**, 112001 (2006).
- [101] H. Nishino *et al.*, Nucl. Instrum. Methods Phys. Res. A **610**, 710 (2009).
- [102] S. Yamada *et al.*, IEEE Transactions on Nuclear Science **57**, 428 (2010).
- [103] S. Yamada, Y. Hayato, Y. Obayashi, and M. Shiozawa, New online system without hardware trigger for the Super-Kamiokande experiment, in *2007 IEEE Nuclear Science Symposium Conference Record*, IEEE, 2007.

- 2774 [104] G. Carminati, Phys. Procedia **61**, 666 (2015).
- 2775 [105] P. A. Čerenkov, Phys. Rev. **52**, 378 (1937).
- 2776 [106] I. Frank and I. Tamm, Coherent visible radiation of fast electrons passing  
2777 through matter, in *Selected Papers*, pp. 29–35, Springer Berlin Heidelberg, Berlin,  
2778 Heidelberg, 1991.
- 2779 [107] The T2K Collaboration, KEK Proposal (2001),  
2780 <http://neutrino.kek.jp/jhfnu/loi/loi.v2.030528.pdf>.
- 2781 [108] Y. Itow *et al.*, (2001), hep-ex/0106019.
- 2782 [109] The K2K Collaboration and S. H. Ahn, (2001), hep-ex/0103001.
- 2783 [110] The T2K Collaboration, KEK Proposal (2006), [http://j-parc.jp/researcher/Hadron/en/pac\\_0606/pdf/p11-Nishikawa.pdf](http://j-parc.jp/researcher/Hadron/en/pac_0606/pdf/p11-Nishikawa.pdf).
- 2785 [111] C. Bronner, Accelerator Neutrino I\_Recent results from T2K, 2022.
- 2786 [112] T2K Collaboration, K. Abe *et al.*, Phys. Rev. Lett. **112**, 061802 (2014),  
2787 <https://link.aps.org/doi/10.1103/PhysRevLett.112.061802>.
- 2788 [113] NINJA Collaboration, T. Fukuda *et al.*, Proposal for precise measurement of  
2789 neutrino-water cross-section in NINJA physics run, Proposal for J-PARC and  
2790 KEK, 2017.
- 2791 [114] T. Ovsiannikova *et al.*, Physics of Particles and Nuclei **48**, 1014 (2017),  
2792 <https://doi.org/10.1134/S1063779617060478>.
- 2793 [115] M. Antonova *et al.*, Journal of Instrumentation **12**, C07028 (2017),  
2794 <http://stacks.iop.org/1748-0221/12/i=07/a=C07028>.
- 2795 [116] The T2K Collaboration, K. Abe *et al.*, Phys. Rev. D **102**, 012007 (2020).
- 2796 [117] K. Abe *et al.*, Progress of Theoretical and Experimental Physics **2021** (2021).
- 2797 [118] The T2K Collaboration, K. Abe *et al.*, Nuclear Instruments  
2798 and Methods in Physics Research Section A: Accelerators, Spectrometers,  
2799 Detectors and Associated Equipment **659**, 106 (2011),  
2800 <http://www.sciencedirect.com/science/article/pii/S0168900211011910>.
- 2801 [119] K. Matsuoka *et al.*, Nuclear Instruments and Methods in Physics Research Section  
2802 A: Accelerators, Spectrometers, Detectors and Associated Equipment **624**, 591

- 2803 (2010), <http://www.sciencedirect.com/science/article/pii/S016890021002098X>.
- 2804 [120] K. Abe *et al.*, Phys. Rev. D. **103** (2021).
- 2805 [121] T. Vladisavljevic, *Predicting the T2K neutrino flux and measuring oscillation parameters* Springer theses, 1 ed. (Springer Nature, Cham, Switzerland, 2020).
- 2806
- 2807 [122] D. Beavis, A. Carroll, and I. Chiang, (1995).
- 2808 [123] P.-A. Amaudruz *et al.*, Nuclear Instruments and Methods in Physics Research  
2809 Section A: Accelerators, Spectrometers, Detectors and Associated Equipment  
2810 **696**, 1 (2012).
- 2811 [124] N. Abgrall *et al.*, Nuclear Instruments and Methods in Physics Research Section  
2812 A: Accelerators, Spectrometers, Detectors and Associated Equipment **637**, 25  
2813 (2011).
- 2814 [125] S. Assylbekov *et al.*, Nuclear Instruments and Methods in Physics Research  
2815 Section A: Accelerators, Spectrometers, Detectors and Associated Equipment  
2816 **686**, 48 (2012).
- 2817 [126] D. Allan *et al.*, Journal of Instrumentation **8**, P10019 (2013).
- 2818 [127] F. Vannucci, Advances in High Energy Physics **2014**, 1 (2014).
- 2819 [128] UA1 magnet sets off for a second new life, 2022.
- 2820 [129] S. Aoki *et al.*, Nuclear Instruments and Methods in Physics Research Section  
2821 A: Accelerators, Spectrometers, Detectors and Associated Equipment **698**, 135  
2822 (2013).
- 2823 [130] K. Suzuki *et al.*, Progress of Theoretical and Experimental Physics **2015**, 53C01  
2824 (2015).
- 2825 [131] S. Brooks, A. Gelman, G. L. Jones, and X.-L. Meng, *Handbook of Markov Chain  
Monte Carlo* (CRC Press, 2011).
- 2826
- 2827 [132] W. R. Gilks, S. Richardson, and D. J. Spiegelhalter, *Markov Chain Monte Carlo in  
Practice* (Chapman & Hall/CRC Interdisciplinary Statistics, 1995).
- 2828
- 2829 [133] C. Wret, *Minimising systematic uncertainties in the T2K experiment using near-  
detector and external data*, PhD thesis, Imperial College London, 2018.
- 2830
- 2831 [134] K. E. Duffy, *Measurement of the Neutrino Oscillation Parameters  $\sin^2 \theta_{23}$ ,  $\Delta m_{32}^2$ ,*

- 2832         $\sin^2 \theta_{13}$ , and  $\delta_{CP}$  in Neutrino and Antineutrino Oscillation at T2K, PhD thesis, Oriel  
2833        College, University of Oxford, 2016.
- 2834 [135] T. Bayes, Rev. Phil. Trans. Roy. Soc. Lond. **53**, 370 (1764).
- 2835 [136] N. Metropolis, A. W. Rosenbluth, M. N. Rosenbluth, A. H. Teller, and E. Teller,  
2836        Journal of Chemical Physics **21** (1970).
- 2837 [137] W. K. Hastings, Biometrika **57** (1970).
- 2838 [138] J. Dunkley, M. Bucher, P. G. Ferreira, K. Moodley, and C. Skordis, Mon. Not. R.  
2839        Astron. Soc. **356**, 925 (2005).
- 2840 [139] Particle Data Group *et al.*, Prog. Theor. Exp. Phys. **2020** (2020).
- 2841 [140] H. Jeffreys, *The Theory of Probability* Oxford Classic Texts in the Physical Sciences  
2842        (, 1939).
- 2843 [141] R. E. Kass and A. E. Raftery, J. Am. Stat. Assoc. **90**, 773 (1995).
- 2844 [142] T. Böhlen *et al.*, Nuclear Data Sheets **120**, 211 (2014),  
2845        <http://www.sciencedirect.com/science/article/pii/S0090375214005018>.
- 2846 [143] R. Brun *et al.*, GEANT: Detector Description and Simulation Tool; Oct 1994 CERN  
2847        Program Library (CERN, Geneva, 1993), <http://cds.cern.ch/record/1082634>,  
2848        Long Writeup W5013.
- 2849 [144] T2K Collaboration, K. Abe *et al.*, Phys. Rev. D **87**, 012001 (2013).
- 2850 [145] C. Zeitnitz and T. Gabriel, Nuclear Instruments and Methods in Physics Research Section A: Accelerators, Spectrometers, Detectors and Associated Equipment **349**, 106 (1994),  
2851        <http://www.sciencedirect.com/science/article/pii/0168900294906130>.
- 2852        http://www.sciencedirect.com/science/article/pii/0168900294906130.
- 2853 [146] A. Fiorentini *et al.*, T2K Technical Note **217** (2017).
- 2854 [147] N. Abgrall *et al.*, Physical Review C **84** (2011).
- 2855 [148] N. Abgrall *et al.*, Physical Review C **85** (2012).
- 2856 [149] N. Abgrall *et al.*, Nuclear Instruments and Methods in Physics Research Section  
2857        A: Accelerators, Spectrometers, Detectors and Associated Equipment **701**, 99  
2858        (2013), <http://www.sciencedirect.com/science/article/pii/S016890021201234X>.
- 2859        http://www.sciencedirect.com/science/article/pii/S016890021201234X.

- 2860 [150] HARP Collaboration, M. Apollonio *et al.*, Phys. Rev. C **80**, 035208 (2009),  
2861 <https://link.aps.org/doi/10.1103/PhysRevC.80.035208>.
- 2862 [151] B. Blau *et al.*, Nuclear Physics B - Proceedings Supplements **113**, 125 (2002).
- 2863 [152] S. Haino *et al.*, Physics Letters B **594**, 35 (2004).
- 2864 [153] NASA, U.S. Standard Atmosphere, 1976, 1976.
- 2865 [154] S. Roesler, R. Engel, and J. Ranft, The Monte Carlo Event Generator DPMJET-III,  
2866 in *Advanced Monte Carlo for Radiation Physics, Particle Transport Simulation and*  
2867 *Applications*, pp. 1033–1038, Springer Berlin Heidelberg, 2001.
- 2868 [155] K. Niita *et al.*, Radiation Measurements **41**, 1080 (2006).
- 2869 [156] T. Sanuki *et al.*, Physics Letters B **541**, 234 (2002).
- 2870 [157] P. Achard *et al.*, Physics Letters B **598**, 15 (2004).
- 2871 [158] K. Sato, Atmospheric Neutrino\_Reviews on neutrino fluxes (low E atm nu),  
2872 2022.
- 2873 [159] Y. Hayato and L. Pickering, The European Physical Journal Special Topics **230**,  
2874 4469 (2021).
- 2875 [160] Y. Hayato, Acta Physica Polonica B **40** (2009).
- 2876 [161] C. L. Smith, Physics Reports **3**, 261 (1972),  
2877 <http://www.sciencedirect.com/science/article/pii/0370157372900105>.
- 2878 [162] O. Benhar, A. Fabrocini, and S. Fantoni, Nuclear Physics A **497**, 423 (1989).
- 2879 [163] R. Bradford, A. Bodek, H. Budd, and J. Arrington, Nuclear  
2880 Physics B - Proceedings Supplements **159**, 127 (2006),  
2881 <http://www.sciencedirect.com/science/article/pii/S0920563206005184>,  
2882 Proceedings of the 4th International Workshop on Neutrino-Nucleus Interac-  
2883 tions in the Few-GeV Region.
- 2884 [164] A. A. Aguilar-Arevalo *et al.*, Physical Review D **81** (2010).
- 2885 [165] R. Gran, J. Nieves, F. Sanchez, and M. J. V. Vacas, Phys. Rev. D **88**, 113007 (2013),  
2886 <https://link.aps.org/doi/10.1103/PhysRevD.88.113007>.
- 2887 [166] C. Berger and L. M. Sehgal, Phys. Rev. D **76**, 113004 (2007).

- 2888 [167] C. Berger and L. M. Sehgal, Phys. Rev. D **79**, 053003 (2009),  
2889 <https://link.aps.org/doi/10.1103/PhysRevD.79.053003>.
- 2890 [168] T. Sjöstrand, Computer Physics Communications **82**, 74 (1994).
- 2891 [169] C. Bronner and M. Hartz, Tuning of the Charged Hadrons Multiplicities for Deep  
2892 Inelastic Interactions in NEUT, in *Proceedings of the 10th International Workshop on*  
2893 *Neutrino-Nucleus Interactions in Few-GeV Region (NuInt15)*, Journal of the Physical  
2894 Society of Japan, 2016.
- 2895 [170] M. Glück, E. Reya, and A. Vogt, The European Physical Journal C **5**, 461 (1998).
- 2896 [171] A. Bodek and U.-k. Yang, Axial and Vector Structure Functions for Electron- and  
2897 Neutrino- Nucleon Scattering Cross Sections at all  $Q^2$  using Effective Leading  
2898 order Parton Distribution Functions, 2010.
- 2899 [172] A. Bodek and U.-K. Yang, (2010).
- 2900 [173] S. Gollapinni, (2016).
- 2901 [174] E. S. P. Guerra *et al.*, Phys. Rev. D **99**, 052007 (2019).
- 2902 [175] GEANT4, S. Agostinelli *et al.*, Nucl. Instrum. Meth. **A506**, 250 (2003).
- 2903 [176] R. Brun, F. Bruyant, M. Maire, A. C. McPherson, and P. Zanarini, (1987).
- 2904 [177] K. Abe *et al.*, Physical Review Letters **121** (2018).
- 2905 [178] K. Abe *et al.*, Physical Review D **91** (2015).
- 2906 [179] R. Patterson *et al.*, Nuclear Instruments and Methods in Physics Research Section  
2907 A: Accelerators, Spectrometers, Detectors and Associated Equipment **608**, 206  
2908 (2009).
- 2909 [180] e. a. S. Berkman, T2K Technical Note **146** (2013).
- 2910 [181] e. a. A. Himmel, T2K Technical Note **219** (2015).
- 2911 [182] F. a. James, (1998), CERN Program Library Long Writeups.
- 2912 [183] X. Li and M. Wilking, T2K Technical Note **319** (2017).
- 2913 [184] S. Tobayama, *An Analysis of the Oscillation of Atmospheric Neutrinos*, PhD thesis,  
2914 British Columbia U., 2016.

- <sup>2915</sup> [185] e. a. D. Barrow, T2K Technical Note **399** (2020).
- <sup>2916</sup> [186] A. Maghrabi, A. Aldosari, and M. Almutairi, Advances in Space Research **68**, 2941 (2021).
- <sup>2918</sup> [187] Super-Kamiokande Collaboration, K. Abe *et al.*, Phys. Rev. D **97**, 072001 (2018), <https://link.aps.org/doi/10.1103/PhysRevD.97.072001>.
- <sup>2920</sup> [188] Particle Data Group, J. Beringer *et al.*, Phys. Rev. D **86**, 010001 (2012).
- <sup>2921</sup> [189] Y. N. and, Journal of Physics: Conference Series **888**, 012191 (2017).
- <sup>2922</sup> [190] M. Jiang, *Study of the neutrino mass hierarchy with the atmospheric neutrino data collected in Super-Kamiokande IV*, PhD thesis, Kyoto University, 2019.
- <sup>2924</sup> [191] S. N. K. Iyogi and Y. Obayashi., T2K Technical Note **027** (2011).
- <sup>2925</sup> [192] LeeKaPik, *Study of the neutrino mass hierarchy with the atmospheric neutrino data observed in Super-Kamiokande*, PhD thesis, Tokyo University, 2012.
- <sup>2927</sup> [193] The Super-Kamiokande Collaboration, R. Wendell *et al.*, Phys. Rev. D **81**, 092004 (2010).
- <sup>2929</sup> [194] Super-Kamiokande Collaboration, J. Hosaka *et al.*, Phys. Rev. D **74**, 032002 (2006).
- <sup>2931</sup> [195] L. M. et al, T2K Technical Note **395** (2020).
- <sup>2932</sup> [196] P. B. et al., T2K Technical Note **212** (2015).
- <sup>2933</sup> [197] W. Parker, *Constraining Systematic Uncertainties at T2K using Near Detector Data*, PhD thesis, Royal Holloway University of London, 2020.
- <sup>2935</sup> [198] V. B. et al., T2K Technical Note **246** (2015).
- <sup>2936</sup> [199] J. Missert, T2K Technical Note **318** (2017).
- <sup>2937</sup> [200] e. a. J. Chakrani, T2K Technical Note **414** (2022).
- <sup>2938</sup> [201] T2K Collaboration, M. Wascko, T2K Status, Results, and Plans, Neutrino 2018, 2018.
- <sup>2940</sup> [202] e. a. Tomislav Vladisavljevic, T2K Technical Note **354** (2020).
- <sup>2941</sup> [203] G. Ambrosini *et al.*, Phys. Lett. B **420**, 225 (1998).

- 2942 [204] e. a. Edward Atkin, T2K Technical Note **344** (2019).
- 2943 [205] e. a. D. Barrow, T2K Technical Note **422** (2022).
- 2944 [206] The MiniBooNE Collaboration, A. A. Aguilar-Arevalo *et al.*, Phys. Rev. D **81**,  
2945 013005 (2010), <https://link.aps.org/doi/10.1103/PhysRevD.81.013005>.
- 2946 [207] P. de Perio and J. Imber, T2K Technical Note **186** (2014).
- 2947 [208] P. de Perio and J. Imber, T2K Technical Note **107** (2012).
- 2948 [209] C. V. Daniel Barrow, T2K-SK Detector Matrix Uncertainties - MaCh3 In-  
2949 tegration, <https://git.t2k.org/t2k-sk/t2ksk-detcovmat/-/tree/feature/MaCh3Integration>, Accessed: 22-06-2022.
- 2950
- 2951 [210] R. Wendell, *Three Flavor Oscillation Analysis of Atmospheric Neutrinos in Super-*  
2952 *Kamiokande*, PhD thesis, University of North Carolina, 2008.
- 2953 [211] A. M. Dziewonski and D. L. Anderson, Phys. Earth Planet. Inter. **25**, 297 (1981).
- 2954 [212] e. a. D. Barrow, T2K Technical Note **425** (2022).
- 2955 [213] R. G. Calland, A. C. Kaboro, and D. Payne, **9**, P04016 (2014).
- 2956 [214] R. Wendell, <http://www.phy.duke.edu/raw22/public/Prob3++/>.
- 2957 [215] F. Kallenborn, C. Hundt, S. Böser, and B. Schmidt, Computer Physics Communi-  
2958 cations **234**, 235 (2019).
- 2959 [216] L. Warsame, MaCh3 Analysis Progress.
- 2960 [217] S. Bourret, J. A. B. Coelho, and V. V. E. and, Journal of Physics: Conference Series  
2961 **888**, 012114 (2017).
- 2962 [218] C. Rott, A. Taketa, and D. Bose, Scientific Reports **5** (2015).
- 2963 [219] K. Hagiwara, N. Okamura, and K. ichi Senda, Journal of High Energy Physics  
2964 **2011** (2011).
- 2965 [220] D. Typinski, Earth Gravity, <http://www.typnet.net/Essays/EarthGravGraphics/EarthGrav.pdf>, Accessed: 24-06-2022.
- 2966
- 2967 [221] R. Barlow and C. Beeston, Comput. Phys. Commun. **77**, 219 (1993).
- 2968 [222] J. S. Conway, Incorporating nuisance parameters in likelihoods for multisource

2969

*spectra*, 2011.

# 2970 List of Figures

2971 2.1	The cross-section of neutrinos from various natural and man-made 2972 sources as a function of neutrino energy. Taken from [25] . . . . .	10
2973 2.2	The solar neutrino flux as a function of neutrino energy for various 2974 fusion reactions and decay chains as predicted by the Standard Solar 2975 Model. Taken from [26]. . . . .	11
2976 2.3	Left panel: The atmospheric neutrino flux for different neutrino flavours 2977 as a function of neutrino energy as predicted by the 2007 Honda model 2978 (“This work”) [43], the 2004 Honda model (“HKKM04”) [44], the Bartol 2979 model [42] and the FLUKA model [46]. Right panel: The ratio of the 2980 muon to electron neutrino flux as predicted by all the quoted models. 2981 Both figures taken from [43]. . . . .	14
2982 2.4	A diagram illustrating the definition of zenith angle as used in the Super 2983 Kamiokande experiment [47]. . . . .	14
2984 2.5	Prediction of $\nu_e, \bar{\nu}_e, \nu_\mu, \bar{\nu}_\mu$ fluxes as a function of zenith angle as cal- 2985 culated by the HKKM model [45]. The left, middle and right pan- 2986 els represent three values of neutrino energy, 0.32GeV, 1.0GeV and 2987 3.2GeV respectively. Predictions for other models including Bartol [42], 2988 Honda [43] and FLUKA [46] are given in [47]. . . . .	15
2989 2.6	Constraints on the atmospheric oscillation parameters, $\sin^2(\theta_{23})$ and 2990 $\Delta m_{23}^2$ , from atmospheric and long baseline experiments: SK [52], T2K 2991 [53], NO $\nu$ A [54], IceCube [55] and MINOS [56]. Figure taken from [57].	16
2992 2.7	Reactor electron antineutrino fluxes for $^{235}\text{U}$ (Black), $^{238}\text{U}$ (Green), $^{239}\text{Pu}$ 2993 (Purple), and $^{241}\text{Pu}$ (Orange) isotopes. The inverse $\beta$ -decay cross-section 2994 (Blue) and corresponding measurable neutrino spectrum (Red) are also 2995 given. Top panel: Schematic of Inverse $\beta$ -decay interaction including 2996 the eventual capture of the emitted neutron. This capture emits a $\gamma$ -ray 2997 which provides a second signal of the event. Taken from [69]. . . . .	19
2998 3.1	A schematic diagram of the Super-Kamiokande Detector. Taken from [88].	25

2999	3.2	The location of “standard PMTs” (red) inside the SK detector. Taken from [86]. . . . .	29
3000			
3001	3.3	Schematic view of the data flow through the data acquisition and online system. Taken from [102]. . . . .	32
3002			
3003	3.4	The cross-section view of the Tokai to Kamioka experiment illustrating the beam generation facility at J-PARC, the near detector situated at a baseline of 280m and the Super Kamiokande far detector situated 295km from the beam target. . . . .	35
3004			
3005			
3006			
3007	3.5	The near detector suite for the T2K experiment showing the ND280 and INGRID detectors. The distance between the detectors and the beam target is 280m. . . . .	36
3008			
3009			
3010	3.6	Top panel: Bird’s eye view of the most relevant part of primary and secondary beamline used within the T2K experiment. The primary beamline is the main-ring proton synchrotron, kicker magnet, and graphite target. The secondary beamline consists of the three focusing horns, decay volume, and beam dump. Figure taken from [118]. Bottom panel: The side-view of the secondary beamline including the focusing horns, beam dump and neutrino detectors. Figure taken from [119]. . . . .	38
3011			
3012			
3013			
3014			
3015			
3016			
3017	3.7	The Monte Carlo prediction of the energy spectrum for each flavour of neutrino ( $\nu_e$ , $\bar{\nu}_e$ , $\nu_\mu$ and $\bar{\nu}_\mu$ ) in the neutrino dominated beam FHC mode (Left) and antineutrino dominated beam RHC mode (Right) expected at SK. Taken from [120]. . . . .	39
3018			
3019			
3020			
3021	3.8	Top panel: T2K muon neutrino disappearance probability as a function of neutrino energy. Middle panel: T2K electron neutrino appearance probability as a function of neutrino energy. Bottom panel: The neutrino flux distribution for three different off-axis angles (Arbitrary units) as a function of neutrino energy. . . . .	41
3022			
3023			
3024			
3025			
3026	3.9	The components of the ND280 detector. The neutrino beam travels from left to right. Taken from [118]. . . . .	42
3027			
3028	3.10	Comparison of data to Monte Carlo prediction of integrated deposited energy as a function of track length for particles that stopped in FGD1. Taken from [123]. . . . .	44
3029			
3030			

3031	3.11 Schematic design of a Time Projection Chamber detector. Taken from [124].	45
3032	3.12 The distribution of energy loss as a function of reconstructed momentum for charged particles passing through the TPC, comparing data to Monte Carlo prediction. Taken from [124].	45
3033		
3034		
3035	3.13 A schematic of the P0D side-view. Taken from [125].	47
3036	3.14 Left panel: The Interactive Neutrino GRID on-axis Detector. 14 modules are arranged in a cross-shape configuration, with the center modules being directly aligned with the on-axis beam. Right panel: The layout of a single module of the INGRID detector. Both figures are recreated from [118].	49
3037		
3038		
3039		
3040		
3041	4.1 Example of using Monte Carlo techniques to find the area under the blue line. The gradient and intercept of the line are 0.4 and 1.0 respectively. The area found to be under the curve using one thousand samples is 29.9 units.	54
3042		
3043		
3044		
3045	4.2 The area under a line of gradient 0.4 and intercept 1.0 for the range $0 \leq x \leq 10$ as calculated using Monte Carlo techniques as a function of the number of samples used in each repetition. The analytical solution to the area is 30 units as given by the red line.	54
3046		
3047		
3048		
3049	4.3 Three MCMC chains, each with a stationary distribution equal to a Gaussian centered at 0 and width 1 (As indicated by the black dotted lines). All of the chains use a Gaussian proposal function but have different widths (or 'step size $\sigma$ '). The top panel has $\sigma = 0.1$ , middle panel has $\sigma = 0.5$ and the bottom panel has $\sigma = 5.0$ .	60
3050		
3051		
3052		
3053		
3054	4.4 The log-likelihood from the fit detailed in <a href="#">DB: Link to AsimovA Sensitivity Section</a> as a function of the number of steps accumulated in each fit. Many independent MCMC chains were run in parallel and overlaid on this plot. The red line indicates the $1 \times 10^5$ step burn-in period after which the log-likelihood becomes stable.	61
3055		
3056		
3057		
3058		

---

3059	4.5 Left: The two dimensional probability distribution for two correlated parameters $x$ and $y$ . The red distribution shows the two dimensional probability distribution when $0 \leq x \leq 5$ . Right: The marginalised probability distribution for the $y$ parameter found when requiring the $x$ to be bound between $-5 \leq x \leq 5$ and $0 \leq x \leq 5$ for the black and red distribution, respectively. . . . .	63
3060		
3061		
3062		
3063		
3064		
3065	5.1 The NEUT prediction of the $\nu_\mu$ -H <sub>2</sub> O cross-section overlaid on the T2K $\nu_\mu$ flux. The charged current (black, solid) and neutral current (black, dashed) inclusive, charged current quasi-elastic (blue, solid), charged current 2p2h (blue, dashed), charged current single pion production (pink), and charged current multi- $\pi$ and DIS (Purple) cross-sections are illustrated. Figure taken from [159]. . . . .	71
3066		
3067		
3068		
3069		
3070		
3071	5.2 Illustration of the various processes which a pion can undergo before exiting the nucleus. Taken from [173]. . . . .	72
3072		
3073	5.3 Event displays from Super Kamiokande illustrating the “crisp” ring from a muon and the typically “fuzzier” electron ring. Each pixel represents a PMT and the color scheme denotes the accumulated charge deposited on that PMT. Figures taken from [181]. . . . .	75
3074		
3075		
3076		
3077	5.4 The difference of the electron-like and muon-like log-likelihood compared to the reconstructed single-ring fit momentum for atmospheric $\nu_e$ (left) and $\nu_\mu$ (right) samples. The black line represents the cut used to discriminate electron-like and muon-like events, which coefficients obtained from Monte Carlo studies. Figures taken from [180]. . . . .	80
3078		
3079		
3080		
3081		
3082	5.5 The electron/muon PID separation parameter for all sub-GeV single-ring events in SK-IV. The charged current (CC) component is broken down in four flavours of neutrino ( $\nu_\mu$ , $\bar{\nu}_\mu$ , $\nu_e$ and $\bar{\nu}_e$ ). Events with positive values of the parameter are determined to be electron-like. . . . .	80
3083		
3084		
3085		
3086	5.6 The variation of the measured dark rate as a function of date, broken down by PMT type. The SK-IV and SK-V periods span September 2008 to May 2018 and January 2019 to July 2020, respectively. The break in measurement in 2018 corresponds to the period of tank repair and refurbishment. Figure adapted from [185]. . . . .	83
3087		
3088		
3089		
3090		

3091	5.7 Comparison of the measured raw charge deposited per event from the 3092 stopping muon data samples between SK-IV (Blue) and SK-V (Red), 3093 split by the primary muon subevent and the associated decay electron 3094 subevent. . . . .	84
3095	5.8 The distribution of the reconstructed momentum from the muon ring 3096 divided by the distance between the reconstructed muon and decay 3097 electron vertices as found in the stopping muon data sets of SK-IV 3098 (Black) and SK-IV (Red). Only events with one tagged decay electron are 3099 considered. A Gaussian fit is considered in the range [2.0, 2.4] MeV/cm 3100 and illustrated as the solid curve. . . . .	85
3101	5.9 The $\chi^2$ difference between the SK-IV and SK-V reconstructed muon 3102 momentum divided by range when the SK-V is modified by the scaling 3103 parameter $\alpha$ . Both additive (Blue) and multiplicative (Black) scaling 3104 factors have been considered. In practice, the additive scaling factor 3105 actually uses the value of $(\alpha - 1.0)$ but is illustrated like this so the 3106 results can be shown on the same axis range. . . . .	86
3107	5.10 A depiction of the topology patterns for fully-contained (FC), partially- 3108 contained (PC) and up-going muon (Up- $\mu$ ) samples included in this 3109 analysis. . . . .	87
3110	5.11 The predicted neutrino flux of the fully contained (FC) sub-GeV and 3111 multi-GeV, partially contained (PC), and upward-going muon (Up- $\mu$ ) 3112 events. The prediction is broken down by the $\nu_x \rightarrow \nu_e$ prediction (top 3113 left), $\nu_x \rightarrow \nu_\mu$ prediction (top right) and $\nu_x \rightarrow \nu_\tau$ prediction (bottom). 3114 Asimov A oscillation parameters are assumed (given in Table 2.2). . . .	89
3115	5.12 The predicted flux of beam neutrinos, as a function of neutrino energy. 3116 The predictions are broken down by the number of decay electrons 3117 associated with the particular events. Asimov A oscillation parameters 3118 are assumed (given in Table 2.2). . . . .	91

3119      6.1	The accumulated beam data, measured as the number of protons on target (POT). The total data (blue) is given which comprises of the neutrino beam (red) and antineutrino (purple) components. The beam power for neutrino and antineutrino beams is given as the markers using the same colour scheme. The timescale runs from Run 1 which started in January 2010 until Run 10 which ended in February 2020. The ratio of accumulated data in neutrino and antineutrino beam is 54.7% : 45.3%. . . . .	93
3127      6.2	Comparison of the SK-IV atmospheric samples between predictions made with the CP-violating Asimov A (Black) and CP-conserving Asimov B (Red) oscillation parameter sets (given in Table 2.2). The subGeV samples CCRES and $\pi^0$ -like samples are given in their reconstructed lepton momentum. All other samples are presented in their reconstructed zenith angle projection. . . . .	100
3133      6.3	The nominal Monte Carlo predictions for the FGD1 and FGD2 samples in neutrino beam mode, broken down into the $CC\nu_\mu 0\pi$ , $CC\nu_\mu 1\pi$ and $CC\nu_\mu$ Other categories. Figures taken from [195]. . . . .	103
3136      6.4	The reconstructed neutrino energy, as defined by Equation 6.2 and Equation 6.3, for the $1R\mu$ -like, $1Re$ -like and $CC1\pi^+$ -like samples. Asimov A oscillation parameter sets are assumed (given in Table 2.2). These samples are the FHC mode samples. For ease of viewing, the $1R\mu$ sample only shows the $0. \leq E_\nu^{rec} < 3.0\text{GeV}$ but the binning extends to $30.0\text{GeV}$ . . . . .	106
3141      6.5	The distribution of the angle between the neutrino beam direction and the reconstructed final state lepton, for the FHC $1Re$ -like sample. The distribution is broken down by neutrino interaction mode into charged current (left) and neutral current (right) components. Asimov A oscillation parameter sets are assumed (given in Table 2.2). <b>DB: Is this needed or will it just bring up more questions?</b> . . . . .	108
3147      6.6	The total uncertainty evaluated on the near detector $\nu_\mu$ flux prediction constrained by the replica-target data, illustrated as a function of neutrino energy. The solid(dashed) line indicates the uncertainty used within this analysis(the T2K 2018 analysis [201]). The solid histogram indicates the neutrino flux as a function of energy. Figure taken from [202]. . . . .	110

3152	6.7	The predicted neutrino energy distribution for subGeV atmospheric and beam samples. FHC and RHC beam samples are summed together Asimov A oscillation parameters are assumed (given in Table 2.2). Beam and atmospheric samples with similar cuts are compared against one another. . . . .	115
3157	6.8	The interaction mode contribution of each sample given as a fraction of the total event rate in that sample. Asimov A oscillation parameters are assumed (given in Table 2.2). The Charged Current (CC) modes are broken into quasi-elastic (QE), 2p2h, resonant charged pion production ( $1\pi^\pm$ ), multi-pion production ( $M\pi$ ), and other interaction categories. Neutral Current (NC) interaction modes are given in interaction mode categories: $\pi^0$ production, resonant charged pion production, multi-pion production, and others. . . . .	116
3165	6.9	Down-going atmospheric subGeV single-ring samples comparing the mean and error of the pre-fit and post-fit Monte Carlo predictions in red and blue, respectively. The magenta histogram illustrates the Monte Carlo prediction using the generated dial values. The black points illustrate the down-going data with statistical errors given. The mean and errors of the Monte Carlo predictions are calculated by the techniques documented in subsection 4.3.4. The pre-fit spectrum is calculated by throwing the cross-section and atmospheric flux dial values from the pre-fit covariance matrix. The post-fit spectrum is calculated by sampling the cross-section dial values from an ND fit MCMC chain, whilst still throwing the atmospheric flux dials from the pre-fit covariance. . . . .	119
3177	6.10	The ring counting parameter as defined in Equation 6.6 for the SubGeV-elike-0dcy and MultiRing-elike-nue samples. . . . .	128
3179	6.11	The ring counting parameter, defined in Equation 6.6, as a function of the number of reconstructed rings as found by the <code>fitQun</code> reconstruction algorithm. Left: true $\nu_\mu$ events with only one muon above the Cherenkov threshold in the final state. Right: true $\nu_\mu$ events with one muon and at least one other charged particle above the Cherenkov threshold in the final state. . . . .	129

3185	6.12 The $\chi^2$ between the hybrid- $\pi^0$ Monte Carlo and data samples, as a function of smear ( $\alpha$ ) and shift ( $\beta$ ) parameters, for events which have 1 $\pi^0$ final state topology. Left: Electron-muon separation PID parameter for events with $30 \geq E_{vis}(\text{MeV}) < 300$ . Right: Electron- $\pi^0$ separation PID parameter for events with $30 \geq E_{vis}(\text{MeV}) < 300$ . . . . .	130
3186		
3187		
3188		
3189		
3190	6.13 The distribution of $\log(L_e/L_\mu)$ compared to $\log(L_e/L_\pi)$ for subGeV events with zero (top left), one (top right) or two (bottom) decay electrons. The correlation in the distribution is calculated as 0.997, 0.999 and 0.996, respectively. . . . .	131
3191		
3192		
3193		
3194	7.1 The density of the Earth given as a function of the radius, as given by the PREM model (Black), and the constant density four-layer approximation (Blue), as used in the official SK-only analysis. . . . .	135
3195		
3196		
3197	7.2 An “oscillogram” that depicts the $P(\nu_\mu \rightarrow \nu_e)$ oscillation probability as a function of neutrino energy and cosine of the zenith angle. The zenith angle is defined such that $\cos(\theta_Z) = 1.0$ represents neutrinos that travel from directly above the detector. The four-layer constant density PREM model approximation is used and Asimov A oscillation parameters are assumed (Table 2.2). . . . .	136
3198		
3199		
3200		
3201		
3202		
3203	7.3 The effect of $\delta_{CP}$ for atmospheric neutrinos given in terms of the neutrino energy and zenith angle. This oscillogram compares the $P(\nu_\mu \rightarrow \nu_e)$ oscillation probability for a CP conserving ( $\delta_{CP} = 0.0$ ) and a CP violating ( $\delta_{CP} = -1.601$ ) value taken from the Asimov A parameter set. The other oscillation parameters assume the Asimov A oscillation parameter set given in Table 2.2. . . . .	137
3204		
3205		
3206		
3207		
3208		

3209      7.4	An illustration of the matter-induced effects on the oscillation probability, given as a function of neutrino energy and zenith angle. The top row of panels gives the $P(\nu_e \rightarrow \nu_e)$ oscillation probability and the bottom row illustrates the $P(\bar{\nu}_e \rightarrow \bar{\nu}_e)$ oscillation probability. The left column highlights the oscillation probability in a vacuum, whereas the middle and right column represents the oscillation probabilities when the four-layer fixed density PREM model is assumed. All oscillation probabilities assume the “Asimov A” set given in Table 2.2, but importantly, the right column sets an inverted mass hierarchy. The “matter resonance” effects at $E_\nu \sim 5\text{GeV}$ can be seen in the $P(\nu_e \rightarrow \nu_e)$ for normal mass hierarchy and $P(\bar{\nu}_e \rightarrow \bar{\nu}_e)$ for inverted hierarchy. . . . .	138
3220      7.5	The oscillation probability for beam neutrino events given as a function of neutrino energy. All oscillation parameters assume the “Asimov A” set given in Table 2.2 unless otherwise stated. Each panel represents a change in one of the oscillation parameters whilst keeping the remaining parameters fixed. . . . .	139
3225      7.6	The number of electron-like events in the FHC and RHC operating mode of the beam, as a function of the oscillation probabilities. Both normal hierarchy (Solid) and inverse hierarchy (Dashed) values of $\Delta m_{23}^2$ are given. . . . .	140
3229      7.7	The oscillation probability $P(\nu_\mu \rightarrow \nu_e)$ , given as a function of neutrino energy and zenith angle, which highlights an example of the “fast” oscillations in the sub-GeV upgoing region. . . . .	142
3232      7.8	Illustration of the averaging procedure for $N = 2$ . The oscillation probabilities calculated on the finer left binning are averaged to obtain the oscillation probabilities in the coarser right binning. These averaged oscillation probabilities with the coarser binning are then applied to each event during the fit. . . . .	144
3237      7.9	Event rate of the SubGeV_elike_0dcy sample as a function of the number of sub-divisions per coarse bin. Each subplot represents the event rate of the sample at a different oscillation parameter set thrown from the PDG priors detailed in Table 2.1. The red line in each subplot represents the mean of the event rate over the different values of subdivisions for that particular oscillation parameter throw. . . . .	146

3243	7.10 Variance of event rate for each atmospheric sample as a function of the number of sub-divisions per coarse bin. The solid red line indicates the 0.1% threshold and the dashed red line indicates the variance at a sub-division $N = 10$ . . . . .	147
3247	7.11 Variance of sample likelihood, when compared to ‘Asimov data’ set at Asimov A, for each atmospheric sample as a function of the number of sub-divisions per coarse bin. The solid red line indicates the 0.1% threshold and the dashed red line is a graphical indication of the variance at a sub-division $N = 10$ . . . . .	148
3252	7.12 The oscillation probability, $P(\nu_\mu \rightarrow \nu_e)$ (top row) and $P(\nu_e \rightarrow \nu_e)$ (bottom row), given as a function of neutrino energy and zenith angle. The left column gives the “fine” binning used to calculate the oscillation probabilities and the right column illustrates the “coarse” binning used to reweight the Monte Carlo events. The fine binning choice is given with $N = 10$ , which was determined to be below the threshold from Figure 7.10 and Figure 7.11. . . . .	149
3259	7.13 The calculation time taken to both calculate the oscillation probabilities and fill the “coarse” oscillograms, following the technique given in section 7.2, for the CUDAProb3 and ProbGPU (Red) calculation engines. CUDAProb3 has both a GPU (Blue) and CPU (Black) implementation, where the CPU implementation is multithreaded. Therefore, 8-threads (solid) and 40-threads (dashed) configurations have been tested. Prob3, which is a CPU single-thread implementation has a mean step time of 1.142s. . . . .	150
3267	7.14 The oscillation probability, $P(\nu_\mu \rightarrow \nu_e)$ (top row) and $P(\nu_e \rightarrow \nu_e)$ (bottom row), given as a function of neutrino energy and zenith angle. The left column gives probabilities where the constant $Z/A = 0.5$ approximation which is used in the official SK-only analysis. The middle column gives the probabilities where $Z/A = [0.468, 0.498]$ values are used, as given in Table 7.1. The right column illustrates the difference in oscillation probability between the two different techniques. . . . .	152

- 3274     7.15 The density of the Earth given as a function of the radius, as given by  
3275       the PREM model (Black), the constant density four-layer approxima-  
3276       tion (Blue), as used in the official SK-only analysis, and the quadratic  
3277       approximation of the PREM model (Red). . . . . 153
- 3278     7.16 The oscillation probability,  $P(\nu_\mu \rightarrow \nu_e)$  (top row) and  $P(\nu_e \rightarrow \nu_e)$  (bot-  
3279       tom row), given as a function of neutrino energy and zenith angle. The  
3280       left column gives probabilities where the four-layer constant density ap-  
3281       proximation is used. The middle column gives the probabilities where  
3282       the density is integrated over the trajectory, using the quadratic PREM  
3283       approximation, for each  $\cos(\theta_Z)$  is used. The right column illustrates the  
3284       difference in oscillation probability between the two different techniques. 155
- 3285     7.17 The oscillation probability,  $P(\nu_\mu \rightarrow \nu_e)$  (top row) and  $P(\nu_e \rightarrow \nu_e)$  (bot-  
3286       tom row), given as a function of neutrino energy and zenith angle. The  
3287       left column gives probabilities where a fixed production height of 25km  
3288       is used. The middle column gives the probabilities where the produc-  
3289       tion height is analytically averaged. The right column illustrates the  
3290       difference in oscillation probability between the two different techniques. 159

# **List of Tables**

3292	2.1	The 2018 Particle Data Group constraints of the oscillation parameters taken from [81]. The value of $\Delta m_{23}^2$ is given for both normal hierarchy (N.H.) and inverted hierarchy (I.H.) and $\sin^2(\theta_{23})$ is broken down by whether its value is below (Q1) or above (Q2) 0.5. . . . .	21
3296	2.2	Reference values of the neutrino oscillation parameters for two different oscillation parameter sets. . . . .	22
3298	3.1	The various SK periods and respective live-time. The SK-VI live-time is calculated until 1 <sup>st</sup> April 2022. SK-VII started during the writing of this thesis. . . . .	24
3301	3.2	The trigger thresholds and extended time windows saved around an event which were utilised throughout the SK-IV period. The exact thresholds can change and the values listed here represent the thresholds at the start and end of the SK-IV period. . . . .	33
3305	3.3	The threshold momentum and energy for a particle to generate Cherenkov light in ultrapure water, as calculated in Equation 3.2 in ultrapure water which has refractive index $n = 1.33$ . . . . .	34
3308	4.1	Jeffreys scale for strength of preference for two models $A$ and $B$ as a function of the calculated Bayes factor ( $B_{AB} = B(A/B)$ ) between the two models [140]. The original scale is given in terms of $\log_{10}(B(A/B))$ but converted to linear scale for easy comparison throughout this thesis.	66
3312	6.1	The amount of data collected in each detector used within this analysis. The data collected at the near and far detector, for both neutrino beam (FHC) and antineutrino beam (RHC), is measured as the number of protons on target (POT). . . . .	92
3316	6.2	The fully contained subGeV samples, defined as events with visible energy $E_{vis} < 1.33\text{GeV}$ , used within this oscillation analysis. . . . .	95

3318      6.3	The fully contained multiGeV samples used within this oscillation analysis. Both the sample name and description are given. . . . .	97
3319		
3320      6.4	The purity of each atmospheric sample used within this analysis, broken down by charged current (CC) and neutral current (NC) interactions and which neutrino flavour interacted within the detector. Asimov A oscillation parameter sets are assumed (given in Table 2.2). Electron neutrino and antineutrino events are separated to illustrate the ability of the separation likelihood cuts used within the multiGeV and multiring sample selections. . . . .	98
3321		
3322		
3323		
3324		
3325		
3326		
3327      6.5	The reconstructed cosine zenith and lepton momentum binning assigned to the atmospheric samples. The “ $\cos(\theta_Z)$ Bins” column illustrates the number of bins uniformly distributed over the $-1.0 \leq \cos(\theta_Z) \leq 1.0$ region for fully and partially contained samples and $-1.0 \leq \cos(\theta_Z) \leq 0.0$ region for up- $\mu$ samples. <b>DB: Does this belong in the appendix?</b> . . . . .	99
3328		
3329		
3330		
3331		
3332		
3333      6.6	The neutrino energy binning for the different neutrino flavours. “Right” sign indicates neutrinos in the FHC beam and antineutrinos in the RHC beam. “Wrong” sign indicates antineutrinos in the FHC beam and neutrinos in the RHC beam. The binning of the detector response is identical for the FHC and RHC modes as well as at ND280 and SK. . .	111
3334		
3335		
3336		
3337		
3338      6.7	List of cut variables that are included within the shift/smear fit documented in [199]. . . . .	121
3339		
3340      6.8	Reconstructed event topology categories on which the SK detector systematics [199] are based. . . . .	122
3341		
3342      6.9	Sources of systematic errors specified within the grouped into the “calibration” systematics model. . . . .	125
3343		
3344      6.10	Visible energy binning for which the correlated SK detector systematics are based . . . . .	126
3345		
3346      7.1	Description of the four layers of the Earth invoked within the constant density approximation of the PREM model [211]. . . . .	134
3347		

